Thesis for the degree of Doctor of Philosophy

Effects of Irradiation and Thermal Ageing on the Nanoscale Chemistry of Steel Welds

Kristina Lindgren

Department of Physics

Chalmers University of Technology

Göteborg, Sweden 2018

Effects of Irradiation and Thermal Ageing on the Nanoscale Chemistry of Steel Welds
Kristina Lindgren

ISBN 978-91-7597-825-3

Doktorsavhandlingar vid Chalmers tekniska högskola
Ny serie nr 4506
ISSN 0346-718X

Department of Physics
Chalmers University of Technology
SE-412 96 Göteborg
Sweden
Telephone + 46 (0)31-772 1000

Cover illustration
Left: an atom probe tomography reconstruction of the irradiated Ringhals R4 reactor pressure vessel surveillance material. The enlarged volume is $10 \times 10 \times 10\,\mathrm{nm}^3$. Middle: thermally aged Ringhals R4 pressurizer weld metal. Right: irradiated Zorita core barrel weld, a loop is shown in the box. All isoconcentration surface thresholds and identities are given in the figure.

Printed by Chalmers Reproservice
Göteborg, Sweden 2018

Effects of Irradiation and Thermal Ageing on the Nanoscale Chemistry of Steel Welds
Kristina Lindgren
Department of Physics
Chalmers University of Technology

Abstract

Structural materials of nuclear power plants degrade during operation due to thermal ageing and irradiation from the reactor core. Effects on the materials are an increase in hardness and tensile strength, and a decrease in ductility and fracture toughness, i. e. embrittlement. The degradation of the mechanical properties stems from changes in the microstructure. In this thesis, the effects of thermal ageing and irradiation on the nanoscale chemistry has been studied using atom probe tomography (APT).

During irradiation, nanometre sized clusters are formed in the reactor pressure vessel (RPV) welds. As the RPV is a life-limiting part of a nuclear power plant, neutron irradiation with high flux is attractive for accelerated studies. Here, the effect of high flux is found to result in a higher number density of smaller NiMnSi-rich clusters for the high Ni and Mn - low Cu welds from Ringhals R4, resulting in similar hardening compared to surveillance material. It is also found that there are some *stable matrix defects* formed in the high flux material, contributing to the embrittlement. The cluster evolution showed no signs of *late blooming phases* (an accelerated degradation at high fluences). Furthermore, thermal ageing during operation for 28 years of a weld from the former Ringhals R4 pressurizer with similar composition is found to result in clusters forming mainly on dislocations, hardening the weld metal.

In ferrite with higher Cr-content, such as the ferritic parts of the mainly austenitic welds from the core barrel of the decommissioned Spanish reactor José Cabrera, spinodal decomposition occurs as well as G-phase ($Ni_{16}Si_7Mn_6$) precipitation. Weld metals irradiated up to 2 dpa are compared with thermally aged welds, confirming that the irradiation is considerably contributing to the changes in the microstructure. After 0.15 dpa, the spinodal decomposition was well developed, and the Cr concentration in the ferrite was found to influence the wavelength more than the difference in irradiation (0.15 to 2 dpa). The G-phase precipitates were more well-developed after 1 dpa neutron irradiation, but no difference could be distinguished between the material irradiated to 1 and 2 dpa.

Keywords: reactor pressure vessel, irradiation damage, thermal ageing, clustering, atom probe tomography, low alloy steel, core barrel, spinodal decomposition

Preface

The research work presented in this thesis was carried out at the Division of Materials Microstructure at the Department of Physics, Chalmers University of Technology, during the time period June 2014 - December 2018, under the supervision of Associate Professor Mattias Thuvander and Professor Krystyna Stiller.

List of appended papers

I. *On the analysis of clustering in an irradiated low alloy reactor pressure vessel steel weld*
K. Lindgren, K. Stiller, P. Efsing, and M. Thuvander
Microscopy and Microanalysis 23, 376-384 (2017)

II. *Evolution of precipitation in reactor pressure vessel steel welds under neutron irradiation*
K. Lindgren, M. Boåsen, K. Stiller, P. Efsing, and M. Thuvander
Journal of Nuclear Materials 488, 222-230 (2017)

III. *Cluster formation in in-service thermally aged pressurizer welds*
K. Lindgren, M. Boåsen, K. Stiller, P. Efsing, and M. Thuvander
Journal of Nuclear Materials 504, 23-28 (2018)

IV. *Thermal ageing of low alloy steel weldments from a Swedish nuclear power plant - the evolution of the microstructure*
K. Lindgren, M. Boåsen, K. Stiller, P. Efsing, and M. Thuvander
Proceedings of Fontevraud 9: Contribution of Materials Investigations and Operating Experience to Light Water NPPs Safety, Performance and Reliability (2018)

V. *Post irradiation annealing of high flux irradiated reactor pressure vessel weld*
K. Lindgren, M. Boåsen, P. Efsing, K. Stiller, and M. Thuvander
In manuscript

VI. *Integrated effect of thermal ageing and low flux irradiation on microstructural evolution of welded stainless steels*
K. Lindgren, M. Bjurman, P. Ekström, P. Efsing, and M. Thuvander
In manuscript

Publications not included in this thesis

Development of matrix microstructure in polycrystalline cubic boron nitride ceramics
K. Lindgren, A. Kauppi and L. K. L. Falk
Journal of the European Ceramic Society 37, 3017-3026 (2017)

Interplay of water and reactive elements in oxidation of alumina-forming alloys
N. Mortazavi, C. Geers, M. Esmaily, V. Babic, M. Sattari, K. Lindgren, P. Malmberg, B. Jönsson, M. Halvarsson, J. E. Svensson, I. Panas and L. G. Johansson
Nature Materials 17, 610-617 (2018)

Microstructural Evolution of Welded Stainless Steels on Integrated Effect of Thermal Aging and Low Flux Irradiation
M. Bjurman, K. Lindgren, M. Thuvander, P. Ekström and P. Efsing
Proceedings of the 18th International Conference on Environmental Degradation of Materials in Nuclear Power Systems -Water Reactors, 703-710 (2018)

Thermal ageing of low alloy steel weldments from a Swedish nuclear power plant - a study of mechanical properties
M. Boåsen, K. Lindgren, J. Roudén, M. Öberg, J. Faleskog, M. Thuvander and P. Efsing
Proceedings of Fontevraud 9: Contribution of Materials Investigations and Operating Experience to Light Water NPPs Safety, Performance and Reliability (2018)

Thermal aging of cast and welded stainless steels on LTO and the influence of the change of reactor materials
M. Bjurman, M. Thuvander, K. Lindgren, and P. Efsing
Proceedings of Fontevraud 9: Contribution of Materials Investigations and Operating Experience to Light Water NPPs Safety, Performance and Reliability (2018)

My contributions to the appended papers

I. Performed the APT measurements, specimen preparation by FIB/SEM lift-out, data analysis and interpretations, and wrote the paper with input from the co-authors.

II. Performed the APT measurements, data analysis and interpretations, specimen preparation by FIB/SEM lift-out, and wrote the paper, with input from co-authors. The hardness measurements were not performed by the first author.

III. Performed the APT measurements, data analysis and interpretations, specimen preparation by electropolishing, and wrote the paper, with input from co-authors. The hardness measurements were not performed by the first author.

IV. Performed the APT measurements, data analysis and interpretations, specimen preparation by FIB/SEM lift-out and electropolishing, and wrote the paper, with input from co-authors.

V. Performed the APT measurements, data analysis and interpretations, specimen preparation by FIB/SEM lift-out, and wrote the paper, with input from co-authors.

VI. Performed the APT measurements, data analysis and interpretations, specimen preparation by FIB/SEM lift-out, and wrote the paper, with input from co-authors.

Contents

1 Introduction **1**
1.1 Aim of this study 2

2 Background **5**
2.1 The Nuclear Reactor 5
2.1.1 Reactor Pressure Vessel Construction 6
2.1.2 The Welds of the Reactor Pressure Vessel 7
2.1.3 Internal Components 9
2.2 Irradiation Damage of the Reactor Pressure Vessel 9
2.2.1 Direct Matrix Damage 10
2.2.2 Solute Clustering 12
2.2.3 Segregation to Grain Boundaries 14
2.2.4 Impact of Features on Mechanical Properties 14
2.3 Thermal Ageing of Reactor Pressure Vessel Steels 15
2.4 Irradiation Damage of the Ferrite of Stainless Steels 16
2.4.1 Theory of Spinodal Decomposition 17
2.4.2 Spinodal Decomposition in Fe-Cr Alloys 19
2.4.3 Nucleation of G-phase 19
2.4.4 Influence on Mechanical Properties 20

3 Experimental Techniques **21**

3.1 Atom Probe Tomography 22
3.1.1 Overview 22
3.1.2 Field Evaporation 23
3.1.3 Data Reconstruction 23
3.1.4 Statistical Tools and Cluster Algorithms 26
3.1.5 Evaluation of Spinodal Decomposition 28
3.1.6 Limitations 28
3.2 Specimen Preparation Methods 30
3.2.1 Electropolishing 30
3.2.2 FIB/SEM Lift-out Technique 31

4 Materials **35**
4.1 Ringhals R4 Reactor Pressure Vessel 35
4.2 Ringhals R4 Pressurizer 39
4.3 José Cabrera Core Barrel and Ringhals R2 Internals 39

5 Summary of Results **43**
5.1 Analysis of Irradiated Materials using APT 43
5.2 Effects of Neutron Fluence and Flux on RPV Weld Metal . . . 45
5.3 Thermal Ageing of Ringhals R4 Pressurizer Weld Metal 48
5.4 Degradation Phenomena in Austenitic Welds 51
5.5 Conclusions 51

6 Outlook **53**

7 Acknowledgements **55**

Bibliography **57**

CHAPTER 1

Introduction

There is a worldwide increasing demand of energy as the population increases. Access to electric energy is of great importance, it can be considered as one of the backbones of modern society, for the industry as well as for the individual. At the same time, the world is facing the challenge of climate change due to the emission of CO_2. In this perspective, the nuclear power plays a role in a mix of many different sources of electricity with low or no CO_2 emission such as hydro, solar, wind as a stable and reliable source of electricity. In the 2018 report from the Intergovernmental Panel on Climate Change (IPCC) on the global warming, electricity from nuclear power is part of their four possible future scenarios on how the global warming could be limited to 1.5 °C [1]. Today, around 11% of the global electricity is produced by nuclear power [2]. In Sweden, the corresponding number is 40% [2, 3].

Needless to say, the energy has to be produced in a safe way. Today, many nuclear power plants in operation are approaching their estimated end of life. In some cases, the lifetime of the reactors is extended (with constant checks of the performance of the reactor). Thus, it is important to understand how long-time operation is affecting the power plant in order to make accurate estimates of the degradation. In Sweden, the nuclear reactors in use were commissioned between 1972 and 1985, with an original designed life-time of 40 years, and thus understanding the effects of ageing is of importance [4]. Extension of

operation of Swedish power plants is based on regular assessments of safety [5].

The environment in the nuclear reactor poses requirements on the structural materials used. The neutron irradiation will affect the materials, leading to a degradation of the mechanical properties. Internal structures will thus degrade with time as a result of the conditions during the operation of the power plant.

The neutron fluence affecting the reactor pressure vessel (RPV) is much lower than for the internal parts. However, the RPV is very complex to replace, so complex that it is not done in practice. During the operational times of years the neutrons interact with the low alloy steel and degrade the mechanical properties. The reactor pressure vessel metal is embrittled due to cluster[1] formation in the material, at the nanometre scale. The nanometre sized clusters hinder dislocation glide and thus contribute to the embrittlement of the material. Therefore, it is important to understand the cluster formation and evolution, and the connection to the mechanical properties.

1.1 Aim of this study

This research was undertaken in order to characterise the development of the microstructure in the low alloy RPV steel weld identical to welds in Ringhals R4, and the thermally aged pressurizer from the same reactor. The Ringhals RPV welds are known for having a high Ni and Mn content, and low Cu content, giving an unexpectedly large change in mechanical properties after irradiation [6]. Atom probe tomography (APT) has been used in order to study the nanometre size clusters formed during irradiation and thermal ageing. There are not many techniques available to characterise nanometre clusters; APT offers high resolution information (position and identification of atoms) in both depth and lateral directions. Thus, it is well suited for characterising the clusters of interest. This project is part of the Måbil (Material, Åldring, Bränsle inom Lärosätesverksamheten) project that is funded by the Swedish Centre of Nuclear Technology (SKC). Funding was also provided by the Nordic Nuclear Safety Research (NKS) collaboration.

In addition to the RPV weld metal, welds from the core barrel, from the decommissioned reactor José Cabrera (Zorita), Spain, is studied using the same technique. In the ferrite part of these materials, spinodal decomposition and formation of nanometre sized G-phase precipitates are the effects of the neutron irradiation, leading to embrittlement of the material. This part of the

[1] The terms precipitates and agglomerates are also commonly used. In this thesis the word cluster is used most of the time, although they in some cases might be precipitates with separate crystallographic structure from the matrix. In *Paper II* the term precipitates is used. Using only APT, the distinction cannot be made.

project is funded by the Electric Power Research Institute (EPRI) and the Swedish Radiation Safety Authority (SSM).

The objectives of this study are:

- To study the evolution of nanometre sized clusters containing Ni, Mn, Si and Cu that are formed during irradiation of the low Cu, high Ni and Mn welds of Ringhals R4 RPV, and to understand their connection to the mechanical properties. There is a theory on so called *late blooming phases* appearing in high Ni, low Cu materials, that would lead to a fast degradation of the mechanical properties after considerable time of operation [7]. These are also looked for in the materials as this would affect the possibilities of extended lifetime of the entire reactor. Furthermore, the influence of flux on the clustering is studied, in order to explain the apparent non-existing difference in mechanical properties of the R4 welds after irradiation inside the reactor (surveillance material) and weld metal irradiated in a higher flux in a materials test reactor (MTR) [8]. This is an important step if the higher flux material is to be used for mechanical testing to describe and predict the degradation of the reactor in operation.

- To study the effects of thermal ageing in the R4 pressurizer welds, that have been in operation for around 28 years at 345 °C. The welding specifications of the R4 pressurizer are the same as these of the Ringhals R4 RPV. The long ageing time is unusual, as many studies are made on materials thermally aged at higher temperatures for shorter times in order to accelerate the ageing, for practical reasons. It is thus a unique opportunity to study long-term thermal ageing at the actual operating temperature. The mechanical properties of the pressurizer are less affected by the ageing than the RPV, but still the change was larger than anticipated from the construction of the power plant. It turned out that the pressurizer contained nanometre sized clusters after ageing, and since they are formed purely by thermal effects they are well suited for comparison with the clusters in the irradiated material.

- To characterise the effects of neutron irradiation and thermal ageing of the remaining ferrite in austenitic welds from internal parts of the José Cabrera reactor and Ringhals R2. This is an opportunity to study spinodal decomposition and G-phase formation in material subjected to realistic operating conditions.

CHAPTER 2

Background

In this chapter, some of the background to the thesis is given. First, the components of a nuclear reactor and their functions are described, then the effects of neutron irradiation and thermal ageing on low alloy steels are discussed. The chapter is concluded with a description of spinodal decomposition and G-phase formation in the ferrite phase of internal, stainless steel, components.

2.1 The Nuclear Reactor

The RPV is an important structural part of the nuclear power plant. It acts as a container of the central parts of the reactor. The core with the UO_2 fuel is placed inside the RPV; the fission process takes place here. ^{235}U is fissile and is used as fuel in most nuclear power plants in operation. The fission takes place through a series of chain reactions. As the natural abundance of ^{235}U is low (0.7%, the most abundant isotope being ^{238}U) the fuel is enriched to 3 to 5% before the manufacturing of the fuel. In the nuclear power plant, the heat from the fission process is converted into electricity. In light water reactors (LWRs) water is used as both coolant and moderator of the neutrons created in the fission process. The neutrons are attenuated by the water (mainly by the hydrogen atoms) in the reactor, since the cross section of the fission reactions

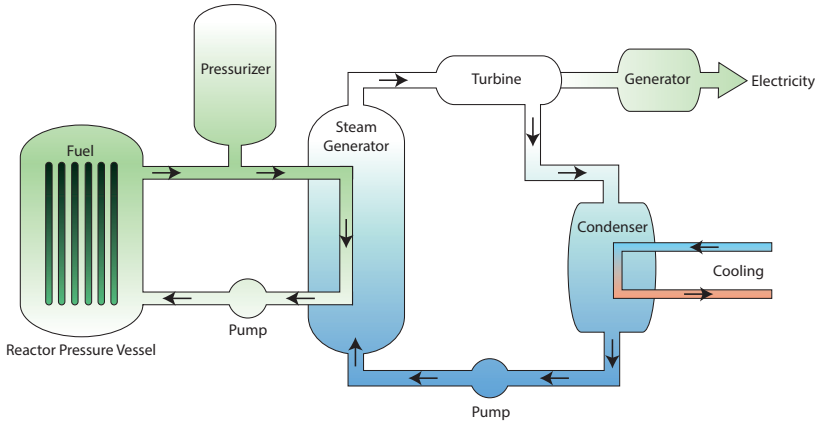

Figure 2.1: Schematic of a pressurised water reactor.

is higher for neutrons with low energy (thermal neutrons).

There are two main types of LWRs, boiling water reactors (BWRs) and pressurised water reactors (PWRs). A BWR consists of one circuit where water is heated and steam is driving the generator. A PWR has two systems; one primary circuit, where the pressure is kept by the use of a pressurizer in order to prevent the water from boiling [9], see Figure 2.1. The pressure of the system is increased by turning on heaters in the pressurizer, and decreased by spraying cool water in the pressurizer. In the secondary circuit, steam is generated and used in the turbine to produce electricity. Due to the differences in design, BWRs and PWRs have different operational temperatures and pressures; a PWR 280-325 °C and about 15 MPa, and a BWR 280-288 °C and about 7 MPa [10]. The RPVs are exposed to different neutron fluences during the life time of the reactor; a PWR has a higher exposure due to a smaller RPV diameter and hence less water between the RPV and the fuel. The materials analysed in this thesis all originate from PWRs.

2.1.1 Reactor Pressure Vessel Construction

The RPV is a life-limiting part of a reactor; it is very complex to replace, and replacement is thus not done in practice. The RPV is constructed from a low alloy steel, and clad with stainless steel on the inside for corrosion resistance. The demands on the RPV are high; high strength and fracture toughness, low ductile-to-brittle transition temperature (DBTT), homogeneous mechanical properties, and good weldability are of importance [9]. The low alloy steel is chosen due to its resistance to thermal stresses [11]. Some alloying elements

are added, for instance Ni for increased fracture toughness and forgeability, Mn for binding sulfur (that otherwise acts embrittling), and Si as a deoxidiser [12]. P and Cu are impurity elements that are known to affect the irradiation susceptibility [13, 14].

The RPVs of the PWRs R3 and R4 in Ringhals are 13 m high, have an inner diameter of 4 m, consist of 20 cm thick steel and weigh 330 tonnes [15]. There are different ways of producing RPVs. One way is to weld forged rings together, using only circumferential welds. Another way to produce the RPV is to start with plates that are bent, and join them with both longitudinal and circumferential welds. It is beneficial to avoid longitudinal welds, in particular in the core (belt-line) region, due to the stress distribution in the vessel.

In order to follow the degradation of the RPV, surveillance specimens are put inside the reactor. In this way, the specimens are irradiated faster (and with a higher flux) than the RPV steel itself, making it possible to remove the surveillance specimens and perform mechanical testing and characterisation of the material.

The construction of the pressurizer is in many ways similar to the RPV. The material is the same, and hence the welds are similar to the RPV welds. The pressurizer is in general smaller than the RPV. Ringhals R4 pressurizer, is for instance 12.8 m high, has an inner diameter of 2.4 m and a weight of 82 tonnes [16]. The pressurizer is not exposed to neutron irradiation, and the temperature inside is slightly higher than in the RPV. It is possible to replace the pressurizer, as was done for Ringhals R4 during the revision in 2011 [16].

2.1.2 The Welds of the Reactor Pressure Vessel

Welding is used to join pieces together, in order to create a joint with no leakage; molten metal is used to fill the gap of the pieces to be joined. The welding affects the microstructure of the RPV material; some different zones can be considered. The base material some distance from the weld is not affected by the welding. The volume close to the weld is known as the heat affected zone. The structure of the weld itself is different from the base metal and might have a different chemical composition dependent on the selection of filler metal. The welding parameters such as voltage, current, and speed, as well as the cooling rate have an impact on the microstructure. Fast cooling results in martensite (having unwanted mechanical properties - it is too hard and brittle). The cooling rate depends on the heat input, and thickness and temperature of the plates. Solidification occurs in a dendritic fashion, giving segregation and compositional variations within the weld [12].

Figure 2.2: Cross-section of a pressurizer weld from Ringhals. The inside (top part in photo) is clad with stainless steel to enhance corrosion resistance.

Welds usually have a higher alloying element content than the base material. This could make the welds more sensitive to radiation and heat and thus, in many reactors, they can be said to be the part of the RPV that is most susceptible to irradiation induced embrittlement.

There are different welding methods, used for different situations. The type of welding used in the RPV is called submerged arc welding (SAW). SAW has high productivity and is always automated, and it is used to join thick plates. For SAW an electrode (filler metal) is used. The filler metal might have a different chemical composition than the base material in order to achieve specific properties. In RPV steel welds the Cu content origins from the filler metal and the coating on the filler metal [14] that increases the electrical conductivity and decreases the wear on the equipment. Both the filler and plates are melted under a layer of flux powder, thus the term submerged. In this way, sparks are avoided. In Figure 2.2 an SAW weld can be seen. The plates have noses into the weld that are needed as a result of the geometrical limitations due to the thickness of the material. After welding, the weld is subjected to a post weld heat treatment (PWHT) in order to achieve the desired mechanical properties and to release stresses. A typical PWHT temperature is around 600 °C.

2.1.3 Internal Components

Inside the RPV, there are many internal structures, such as tubes, structures holding the fuel and control rods in place, and shielding the vessel from the neutrons. One of these internal structures is the core barrel. The water of the primary circuit enters the RPV from the side, then it flows down between the RPV wall and the core barrel. It then flows through the core barrel where the fuel rod assemblies are located, and gets heated. Many of the internal components are made out of austenitic stainless steel (with some remaining ferrite in the welds).

2.2 Irradiation Damage of the Reactor Pressure Vessel

The RPV is affected by the neutrons emitted from the fission process. The irradiation damage time scale spans over many orders of magnitude; neutrons interact with atoms in the bulk material and cascades are created on the picosecond scale (10^{-12} s), whereas the lifetime of a reactor is in the order of 40-60 years (10^{9} s). Due to the short timescale and the small length scale of the initial damage, experimental data on the damage process cannot achieved in-situ. The damage can be studied by modelling on different scales, and the effect on mechanical properties and microstructure can be characterised experimentally using various techniques.

The neutron flux is low, in fact the RPV is subjected to low fluences in a life-time; in around 40 years it is subjected to 0.0075 - 0.24 displacements per atom (dpa) corresponding to $5 \cdot 10^{22}$ n/m^2 to $1.6 \cdot 10^{24}$ n/m^2, compared to internal elements such as fuel cladding tubes and internal spacer grids that get doses up to 80 dpa or $5 \cdot 10^{26}$ n/m^2 [10]. However, the interaction with the neutrons is enough to affect the mechanical properties of the RPV weld metal. It is mainly the belt-line region that is subjected to neutron damage due to the geometry of the reactor i. e. due to the vicinity to the fuel. Other parts, such as the RPV head, are not affected by the neutron radiation.

In order to understand the evolution of the mechanical properties, the structural changes of the irradiated material can be studied. The connection between the mechanical properties and the microstructure is a link to further be able to understand the mechanisms and predict the ageing process.

A standard method to characterise the embrittlement of irradiated RPV welds is impact testing, or Charpy V-notch testing [7]. In short, the energy absorbed during fracture is measured. The specimen is in the shape of a bar with a pre-prepared notch. The measurement is repeated several times at different temperatures to obtain a curve of absorbed energy as a function of temperature.

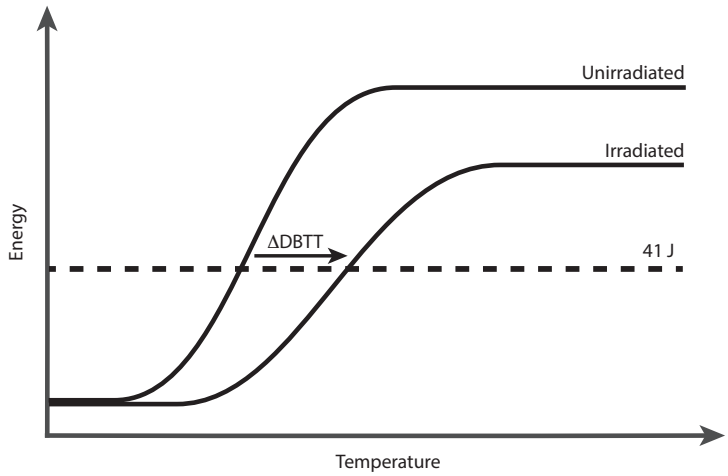

Figure 2.3: Schematic ductile-to-brittle transformation temperature shift for RPV steels measured by Charpy impact testing. The DBTT is often given at 41 J.

At some temperature the behaviour of a bcc material will change from brittle (low temperatures, low energies absorbed) to ductile (high temperatures, more energy absorbed). This can be illustrated by the ductile-to-brittle-transition temperature (DBTT), commonly given at 41 J, see Figure 2.3. The irradiation leads to an increase in the DBTT and in a reduction of the upper shelf energy, reducing the energy absorbed at fracture by the Charpy specimen for high temperatures.

Both tensile testing and hardness measurements can also be performed in order to characterise the ageing of the steel. For Vickers hardness test a pyramid-shaped indent is pushed with a known force into the material, and the resulting area of the indentation is measured. Thus, the amount of material needed is smaller than for Charpy V testing. However, not all the embrittling processes are hardening - for instance the segregation of P to grain boundaries is not, but it affects the possibility of intergranular cracking and can lead to embrittlement without affecting the hardness [17–19].

2.2.1 Direct Matrix Damage

Neutrons with an energy spectrum from 0.025 eV (thermal neutrons) up to 17 MeV are produced in the reactor [20]. The lowest neutron energy needed to damage the RPV material is considered to be between 0.5 and 1 MeV (fast neutrons), dependent on reactor design. For western reactors, 1 MeV is used as the threshold energy for the neutrons to be included in the given fluence.

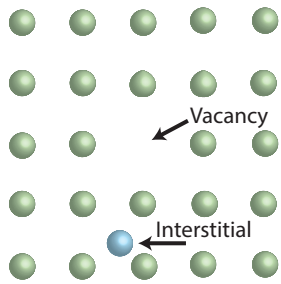

Figure 2.4: Schematic of a Frenkel pair. After a few picoseconds many of the Frenkel pairs have been annihilated by recombination.

The neutron interacts with an Fe lattice atom with a relatively low probability and might therefore travel some distance (in the order of centimeters) in the bulk of the material. The first atom the neutron collides with is known as the primary knock-on atom (PKA). The PKA will receive energy from the neutron and leaves it position, creating a cascade, knocking out other atoms in its path in volumes with sizes of a few nanometers. The neutron of the collision will continue to hit matrix atoms that create new cascades until the neutron energy is too low. For bcc Fe, the displacement threshold energy is around 40 eV [10].

A Frenkel pair, consisting of one vacancy and one interstitial is illustrated in Figure 2.4. Most of the Frenkel pairs created during neutron irradiation are recombined within a few picoseconds. The vacancies and interstitials that do not recombine might interact with other features in the vicinity and affect the microstructure by increasing the diffusion, which without irradiation is so low that almost no significant diffusion takes place at reactor temperatures during the lifetime of the RPV.

Matrix defects, such as interstitial loops and small clusters of vacancies, too small to study using transmission electron microscopy (TEM), are affecting the RPV yield strength [21–25]. The contribution of matrix defects, which are stable at reactor temperatures, to the yield strength is commonly considered to be proportional to the square root of neutron fluence ($\Delta\sigma_{y,matrixdefects} \propto \sqrt{\phi t}$) [26, 27], where ϕ is the flux, t is the time, and thus ϕt the fluence). In general, the contribution from matrix defects to the embrittlement is considered to be small in comparison to the effect of alloy element clusters [28].

There are also matrix defects that are unstable at operational temperatures, i. e. they might reach a steady state number density, where they are created and annihilated at the same rate. The presence of matrix defects is affected by the material composition and the irradiation, for instance the neutron flux [29]. For low fluxes (such as normal operation in a reactor or in surveillance mate-

rial) no unstable matrix damage remains in some materials [30, 31] whereas increased flux (above around 10^{16} n/(m^{2}s), such as in MTRs) gives an unstable matrix damage contribution under some conditions [32].

2.2.2 Solute Clustering

In general, two different families of nanometre sized clusters[1] are considered to form during irradiation in RPV welds; Cu-rich clusters and NiMnSi-rich clusters, dependent on the composition of the weld [33–38]. There is no strict boundary between them composition-wise; Cu-rich clusters contain some Ni, Mn and Si, but smaller amounts than the NiMnSi-rich clusters, that in turn most often also contain some Cu. Their difference in composition suggests differences in formation mechanisms. The composition of the clusters is dependent on the composition of the weld, low-Cu welds ($< 0.1\%$) give NiMnSi-rich clusters, such as in the irradiated Ringhals RPV material analysed in this project. The clusters can be found on dislocation lines as well as in the matrix [39–41].

A relatively high Cu content (up to 0.4%) was found to be detrimental for mechanical properties after neutron irradiation in the late 1960s. The high Cu was found to correlate with more embrittlement, that in turn was found to be due to the formation of Cu-rich clusters forming during irradiation [42–45]. After this insight, many RPV steel welds were fabricated containing less Cu. The small, Cu-rich clusters formed during irradiation are believed to be too small for being separate phases (thermally aged RPV steels might however contain larger precipitates with other crystal structures such as 9R [46]). The Cu-rich clusters are believed to form due to supersaturation of Cu in bcc Fe; the solubility of Cu is very low, around 30-42 atomic parts per million (appm) at RPV relevant temperatures [7, 47]. Strong Ni-Mn bonds and the interfacial energy towards the Fe in the matrix often result in a Cu-rich core with a shell of Ni and Mn atoms [32, 48, 49]. The cluster formation results in hardening. The effect of Cu precipitation on DBTT is generally considered to be saturating, due to the depletion of Cu from the matrix.

Odette et al. stated that the effect on mechanical properties of NiMnSi-rich clusters can be accelerated at high fluence and gave them the name *late blooming phases* [7, 32, 34]. The phenomenon and its naming is a matter of discussion, with some results pointing towards them not being late blooming, or precipitates [50]. In this thesis, the term NiMnSi-rich clusters is used, with no assumptions made on their crystal structure and whether they bloom late or not.

[1] See earlier footnote on cluster/precipitate/agglomeration choice of vocabulary.

The formation of NiMnSi-rich clusters is a matter of more discussion than the formation of the Cu-rich clusters. The Ni, Mn and Si contents are all below the solubility limit in Fe-Ni, Fe-Mn and Fe-Si binary alloys [23], and thus supersaturation should not be the driving force, unless the synergy between the alloying elements drastically changes the solubility limits. The NiMnSi-rich clusters generally form in RPV weld metals with low Cu and high Ni content. The formation is believed to be accelerated by Cu, in terms of clustering on Cu embryos [51, 52]. However, examples are found where NiMnSi-rich clusters form in Cu-free steels [47], and in low-Cu steels, but without any Cu atoms in the clusters [53].

The thermodynamic stability of the clusters is a matter of debate, with some claiming that they are not stable [50, 54, 55], i. e. they would not grow in the absence of the point defects created by neutron irradiation. Monte Carlo simulations show that the role of self-interstitials and vacancies in the formation is vital and that the growth of clusters without Cu is slower than the growth of Cu-rich clusters [50, 56]. The NiMnSi-rich clusters are believed to form on small interstitial loops, which are immobilised by solute atoms, primarily Mn and Ni [57]. In Fe-Mn model alloys, Mn has been observed to significantly increase the number of loops during neutron irradiation [58]. The loops are generally not observable by TEM, in a RPV steel they would be below the size when they can be detected [10]. Other solute atoms (Ni, Mn, Si, Cu, and P) are dragged there by vacancies and by a dumbbell mechanism occurring in irradiated materials (only Mn and P) [56, 59]. Kinetic object Monte Carlo simulations using this model give an estimated number of interstitial loops that corresponds well to the number density of NiMnSi-rich clusters in the irradiated Ringhals surveillance material as detected by APT [59]. Other results are pointing towards thermodynamically stable precipitates due to synergetic effects between Ni, Mn and Si, describing the NiMnSi-rich clusters as intermetallic phases, such as Γ_2 or G-phase, based on thermodynamic models [60], X-ray diffraction [61], and comparing compositions to APT results [51, 62]. The transition from a relatively matrix coherent cluster to for instance G-phase is then vital, with results pointing towards a lower energy after such transition, but density functional theory simulations show that it is uncertain whether all requirements for such a transition are met [63].

The beginning-of-life mechanical properties of the high-Ni RPV steel welds are good, but the impact of irradiation during operation needs to be further understood [64, 65]. This is one of the motivations of this thesis.

The neutron flux, i. e. the number of neutrons per time and unit area, is known to affect the cluster characteristics [66, 67]. As the entire reactor would have to permanently be closed down in order to obtain material from the RPV, surveillance material irradiated inside the reactor at higher flux is commonly analysed. A typical flux in such materials is usually around four times higher

than in the RPV (a lead factor equal to four) [5, 68]. Furthermore, materials irradiated in MTRs for a few weeks or months instead of years are also of interest, having an even higher neutron flux. The clustering of solute elements is affected by the higher flux due to an increase in diffusion as the number of Frenkel pairs at any given time is higher. The result of a higher flux is commonly smaller clusters with higher number density [66, 69–72]. In this thesis, the effects of flux on high Ni and Mn content Ringhals R4 welds are investigated.

2.2.3 Segregation to Grain Boundaries

The matrix defects created by the fast neutrons lead to increased diffusion in the material. Point defects (vacancies and interstitials) will move towards grain boundaries that act as sinks, resulting in radiation induced segregation (RIS). The effect can be explained as the inverse Kirkendall effect [9, 26]. When considering the flow of vacancies towards the grain boundary, this must be followed by an equal flow of atoms in the opposite direction. If the net flow of one type of atoms is smaller than for an other type of atoms, this results in the first type of atoms having higher concentrations at the grain boundary. In the same way, the net flow of interstitials may also vary for different atomic spieces. In RPV weld metals, P tends to segregate to grain boundaries when the material is irradiated [73, 74], increasing the risk of intergranular failure and thus having an embrittling effect. A higher P content, but also higher temperature, fluence, and Ni content in the material result in more segregation to grain boundaries [13, 73]. C segregated to grain boundaries will, on the other hand, have a positive effect by strengthening the boundary [75, 76]. In this thesis, the effects of segregation to grain boundaries are not further looked into.

2.2.4 Impact of Features on Mechanical Properties

The ductility of the RPV is connected to the ability of line dislocations to move within the material. As long as the dislocations can move freely, the material can be deformed without fracture and is thus ductile. However, during irradiation, the clusters and the matrix damage form obstacles for the dislocations in the RPV, and the material becomes less ductile. One way of describing the bowing of dislocations around obstacles, hindering the dislocation glide, is the dispersed barrier hardening (DBH) model, contributing to the yield strength as

$$\Delta\sigma_y = \alpha M G b \sqrt{N d} \tag{2.1}$$

where M is the Taylor factor (close to 3), G is the shear modulus, b is the Burgers vector, N is the number density and d is the mean diameter of the feature. α is the strength of the barrier; $\alpha = 1$ is the case of Orowan hardening, meaning that line dislocations bow around the barrier [26, 69, 77].

The clusters contribute to the yield strength in terms of dispersed barrier hardening (equation 2.1). The values of α are reported to be $0.10 - 0.15$ [36, 69, 78]. The clusters have high number density, and thus they contribute to a large part of the increased strength i. e. the embrittlement of the material.

Another model that is commonly used for the cluster contribution to the yield strength is the Russell-Brown (RB) model [79]. This model describes the cluster contribution as

$$\Delta\sigma_y = \frac{MGb}{L}\Big(1 - \frac{E_1^2}{E_2^2}\Big)^{3/4} \tag{2.2}$$

with

$$L = \frac{\sqrt{\pi}d}{2\sqrt{f_v}} \tag{2.3}$$

and

$$\frac{E_1^2}{E_2^2} = \frac{E_1^\infty \log\frac{d}{2r_0}}{E_2^\infty \log\frac{R}{r_0}} + \frac{\log\frac{2R}{d}}{\log\frac{R}{r_0}} \tag{2.4}$$

where L is the spacing between clusters in the slip plane, f_v is the cluster volume fraction, $\frac{E_1^\infty}{E_2^\infty}$ is the ratio of the energies per unit length of dislocation in infinite media, and R and r_0 are the outer and inner cut off of the dislocations, respectively.

In addition to the models above, it is common to show a correlation between the square root of the volume fraction of the precipitates and the hardness (see for instance [80–82]). Assuming small variations in cluster size, both models above have a square root dependence of the volume fraction on strength.

2.3 Thermal Ageing of Reactor Pressure Vessel Steels

Thermal ageing can also contribute to embrittlement of RPV steels. In an LWR, the temperature in the RPV (around 290 °C) is generally considered to be too low for thermal ageing to occur due to the slow diffusion of solute elements [83]. However, there are other parts in the primary loop that have higher temperatures such as the pressurizer of a PWR. Furthermore, thermally aged materials are studied to compare with, and as a complement to, irradiated materials. The composition of the welds affects the temperature needed for thermal ageing to happen, for instance a combination of high Ni (1.66 at.%)

and high Cu (0.44 at.%) gives a significant hardness increase (80 HV) after 100,000 h at a temperature as low as 330 °C [84], whereas 140,000 h at 310 – 320 °C had no impact on hardness in VVER-1000 weld metals with similar Ni content but considerably lower Cu contents (0.03-0.09 wt.%) [18].

The effect of thermal ageing is similar to that of radiation damage, solute clustering[2] of Cu, Ni, Mn and Si, and possibly segregation of P to grain boundaries due to increased diffusion, take place [17, 18, 84, 85]. However, there is no matrix damage, as there are no neutrons interacting with the atoms, creating cascades. The increase in diffusion with temperature is thus due to only vacancies dragging the solutes, as there are no self-interstitials in the absence of irradiation. The cluster formation is driven by the low Cu solubility in Fe. Just as in the irradiated material, Ni, Mn, and Si are known to reduce the interfacial energy between the Cu and the Fe, and thus form a shell around the Cu-rich core, as seen in simulations [86, 87], and as observed using APT [84, 88–90] in model alloys and RPV materials. In high Cu RPV materials (0.32-0.55 at.%), Hyde et al. found that thermal ageing results in clusters with a higher Cu content than the clusters in the same material when irradiated [88]. In this thesis, the pressurizer welds of Ringhals R4 (with high Ni and Mn, and low Cu content) that have been in operation, i. e. thermally aged, for 28 years (190,000 h) at 345 °C are analysed.

2.4 Irradiation Damage of the Ferrite of Stainless Steels

Many of the internal components in a nuclear power plant are made from stainless steel, like 304, 304L, 316, 316L, 321 and 347, welded or clad by alloys 308 and 309, due to the good corrosion resistance at reactor relevant temperatures [65]. These alloys are austenitic, but the welds contain small amounts of ferrite. Just like the low alloy steel in the RPV, these materials are affected by the neutron irradiation during operation. Due to their position closer to the core, the doses can be much higher than for the RPV, up to 100 dpa or more during the operational time of the reactor, dependent on position. Just as in the RPV, the neutrons will interact with the material, creating increased possibilities for diffusion. In austenite, Ni-Si particles (possibly γ', i. e. Ni_3Si and its precursors) are known to form as a result [91–94]. In ferrite, phase decomposition into Cr-rich and Cr-poor volumes occurs (spinodal decomposition), and precipitation of nanometre sized $Mn_6Ni_{16}Si_7$ precipitates known as *G-phase*. The change of microstructure changes the mechanical properties, giving a decreased fracture toughness. In this section, the focus will be on the degradation of the ferrite.

[2] In thermally aged materials, some of the larger "clusters" might be precipitates.

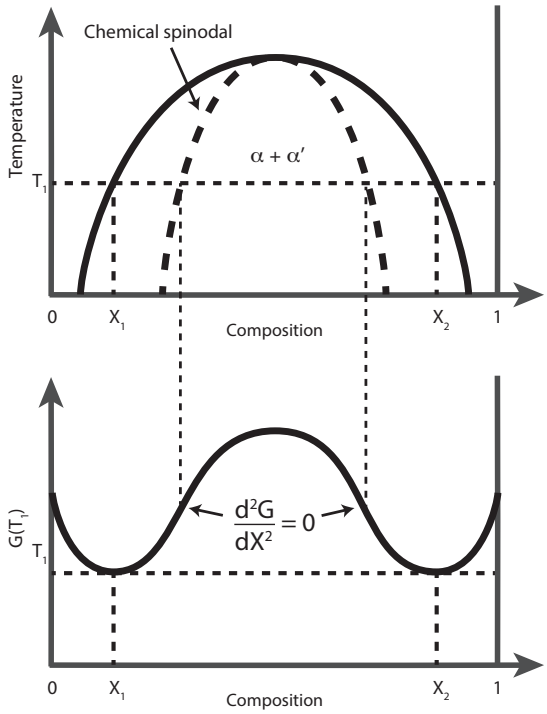

Figure 2.5: Between the spinodals, an alloy will decompose spontaneously. Between the spinodal and the miscibility gap, phase decomposition might happen through classical nucleation and growth.

2.4.1 Theory of Spinodal Decomposition

Spinodal decomposition is a spontaneous phase transformation as there is no barrier to transformation [95]. In a phase diagram such as the one in the upper part of Figure 2.5 there is a miscibility gap where the α and α' phases are stable. Materials go from the single phase above to the miscibility gap during quenching. Inside the spinodal, uphill diffusion will take place as this will decrease Gibb's free energy. The uphill diffusion will continue until the equilibrium compositions X_1 and X_2 are reached (Figure 2.5).

The chemical spinodal is defined as

$$\frac{\mathrm{d}^2 G}{\mathrm{d}X^2} < 0 \tag{2.5}$$

where G is Gibb's free energy and X is the mole fraction of one of the elements. However, it is of little practical use as there are also other factors affecting the spinodal decomposition in a material. Both the chemical difference (different

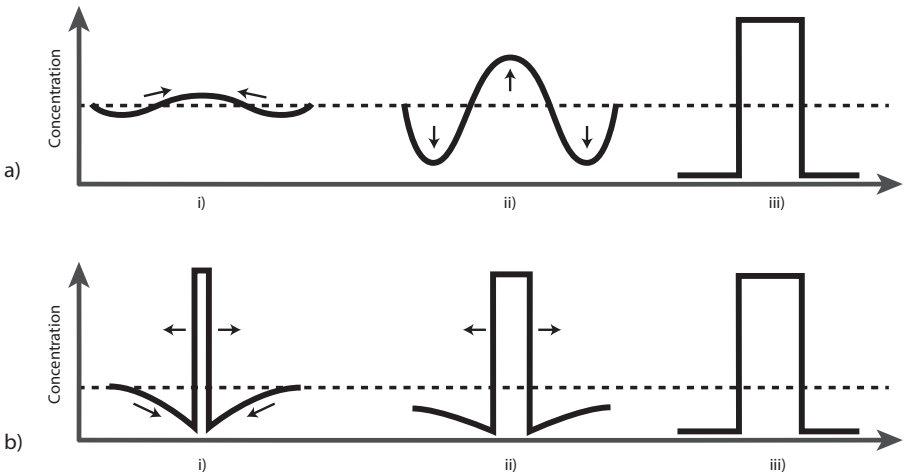

Figure 2.6: A schematic comparison of spinodal decomposition (a) and nucleation and growth outside the spinodal region (b). Time increases from i) to iii).

energies of bonding dependent on which atoms are binding to each other) and the coherency stresses of the phases also affect the decomposition. Thus, those factors are included in the coherent spinodal, saying that decomposition takes place when

$$\frac{\mathrm{d}^2 G}{\mathrm{d}X^2} + \frac{2K}{\lambda^2} + 2\eta^2 E' V_m < 0 \tag{2.6}$$

where the second term describes the bonding difference and the third term the coherency stresses. K is a constant that is dependent on the different bond energies of like and unlike atoms, λ is the wavelength of the spinodal decomposition, $\eta = \frac{1}{a}\frac{\mathrm{d}a}{\mathrm{d}X}$ where a is the lattice parameter, $E' = E/(1-\nu)$ where E is Young's modulus and ν is Poission's ratio. V_m is the molar volume.

The coherent spinodal decomposition has a lower upper temperature limit than the chemical spinodal. The wavelength of the spinodal decomposition has a lower limit given by equation 2.6.

Between the spinodal and the miscibility gap, the phase transformation will take place through nucleation and growth as the alloy is metastable. A comparison of the two possibilities and their effect on compositions can be seen in Figure 2.6.

Spinodal decomposition at early stages can be seen as sinusoidal differences in composition [96],

$$f(x,y,z) = C_0 + A\sin\frac{2\pi(x+y+z)}{\lambda} \tag{2.7}$$

where C_0 is the average composition, A is the amplitude of the decomposition, λ is the wavelength, and x, y and z are the coordinates in the three dimensions. However, at later stages the decomposition will not be symmetrical around the average composition as one phase might reach a minimum content of the other element [97]. The microstructure resulting from spinodal decomposition is in general a complex network of high- and low- concentration volumes.

2.4.2 Spinodal Decomposition in Fe-Cr Alloys

Thermally induced spinodal decomposition in Fe-Cr is known to occur at intermediate temperatures ($300 - 500\,^{\circ}\mathrm{C}$). In ferrite, the Fe-rich phase is known as α and the Cr-rich phase as α' (both phases are bcc). In nuclear power plants, austenitic stainless steels with remaining ferrite in the welds, and duplex stainless steels are used for the internal parts due to their good corrosion resistance, weldability, and mechanical properties. Both the composition of the ferrite of these steels, and the temperatures are in the range where spinodal decomposition occurs, whereas the austenite part is unaffected in absence of irradiation [97, 98]. Both spinodal decomposition in model Fe-Cr alloys and actual alloys have been studied. An increased amount of Cr accelerates the decomposition [99]. In real alloys, the addition of alloying elements (Ni, Si, Mo, Mn,...) is known to affect the decomposition. For instance, Hedström et al. showed that both addition of Ni and Mn accelerate the decomposition of ternary model alloys containing 20% Cr [100].

Adding irradiation gives further complexity to the degradation of the material. The neutrons will interact with the material, creating vacancies and interstitials and increased diffusion, hence making the spontaneous process of spinodal decomposition faster [101, 102]. In this thesis, spinodal decomposition in a neutron irradiated weld from the Spanish reactor José Cabrera (Zorita) is characterised and compared to thermally aged pipe welds from Ringhals R2.

2.4.3 Nucleation of G-phase

G-phase ($Ti_6Ni_{16}Si_7$) is a cubic phase with a lattice parameter four times that of bcc Fe. The Ti in the composition can be replaced by other elements, commonly Mn. The nanometre sized G-phase precipitates were crystallographically identified in the ferrite of thermally aged cast alloy CF8 alloys using TEM by Bentley et al. in 1985 [103]. The ferrite composition affects the formation of the G-phase, for instance Ni, Si, Mo and C are believed to increase the G-phase precipitation [97, 104]. In alloys containing no Mo, G-phase precipitation is only observed at ferrite/austenite boundaries [97].

Nucleation of G-phase exclusively happens at the α - α' boundaries, where the exchange of atoms during the phase separation leads to diffusion of others. The Fe-rich α rejects Ni atoms, and the Cr-rich α' rejects Si, resulting in a total movement of both elements to the boundaries, where they meet and form G-phase together with Mn [97, 105, 106]. Later in this thesis, results on G-phase precipitation are shown in the irradiated core barrels welds from the José Cabrera (Zorita) reactor.

2.4.4 Influence on Mechanical Properties

The spinodal decomposition is found to affect the mechanical properties of ferrite containing steels with high Cr content, due to the strain between Fe-rich and Cr-rich phases, and to lattice friction forces. The result of this is hardness increase and embrittlement. The decomposition is responsible for what is known as the "475 °C embrittlement". The total effect is dependent on the amount, size and distribution of the ferrite in the duplex steel [98].

The influence of G-phase to the hardness of the steel is harder to distinguish, due to the complexity of the system. There are studies that suggest that the G-phase contributes to the hardness [107–109], and other studies that show no or little contribution [110, 111]. There is also a possibility of indirect contribution to the hardening, suggesting that the G-phase contributes to local change in composition (Ni content) and thus the kinetics of the spinodal decomposition is affected [97].

CHAPTER 3

Experimental Techniques

The main experimental characterisation technique used in this thesis is APT. Due to the small size of the clusters of interest, APT is one out of few methods that can be used. Other techniques that are also used for cluster studies in RPV welds are small angle neutron scattering (SANS) (see for instance [112–115]) and transmission electron microscopy (TEM) ([116–118]). SANS enables studies of larger volumes and gives cluster characteristic averages, but needs to be combined with APT for assumptions of cluster compositions. The small cluster size is challenging in TEM, as matrix above and underneath will also contribute to the chemical composition and crystal structures recorded when illuminating a thin lamella with electrons. In this chapter the APT technique and its merits and limitations are described, as well as data analysis for clustering and spinodal decomposition. The chapter is ended with a section on specimen preparation for APT.

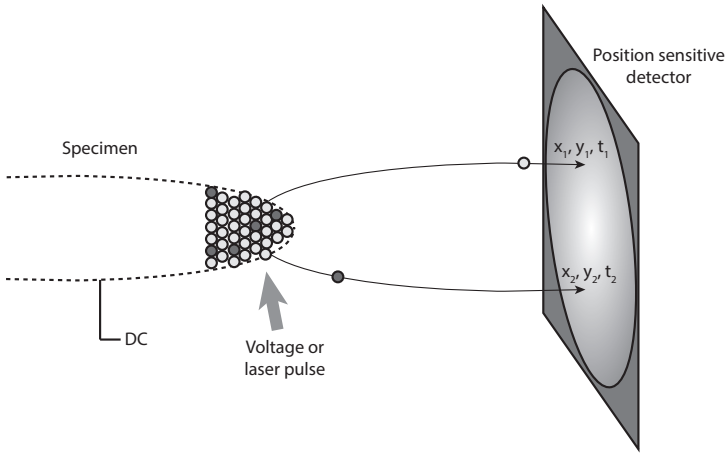

Figure 3.1: Schematic of the experimental setup of APT. Ions are field evaporated by means of a direct current field and laser or voltage pulses. For each ion the time of flight and the position on the detector are recorded.

3.1 Atom Probe Tomography

3.1.1 Overview

Atom probe tomography (APT) is a destructive characterisation technique in which atoms can be identified in terms of both type and position within the specimen. APT is used for detailed material characterisation, with a near-atomic resolution. Common phenomena studied are clustering, segregation to grain boundaries and interfaces, and phase transformations. The technique is well suited for metals that are conducting, but also semiconductors and oxides and even biological materials can be studied. The typical analysed volume is in the order of $50 \times 50 \times 200\,\mathrm{nm}^3$. Unless stated otherwise, the references for this chapter are [119–121].

The basic principle of APT can be seen in Figure 3.1. A needle-shaped specimen in ultra-high vacuum and at low temperatures (typically $30 - 70\,\mathrm{K}$) is subjected to a direct electric field. When the specimen is subjected to a pulse, either voltage or laser, the field might be high enough to ionise and tear off atoms from the apex of the needle in the field evaporation process. The positive ion leaves the specimen surface and hits a position sensitive detector. The time of flight is measured for each ion in order to determine the chemical identity. The information on the position, time of flight and the sequence of ions can be used in order to make a 3D reconstruction of the analysed material. The electric field results in high stresses in the specimen; in fact many APT

analyses are ended by specimen fracture.

3.1.2 Field Evaporation

Field evaporation is the most central process in atom probe analysis. A direct current (DC) voltage is applied to the specimen; the field at the tip is strong, tens of V/nm. If the apex is considered to be smooth and spherical, the electrical field can be described as

$$F = \frac{V}{k_f R} \tag{3.1}$$

where F is the electrical field, V is the voltage, k_f is the field factor and R is the radius of the tip. The field factor is a constant that is dependent on the shape of the tip and the electrostatic environment. A smaller radius of the tip gives a higher field with the same voltage, giving a need of an increased voltage for the same evaporation rate (i. e. number of ions evaporated per pulse) when the radius of the needle is increased during analysis. The penetration depth of the field is very small (for metals less than the size of an atom in the lattice), and hence only atoms at the very surface of the tip are evaporated, atom by atom.

The pulsing is used to overcome the evaporation barrier at a specific, known time. The evaporation is dependent on both the temperature and the electric field. Thus, both voltage pulsing and laser pulsing, effectively meaning heating the specimen, can be used to evaporate the ion, see Figure 3.2. The pulse fraction should be high enough for all elements in the specimen to evaporate, since different elements have different evaporation fields. If the field is not high enough there will be preferential evaporation of the atoms with lower evaporation fields, biasing the composition of the measurement. However, the stresses associated with high fields give a higher probability of specimen fracture that would end the analysis.

3.1.3 Data Reconstruction

In order to make a three dimensional reconstruction of the analysis data, the position of impact on the detector and the sequence of the ions are used for spatial coordinates and the time of flight is used for chemical identification.

The time of flight, the time from the pulse until the ion hits the detector, is recorded during the analysis. The ion leaves the tip surface with zero velocity and is accelerated within a few atomic distances from the tip to the kinetic

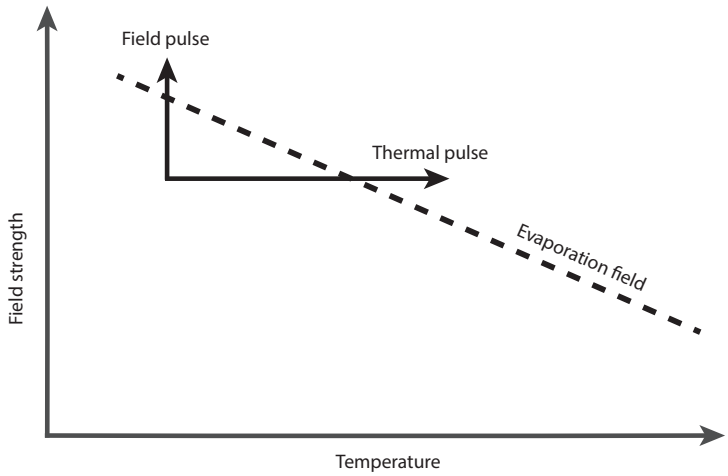

Figure 3.2: Schematic of pulsing and evaporation field. Field pulsing corresponds to voltage pulsing and thermal pulsing to laser pulsing.

energy $E_c = \frac{mv^2}{2}$ where m is the mass and v is the velocity of the ion. The potential energy from the field is $E_p = neV$ where ne is the charge of the ion and V is the voltage. The distance from the tip to the detector, l, is known, and thus the velocity $v = \frac{l}{t_{flight}}$. Combining the three relations gives

$$\frac{m}{n} = 2eV\Big(\frac{t_{flight}}{l}\Big)^2 \tag{3.2}$$

i.e. the mass-to-charge ratio. This ratio is then used for the identification of ions in the mass spectrum, see Figure 3.3. The mass-to-charge ratio detected has some variations, giving widths to the peaks. Therefore, a range is usually given for each ion. For voltage pulsed runs, the width of the peak in the mass spectrum is mainly the result of the extent of the voltage pulse in time. When running analyses in laser pulsed mode, the peaks are often wider and so called thermal tails contribute to the background, due to the transport of heat away from the specimen apex.

The position of the ions in the specimen is reconstructed using the impact position on the detector. The ion trajectories are dependent on the three dimensional field between the tip and the detector, that is dependent on the local environment close to the surface as well as further away. There are some different protocols on how to perform the reconstruction, one commonly used is based on the publication by Bas et al. [122].

The choice of reconstruction parameters is vital, if they are not properly chosen distances and shapes in the reconstruction will be distorted. The analysed volume might get compressed or elongated. For the reconstruction both the field

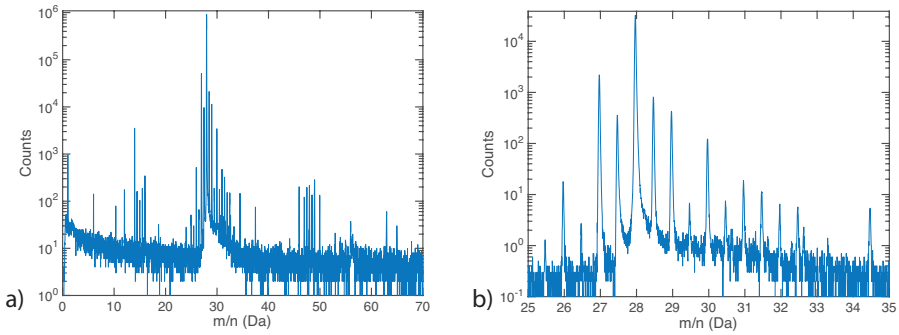

Figure 3.3: Example of a spectrum from a voltage pulsed analysis for ion identification. This material is the Ringhals R4 weld. a) Full spectrum. b) Enlarged part of the spectrum from 25 to 35 Da. The peak at 28 Da corresponds to $^{56}Fe^{++}$ that is the most abundant ion in the analysis. The binning of the histograms are different in a) and b).

F and the shape of the apex dependent field factor k_f are needed. Also, the image compression factor is needed. The image compression factor describes the ratio between the crystallographic angle and the observed angle,

$$\xi = \frac{\theta_{crys}}{\theta_{obs}} \tag{3.3}$$

and can be calibrated using the crystallographic information from the detector hit map, namely the distances between poles with known plane distances and the usage of $\theta_{obs} = arctan\frac{D}{L}$ where D is the distance to the detector and L is the distance in the hit map (the simplification is possible since the specimen tip has a negligible radius compared to D). There are some different ways of estimating the shape of the specimen for determination of the field factor k_f. Equation (3.1) can be used with a knowledge of the evaporation field for the material analysed, connecting to the voltage. The radius could be determined by TEM, beneficial if there are different phases with different evaporation fields in the analysis. One way of knowing if the parameters are correct is by evaluation of the atomic planes at crystallographic poles. The analysis of the poles gives high quality data in the direction of analysis in some materials, such as low alloy steel. Known features could also be used for finding reconstruction parameters; for instance precipitates growing with certain angles or in certain shapes.

3.1.4 Statistical Tools and Cluster Algorithms

Once the reconstruction is performed there are literally millions of data points. In this section, some statistical methods and some cluster analysis methods are briefly described. Note that the words cluster and precipitate are used interchangeably.

The radial distribution function (RDF), is also known as the pair correlation function and denoted $g(r)$. It describes the normalised probability of finding other atoms of the same species at a distance r from the reference atom. It can be related to the number density $\rho(r)$ and average number density $\rho_{av}(r)$ of atoms by

$$g(r) = \frac{\rho(r)}{\rho_{av}(r)} \tag{3.4}$$

When $g(r)$ is larger than unity for small distances, there is clustering of the specific element(s) studied.

Isoconcentration surfaces can be used to illustrate clusters as well as other features such as layers, grain boundaries and line dislocations [120]. The surface is defined at a specific concentration of an element. These surfaces can also be used to create proximity histograms, proxigrams, where the concentration of different elements is shown as a function of the distance from the surface [123]. For small precipitates proxigrams might give poor statistics on the inside of the surface due to the small number of atoms.

The maximum separation method (MSM) is a method that utilises the distance between solute atoms to identify clusters [35, 124, 125]. Two solute atoms are considered being within the same cluster if they are closer to each other than a distance d_{max}, see Figure 3.4. A smallest number of atoms considered being a cluster, N_{min} can be chosen in order for random fluctuations in the matrix not to be considered as clusters. A higher order, N, than one (the nearest neighbour), can be set, meaning that the N:th nearest neighbour is considered. In order to determine cluster composition, a parameter L (envelope distance) can be chosen in order to include other atoms than the solute ones used for cluster identification. L is the distance from the solute atoms that is considered being part of the cluster. In order to get rid of the matrix atom halo, another distance E, the erosion distance, can be used to remove atoms from the cluster surface. There are other methods of detecting clusters, see reference [64] for a review.

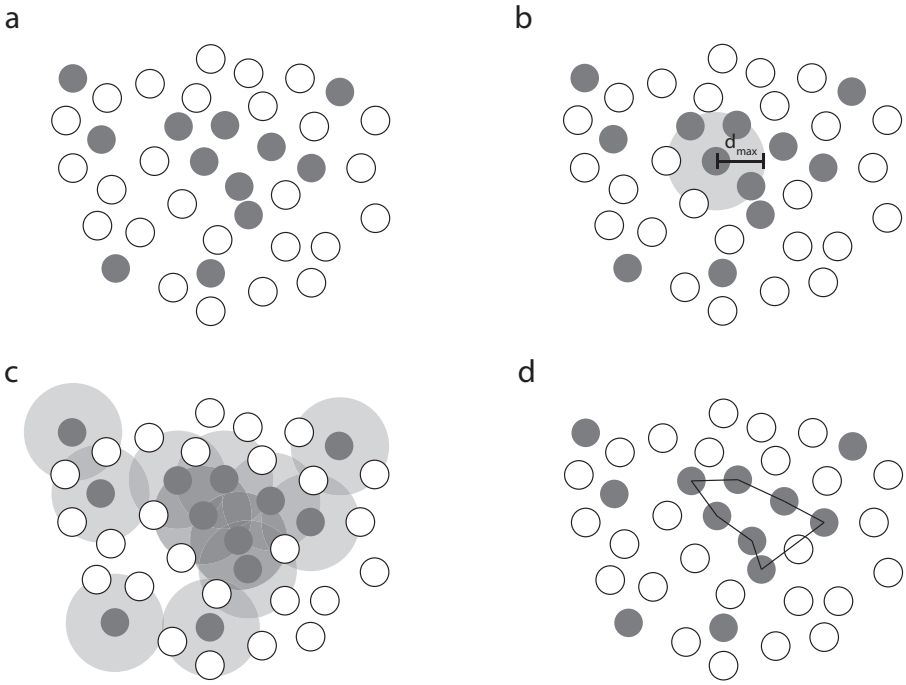

Figure 3.4: Schematic of the MSM. a) Solute atoms (filled) in the matrix (white atoms). b) Atoms within the distance d_{max} from a solute atom might be part of the same cluster. c) The vicinity of all solute atoms are checked. d) Atoms identified as being in the same cluster are marked with a line.

3.1.5 Evaluation of Spinodal Decomposition

APT is a useful technique when interested in finding the wavelength and amplitude of spinodal decomposition, as described in equation 2.7. One commonly used method is the Langer-Bar-on-Miller (LBM) method [121, 126], where two Gaussian distributions are fitted to the frequency distribution of Cr, and the amplitude of the spinodal decomposition is taken as the difference in Cr average content between the distributions. The results obtained by this method are dependent on block size (commonly 33, 50 or 100), that is determined by the user.

In this thesis, another method developed by Zhou et al., based on the RDF (equation 3.4) is used [127]. Assuming sinusoidal variation in Cr concentration (equation 2.7), the amplitude A of the decomposition will be connected with the normalised and extrapolated Cr RDF at zero distance as

$$A = C_0\sqrt{2(RDF(0) - 1)} \tag{3.5}$$

where C_0 is the average Cr content. The wavelength of the spinodal decomposition can be determined by the local maximum of the RDF of Cr (corresponding to many Cr atoms having another Cr atom at that specific distance). This method has the benefit of being user independent. The limitation in this method lays in the assumption of a sinusoidal variation in composition; this is probably true for early stages of decomposition. However, as the process evolves, the lower limit of one of the phase contents might be reached. What then happens is that the size of the volumes of the two phases will be different, and the decomposition will no longer be sinusoidal. Furthermore, it is also possible that the interface between the phases will get sharper when the decomposition evolves, and thus it will evolve towards a compositional profile more similar to a square wave.

3.1.6 Limitations

Even though APT is a powerful technique there are certain limitations. First of all, it is not possible to analyse any material. The implementation of laser pulsing in APT made it possible to expand from analyses of conductive materials only to semiconductors, minerals, biological materials and more. However, many materials prove hard to analyse due to uneven evaporation, and early specimen fracture. This limitation does not concern the steels analysed in this work, that runs well in the APT as they are conductive and have suitable mechanical properties.

An issue for atom identification is peak overlap, two isotopes having the same mass-to-charge ratio. The overall composition of the analysis could generally

be obtained by deconvolution of the peaks since the other isotopes of the same element can be used together with the known natural isotope abundance. However, the identity of each individual atom is still unknown. In some cases, the amount of overlap is very high, for instance in analyses of oxides with many molecular ions, or polymers, containing hydrides that make ranging of the spectrum a true challenge. In steels such as the RPV welds, the $^{28}Si^{++}/^{14}N^{+}$ overlap makes quantification of nitrogen hard. There is also an overlap for $^{58}Ni/^{58}Fe$, making the cluster interfaces of NiMnSi-rich clusters more diffuse. Furthermore, aluminium only has one naturally occurring isotope, that comes as $^{27}Al^{+}$, overlapping with $^{54}Fe^{++}$ when laser pulsed analyses of steel are conducted.

The spatial resolution is almost atomic, but it is not perfect. Crystallographic planes can only be detected in some fairly pure materials and even then only at crystallographic poles. For some materials and atomic species there is surface migration prior to field evaporation, giving the reconstruction a dependence of the crystallography [128, 129]. The issue is more pronounced when using laser pulsing. One example of this redistribution is Si in low alloy steels.

Different evaporation fields of different phases alter the evaporation sequence, resulting in the so called local magnification effect [130, 131]. Hence, for instance a cluster containing a high evaporation field element will evaporate later than the surrounding matrix. The cluster will form a small protrusion on the tip surface, with another radius than the full tip, and thus the trajectories of the cluster ions are affected, making the cluster appear diluted by matrix atoms. If the evaporation field of the cluster is lower, then an area with a larger local radius will form in the needle surface, also affecting the ion trajectories. In the case of the clusters in RPV steels, this has generated discussion on the true Fe content of the clusters, since APT analysis generally gives a composition of around 50% Fe. Studies have shown that the Fe content of the clusters probably is considerably lower [116, 132–134]. A sign of this phenomenon is an unphysically high atomic density within the clusters in the reconstruction, since the clusters have a low evaporation field, especially for Cu-rich clusters. The exact Fe content is unknown, and when evaluating cluster composition and size, the assumptions on the Fe content made need to be mentioned.

Another consequence of the different evaporation fields of different phases is that the reconstruction of an analysis made over two or more phases might be hard to perform as the reconstruction parameters thus might vary in the same analysis. For instance, some carbides in metal matrixes will appear to have a lower atomic density; something that they do not have in reality. Furthermore, carbides are hard to analyse due to C atoms evaporating as cascades. Due to the detector having a dead time, the carbon content is then underestimated [135].

3.2 Specimen Preparation Methods

There are some requirements on the APT specimen. The specimen needs to be in the shape of a needle, and the tip radius of curvature should be around 50-150 nm in order to create fields high enough for evaporation at voltages of operation in the atom probe (usually 2-10 kV). The cross-section of the needle needs to be circular in order for the reconstruction to be accurate. The feature of interest needs to be close enough to the specimen tip (around 100 nm) in order to be captured in the analysis. The surface of the specimen should be smooth and free from protrusions and cracks that might increase the risk of fracture and make the reconstruction less like the specimen. The taper angle of the needle should be small for obtaining long runs, but very long and thin needles might have a higher risk of fracture. Typically, the angle is around 5°. Also, there should be no secondary tips close to the tip of interest that might field evaporate and contribute to the signal. These requirements can be fulfilled using electropolishing or doing a focused ion beam/scanning electron microscope (FIB/SEM) lift-out that is described below.

3.2.1 Electropolishing

Electropolishing is a convenient, fast and cheap method for specimen preparation of electrically conducting materials. In order for the cross section of the resulting needle to be circular the cross section of the starting blank needs to be either circular or square. Common measures are $0.3 \times 0.3\,\mathrm{mm}^2$, with a length of around 15 mm. Two needles can be produced from the same blank. The blanks need to be cut without introducing any stress or heat that might change the microstructure of the material, making a low speed saw with cooler/lubricant one alternative.

The electropolishing can be done in different ways, but the principle is the same. Here a two-step double layer technique is described, see Figure 3.5. The idea is to create a necked specimen in the first step, in a high concentration electrolyte. The very sharp tips are created in the second step in a dilute electrolyte in a controlled way. In the first step, a thin layer (a couple of mm) of a high concentration electrolyte is put on top of a dense, inert liquid such as polyflourinated polyether or Galden®. The blank (anode) is hung in this liquid so that the middle of the blank is in the electrolyte. There is also a counter electrode (cathode), in the shape of a loop or a stick, in the electrolyte. The counter electrode is made from a noble metal such as Au or Pt. When a voltage is applied the specimen is polished in the electrolyte region. The blank could be moved up and down in order to avoid reactions at the electrolyte - air interface (crucial at high air humidity) and in order to get a smaller taper angle. When there is a necked region with a small

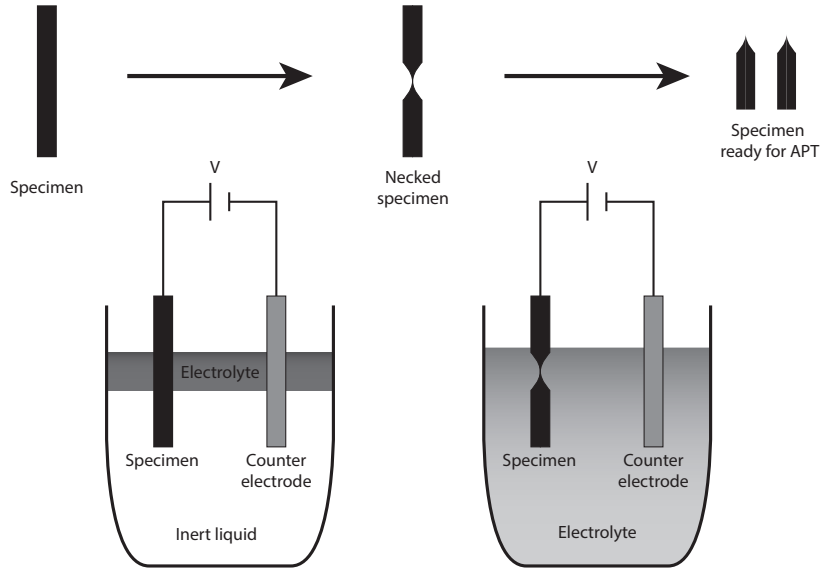

Figure 3.5: The two-step electropolishing procedure. A neck is etched in the first step. In the second step the blank is further etched until two specimens are created.

radius the specimen can be moved to a low concentration electrolyte. The electropolishing is continued until the neck no longer can support the weight of the lower part of the blank and it drops to the bottom of the electrolyte. The switching off can be automated by turning off the voltage when the current drops due to the smaller anode after dropping half of the blank. The lower part of the blank can also be used as a specimen. If needed, the specimens can be subjected to some pulsed electropolishing to get rid of surface oxides after this step. They can also be examined in the optical microscope or even in the scanning electron microscope (SEM) or TEM, or FIB/SEM and further oxides can be removed by Ga-ion milling if needed. The choice of electrolyte and voltage for the different steps is dependent on the material, see Table 2.1 in [119] for a summary.

3.2.2 FIB/SEM Lift-out Technique

Focused ion beam/scanning electron microscopy (FIB/SEM) can also be used for making APT specimen. The microscope is equipped with both an electron column and an ion column, at an angle (52° in an FEI Versa for instance), see Figure 3.6. Both the electron beam and the ion beam can be used for imaging and depositing an other element, for instance Pt. The ion beam can also be used for milling material in a highly controlled manner. Site specific

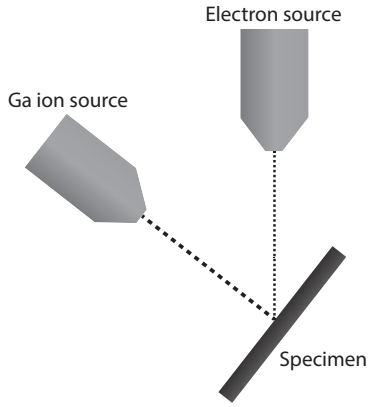

Figure 3.6: Schematic of the FIB/SEM.

regions can be lifted out if there is a feature of interest, for instance a grain boundary. The volume of the material needed is small, that could be beneficial for instance if the material is slightly radioactive and small volumes of material are preferred.

There are different ways of making a lift-out depending on the material, and the position of the feature of interest. Here, a standard lift-out finalised with annular milling [136, 137] is described, that can be used for site-specific specimen preparation from bulk material. First, a site of interest is chosen. A layer of Pt is deposited in the shape of a square, see Figure 3.7. The area of the square is typically in the order of $25 \times 2\,\mu\text{m}^2$. Then, a high ion beam current is used to cut along the long edges of the deposited area, with an angle of 30° to the surface of the bulk specimen. The width of the cuts needs to be enough to avoid redeposition of the milled material reconnecting the lift-out with the bulk. One of the short edges is cut loose. Then, a micromanipulator is attached to the end of the bar using Pt deposition. The other end of the lift-out is cut with the ion beam. Then, the wedge can be lifted out from the bulk. The specimen can be placed on some different types of holders, for instance a prepared TEM-half-grid for correlative microscopy or a prefabricated Si-post coupon (as in the figure). The specimen is attached on one side of the wedge and then cut free using Ga ions. The process is continued for as many specimens as are needed or until the bar is consumed. The Si posts are rotated and Pt is deposited on the other side as well. The specimen can then be sharpened using annular milling. The milling is commenced with large inner and outer radii and a high ion beam current. Successively, the radii and current are decreased until the needle is sharp and located in the position of interest. The final step is a short milling session with low voltage and current in order to get rid of ion beam damage, i. e. the amorphous surface layer, and Ga implantation from the milling.

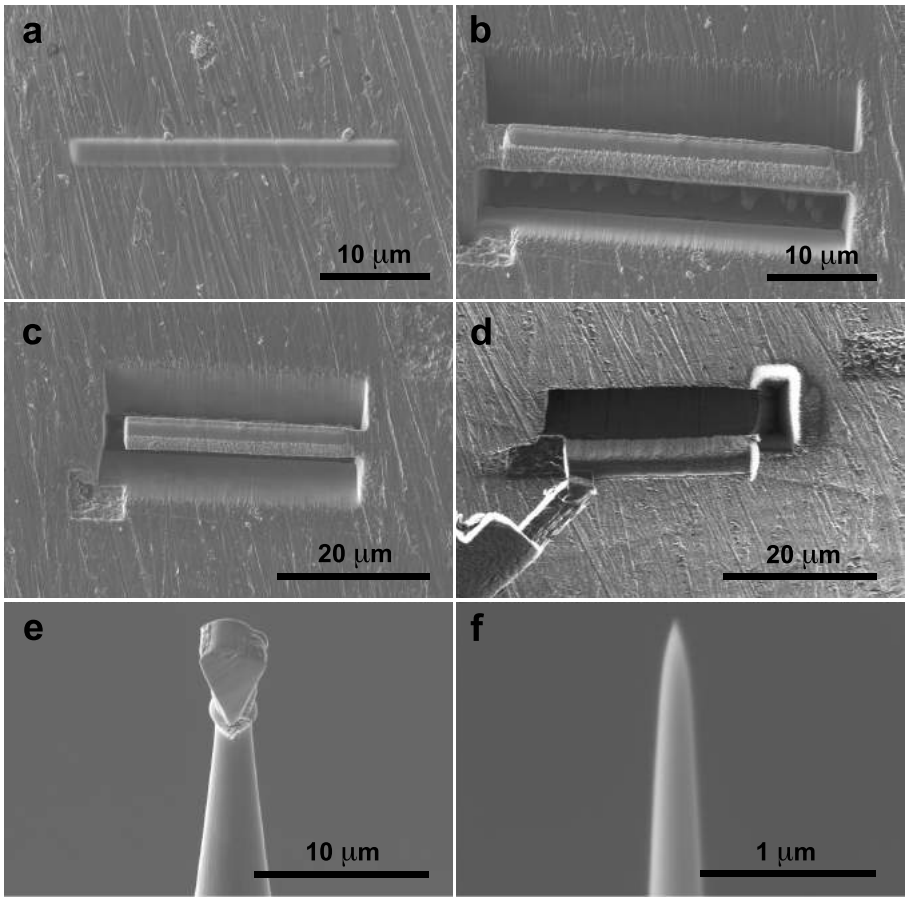

Figure 3.7: Liftout procedure. a) Pt deposition on the site of interest. b) Trenches are milled on both sides of the Pt strip. c) One side of the volume of interest is cut. d) The volume of interest is attached to the micromanipulator, cut on the other side and lifted out. e) A piece of the lift-out is attached to a Si post. f) The specimen is sharpened using annular milling, ready for analysis in the atom probe.

CHAPTER 4

Materials

Three main sets of weld metals were analysed; the irradiated Ringhals R4 reactor pressure vessel steel surveillance and Halden irradiated materials in *Papers I*, *II*, *IV*, and *V*, the thermally aged Ringhals R4 pressurizer in *Papers III* and *IV*, and the core barrel material from the Zorita nuclear power plant in *Paper VI*.

4.1 Ringhals R4 Reactor Pressure Vessel

The materials studied are identical to the RPV welds in Ringhals R4. R4 is a PWR commissioned in November 1983, designed by Westinghouse Electric Company [6, 138]. The composition of the RPV welds can be seen in Table 4.1. The welds are high in Ni and Mn, and low in Cu, compared to other reactors worldwide. The RPV itself was fabricated by Uddcomb using SA 508 class 2 Klöckner Werke ring forgings. The welding was done by SAW with a PWHT at 620 °C in order to relieve internal stresses. The surveillance blocks were supplied by the same company, produced in accordance to the same welding procedure specification (WPS).

The welds consist of mainly bainite. The general microstructure of the weld

Table 4.1: Composition of Ringhals R4 RPV weld metal. Fe balance [6].

	Cu	Ni	Mn	Mo	Si	C	P	S	Cr	Al	Co
at.%	0.04	1.58	1.37	0.29	0.28	0.31	0.027	0.007	0.04	0.05	0.01
wt.%	0.05	1.66	1.35	0.50	0.14	0.068	0.015	0.004	0.04	0.024	0.01

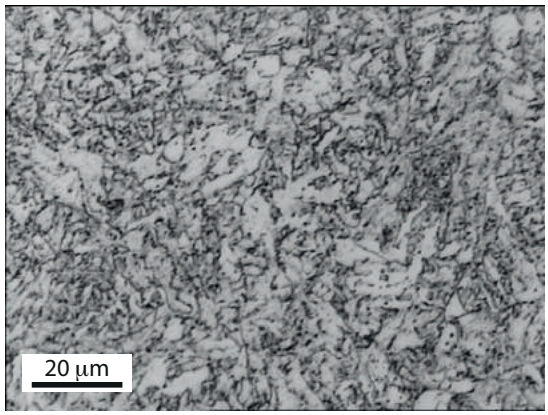

Figure 4.1: Microstructure of the RPV weld metal imaged using a light optical microscope.

is shown in Figure 4.1.

In Table 4.2, the fluence and flux for the four studied materials can be seen. One unirradiated reference material has been studied, as well as two materials irradiated in the OECD Halden Materials Test Reactor in high flux, and one surveillance material irradiated inside the RPV of R4. The difference in flux between the Halden irradiated materials and the surveillance material is around 20 times. The lead factor of the surveillance material is around 3, i. e. the surveillance material flux is around 3 times higher than the flux experienced by the R4 RPV. The irradiation temperature of the Halden irradiated materials was $290 - 295\,^{\circ}\mathrm{C}$. The surveillance material was irradiated inside the reactor, the temperature was $284\,^{\circ}\mathrm{C}$. The main neutron irradiation spectrum differences between Halden and Ringhals is for the low energy neutrons ($0.1 - 1\,\mathrm{eV}$) that do not influence the material damage [8, 67].

Table 4.2: Irradiation fluence and flux. H refers to materials irradiated in Halden, S refers to surveillance material.

Name	Fluence ($10^{23}\,\mathrm{n/m^2}$)	Flux $10^{16}\,\mathrm{n/m^2 s}$)
Reference	0	-
H2.0	2.0	2.3
H6.4	6.4	3.8
S4.6	4.6	0.15

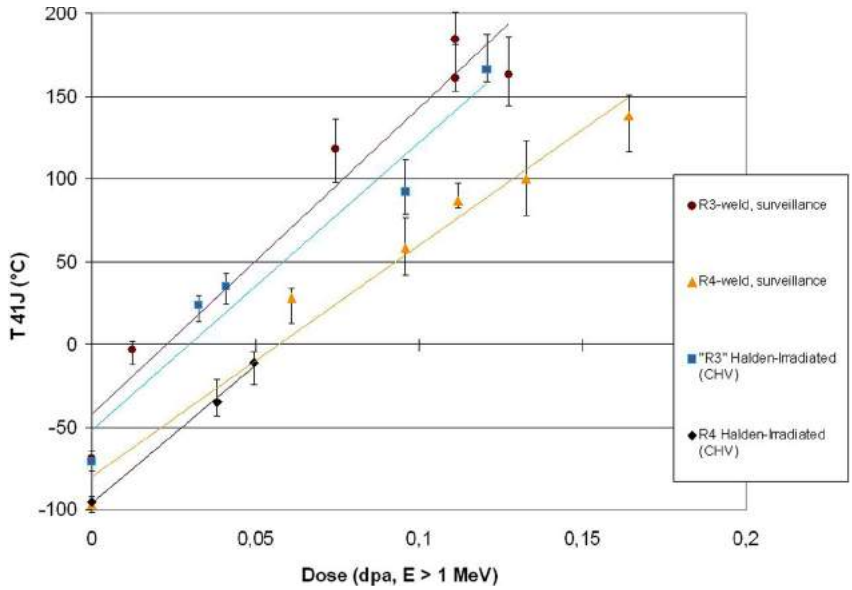

Figure 4.2: The transition temperature from Charpy V testing (CHV) for different doses of the Ringhals R3 and R4 surveillance material and the material irradiated in Halden. Reproduced, with permission from [8], copyright ASTM International, 100 Barr Harbor Drive, West Conshohocken, PA 19428.

The beginning of life DBTT for Ringhals R4 welds was quite low, $-75\,^{\circ}\mathrm{C}$ [6]. The influence of the dose on the DBTT for the surveillance material of R4 can be seen in Figure 4.2. The shift is unexpectedly high, $162\,^{\circ}\mathrm{C}$ for a fluence of $6 \cdot 10^{23}\,\mathrm{n/m^2}$ [6]. The large shift is generally attributed to the high Ni and Mn content of the welds. The surveillance material of Ringhals R3 and R4 has been analysed using APT by Miller et al. [52] and Styman et al. [80]. They found a high number density (around $4 \cdot 10^{23}\,/\mathrm{m^3}$) of nanometre sized clusters containing Ni, Mn, Si, and some Cu. Styman et al. also performed post irradiation annealing on the R3 welds to study the cluster dissolution. Cluster dissolution started after annealing 30 min at $450\,^{\circ}\mathrm{C}$, led by Mn atoms, and continued during further annealing at $500\,^{\circ}\mathrm{C}$. The hardness was recovered with the clusters dissolving. Furthermore, Hyde et al. studied the Ringhals R3 surveillance materials using SANS [139]. The results were consistent with the results from APT, and the combination with simulations also showed that features that are unresolvable in the experiment should not significantly impact the total volume fraction of features.

The mechanical properties of the Halden irradiated materials are described in [8, 140]. What was found was that even though there is a significant difference in flux between the surveillance material and the material irradiated

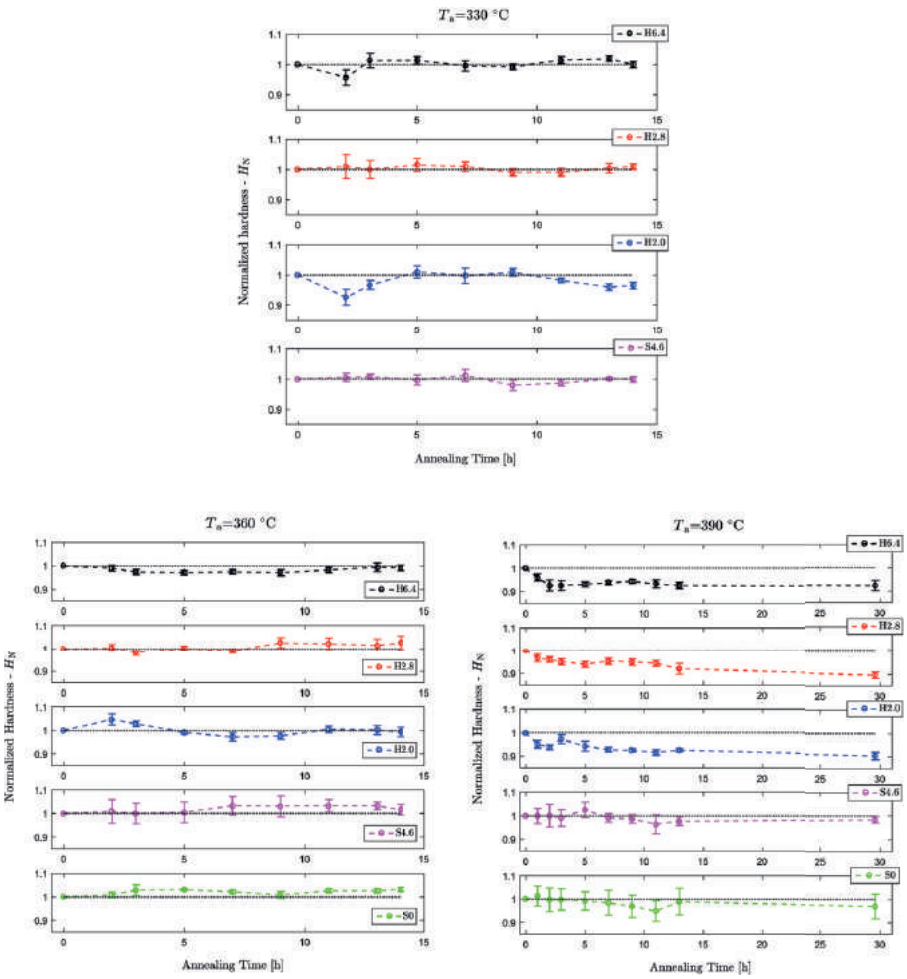

Figure 4.3: Relative hardness after annealing the RPV weld metals at 330 °C, 360 °C, and 390 °C. Reprinted from Journal of Nuclear Materials, 484, Boåsen, M., Efsing, P., Ehrnstén, U., On flux effects in a low alloy steel from a Swedish reactor pressure vessel, 110-119, Copyright (2018), with permission from Elsevier.

in Halden, the change in mechanical properties (DBTT, see Figure 4.2, and hardness) shows the same dependence on fluence [8]. However, a difference in hardness could be seen during the initial hours when annealing the materials at a temperature of 390 °C, when the hardness of the high flux materials decreased by a few percent (but not back to the hardness of the reference material), whereas the surveillance material kept the same hardness, see Figure 4.3 [140]. The difference was tentatively attributed to small clusters in the high flux material dissolving, but is further discussed in the results section in this thesis and in *Paper V*.

4.2 Ringhals R4 Pressurizer

In 2011, the pressurizer of Ringhals R4 was removed and replaced during outage. The base metal is of the type A533 Grade B Class 1, welded by Uddcomb, and thus having the characteristic high Ni and high Mn, and low Cu content in the welds, just as the Ringhals R4 RPV. A stress relief treatment at 620 °C was done after welding. The analysed welds were in operation for 28 years at 345 °C. Two different welds were analysed, one circumferential (W1), where the outer SAW welded part was analysed, and the inner part was welded by manual metal arc welding due to space limitation during fabrication. The second weld, W2, is vertical and SAW welded through the entire thickness. Both welds can be seen in Figure 4.4. The check-in transition temperature for the outer part of W1 was reported to be −51 °C, and the yield stress 579 MPa. Boåsen et al. performed mechanical testing on W1 after 28 years of operation, measuring a yield strength of 656 MPa, i. e. an increase of 77 MPa [141]. In *Paper III* and *IV*, studies of the W2 weld are presented.

4.3 José Cabrera Core Barrel and Ringhals R2 Internals

The nuclear power station José Cabrera in Almonacid de Zorita, outside Madrid in Spain, was decommissioned in 2006. The commissioning was in 1968. The core barrel of the Zorita power plant consists of stainless steel 304 plates. In this work, the welds (type 308) have been analysed. The welds contain $5 - 7$ % of ferrite (as measured by ferritescope) [142, 143]. The small volume of ferrite can also be seen in the SEM image in Figure 4.5. The typical width of the ferrite is around 200 nm, making specimen preparation using FIB/SEM necessary for APT specimen containing ferrite.

In Table 4.3 the ageing conditions are given. The samples CB-0.15, CB-1 and CB-2 come from different positions of the core barrel, being exposed to different flux during the life-time of the reactor. Initially, the CB-0.15 material was chosen to be the reference of a low-dose material. However, it was found that

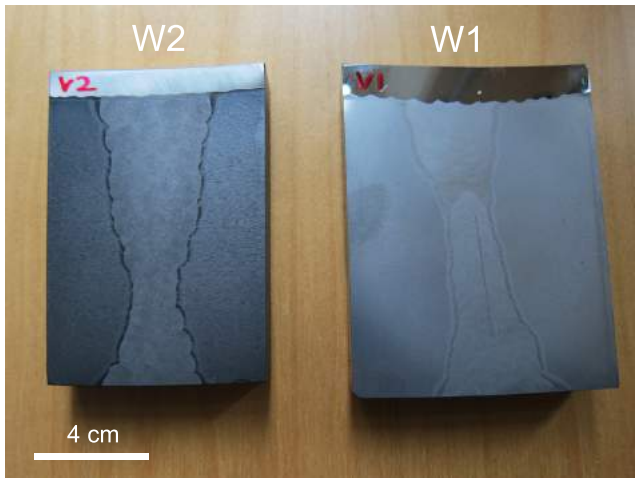

Figure 4.4: The pressurizer welds W1 and W2.

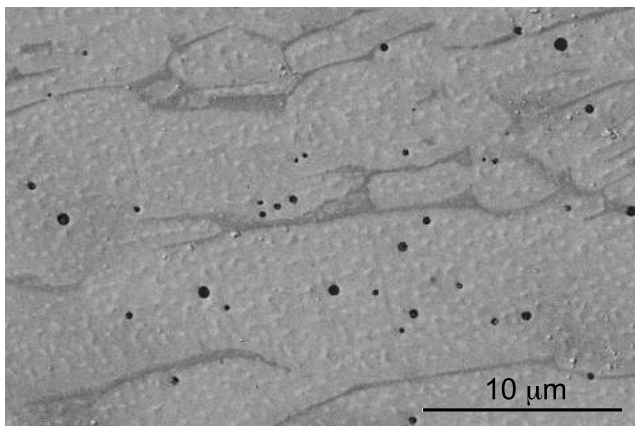

Figure 4.5: Scanning electron micrograph of core barrel weld.

Table 4.3: Irradiation fluence and temperatures of the core barrel (CB) and reference material welds.

Name	Dose (dpa)	Temperature (°C)	Time (h)
CB-0.15	0.15	280-285	231,000
CB-1	1	280-285	231,000
CB-2	2	280-285	231,000
CL	0	291 (274)	70,000 (22,000)
HL	0	325 (303)	70,000 (22,000)

the degradation of this material was well developed already after 0.15 dpa, and thus a hot leg (HL) weld and a crossover leg (CL) weld that had not been exposed to neutrons were introduced as references. These welds originate from the PWR Ringhals R2 internals, a 308 type weld used for CF8M cast components [143]. After initial ageing for 70,000 h, both CL and HL were further aged at lower temperatures for 22,000 h (also in-reactor). The HL material is less relevant than the CL material, as the temperature is significantly higher, more than compensating for the shorter ageing time [144].

The overall nominal composition of the Zorita materials and the HL and CL is expected to be similar [143, 145]. However, HL and CL have a significantly higher ferrite Ni content than the irradiated materials. This could be due to an overall difference in composition, or due to a slower cooling rate during manufacturing of CL and HL, making the Ni partition from the austenite to a higher extent. All the materials in Table 4.3 are further discussed in *Paper VI*.

CHAPTER 5

Summary of Results

In this chapter, the results of the appended papers are summarised and shortly discussed in relation to each other. First, *Paper I* is described. It contains details on the evaluation method of the clustering in the Ringhals RPV welds. This is needed for the cluster analysis in the following papers. In *Paper II*, the viability of using MTRs with higher neutron flux in order to predict the clustering of NiMnSi-rich clusters is described. This is discussed in relation to *Paper V*, where the presence of irradiation induced matrix defects, and the effect of flux, in the Ringhals R4 RPV welds are discussed, as well as cluster dissolution during post irradiation annealing (PIA). *Paper III* brings up the topic of thermal ageing in the former pressurizer of Ringhals. In *Paper IV*, the clusters formed from irradiation and thermal ageing are compared. Finally, this chapter is concluded with results from *Paper VI*, where the spinodal decomposition and G-phase formation in the José Cabrera (Zorita) core barrel welds are characterised.

5.1 Analysis of Irradiated Materials using APT

The analysis of irradiation induced clusters in RPV steels is a challenge. There are two steps from the actual material to the results; first of all, the resolution

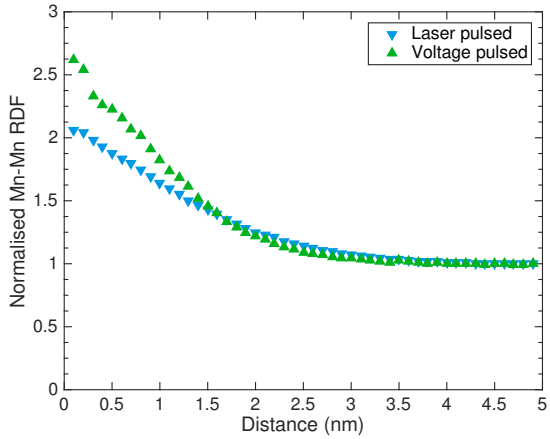

Figure 5.1: Normalised Mn-Mn radial distribution functions for a laser pulsed analysis and a voltage pulsed analysis of material H6.4. Data from *Paper I* [146] replotted.

of the APT, which is affected by the field evaporation phenomena and local magnification effects (matrix atoms end up inside the clusters due to the difference in field). This, together with the less than 100% detection efficiency of the instrument, makes the clusters appear more diffuse in the APT data than they were in the material. Some surface diffusion may occur prior to evaporation, and furthermore there might be local magnification effects due to the crystallography. Collapsing atomic planes, giving an increased number of multiple events, result in evaporation between the pulses, and thus atoms are not detected. All of these phenomena result in volumes with high or low density, dependent on the crystallography of the evaporating surface. P and Si are strongly affected by surface diffusion, but also other elements appear heterogeneously distributed, such as the clustering elements Ni and Mn. This effect is larger for laser pulsed analysis than for voltage pulsed analysis. The RDF of Mn-Mn in the irradiated Ringhals R4 material is shown in Figure 5.1 to illustrate this. A high RDF value for small distances indicates a more well-defined clustering. In addition to this, the definition of a cluster, or the cluster algorithm and parameters, need to be defined in a way that differentiates the clusters from random matrix fluctuations. In the case of the Ringhals R4 materials, the material is both high in Ni and Mn, and thus, the clusters consist of mainly Ni and Mn, making them suitable elements for cluster identification. However, there is still a considerable amount of Ni in the matrix, complicating cluster identification as it decreases the relative contrast.

In *Paper I*, MSM (see Chapter 3.1.4) is used to identify clusters in the high flux irradiated Ringhals R4 welds. Suitable solute atoms for cluster definitions were found to be Ni (29 Da peak excluded due to the overlap with $^{58}Fe^{++}$), and Mn, and in the case of voltage pulsed analyses, Si. Using Cu only would

give more well-defined clusters when analysing RDFs, but would on the other hand give different cluster compositions as the Cu is not evenly distributed within the clusters, and thus the results would be less representative. Using Cu in addition to Ni and Mn gave a negligible improvement due to the low Cu content. Suitable parameters were found through various methods, which were giving similar results. For the irradiated Ringhals welds, a $d_{max} = 0.5\,\text{nm}$ and $N_{min} = 18$ are reasonable choices.

MSM could be used with first nearest neighbour (order=1) or considering higher orders of neighbours. When comparing the first order and eight order (with a different optimised d_{max}) in the H2.0 material containing small and diffuse clusters, it was found that the eigth order require higher N_{min} values, and thus the smallest clusters could not be detected in this material. Therefore, the first order was used (which is also the most common choice in literature).

A sensitivity analysis was made to show how much the parameter choice affects the cluster analysis. The larger and more well-defined clusters in material H6.4 (Table 4.2) were, as expected, less affected by small changes in clustering parameters. Changing $d_{max} \pm 0.05\,\text{nm}$ and $N_{min} \pm 2$, that are within a reasonable parameter range, the number density decreased by 7% or increased by 5%, i. e. the changes are small. The same analysis for material H2.0, which contains smaller clusters, the decrease was 35% and the increase 26%, showing that the results are very sensitive to the exact choice of parameters, due to the nature of the APT data.

5.2 Effects of Neutron Fluence and Flux on RPV Weld Metal

In *Paper II*, the clusters formed in surveillance material (lead factor of around 3) were compared with high flux MTR irradiated materials (lead factor of 45-75) with different fluence, see Table 4.2. In all materials, clusters containing mostly Ni and Mn, but also Si and Cu were formed during neutron irradiation. The clusters were found evenly distributed in the matrix, and also on dislocations, see Figure 5.2. By comparing the high flux materials H2.0 and H6.4, the effect of fluence can be studied. The cluster number density increases fast when the irradiation is commenced and up to $2.0 \cdot 10^{23}\,\text{n/m}^2$ (material H2.0, with number density of around $4.3 \cdot 10^{23}\,\text{clusters/m}^3$, see Table 5.1). In material H6.4 (irradiated to $6.4 \cdot 10^{23}\,\text{n/m}^2$), the number density of clusters is slightly higher, in average around $6.6 \cdot 10^{23}\,\text{clusters/m}^3$, but the rate of the increase has decreased. In comparison, the surveillance material S4.6 has a lower number density than material H2.0, so clearly the cluster number density depends on flux.

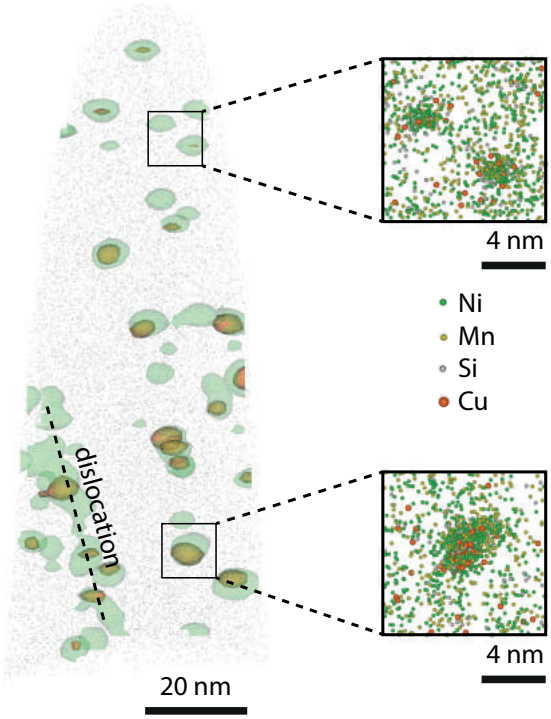

Figure 5.2: Reconstruction of APT analysis, material H6.4. Green surfaces correspond to 5 at.% Ni+Mn+Si, and orange surfaces to 1.2 at.% Cu. The boxes show all Ni, Mn, Si, and Cu atoms within two volumes of $10 \times 10 \times 10\,\mathrm{nm}^3$. Figure from *Paper II* [147].

Table 5.1: The number densities and average diameters after irradiation.

Name	Average number density (10^{23} clusters/m^3)	Average diameter (nm)
Reference	0	-
H2.0	4.3	1.5
H6.4	6.6	1.8
S4.6	3.1	2.5

The size distributions of the clusters are also affected by the neutron fluence and flux, see Table 5.1. The average size of clusters grows from 1.5 nm in H2.0 to 1.8 nm in H6.4. There is a clear flux effect as the cluster diameter of S4.6 is considerably larger (2.5 nm in diameter) although the fluence is lower than for H6.4. There are no signs of so called *late blooming phases*, a sudden increase in clustering after longer times.

Earlier studies of mechanical properties [8] (Figure 4.2) have shown no influence of flux for the Ringhals welds. The welds irradiated in high flux in Halden follow the same trend regarding hardness increase and DBTTs as the surveillance material. However, the high flux materials contain a higher number density of smaller clusters than the surveillance material, compensating for each other in terms of effect on embrittlement. It was found that the dispersed barrier hardening model (see Chapter 2.2.4) with a fitted $\alpha = 0.15$ described the hardness increase based on the cluster characteristics obtained.

The composition of the clusters was similar in all irradiated materials, with small effects of the fluence and flux. It was, however, interesting to find that the size difference between the high flux materials and the surveillance material was mostly explained by an increased number of Ni, Mn and Si atoms in the clusters, whereas the number of Cu atoms was similar. The possibility of formation of phases such as Γ_2 (Ni_3Mn_2Si) and G-phase ($Ni_{16}Mn_6Si_7$) was discussed, but no conclusions on a possible phase transformation could be made based on the current data. The compositions of the clusters did not match any of these two phases.

Annealing studies of the H6.4 weld are presented in *Paper V*. The high flux material was analysed using APT after annealing at 390 °C, 405 °C, 420 °C and 450 °C for 24-30 h. Earlier hardness measurements (Figure 4.3, [140]) show an initial decrease in hardness after annealing at 390 °C for the high flux material H6.4, but not for the surveillance material S4.6. An initial hypothesis of this being due to faster cluster dissolution was turned down as there is no barrier for cluster dissolution, and no difference in cluster characteristics were found before and after annealing at 390 °C. A possible explanation is the presence of matrix defects that are stable at reactor temperatures, but dissolved at 390 °C, which are formed due to the effect of the higher flux. Assuming this, and thus removing their contribution to the hardness, the dispersed barrier hardening

model α parameter is fitted to 0.12, that is also within the interval found in RPV welds in literature [78]. Thus, the hardness contribution of possible matrix defects is small in comparison to the contribution from the clusters in the high flux MTR irradiated material.

At 405 °C, the cluster dissolution starts, by a strongly decreased cluster number density, and a change in cluster composition. Ni, Mn and Si atoms leave the clusters. The remaining clusters are slightly smaller than the original clusters, but contain more Cu atoms, i. e. there is a coarsening process with respect to Cu taking place at 405 °C. The remaining clusters are sitting on dislocations to a larger extent than the initial clusters. Annealing at even higher temperatures further reduces the cluster number density. After annealing for 24 h at 450 °C only a small number of remaining clusters was found.

5.3 Thermal Ageing of Ringhals R4 Pressurizer Weld Metal

The Ringhals R4 pressurizer was studied after operation at 345 °C for 28 years in *Paper III*, and in *Paper IV*, where it is compared to the irradiated surveillance material. It was found that thermal ageing at this temperature resulted in clusters with an average diameter of 1.9 ± 0.3 nm forming, containing Ni, Mn, Si and Cu. Cluster formation at these temperatures in low Cu materials was not expected. The clusters are located mainly at dislocations, that were present from fabrication, see Figure 5.3. The number density is smaller than for the irradiated materials, $0.16 \pm 0.05 \cdot 10^{23}$ clusters/m^3. Furthermore, the cluster distribution is heterogeneous, as the dislocations are not evenly distributed within the weld metal. The first 300 nm in Figure 5.3 contain no Mo-enriched dislocations, and the number of clusters in this volume is much lower than in the volume with dislocations. The hardness of the material increased with $\Delta\text{HV} = 32 \pm 7\,\text{kg/mm}^2$, an increase that is attributed to the clusters, as P segregation to grain boundaries also occuring during thermal ageing should give a non-hardening contribution to the embrittlement [17, 18]. When the pressurizer weld was annealed at 620 °C for one hour (simulating PWHT), the initial hardness was regained, presumably mainly due to cluster dissolution.

In addition to clusters on dislocations, there were also clusters containing Ni, Mn, Si and Cu nucleated on other clusters, presumably carbonitrides, containing V, and sometimes Cr. These carbonitrides were found in irradiated and thermally aged material, both before and after ageing, see Figure 5.4. The number of V, Cr, N, and C atoms in these clusters varies, as seen in the figure. The number density of these features is low; in many analyses no carbonitrides at all were found. They are not believed to be affected by the ageing in any

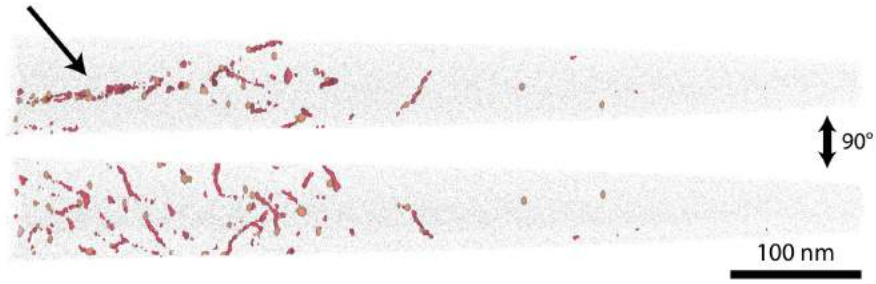

Figure 5.3: Reconstruction of APT analysis of the pressurizer. Orange surfaces correspond to 1.1 at.% Cu, and red surfaces to 2.0 at.% Mo. The arrow indicates a plane of dislocations decorated with clusters. Figure from *Paper III* [148].

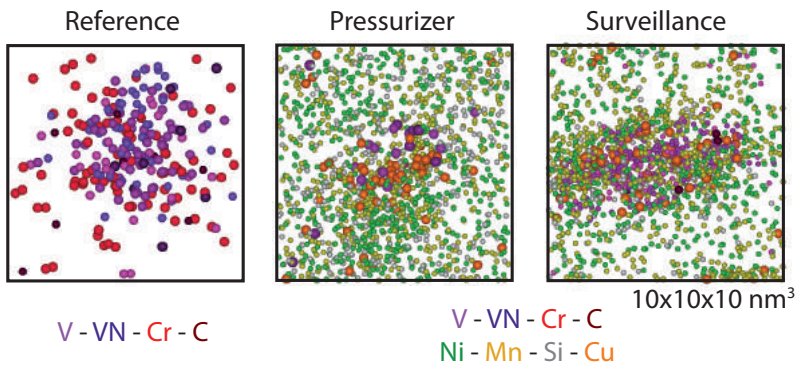

Figure 5.4: Examples of the V-containing clusters, in reference material, thermally aged pressurizer, and the surveillance material. In the reference material, only V, VN, Cr and C are shown in a cube with 10 nm sides. In the aged materials, Ni, Mn, Si and Cu are also included.

other way than acting as points of nucleation for the NiMnSi-rich clusters.

The cluster composition profile of the pressurizer is shown in Figure 5.5. The composition is compared with the surveillance material cluster profile. There is a very clear Cu-rich core of the pressurizer clusters, surrounded by Ni and Mn. The Si content in the thermally aged clusters is low in comparison to the irradiated material. There is also a difference in the Ni/Mn ratio, which is around one for the clusters in the pressurizer, but 2.4 for the surveillance material (corresponding ratios for material H6.4 is 1.7 and for H2.0 1.4). One possible explanation might be the differences in thermal diffusion and irradiation enhanced diffusion for the different atoms. Thermal diffusion is driven by vacancies only, but during irradiation, there are also interstitials that are affecting the diffusion, in case of P and Mn transport by the dumbbell mechanism [56]. PIA for 24 h at 405 °C and higher temperatures also change the

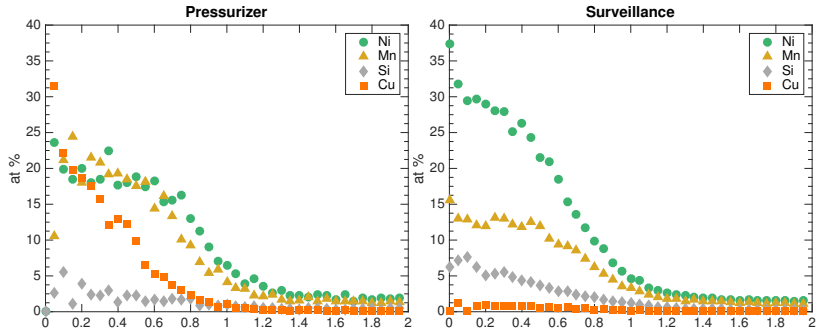

Figure 5.5: Normalised cluster composition profiles for the pressurizer and the surveillance material welds. The x-axis represents the relative radius, i. e. 1 corresponds to the cluster edge, and 0 to the cluster centre. Figure from *Paper IV* [149].

cluster Ni/Mn ratio to around one. The total amount of Ni, Mn and Si in the materials are similar, making this an effect of the ageing conditions rather than initial chemistry.

The results of the pressurizer show that there will be effects of annealing of the irradiated materials also at lower temperatures than 405 °C, given long enough times. At 345 °C, clusters nucleate on dislocations and grow slowly (after 28 years there are clusters, for other times the evolution is currently unknown), at 405 °C, most of the Ni, Mn and Si leaves the clusters within 24 h, and Cu-rich clusters coarsen. At 420 °C the clusters dissolve. In other words, the impact of thermal ageing and annealing over time is complex.

A central question is the difference between the thermally aged and the irradiated RPV welds regarding the nucleation of the clusters. In the thermally aged materials, it appears that the clusters nucleate on a range of different features; boundaries, dislocations and small vanadium carbonitrides, and a few clusters directly in the matrix. In the irradiated materials, defects are provided to nucleate on in the matrix, as the neutron irradiation result in matrix defects, such as small clusters of vacancies and interstitial loops. Vacancies has previously been observed by positron annihilation spectroscopy (PAS) to be associated with Cu in Fe-Cu model alloys, acting as points of nucleation [150]. Interstitial loops have been found to be the nucleation points of clusters and results match cluster number densities in Ringhals surveillance materials in the object kinetic Monte Carlo model by Messina et al. and Chiapetto et al. [59, 151]. In thermally aged RPV welds with higher Cu content, clusters have been found to be homogeneously distributed within the matrix [84, 88], thus indicating the Cu content as important for nucleation. In the low Cu Ringhals R4 pressurizer welds, any dislocation or other feature is attractive

for nucleation of clusters.

5.4 Degradation Phenomena in Austenitic Welds

The degradation in the ferrite of the austenitic welds in the HL material from Ringhals R2 and the irradiated Zorita core barrel (*Paper VI*) is of a different nature than in the RPV, due to the much higher Cr content. The ferrite spinodally decomposes into Fe-rich and Cr-rich volumes. Already after irradiation to 0.15 dpa (material CB-0.15) the effect is almost saturated, and no difference can be seen between irradiation to 1 (CB-1) and 2 dpa (CB-2) in the ferrite. The G-phase formation differs from material CB-0.15 to CB-1 and CB-2, where the clusters are more well-defined.

In the austenite of the irradiated materials, small P clusters are found after irradiation to 0.15 dpa. In the CB-1 and CB-2 materials, Ni-Si precipitates were found, as well as loops enriched in Ni and Si. The Ni/Si ratios of the precipitates and loop segregations were found to be between 1.6 and 2.7. In the thermally aged materials, the austenite was found to be unaffected by ageing.

The ferrite/austenite boundaries were affected by ageing. The amount of Ni and Si segregating to the interface increased with dose. In CB-1 and CB-2, the Ni and Si form elongated precipitates on the boundary, similar to those found at a low angle grain boundary. The distribution of other solute elements such as P is also found to vary dependent on dose. The P content on the interface is higher in CB-0.15 than in CL. However, CB-1 and CB-2 show a decreasing trend in boundary P content.

In the CL material, thermally aged at a temperature similar to the temperature of the irradiated materials, no spinodal decomposition or G-phase precipitation is detected. The distribution of elements in the austenite is found to be random after thermal ageing. It is thus concluded that the irradiation plays a crucial role in the degradation of the welds. The work on the austenitic welds is ongoing, and the results will be further complemented by more characterisation techniques in order to be able to discuss the degradation and the impact on properties in detail.

5.5 Conclusions

This thesis contributes to understanding the behaviour of high Ni and Mn, low Cu, RPV weld metals under neutron irradiation, and the difference in cluster characteristics when irradiated at high fluxes. The increase in cluster number density and size is gradual in the Ringhals R4 welds, and does not appear to

accelerate at high fluences. Thus, the results do not implicate the presence of so called *late blooming phases* in the material, but rather a continuous (but retarding) precipitation and growth for the fluences analysed. The use of a higher flux (lead factors up to 75) to simulate the neutron irradiation in a PWR in operation results in similar hardening as in the surveillance material, due to slightly smaller clusters with a slightly higher number density forming. A small part of the contribution to hardness probably comes from matrix defects that are behaving differently dependent on flux.

Furthermore, long term thermal ageing of the Ringhals R4 pressurizer welds, which have similar composition as the RPV welds, results in clusters located mainly on dislocations. The number density of these is one order of magnitude lower than in the irradiated welds, but the clusters' size is similar, and the compositions of the clusters are similar but irradiated clusters contain less Cu, as expected from other studies. All these results are relevant in the context of comparing microstructural observations with both atomistic studies and the large scale mechanical properties of the materials, in order to further understand the mechanisms of degradation and the effects on properties.

The austenitic welds with remaining ferrite show the multiple types of degradation occurring in components exposed to both irradiation and heat in a reactor in operation. After irradiation to 0.15 dpa, the microstructure of the ferrite of the weld was strongly affected by irradiation. Due to the complexity when many phenomena are occurring, this part of the project needs further work to be concluded.

CHAPTER 6

Outlook

Based on the conclusions in the previous chapter and the knowledge within the field, the following complementary investigations are suggested.

- In order to further study the effect of flux, an actual RPV that has been in operation could be studied. No reactor with the high Ni and Mn, and low Cu content has been analysed after decommissioning using APT so far.
- A further investigation of the matrix damage, and its contribution to mechanical properties in the high Ni and Mn RPV materials. In the Halden irradiated RPV welds, part of the hardness increase during irradiation is probably from matrix damage. However, the methodology of using hardness measurements and APT is indirect, and direct measurements such as PAS and possibly also simulations would be of value. Furthermore, in this project nothing could be concluded using only APT and hardness measurements on the matrix damage in the surveillance material, thus further understanding would be useful.
- Understanding the differences in the compositions of the irradiated clusters, and how these differences compare to the composition of the clusters in the thermally aged pressurizer would be interesting. It would be in-

teresting to compare the APT results with for instance modelling results to understand more of the mechanisms behind the differences.

- The austenitic welds need to be further characterised using TEM in order to obtain larger field of view to make more general conclusions of the degradation.

CHAPTER 7

Acknowledgements

The Swedish Centre for Nuclear Technology (SKC) is acknowledged for funding. Vattenfall Ringhals is acknowledged for providing the irradiated materials and VTT for cutting the hot materials and sending them to us. The Nordic Nuclear Safety Research (NKS) collaboration is acknowledged for funding. Furthermore, the Electric Power Research Institute (EPRI) is acknowledged for funding and for the irradiated material for the Zorita project. The Swedish Radiation Safety Authority (SSM) is also acknowledged for funding.

On a personal level, I would like to thank my supervisor Mattias Thuvander. You have been helpful with many things, from practical advice in the lab and in terms of discussions on interpretations, analysis, results, possible ways forward and ideas. Thank you for your time and curiosity, and taking my side! Also, thank you Krystyna Stiller for being my co-supervisor, and sharing your energy and enthusiasm!

I am very thankful to Pål Efsing (Vattenfall and KTH) and Jenny Roudén, Ringhals. Magnus Boåsen at Solid Mechanics, KTH, thank you for the collaboration, helping me with the connection between my results and the "real", large-scale world, and the many discussions on the RPV material. Also thank you for the good company during trips and meetings!

Furthermore, thank you Martin Bjurman (KTH and Studsvik) for the collaboration on the Zorita materials.

Thank you Ulla Ehrnstén, VTT, and Grace Burke, University of Manchester, for fruitful discussions and support!

Here at Chalmers, I would like to thank Stefan Allard and Anders Nordlund for helping me with transports of my materials, and storage. Furthermore, thank you Burcak Ebin for help with the annealing.

Dear collegues; former and present colleagues in the M2 and EOG divisions and CMAL; what would the coffee breaks be without you? You make working here very enjoyable! I would like to specially thank Anders, Stefan, Katarina and Reza for help in the lab, and Ola for invaluable help with my computer in times of crisis. Thank you Lena for the introduction to the world of electron microscopy! My former long-time office mate Masoud: thank you for your generosity and the good times, and letting me have the desk by the window!

I would also like to thank my family; my parents Karin and Erik and my sister Anna-Märta, and Karl. Last but not least, thank you Mikael for being who you are, and supporting me when I have a hard time.

Kristina Lindgren

Göteborg, November 2018

Bibliography

[1] Interngovermental Panel on Climate Change (IPCC). Global warming of 1.5 °C - an IPCC special report on the impacts of global warming of 1.5 °C above pre-industrial levels and related global greenhouse gas emission pathways, in the context of strengthening the global response to the threat of climate change, sustainable development, and efforts to eradicate poverty. Report, 2018.

[2] Key world energy statistics. Report, International Energy Agency, 2016.

[3] Statistiska Centralbyrån (SCB). *80 procent av elen kommer från vattenkraft och kärnkraft - http://www.scb.se/hitta-statistik/sverige-i-siffror/miljo/energi/, accessed 02-11-2018*. 2018.

[4] SSM. Investigation of long-term safety in the Swedish nuclear power industry and measures owing to the accident at Fukushima Dai-ichi. Report, Strålsäkerhetsmyndigheten (Swedish Radiation Safety Authority), 2013.

[5] P. Efsing and P. Ekström. *Swedish RPV Surveillance Programs*, book section Stp160320170012, pages 219–231. ASTM International, West Conshohocken, 2018.

[6] P. Efsing, C. Jansson, T. Mager, and G Embring. Analysis of the ductile-to-brittle transition temperature shift in a commercial power plant with high nickel containing weld material. *Journal of ASTM International*, 4(7), 2007.

[7] G. R. Odette and G. E. Lucas. Recent progress in understanding reactor pressure vessel steel embrittlement. *Radiation Effects and Defects in Solids*, 144(1-4):189–231, 1998.

[8] P. Efsing, J. Roudén, and P. Nilsson. Flux effects on radiation induced aging behaviour of low alloy steel weld material with high nickel and manganese content. *Effects of radiation on nuclear materials*, 26:119–134, 2014.

[9] Wolfgang Hoffelner. *Materials for Nuclear Plants: From Safe Design to Residual Life Assessments*. Springer, London, 2013.

[10] M. Hernández-Mayoral and M. J. Caturla. *Microstructure evolution of irradiated structural materials in nuclear power plants*, book section 8, pages 189–235. Woodhead Publishing Series in Energy. Woodhead Publishing, Cambridge, 2010.

[11] *Irradiation Embrittlement of Reactor Pressure Vessels (RPVs) in Nuclear Power Plants*. Woodhead Publishing, 2015.

[12] H.K.D.H. Bhadeshia and R.W.K. Honeycombe. *Steels Microstructure and properties*. Butterworth-Heinemann, 3 edition, 2006.

[13] G. R. Odette and G. E. Lucas. Embrittlement of nuclear pressure vessels. *Journal of Microscopy*, 53(7):18–22, 2001.

[14] M. K. Miller, P. Pareige, and M. G. Burke. Understanding pressure vessel steels: An atom probe perspective. *Materials Characterization*, 44(1-2):235–254, 2000.

[15] Vattenfall. *Tekniska Data Ringhals, https://corporate.vattenfall.se/globalassets/sverige/om-vattenfall/om-oss/var-verksamhet/ringhals/pdf-ovriga/tekniska-data-utforlig-info-151207.pdf, accessed 14-10-2016*. 2016.

[16] Vattenfall. *Vad visar tryckhållaren? https://corporate.vattenfall.se/press-och-media/nyheter/import-nyheter/vad-visar-tryckhallaren/, accessed 16-08-2018*. Vattenfall, 2012.

[17] H. Nakata, K. Fujii, K. Fukuya, R. Kasada, and A. Kimura. Grain boundary phosphorus segregation in thermally aged low alloy steels. *Journal of Nuclear Science and Technology*, 43(7):785–793, 2006.

[18] Y. I. Shtrombakh, B. A. Gurovich, E. A. Kuleshova, D. A. Maltsev, S. V. Fedotova, and A. A. Chernobaeva. Thermal ageing mechanisms of VVER-1000 reactor pressure vessel steels. *Journal of Nuclear Materials*, 452(1-3):348–358, 2014.

[19] B. A. Gurovich, A. A. Chernobaeva, D. Yu Erak, E. A. Kuleshova, D. A. Zhurko, V. B. Papina, M. A. Skundin, and D. A. Maltsev. Chemical composition effect on VVER-1000 RPV weld metal thermal aging. *Journal of Nuclear Materials*, 465:540–549, 2015.

[20] M. Brumovsky. *Irradiation hardening and materials embrittlement in light water reactor (LWR) environments*, book section 11, pages 357–373. Woodhead Publishing Series in Energy. Woodhead Publishing, Cambridge, 2010.

[21] T. Toyama, Y. Nagai, Z. Tang, M. Hasegawa, A. Almazouzi, E. van Walle, and R. Gerard. Nanostructural evolution in surveillance test specimens of a commercial nuclear reactor pressure vessel studied by three-dimensional atom probe and positron annihilation. *Acta Materialia*, 55(20):6852–6860, 2007.

[22] J. C. van Duysen, J. Bourgoin, P. Moser, and C. Janot. Study by positron annihilation of neutron damage in a pressurized water reactor (PWR)pressure vessel steel after a 13-year irradiation in the CHOOZ A reactor surveillance program. *ASTM STP 1170*, pages 132–138, 1993.

[23] J. C. van Duysen and G. Meric de Bellefon. 60th anniversary of electricity production from light water reactors: Historical review of the contribution of materials science to the safety of the pressure vessel. *Journal of Nuclear Materials*, 484:209–227, 2017.

[24] R. Chaouadi and R. Gérard. Copper precipitate hardening of irradiated rpv materials and implications on the superposition law and re-irradiation kinetics. *Journal of Nuclear Materials*, 345(1):65–74, 2005.

[25] M. Shimodaira, T. Toyama, K. Yoshida, K. Inoue, N. Ebisawa, K. Tomura, T. Yoshiie, M. J. Konstantinovic, R. Gérard, and Y. Nagai. Contribution of irradiation-induced defects to hardening of a low-copper reactor pressure vessel steel. *Acta Materialia*, 155:402–409, 2018.

[26] G. S. Was. *Fundamentals of Radiation Materials Science*. Springer, Berlin, 2007.

[27] G. R. Odette, T. Yamamoto, and D. Klingensmith. On the effect of dose rate on irradiation hardening of RPV steels. *Philosophical Magazine*, 85(4-7):779–797, 2005.

[28] A. Kryukov, L. Debarberis, A. Ballesteros, V. Krsjak, R. Burcl, S. V. Rogozhkin, A. A. Nikitin, A. A. Aleev, A. G. Zaluzhnyi, V. I. Grafutin, O. Ilyukhina, Yu V. Funtikov, and A. Zeman. Integrated analysis of WWER-440 RPV weld re-embrittlement after annealing. *Journal of Nuclear Materials*, 429(1-3):190–200, 2012.

[29] M. G. Burke, R. J. Stofanak, J. M. Hyde, C. A. English, and W. L. Server. Microstructural aspects of irradiation damage in A508 Gr 4N forging steel: Composition and flux effects. *Journal of ASTM International*, 1(4):1–14, 2004.

[30] R. Chaouadi and R. Gérard. Neutron flux and annealing effects on irradiation hardening of RPV materials. *Journal of Nuclear Materials*, 418(1-3):137–142, 2011.

[31] R. Chaouadi and R. Gérard. Confirmatory investigations on the flux effect and associated unstable matrix damage in RPV materials exposed to high neutron fluence. *Journal of Nuclear Materials*, 437(1-3):267–274, 2013.

[32] G. R. Odette and R. K Nanstad. Predictive reactor pressure vessel steel irradiation embrittlement models: issues and opportunities. *JOM*, 61(7):17–23, 2009.

[33] G. R. Odette and B. D. Wirth. A computational microscopy study of nanostructural evolution in irradiated pressure vessel steels. *Journal of Nuclear Materials*, 251:157–171, 1997.

[34] G. R. Odette. Radiation induced microstructural evolution in reactor pressure vessel steels. *Materials Research Society Symposium Proceedings*, 373:137–148, 1995.

[35] J. M. Hyde and C. A. English. An analysis of the structure of irradiation induced Cu-enriched clusters in low and high nickel welds. In *Materials Research Society Symposium*, volume 650, pages R6.6.1–R6.6.12, 2000.

[36] A. Wagner, A. Ulbricht, F. Bergner, and E. Altstadt. Influence of the copper impurity level on the irradiation response of reactor pressure vessel steels investigated by SANS. *Nuclear Instruments and Methods in Physics Research Section B: Beam Interactions with Materials and Atoms*, 280:98–102, 2012.

[37] P. Pareige, J. C. van Duysen, and P. Auger. An APFIM study of the microstructure of a ferrite alloy after high fluence neutron irradiation. *Applied Surface Science*, 67(1-4):342–347, 1993.

[38] P. Auger, P. Pareige, S. Welzel, and J-C Van Duysen. Synthesis of atom probe experiments on irradiation-induced solute segregation in french ferritic pressure vessel steels. *Journal of Nuclear Materials*, 280(3):331–344, 2000.

[39] M. K. Miller and K. F. Russell. Embrittlement of RPV steels: An atom probe tomography perspective. *Journal of Nuclear Materials*, 371(1-3):145–160, 2007.

[40] M. K. Miller, R. K. Nanstad, M. A. Sokolov, and K. F. Russell. The effects of irradiation, annealing and reirradiation on RPV steels. *Journal of Nuclear Materials*, 351(1-3):216–222, 2006.

[41] P. Pareige, B. Radiguet, A. Suvorov, M. Kozodaev, E. Krasikov, O. Zabusov, and J. P. Massoud. Three-dimensional atom probe study of irradiated, annealed and re-irradiated VVER 440 weld metals. *Surface and Interface Analysis*, 36(56):581–584, 2004.

[42] U. Potapovs and J. R. Hawthorne. The effect of residual elements on the response of selected pressure-vessel steels and weldments to irradiation at 550F. *Nuclear Applications*, 6(1):27–46, 1969.

[43] Smidt F. A. and H. E. Watson. Effect of resdial elements on radiation strengthening in iron alloys, pressure vessel steels, and welds. *Metallurgical Transactions*, 3(8):2065–2073, 1972.

[44] G. R. Odette. On the mechanism of irradiation embrittlement of reactor pressure vessel steels. *Scripta Metallurgica*, 17(10):1183–1188, 1983.

[45] J. E. Zelenty. Understanding thermally induced embrittlement in low copper RPV steels utilising atom probe tomography. *Materials Science and Technology*, 31(8):981–988, 2015.

[46] P. J. Othen, M. L. Jenkins, G. D. W. Smith, and W. J. Phythian. Transmission electron microscope investigations of the structure of copper precipitates in thermally-aged Fe-Cu and Fe-Cu-Ni. *Philosophical Magazine Letters*, 64(6):383–391, 1991.

[47] E. Meslin, B. Radiguet, P. Pareige, and A. Barbu. Kinetic of solute clustering in neutron irradiated ferritic model alloys and a French pressure vessel steel investigated by atom probe tomography. *Journal of Nuclear Materials*, 399(2-3):137–145, 2010.

[48] CL. Liu, G-R. Odette, B.D. Wirth, and G.E. Lucas. A lattice Monte Carlo simulation of nanophase compositions and structures in irradiated pressure vessel Fe-Cu-Ni-Mn-Si steels. *Materials Science and Engineering*, A238:202–209, 1997.

[49] S. C. Glade, B. D. Wirth, G. R. Odette, P. Asoka-Kumar, P. A. Sterne, and R. H. Howell. Positron annihilation spectroscopy and small-angle neutron scattering characterization of the effect of Mn on the nanostructural features formed in irradiated Fe-Cu-Mn alloys. *Philosophical Magazine*, 85(4-7):629–639, 2005.

[50] R. Ngayam-Happy, C. S. Becquart, C. Domain, and L. Malerba. Formation and evolution of MnNi clusters in neutron irradiated dilute Fe alloys modelled by a first principle-based AKMC method. *Journal of Nuclear Materials*, 426(1–3):198–207, 2012.

[51] P. B. Wells, T. Yamamoto, B. Miller, T. Milot, J. Cole, Y. Wu, and G. R. Odette. Evolution of manganese–nickel–silicon-dominated phases in highly irradiated reactor pressure vessel steels. *Acta Materialia*, 80:205–219, 2014.

[52] M. K. Miller, K. A. Powers, R. K. Nanstad, and P. Efsing. Atom probe tomography characterizations of high nickel, low copper surveillance RPV welds irradiated to high fluences. *Journal of Nuclear Materials*, 437(1-3):107–115, 2013.

[53] M. K. Miller, A. A. Chernobaeva, Y. I. Shtrombakh, K. F. Russell, R. K. Nanstad, D. Y. Erak, and O. O. Zabusov. Evolution of the nanostructure of VVER-1000 RPV materials under neutron irradiation and post irradiation annealing. *Journal of Nuclear Materials*, 385(3):615–622, 2009.

[54] G. Bonny, D. Terentyev, A. Bakaev, E. E. Zhurkin, M. Hou, D. Van Neck, and L. Malerba. On the thermal stability of late blooming phases in reactor pressure vessel steels: An atomistic study. *Journal of Nuclear Materials*, 442(1–3):282–291, 2013.

[55] E. Meslin, B. Radiguet, P. Pareige, C. Toffolon, and A. Barbu. Irradiation-induced solute clustering in a low nickel FeMnNi ferritic alloy. *Experimental Mechanics*, 51(9):1453–1458, 2011.

[56] L. Messina. *Multiscale Modeling of Atomic Transport Phenomena in Ferritic Steels*. Thesis, 2015.

[57] G. Bonny, D. Terentyev, E. E. Zhurkin, and L. Malerba. Monte carlo study of decorated dislocation loops in FeNiMnCu model alloys. *Journal of Nuclear Materials*, 452(1-3):486–492, 2014.

[58] K. Yabuuchi, M. Saito, R. Kasada, and A. Kimura. Neutron irradiation hardening and microstructure changes in Fe–Mn binary alloys. *Journal of Nuclear Materials*, 414(3):498–502, 2011.

[59] L. Messina, M. Chiapetto, P. Olsson, C. S. Becquart, and L. Malerba. An object kinetic Monte Carlo model for the microstructure evolution of neutron-irradiated reactor pressure vessel steels. *physica status solidi (a)*, 2016.

[60] W. Xiong, H. Ke, R. Krishnamurthy, P. Wells, L. Barnard, G. R. Odette, and D. Morgan. Thermodynamic models of low-temperature Mn–Ni–Si precipitation in reactor pressure vessel steels. *MRS Communications*, pages 1–5, 2014.

[61] D. J. Sprouster, J. Sinsheimer, E. Dooryhee, S. K. Ghose, P. Wells, T. Stan, N. Almirall, G. R. Odette, and L. E. Ecker. Structural characterization of nanoscale intermetallic precipitates in highly neutron ir-

radiated reactor pressure vessel steels. *Scripta Materialia*, 113:18–22, 2016.

[62] P. B. Wells. *The Charachter, Stability and Consequences of Mn-Ni-Si precipitates in Irraiduated Reactor Pressure Vessel Steels.* Thesis, 2016.

[63] D. J. M. King, P. A. Burr, S. C. Middleburgh, T. M. Whiting, M. G. Burke, and M. R. Wenman. The formation and structure of Fe-Mn-Ni-Si solute clusters and G-phase precipitates in steels. *Journal of Nuclear Materials*, 505:1–6, 2018.

[64] E. A. Marquis and J. M. Hyde. Applications of atom-probe tomography to the characterisation of solute behaviours. *Materials Science and Engineering: R: Reports*, 69(4-5):37–62, 2010.

[65] S. J. Zinkle and G. S. Was. Materials challenges in nuclear energy. *Acta Materialia*, 61(3):735–758, 2013.

[66] F. Bergner, A. Ulbricht, H. Hein, and M. Kammel. Flux dependence of cluster formation in neutron-irradiated weld material. *Journal of Physics: Condensed Matter*, 20(10):104262, 2008.

[67] A. Ballesteros, R. Ahlstrand, C. Bruynooghe, A. Chernobaeva, Y. Kevorkyan, D. Erak, and D. Zurko. Irradiation temperature, flux and spectrum effects. *Progress in Nuclear Energy*, 53(6):756–759, 2011.

[68] R. E. Stoller. The effect of neutron flux on radiation-induced embrittlement in reactor pressure vessel steels. *Journal of ASTM International*, 1(4):326–337, 2004.

[69] A. Wagner, F. Bergner, R. Chaouadi, H. Hein, M. Hernández-Mayoral, M. Serrano, A. Ulbricht, and E. Altstadt. Effect of neutron flux on the characteristics of irradiation-induced nanofeatures and hardening in pressure vessel steels. *Acta Materialia*, 104:131–142, 2016.

[70] K. Dohi, K. Nishida, A. Nomoto, N. Soneda, H. Matsuzawa, and M. Tomimatsu. Effect of neutron flux at high fluence on microstructural and hardness changes of RPV steels. *ASME 2010 Pressure Vessels and Piping Division K-PVP Conference*, 2010.

[71] N. Soneda, K. Nishida, A. Nomoto, and K. Dohi. Flux effect on embrittlement of reactor pressure vessel steels irradiated to high fluences. *Fontevraud 8: Conference on Contribution of Materials Investigations and Operating Experience to LWRs' Safetyy, Performance and Reliability*, 2014.

[72] K. Fukuya, K. Ohno, H. Nakata, S. Dumbill, and J. M. Hyde. Microstructural evolution in medium copper low alloy steels irradiated in a pressurized water reactor and a material test reactor. *Journal of Nuclear Materials*, 312(2-3):163–173, 2003.

[73] M.K. Miller and K.F. Russell. APFIM characterization of a high phosphorus Russian RPV weld. *Applied Surface Science*, 94/95:378–383, 1996.

[74] A. V. Nikolaeva, Y. A. Nikolaev, and Y. Kevorkyan. Grain-boundary segregation of phosphorous in low-alloy steel. *Atomic Energy*, 91(1):534–542, 2001.

[75] S. Suzuki, S. Tanii, K. Abiko, and H. Kimura. Site competition between sulfur and carbon at grain boundaries and their effects on the grain boundary cohesion in iron. *Metallurgical and Materials Transactions A*, 18 A:1109–1115, 1987.

[76] G. Tauber and H. J. Grabke. Grain boundary segregation of sulfur, nitrogen and carbon in alpha-iron. *Berichte der Bunsengesellschaft für physikalische Chemie*, 82(3):298–302, 1978.

[77] A. K. Seeger. On the theory of radiation damage and radiation hardening. *Proceedings of the Second UN Conference on Peaceful Uses of Atomic Energy*, 6:250–273, 1958.

[78] F. Bergner, F. Gillemot, M. Hernández-Mayoral, M. Serrano, G. Török, A. Ulbricht, and E. Altstadt. Contributions of Cu-rich clusters, dislocation loops and nanovoids to the irradiation-induced hardening of Cu-bearing low-Ni reactor pressure vessel steels. *Journal of Nuclear Materials*, 461:37–44, 2015.

[79] K. C. Russell and L. M. Brown. A dispersion strenghtening model based on differing elastic moduli applied to the iron-copper system. *Acta Metallurgica*, 20:969–974, 1972.

[80] P. D. Styman, J. M. Hyde, D. Parfitt, K. Wilford, M. G. Burke, C. A. English, and P. Efsing. Post-irradiation annealing of Ni–Mn–Si-enriched clusters in a neutron-irradiated RPV steel weld using atom probe tomography. *Journal of Nuclear Materials*, 459:127–134, 2015.

[81] L. Liu, K. Nishida, K. Dohi, A. Nomoto, N. Soneda, K. Murakami, Z. Li, D. Chen, and N. Sekimura. Effects of solute elements on hardening and microstructural evolution in neutron-irradiated and thermally-aged reactor pressure vessel model alloys. *Journal of Nuclear Science and Technology*, pages 1–8, 2016.

[82] N. Soneda, K. Dohi, A. Nomoto, K. Nishida, and S. Ishino. Embrittlement correlation method for the Japanese reactor pressure vessel materials. *Journal of ASTM International*, 7(3):1–20, 2010.

[83] M. Kolluri, A. Kryukov, A. J. Magielsen, P. Hähner, V. Petrosyan, G. Sevikyan, and Z. Szaraz. Mechanical properties and microstructure of long

term thermal aged WWER 440 RPV steel. *Journal of Nuclear Materials*, 486:138–147, 2017.

[84] P. D. Styman, J. M. Hyde, A. Morley, K. Wilford, N. Riddle, and G. D. W. Smith. The effect of Ni on the microstructural evolution of high Cu reactor pressure vessel steel welds after thermal ageing for up to 100,000 h. *Materials Science and Engineering: A*, 736:111–119, 2018.

[85] P. D. Styman, J. M. Hyde, K. Wilford, A. Morley, and G. D. W. Smith. Precipitation in long term thermally aged high copper, high nickel model RPV steel welds. *Progress in Nuclear Energy*, 57:86–92, 2012.

[86] A. Seko, N. Odagaki, S. R. Nishitani, I. Tanaka, and H. Adachi. Free-energy calculation of precipitate nucleation in an Fe-Cu-Ni alloy. *Materials Transactions*, 45(7):1978–1981, 2004.

[87] A. T. Al-Motasem, M. Posselt, and F. Bergner. Nanoclusters in bcc-Fe containing vacancies, copper and nickel: Structure and energetics. *Journal of Nuclear Materials*, 418(1-3):215–222, 2011.

[88] J. M. Hyde, G. Sha, E. A. Marquis, A. Morley, K. B. Wilford, and T. J. Williams. A comparison of the structure of solute clusters formed during thermal ageing and irradiation. *Ultramicroscopy*, 111(6):664–71, 2011.

[89] Q. Liu, J. Gu, and W. Liu. On the role of Ni in Cu precipitation in multicomponent steels. *Metallurgical and Materials Transactions A*, 44(10):4434–4439, 2013.

[90] J. T. Buswell, C. A. English, M. G. Hetherington, W. J. Phythian, G. D. W. Smith, and G. M. Worrall. An analysis of small clusters formed in thermally aged and irradiated FeCu and FeCuNi model alloys. *Effects of radiation on nuclear materials: 14th international symposium*, 2:127–153, 1990.

[91] A. Etienne, B. Radiguet, P. Pareige, J. P. Massoud, and C. Pokor. Tomographic atom probe characterization of the microstructure of a cold worked 316 austenitic stainless steel after neutron irradiation. *Journal of Nuclear Materials*, 382(1):64–69, 2008.

[92] Z. Jiao and G. S. Was. Novel features of radiation-induced segregation and radiation-induced precipitation in austenitic stainless steels. *Acta Materialia*, 59(3):1220–1238, 2011.

[93] E. A. Kenik and J. T. Busby. Radiation-induced degradation of stainless steel light water reactor internals. *Materials Science and Engineering: R: Reports*, 73(7-8):67–83, 2012.

[94] Y. Chen, P. H. Chou, and E. A. Marquis. Quantitative atom probe tomography characterization of microstructures in a proton irradiated 304 stainless steel. *Journal of Nuclear Materials*, 451(1-3):130–136, 2014.

[95] D. A. Porter and K. E. Easterling. *Phase Transformations in Metals and Alloys*. Nelson Thornes, Cheltenham, second edition, 2001.

[96] J. W. Cahn. On spinodal decomposition. *Acta Metallurgica*, 9:795–801, 1961.

[97] F. Danoix and P. Auger. Atom probe studies of the Fe-Cr system and stainless steels aged at intermediate temperature: a review. *Materials Characterization*, 44:177–201, 2000.

[98] A. Pineau and J. Besson. *Thermal Embrittlement of Cast Duplex Stainless Steels: Observations and Modelling*, book section 5, pages 161–208. 2013.

[99] W. Xiong, P. Hedström, M. Selleby, J. Odqvist, M. Thuvander, and Q. Chen. An improved thermodynamic modeling of the Fe–Cr system down to zero kelvin coupled with key experiments. *Calphad*, 35(3):355–366, 2011.

[100] P. Hedström, F. Huyan, J. Zhou, S. Wessman, M. Thuvander, and J. Odqvist. The $475^{\circ}c$ embrittlement in Fe–20Cr and Fe–20Cr–X (X=Ni, Cu, Mn) alloys studied by mechanical testing and atom probe tomography. *Materials Science and Engineering: A*, 574:123–129, 2013.

[101] M. K. Miller, R. E. Stoller, and K. F. Russell. Effect of neutron-irradiation on the spinodal decomposition of Fe-32% Cr model alloy. *Journal of Nuclear Materials*, 230:219–225, 1996.

[102] F. Soisson and T. Jourdan. Radiation-accelerated precipitation in Fe–Cr alloys. *Acta Materialia*, 103:870–881, 2016.

[103] J. Bentley, M.K. Miller, S.S. Brenner, and J.A. Spitznagel. Identification of G-phase in aged cast CF 8 type stainless steel. *Proceedings - Annual Meeting, Electron Microscopy Society of America*, 43:328–329, 1985.

[104] F. Danoix, P. Auger, and D. Blavette. An atom-probe investigation of some correlated phase transformations in Cr, Ni, Mo containing supersaturated ferrites. *Surface Science*, 266(1-3):364–369, 1992.

[105] A. Mateo, L. Llanes, M. Anglada, A. Redjaimia, and G. Metauer. Characterization of the intermetallic G-phase in an AISI 329 duplex stainless steel. *Journal of Materials Science*, 32(17):4533–4540, 1997.

[106] C. Pareige, J. Emo, S. Saillet, C. Domain, and P. Pareige. Kinetics of G-phase precipitation and spinodal decomposition in very long aged ferrite of a Mo-free duplex stainless steel. *Journal of Nuclear Materials*, 465:383–389, 2015.

[107] F. Danoix, P. Bas, J. P. Massoud, Guttermanm M., and P. Auger. Atom probe and transmission electron microscopy study of reverted stainless steels. *Applied Surface Science*, 67:348–355, 1993.

[108] T. R. Leax, S.S. Brenner, and J.A. Spitznagel. Atom probe examination of thermally aged CF8M cast stainless steel. *Metallurgical Transactions A*, 23A:2725–2736, 1992.

[109] W. Guo, D. A. Garfinkel, J. D. Tucker, D. Haley, G. A. Young, and J. D. Poplawsky. An atom probe perspective on phase separation and precipitation in duplex stainless steels. *Nanotechnology*, 27(25):254004, 2016.

[110] C. Pareige, S. Novy, S. Saillet, and P. Pareige. Study of phase transformation and mechanical properties evolution of duplex stainless steels after long term thermal ageing (>20years). *Journal of Nuclear Materials*, 411(1-3):90–96, 2011.

[111] S. Mburu, R. P. Kolli, D. E. Perea, S. C. Schwarm, A. Eaton, J. Liu, S. Patel, J. Bartrand, and S. Ankem. Effect of aging temperature on phase decomposition and mechanical properties in cast duplex stainless steels. *Materials Science and Engineering: A*, 690:365–377, 2017.

[112] R. M. Boothby, J. M. Hyde, H. Swan, D. Parfitt, K. Wilford, and P. Lindner. SANS examination of irradiated RPV steel welds during in-situ annealing. *Journal of Nuclear Materials*, 461:45–50, 2015.

[113] F. Bergner, A. Ulbricht, and H. W. Viehrig. Acceleration of irradiation hardening of low-copper reactor pressure vessel steel observed by means of SANS and tensile testing. *Philosophical Magazine Letters*, 89(12):795–805, 2009.

[114] A. Ulbricht, E. Altstadt, F. Bergner, H. W. Viehrig, and U. Keiderling. Small-angle neutron scattering investigation of as-irradiated, annealed and reirradiated reactor pressure vessel weld material of decommissioned reactor. *Journal of Nuclear Materials*, 416(1-2):111–116, 2011.

[115] R. G. Carter, N. Soneda, K. Dohi, J. M. Hyde, C. A. English, and W. L. Server. Microstructural characterization of irradiation-induced Cu-enriched clusters in reactor pressure vessel steels. *Journal of Nuclear Materials*, 298:211–224, 2001.

[116] P. D. Edmondson, C. M. Parish, and R. K. Nanstad. Using complimentary microscopy methods to examine Ni-Mn-Si-precipitates in highly-irradiated reactor pressure vessel steels. *Acta Materialia*, 134:31–39, 2017.

[117] S. Lozano-Perez, G. Sha, J. M. Titchmarsh, M. L. Jenkins, S. Hirosawa, A. Cerezo, and G. D. W. Smith. Comparison of the number densities of nanosized Cu-rich precipitates in ferritic alloys measured using EELS and EDX mapping, HREM and 3DAP. *Journal of Materials Science*, 41(9):2559–2565, 2006.

[118] J. J. H. Lim, J. M. Hyde, S. Lozano-Perez, and C. R. M. Grovenor. Microstructural characterization of irradiation-induced MnNi-rich solute cluster in highly neutron-irradiated MnNiMo alloyed weld metals. *Effects of Radiation on Nuclear Materials*, 26:57–73, 2014.

[119] M. K. Miller. *Atom Probe Tomography: Analysis at the Atomic Level*. Kluwer Academic/Plenum Publishers, New York, 2000.

[120] B. Gault, M. P. Moody, J. M. Cairney, and S. P. Ringer. *Atom Probe Microscopy*. Springer, New York, 2012.

[121] M. K. Miller and R. G. Forbes. *Atom-Probe Tomography: The Local Electrode Atom Probe*. Springer, New York, 2014.

[122] P. Bas, A. Bostel, B. Deconihout, and D. Blavette. A general protocol for the reconstruction of 3D atom probe data. *Applied Surface Science*, 87/88:298–304, 1995.

[123] O. C. Hellman, J. A. Vandenbroucke, J. Rüsing, D. Isheim, and D. N. Seidman. Analysis of three-dimensional atom-probe data by the proximity histogram. *Microscopy and Microanalysis*, 6(5):437–444, 2000.

[124] A. Heinrich, T. Al-Kassab, and R. Kirchheim. Investigation of the early stages of decomposition of Cu–0.7at.% Fe with the tomographic atom probe. *Materials Science and Engineering: A*, 353(1-2):92–98, 2003.

[125] D. Vaumousse, A. Cerezo, and P.J. Warren. A procedure for quantification of precipitate microstructures from three-dimensional atom probe data. *Ultramicroscopy*, 95:215–221, 2003.

[126] J. S. Langer, M. Bar-on, and Harold D. Miller. New computational method in the theory of spinodal decomposition. *Physical Review A*, 11(4):1417–1429, 1975.

[127] J. Zhou, J. Odqvist, M. Thuvander, and P. Hedstrom. Quantitative evaluation of spinodal decomposition in Fe-Cr by atom probe tomography and radial distribution function analysis. *Microsc Microanal*, 19(3):665–75, 2013.

[128] J. M. Hyde, M. G. Burke, B. Gault, D. W. Saxey, P. Styman, K. B. Wilford, and T. J. Williams. Atom probe tomography of reactor pressure vessel steels: an analysis of data integrity. *Ultramicroscopy*, 111(6):676–82, 2011.

[129] B. Gault, F. Danoix, K. Hoummada, D. Mangelinck, and H. Leitner. Impact of directional walk on atom probe microanalysis. *Ultramicroscopy*, 113:182–191, 2012.

[130] M. K. Miller and M. G. Hetherington. Local magnification effects in the atom probe. *Surface Science*, 246(1-3):442–449, 1991.

[131] F. Vurpillot, A. Bostel, and D. Blavette. Trajectory overlaps and local magnification in three-dimensional atom probe. *Applied Physics Letters*, 76(21):3127–3129, 2000.

[132] A. Morley, G. Sha, S. Hirosawa, A. Cerezo, and G. D. Smith. Determining the composition of small features in atom probe: bcc Cu-rich precipitates in an Fe-rich matrix. *Ultramicroscopy*, 109(5):535–40, 2009.

[133] S. Shu, B. D. Wirth, P. B. Wells, D. D. Morgan, and G. R. Odette. Multi-technique characterization of the precipitates in thermally aged and neutron irradiated Fe-Cu and Fe-Cu-Mn model alloys: Atom probe tomography reconstruction implications. *Acta Materialia*, 146:237–252, 2018.

[134] S. Lozano-Perez, J. M. Titchmarsh, and M. L. Jenkins. Determination of the Fe content of embedded Cu-rich particles in ferritic alloys using energy-filtered TEM. *Ultramicroscopy*, 106(2):75–91, 2006.

[135] M. Thuvander, J. Weidow, J. Angseryd, L. K. Falk, F. Liu, M. Sonestedt, K. Stiller, and H. O. Andren. Quantitative atom probe analysis of carbides. *Ultramicroscopy*, 111(6):604–8, 2011.

[136] D. J. Larson, D. T. Foord, A. K. Petford-Long, H. Liew, M. G. Blamire, A. Cerezo, and G. D. W. Smith. Field-ion specimen preparation using focused ion-beam milling. *Ultramicroscopy*, 79(1-4):287–293, 1999.

[137] K. Thompson, D. Lawrence, D. J. Larson, J. D. Olson, T. F. Kelly, and B. Gorman. In situ site-specific specimen preparation for atom probe tomography. *Ultramicroscopy*, 107(2-3):131–9, 2007.

[138] J. Blomström, P. Efsing, J. Roudén, A. Karlsson, and P. Nilsson. Ringhals 3 and 4 – from problem to solution - managing ageing of RPV weld with high Ni and Mn-content for long term irradiation. *Proceedings - Fontevraud 9: Contribution of Materials Investigations and Operating Experience to Light Water NPPs' Safety, Performance and Reliability*, 2018.

[139] J. M. Hyde, R. M. Boothby, H. Swan, N. Riddle, K. Wilford, M. G. Burke, and P. Efsing. A sensitivity study using maximum entropy to interpret SANS data from the Ringhals Unit 3 NPP. *Journal of Nuclear Materials*, 509:417–424, 2018.

[140] M. Boåsen, P. Efsing, and U. Ehrnstén. On flux effects in a low alloy steel from a Swedish reactor pressure vessel. *Journal of Nuclear Materials*, 484:110–119, 2017.

[141] M. Boåsen, K. Lindgren, J. Roudén, M. Öberg, J. Faleskog, M. Thuvander, and P. Efsing. Thermal ageing of low alloy steel weldments from a swedish nuclear power plant – a study of mechanical properties. *Proceedings - Fontevraud 9: Contribution of Materials Investigations and Operating Experience to Light Water NPPs' Safety, Performance and Reliability*, 2018.

[142] M. Bjurman, K. Lindgren, M. Thuvander, P. Ekström, and P. Efsing. Microstructural evolution of welded stainless steels on integrated effect of thermal aging and low flux irradiation. *the 18th International Conferece on Environmental Degradation of Materials in Nucler Power Systems - Water Reactors*, pages 703–710, 2018.

[143] M. Bjurman, M. Thuvander, K. Lindgren, and P. Efsing. Thermal ageing and irradiation of cast and welded stainless steels and the influence on LTO. *Proceedings - Fontevraud 9: Contribution of Materials Investigations and Operating Experience to Light Water NPPs' Safety, Performance and Reliability*, 2018.

[144] M. Bjurman, B. Forssgren, and P. Efsing. *Fracture Mechanical Testing of In-Service Thermally Aged Cast Stainless Steel*, pages 58–80. ASTM international, West Conshohocken, PA, 2017.

[145] A. Jenssen, J. Stjärnsäter, K. Kese, R. Carter, J. Smith, A. Demma, and M. Hiser. Fracture toughness testing of an irradiated PWR core barrel weld. *Proceedings - Fontevraud 9: Contribution of Materials Investigations and Operating Experience to Light Water NPPs' Safety, Performance and Reliability*, 2018.

[146] K. Lindgren, K. Stiller, P. Efsing, and M. Thuvander. On the analysis of clustering in an irradiated low alloy reactor pressure vessel steel weld. *Microsc Microanal*, 23(2):376–384, 2017.

[147] K. Lindgren, M. Boåsen, K. Stiller, P. Efsing, and M. Thuvander. Evolution of precipitation in reactor pressure vessel steel welds under neutron irradiation. *Journal of Nuclear Materials*, 488:222–230, 2017.

[148] K. Lindgren, M. Boåsen, K. Stiller, P. Efsing, and M. Thuvander. Cluster formation in in-service thermally aged pressurizer welds. *Journal of Nuclear Materials*, 504:23–28, 2018.

[149] K. Lindgren, M. Boåsen, K. Stiller, P. Efsing, and M. Thuvander. Thermal ageing of low alloy steel weldments from a Swedish nuclear power plant – the evolution of the microstructure. *Proceedings - Fontevraud 9: Contribution of Materials Investigations and Operating Experience to Light Water NPPs' Safety, Performance and Reliability*, 2018.

[150] Y. Nagai, Z. Tang, M. Hassegawa, T. Kanai, and M. Saneyasu. Irradiation-induced Cu aggregations in Fe: An origin of embrittlement of reactor pressure vessel steels. *Physical Review B*, 63(13), 2001.

[151] M. Chiapetto, L. Messina, C. S. Becquart, P. Olsson, and L. Malerba. Nanostructure evolution of neutron-irradiated reactor pressure vessel steels: Revised object kinetic Monte Carlo model. *Nuclear Instruments and Methods in Physics Research Section B: Beam Interactions with Materials and Atoms*, 393:105–109, 2017.

Paper I

On the analysis of clustering in an irradiated low alloy reactor pressure vessel steel weld

K. Lindgren, K. Stiller, P. Efsing, and M. Thuvander

Microscopy and Microanalysis 23, 376-384 (2017)

Microsc. Microanal. 23, 376–384, 2017
doi:10.1017/S1431927617000162

Microscopy AND Microanalysis

On the Analysis of Clustering in an Irradiated Low Alloy Reactor Pressure Vessel Steel Weld

Kristina Lindgren,[1,*] Krystyna Stiller,[1] Pål Efsing,[2] and Mattias Thuvander[1]

[1]*Department of Physics, Chalmers University of Technology, Göteborg SE 412 96, Sweden*
[2]*Vattenfall Ringhals AB, Väröbacka SE 430 22, Sweden*

Abstract: Radiation induced clustering affects the mechanical properties, that is the ductile to brittle transition temperature (DBTT), of reactor pressure vessel (RPV) steel of nuclear power plants. The combination of low Cu and high Ni used in some RPV welds is known to further enhance the DBTT shift during long time operation. In this study, RPV weld samples containing 0.04 at% Cu and 1.6 at% Ni were irradiated to 2.0 and 6.4×10^{23} n/m^2 in the Halden test reactor. Atom probe tomography (APT) was applied to study clustering of Ni, Mn, Si, and Cu. As the clusters are in the nanometer-range, APT is a very suitable technique for this type of study. From APT analyses information about size distribution, number density, and composition of the clusters can be obtained. However, the quantification of these attributes is not trivial. The maximum separation method (MSM) has been used to characterize the clusters and a detailed study about the influence of the choice of MSM cluster parameters, primarily on the cluster number density, has been undertaken.

Key words: reactor pressure vessel steel, clustering, atom probe tomography, irradiation damage, maximum separation method

Introduction

The reactor pressure vessel (RPV) of nuclear power plants is subjected to both heat and neutron irradiation, leading to gradual changes in properties, a phenomenon known as aging. The effects of the aging become important after long operating times as the RPV welds become more and more embrittled. The embrittlement is connected to the formation of various features on the nanometer scale, hindering dislocation glide when the material is subjected to stress (Odette & Lucas, 1998). Nanometer-sized clusters containing Cu, Ni, Mn, and Si form, depending on the composition of the steel. For low Cu high Ni steels, clusters with small amounts of Cu, or even without Cu, form (Miller et al., 2009, 2013; Meslin et al., 2010*b*). The small scale of these features makes them suitable for atom probe tomography (APT) studies. This allows for quantitative measurements of important parameters, like number density, size distribution, and composition of the clusters that in turn influence the mechanical properties of the steel.

Some different techniques to identify clusters using APT have been developed during the last two decades, and a review of methods can be found in reference (Marquis & Hyde, 2010). The maximum separation method (MSM) is one method that identifies clusters based on the distances between solute atoms (Hyde & English, 2000; Heinrich et al., 2003; Vaumousse et al., 2003). The parameters might need to be chosen for each system, dependent on the cluster size and composition, and the matrix composition. The detection efficiency and background noise might also affect the choice of parameters (Gault et al., 2012). The MSM is a widely used method for cluster identification due to it being fast and easy to use and that it is implemented in the most commonly used software.

When applying the MSM, five parameters usually need to be considered. The maximum distance between two solute atoms considered to form a cluster is denoted d_{max}. The parameter N_{min} is the smallest number of solute atoms regarded to be a cluster and not random fluctuations. The order, N, denotes how many solute atoms that need to be located within the distance d_{max}. Most commonly, $N = 1$ is used, that is only the nearest neighboring atom distance is taken into account. Higher orders can give more robust results, avoiding effects from small density fluctuations, but might not be suitable for small clusters (Stephenson et al., 2007). When measuring the composition of the cluster, the envelope distance L is the distance around the solute atoms defining which nonsolute atoms that are to be included in the cluster. Finally, E is the erosion distance; it removes the thin shell of atoms outside the cluster that would otherwise be counted as belonging to the cluster due to the introduction of L. As a consequence, the measured number density of clusters is only influenced by the choice of d_{max}, N_{min}, and N, whereas the choice of E and L influences size and composition of the clusters.

The choice of the value for the parameter d_{max} is a trade-off (Vaumousse et al., 2003). If d_{max} is too large, features that might be random matrix fluctuations are considered to be clusters, which increases the measured cluster number density. However, a too small value of d_{max} will not be able to identify all clusters. N_{min} is also vital and the appropriate value

Received June 30, 2016; accepted January 14, 2017
*Corresponding author. kristina.lindgren@chalmers.se

to use is dependent on the choice of d_{max} (Hyde et al., 2011*b*). Random fluctuations (noise) in the solute distribution in the matrix might be classified as clusters with an unsuitable choice of parameters, especially with a too small value of N_{min}.

Several methods have been proposed for choosing the parameters for the MSM, often based on comparing the reconstructed atom distribution with random distributions (Cerezo & Davin, 2007; Styman et al., 2013). The MSM has also been compared with other methods, for instance, the use of isoconcentration surfaces, that with the right parameters might give similar results, for example in the case of Cu clusters in Fe (Kolli & Seidman, 2007). Data sets have been simulated in order to further understand the influence of the choice of MSM parameters (Hyde et al., 2011*b*), that is, when "the correct answer" is known. The results have also been compared with other techniques, for instance small angle neutron scattering, positron annihilation spectroscopy, and transmission electron microscopy (Meslin et al., 2010*a*).

The irradiated RPV weld material of interest in this paper contains clusters of mainly Ni, Mn, and Si. Some of the clusters also contain Cu. The material has been exposed to accelerated neutron irradiation in a test reactor. The relatively high concentration of Ni and Mn in the matrix and the small size (some down to ~1 nm) make the clusters hard to identify and define. This paper is concerned with discussing the identification of these small and diffuse clusters and with comparing some different methods for choosing the d_{max} and N_{min} parameters for the MSM. Most of the previous APT studies of RPV steel have applied voltage pulsing. Voltage pulsing has some benefits over laser pulsing; in particular it gives less surface diffusion of P and Si related to the crystallography (Hyde et al., 2011*a*). However, the risk of specimen fracture is experienced to be higher, especially for specimens prepared using the focused ion beam (FIB) lift-out technique. Laser pulsing might be used to increase the probability of finding grain boundaries or other sparse features like dislocations. Here, very long laser pulsed runs are also analyzed and compared with voltage pulsed analyses.

Materials and Methods

The two materials studied are practically identical to the RPV welds of the pressurized water reactor (PWR) Ringhals R4 in Sweden. The welds were post weld heat treated at 620°C in order to relieve internal stresses. They were irradiated to 2.0 and 6.4×10^{23} n/m^2 in high flux [2.3 and 3.8×10^{16} n/(m^{2}s), respectively] in the research reactor in Halden, Norway. In this test reactor, the spectrum for neutrons with energies above 1 MeV, that damage the material, can be considered to impact the material in the same way as the neutrons of a PWR in operation (Efsing et al., 2014). The temperature in the reactor was 290–295°C. The nominal chemical composition of the welds can be seen in Table 1.

Samples for APT were prepared in a FIB/scanning electron microscope (FIB/SEM), an FEI Versa 3D (FEI, Hillsboro, OR, USA), using a standard lift-out method and annular milling (Larson et al., 1999) as the material was slightly active, electropolishing was problematic. The analyses were performed using a LEAP 3000X HR (Imago Scientific Instruments, Madison, WI, USA), which has a detection efficiency of about 37%, according to the supplier. Both laser and voltage pulsing were used in order to get good statistics and to get the correct Si and P distribution (reference Hyde et al., 2011*a* shows effects of surface migration in similar materials), respectively. Voltage analyses were performed at 50 K with a pulse fraction of 20% and a target evaporation rate of 0.2%. In laser mode, the temperature was 30 K, the laser energy 0.3 nJ and the target evaporation rate 0.5%. In both cases the pulse frequency was 200 kHz. For voltage pulsed analyses, around 2 million atoms were collected before specimen fracture, whereas 25–70 million atoms were collected for the laser pulsed analyses before they were stopped.

Table 1. Chemical Composition of the Ringhals R4 Welds in at%.

Cu	Ni	Mn	Mo	Si	C	P	S	Cr	Al	Co	Fe
0.04	1.58	1.37	0.29	0.28	0.31	0.027	0.007	0.04	0.05	0.01	Bal.

Data from Efsing et al. (2007).

The data analysis was performed in the IVAS 3.6.10 software (Cameca Inc., Madison, WI, USA). Reconstruction parameters were chosen so that the plane distance at low index poles corresponded to a lattice parameter of 0.287 nm (bcc α-iron). These parameters gave the clusters a basically spherical shape. For laser analyses an evaporation field of 23 V/nm was used with a k-factor of 4.0 and for voltage analyses 33 V/nm and 5.3 were found to be the best parameters. An image compression factor of 1.65 was used for all reconstructions.

Results

Microstructure

A reconstruction of a full analysis of the material irradiated to 6.4×10^{23} n/m^2 can be seen in Figure 1a, where Cu atoms, as well as 8.2% Ni + Mn + Si isoconcentration surfaces, are shown. In the middle part a dislocation line is evident (marked by an arrow). The dislocation line is enriched in P and cuts the edges of the analysis volume. For further analysis of clusters, similar lines are removed as the formation mechanism, composition, number densities, and shapes may be different for clusters in the matrix and at dislocations. Apart from at the dislocations, the clusters are evenly distributed in the volume.

One of the larger clusters is cut from the analysis and the Ni, Mn, Si, and Cu atoms are shown in Figure 1b. As seen, the number of Cu atoms is relatively low. In Figure 1c, two or three small clusters are shown, depending on what cluster definition is used. These clusters are rather diffuse, and hence harder to identify than the larger clusters. The matrix contains significant amounts of Ni, Mn, and Si, whereas the Cu concentration outside clusters is small, due to the low Cu bulk concentration.

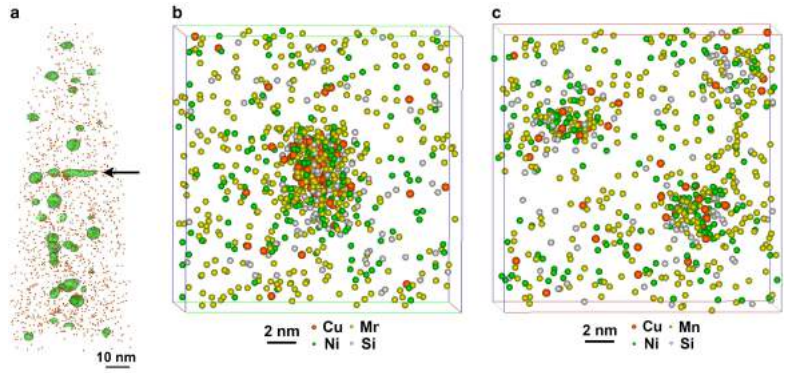

Figure 1. Reconstructions of a voltage pulsed atom probe tomographic analysis of the material irradiated to 6.4×10^{23} n/m^2. **a:** The entire analyzed volume. Green surfaces are 8.2% Ni + Mn + Si isoconcentration surfaces. Orange dots are Cu atoms. One elongated cluster is part of a dislocation line crossing the edge of the analysis volume (arrow). **b:** A large cluster in the material. Ni, Mn, Si, and Cu atoms are shown. **c:** Two or three small and diffuse clusters in the same analysis.

Cluster Identification

For voltage pulsed analyses Ni, Mn, and Si were used for cluster identification. When laser analyses were considered, only Ni and Mn were used, because Si was strongly affected by surface diffusion, as previously reported (Hyde et al., 2011*a*). The usage of Cu only for cluster identification would give well-defined clusters when studying the statistical distributions, for instance nearest neighbor distributions (NNDs) and radial distribution functions (RDFs). However, the low Cu concentration in the material and the fact that the Cu atoms are not homogeneously distributed within the clusters, make it necessary to use more types of atoms. In fact, when using Ni and Mn as clustering elements, the Cu contribution to the clusters becomes insignificant.

In the mass spectrum, there is an overlap at 29 Da, for $^{58}Fe^{2+}/^{58}Ni^{2+}$, see Supplementary Figures 1 and 2. The natural isotopic abundance of ^{58}Fe and ^{58}Ni is 0.28 and 68%, respectively. Hence, with a Ni content of 1.58% and an Fe content of 96%, a deconvolution of the 29-peak implies 80% of the peak being Ni and 20% Fe. The effect of the exclusion of the 29-peak can be seen in the RDF for Ni in Figure 2. The higher values at short distances indicate a more distinct clustering signal (meaning that the contrast between cluster and matrix is improved). Thus, the 29-peak was not used for cluster identification. The possible disadvantage of excluding this peak, which would be degraded statistics, is regarded as less important than the improved contrast. However, when considering the composition of the clusters, the 29-peak should be deconvoluted according to the isotopic abundance. The peak at 58 Da ($^{58}Fe^{+}/^{58}Ni^{+}$ overlap) was assigned as Ni as the Fe percentage of this peak is small even for laser pulsed analyses (Supplementary Figure 1c), as Fe to a smaller extent than Ni is field evaporated as 1 + ions. As the RDFs with and without the 58-peak assigned to Ni are virtually the same (Fig. 2), this peak does not influence the cluster–matrix contrast and therefore most likely not the cluster identification.

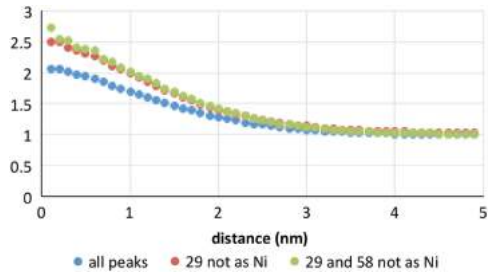

Figure 2. Radial distribution functions (bulk normalized concentrations) of Ni with and without the 29 Da peak and the 58 Da peak ranged as Ni. Laser pulsed analysis of material irradiated to 6.4×10^{23} n/m^2.

Supplementary Figures 1 and 2

Supplementary Figures 1 and 2 can be found online. Please visit journals.cambridge.org/jid_MAM.

Comparison of Laser/Voltage Pulsing for Cluster Analysis

The RDFs for voltage and laser pulsed analyses were compared, see Figure 3. Here, Mn–Mn is considered since this makes the RDF independent of the overlap issues connected to Ni discussed in the previous section. The curves indicate that clusters are more diffuse in the laser pulsed analyses. The cluster number density obtained from the analysis shows no significant dependence on pulse mode, as the variation is larger within and between analyses due to the varying local chemical composition in the welds. However, the RDFs indicate that voltage pulsing gives higher quality data, not only in that it gives less Si surface diffusion, but also that the positioning of other elements is more precise. This is

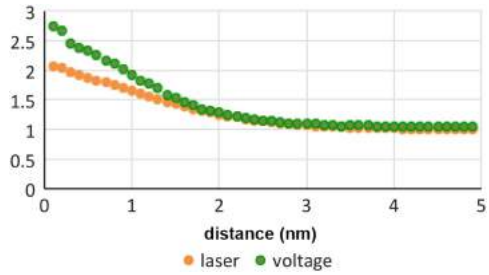

Figure 3. Radial distribution functions (bulk normalized concentrations) of Mn for voltage and laser pulsed analyses of the material irradiated to 6.4×10^{23} n/m^2.

probably due to some degree of surface diffusion before evaporation induced by the laser pulse, as described in (Gault et al., 2010). Here, both laser and voltage pulsed analyses are considered, as laser pulsing gives larger analysis volumes, providing improved statistics. This is valuable when investigating, for instance, cluster size distributions.

Maximum Separation Method Parameters

The parameters L and E are not studied in this paper. They are of importance for determination of cluster composition, but not for cluster identification. The choice of d_{max} will influence the smallest possible N_{min} that can be chosen without risking false identification of random matrix compositional fluctuations as clusters. Figure 4 shows the influence of d_{max} and N_{min} on the number of identified clusters for the materials irradiated to the two different fluences. The data comes from laser pulsed analyses, and hence Ni and Mn are used for cluster identification as the Si signal is unreliable when laser pulsing is applied. The peaks at $d_{max} = 0.85$ nm correspond mainly to the random distribution of the elements in the matrix. The distributions at lower d_{max} correspond to the actual clusters in the material. Ideally, the distribution should be bimodal and hence make it easy to separate the clusters from the matrix. The cluster count as a function of d_{max} starts to increase around 0.3 nm that corresponds to the lattice parameter of bcc Fe (0.287 nm). The choice of d_{max} and N_{min} should be made so that as many of the "real" clusters as possible are identified (high enough value of d_{max}), but without risking that random fluctuations in the solute distribution are falsely identified (i.e., avoid the peak at 0.85 nm in Fig. 4 and too low values of N_{min}). For d_{max} this would correspond to a plateau in the distribution, as seen around 0.4–0.6 nm for the high fluence material. Choosing parameters at this plateau in both N_{min} and d_{max} has the benefit of giving robust results, so if slightly different analyses should be compared, the same parameters may be chosen. Figure 4 indicates a difference between the clusters in the two materials; the clusters in the material with the higher fluence are more well defined.

The number of detected clusters can be compared to the number of clusters detected in a data set with the same

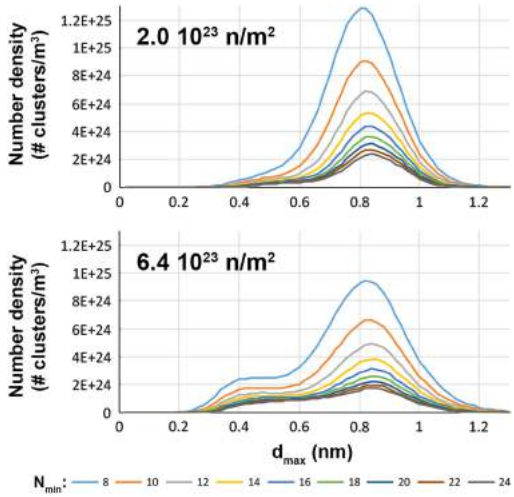

Figure 4. Influence of d_{max} and N_{min} on the cluster number density determined using the maximum separation method in the material irradiated to 2.0×10^{23} and 6.4×10^{23} n/m^2. Ni and Mn were used to identify the clusters in these laser pulsed analyses.

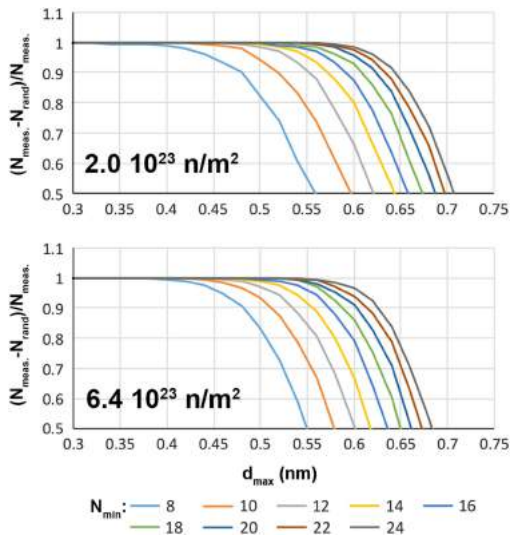

Figure 5. Normalized number of nonrandom clusters as a function of d_{max} for some different N_{min}. Laser pulsed analysis, material irradiated to 2.0×10^{23} and 6.4×10^{23} n/m^2.

composition, but with randomly distributed atoms. The choice of parameters should be made so that the risk of identifying random fluctuations in the composition as clusters is small, while avoiding exclusion of real clusters due to too strict cluster definitions. In Figure 5, the number of detected clusters ($N_{meas.}$) is compared with the number of random clusters (N_{random}) as $(N_{meas.} - N_{random})/N_{meas.}$ dependent on d_{max} and

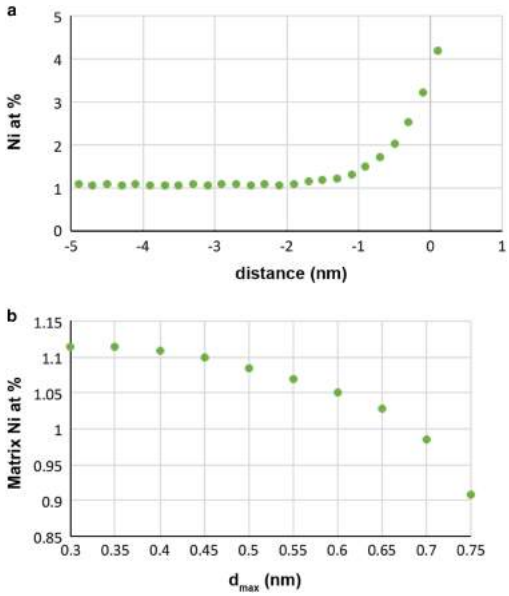

Figure 6. a: Proxigram of isoconcentration surfaces (Ni + Mn = 5.5%). Composition of matrix is 1.08 at%. **b:** Matrix Ni content as a function of d_{max}. Laser pulsed analysis, $N_{min} = 18$, material irradiated to 2.0×10^{23} n/m^2.

N_{min} (Williams et al., 2013). The randomization for N_{random} is obtained retaining the positions of the atoms and randomizing their identity. In the limit of no random clusters, this ratio approaches unity. The plots give an opportunity to put a threshold value or tolerance level, which can be set the same for different analyses giving different parameter choices. This gives the same statistical risk of defining random matrix fluctuations as clusters. However, it does not give any indications to whether clusters are missed.

For a specific N_{min}, a suitable value of d_{max} can also be found by comparing matrix solute levels with that from isoconcentration surfaces. In Figure 6a, a proxigram obtained from isoconcentration surfaces with a threshold of Ni + Mn = 5.5% is shown, indicating a matrix Ni content of around 1.08%. In Figure 6b, the concentration of Ni in the matrix is shown as a function of the choice of d_{max}, when applying the MSM with $N_{min} = 18$. A comparison of the matrix concentration suggests a d_{max} of 0.50 nm for the low fluence material (Fig. 6) and 0.55 nm for the high fluence material. This method is dependent on manual determination of a reasonable threshold for the isoconcentration surfaces, and will depend slightly also on the parameters used, such as voxel size and delocalization.

NNDs would be useful for finding the clustering parameters as they are not dependent on d_{max} and N_{min}, but on the reconstructed data itself. Stephenson et al. (2007) used the NNDs for finding d_{max}. The NND is a superposition of two complete spatial randomness (CSR) distributions; one

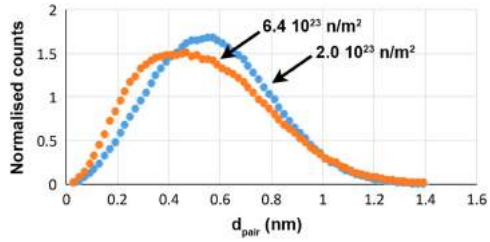

Figure 7. Nearest neighbor distributions (Mn and Ni, 29 Da peak excluded) for the material irradiated to 2.0×10^{23} and 6.4×10^{23} n/m^2, laser pulsed analyses.

for the clusters and one with a larger nearest neighbor (NN) distance for the matrix. By fitting a sum of two CSR distributions and using the cluster part of this fit, a d_{max} can be found. Jägle et al. (2014) chose a different approach to pick parameters, also using NND. For each d_{max}, the clusters are removed and the matrix is compared with the matrix part of the full analysis CSR distribution. The random distribution and the matrix distribution are compared and the difference between them is minimized. For the materials analyzed here this method is hard to apply for the first-order NN due to the NND not being bimodal, see Figure 7. Thus, the fits of CSR distributions were arbitrary. An attempt to use the method developed by Jägle et al. was made to instead compare the distribution with a random distribution of the total analysis. This is not strictly correct as the full analysis contains slightly more Ni and Mn than the matrix, but the resulting values should be reasonably close. This gives d_{max} of 0.55 nm (low fluence sample) and 0.50 nm (high fluence sample).

Higher Orders

Higher order NNs can be used in the cluster analysis. This makes the analysis less local for high orders, but the contribution of clusters is more clearly resolved in the NND. In Figure 8a, the $N = 8$ NND is bimodal (contribution from clusters for a lower d_{pair} and from matrix for a higher d_{pair}), whereas the $N = 1$ NND has no bimodal shape since the contribution from clusters and matrix are overlapping. Chen et al. (2014) picked the order based on Gaussian distributions fitted to the NNDs and by comparing the amplitude of the cluster contribution and the matrix contribution. For the materials discussed here, this method gives the eighth order as optimal. When changing the order, the other parameters need to be re-optimized; a d_{max} of 0.75 nm is a reasonable choice following the approach presented above. However, the relative number of nonrandom clusters also depends on the order, see Figure 8b. The major contribution to the lower values of the relative number of nonrandom clusters for the same $N_{min,}$ for a higher order, stems from the higher probability of finding a random cluster. Possibly, this is an effect of increasing d_{max}. Hence, N_{min} needs to be larger for higher orders for this material in order to avoid classifying random matrix composition fluctuations as clusters,

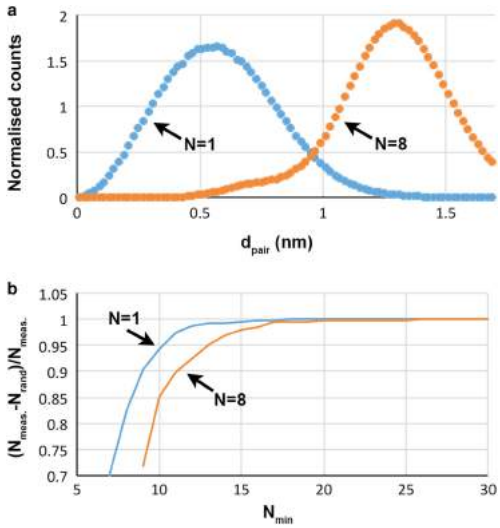

Figure 8. Material irradiated to 2.0×10^{23} n/m^2, laser pulsed analysis. **a:** Nearest neighbor distribution for Ni and Mn for first- and eighth-order nearest neighbors. **b:** Relative number of nonrandom clusters for first- and eighth-order dependent on N_{min}. d_{max} is 0.5 nm for $N = 1$ and 0.75 nm for $N = 8$.

decreasing the possibility of identifying small clusters. For this material the small clusters are of interest and hence the use of higher orders seems to be disadvantageous.

Influence of Density Variations

The atom density within a data set varies, due to crystallographic effects (i.e., trajectories being altered at the edges of the atomic planes) (Stephenson et al., 2007; Gault et al., 2012). The MSM is affected by this effect as it is using distances to define clusters. Close to poles, the density is much lower than elsewhere, see Figure 9a. The expected density with a detection efficiency of 37% is 31 atoms/nm^3 for bcc iron. Histograms of the density distributions for one laser analysis and one voltage analysis can be seen in Figure 9b. In general, the density distributions are wider when using laser pulsing. The distribution will also differ depending on which crystallographic directions are included within the field of view. A part of the contribution to low density in Figure 9b comes from the edges of the analyzed volume. There is a large spread in the density, up to around 60 atoms/nm^3, in some cases up to 75 atoms/nm^3 or more.

In regions of low density, the cluster parameter d_{max} will tend to be too small, and some small clusters might be missed in these regions. In order to avoid this, Stephenson et al. (2007) excluded volumes of low density at poles and high-density volumes around these low-density volumes by the use of 100 NN distances. Clusters in high-density regions might be too large or too many due to d_{max} being too large, that is random fluctuations in these regions being identified as clusters. Thus, also high-density volumes can be removed in order to improve the cluster analysis. In this paper, iso-density surfaces are used for their simplicity, with a voxel size of $2 \times 2 \times 2$ nm^3 (and delocalization of $3 \times 3 \times 1.5$ nm^3) in order to make the surfaces smooth. The effect of removing the regions can be seen in Figure 10. A full analysis is compared with an analysis where all volumes with a density smaller than 25 atoms/nm^3 were removed and one where all volumes of density <25 and >55 atoms/nm^3 were removed. The limits were put so that the volume remaining should still be large, in this case the number of ions used decreased by merely 15%. The NND in Figure 10a shows a small effect from removing the low-density regions. In Figure 10b the influence on the choice of N_{min} is shown for a d_{max} of 0.50 nm. Removing the volumes of high density makes it possible to choose a smaller N_{min} and thereby detect smaller clusters without the risk of identifying random fluctuations in the matrix composition as clusters. With a level of tolerance of 0.995, N_{min} could be decreased from 16 to 13 owing to the removal of high-density regions.

Discussion

The MSM method has been used in order to identify fine-scale clustering in irradiated RPV welds. The results of the method are strongly dependent on the choice of parameters, and the parameters need to be adjusted dependent on the features studied, which is important to consider when comparing different analyses and different studies. Here, some approaches to the choice of parameters are studied. Using the relative number of nonrandom clusters (Fig. 5), with a threshold value close to 1, is a relatively easy and fast way of finding a reasonable value for d_{max}. The elegant methods proposed by Stephenson et al. and Jägle et al. require some more advanced analysis of the data set, fitting CSR distributions to the first-order NNDs that are not bimodal for small and diffuse clusters. The simplified version of the method proposed by Jägle et al. gave similar values for the parameters as the comparison with isoconcentration surfaces and the usage of relative number of nonrandom clusters.

A sensitivity analysis, investigating the impact on the cluster number density to small changes in the parameters, was performed for the two irradiated materials. According to the analysis above, d_{max} was set to 0.50 nm and N_{min} to 18, that is with a low tolerance to random clusters (see Fig. 5). For the sensitivity analysis, d_{max} was varied by $\pm$0.05 nm and N_{min} was varied by $\pm$2. These variations are regarded as moderate and represent reasonable parameters. For the high fluence material, the cluster number density was found to be 7.7×10^{23} clusters/m^3 (with $d_{max} = 0.50$ nm and $N_{min} = 18$). The impact on the number density of changing the parameters within the stated ranges was small. At most, the number density decreased by 7% or increased by 5%. However, the cluster number density of the low fluence

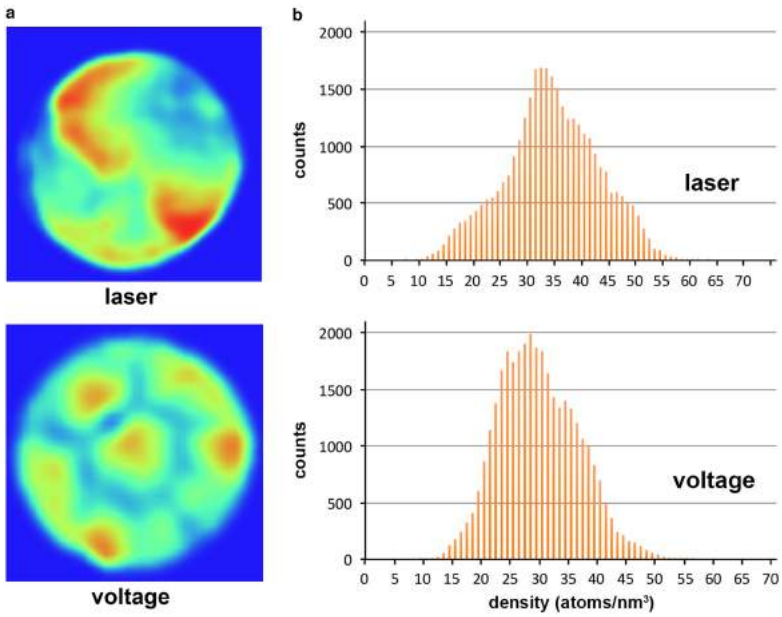

Figure 9. a: The density variations in sections of one sample analyzed in voltage mode and one sample analyzed in laser mode of the material irradiated to 6.4×10^{23} n/m^2. Some effects of crystallography are seen for both laser and voltage pulsed analyses. The maximum density in the heat maps is 55 and 70 atoms/nm^3 for the voltage and laser pulsed analyses, respectively. **b:** Density variations in analysis of material irradiated to 6.4×10^{23} n/m^2.

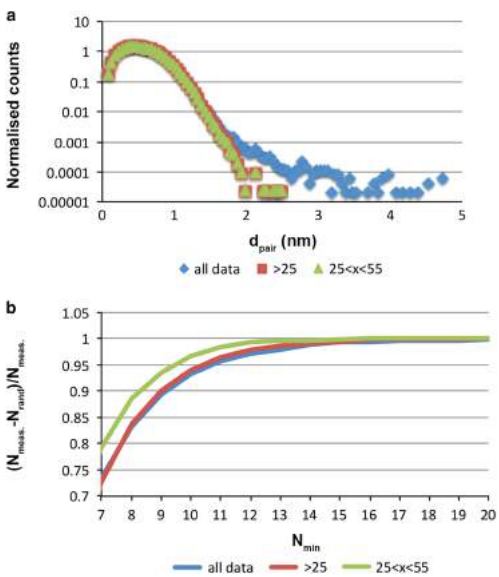

Figure 10. a: Nearest neighbor distributions (Ni and Mn as solutes) for all data and for data where volumes with densities of <25 or >55 atoms/nm^3 are excluded, material irradiated to 6.4×10^{23} n/m^2. **b:** Relative number of nonrandom clusters as a function of N_{min} for the same density ranges, laser pulsed analyses.

material was more sensitive to the selection of MSM parameters. With the same variation in the parameters as above, the initial cluster number density of 3.1×10^{23} clusters/m^3 was varying from a decrease of 35% to an increase of 26%. This again shows us that the clusters in the low fluence material are less well defined (as can be seen in the RDFs in Fig. 11), and also the importance of the selection of parameters.

Density variations affect methods based on distances in the data set. For the MSM, an even density of atoms in the data set is preferred. However, the density usually varies substantially between different parts of the analyzed volume, mainly due to crystallographic effects. This effect is strong for metals with low alloy content, like the RPV welds considered here. In the case of laser pulsed analyses, the density may vary also depending on uneven heating by the laser pulses. Clusters in low-density regions might be left out due to the longer distance between atoms, whereas random concentration fluctuations in high-density regions might be identified as clusters. Hence, removing regions of low and high density will improve the outcome of the analysis.

As seen above, the outcome of the MSM, when applied to real APT data, is sensitive to the choice of the clustering parameters, and it is not possible to exactly determine the cluster number density. There are two main reasons why this is not possible. First, the APT data are not a perfect representation of the material, due to the limited detection efficiency, imprecise positioning of the atoms, density

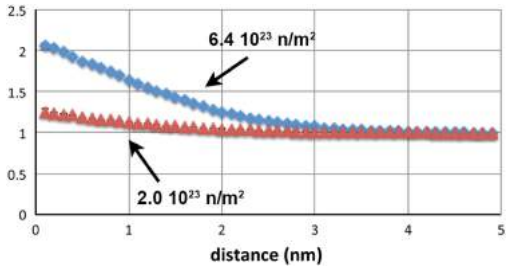

Figure 11. Radial distribution functions (bulk normalized concentrations) of Mn for the material irradiated to 2.0 and 6.4×10^{23} n/m^2.

variations, background and peak overlap in the mass spectrum, detector dead time, etc. Second, there is no generally accepted definition of clusters in physical metallurgy. In principle, there will be a gradual transition from the smallest deviation from randomness to well-developed precipitates, and the question of where to set the limit in terms of size and compositional variation remains to be answered. Anyhow, MSM is a versatile method to characterize clustering, and as long as the choice of parameters is motivated and the parameters used are stated, it is considered to be a very useful method for APT studies. However, more sophisticated methods not relying on user selected parameter values would be preferred.

Conclusions

Ni–Mn–Si clusters in an irradiated RPV steel weld have been studied using APT. The quantification of the clustering is crucial and the analysis needs to be made with some care, considering the following points:

- Voltage pulsing gives more well-defined clusters than laser pulsing, though laser pulsing can be used for improving the cluster statistics, for example, when measuring the size distribution.
- The clusters are more well defined when the peak at 29 Da is not used for cluster identification, due to the $^{58}Fe^{2+}$/$^{58}Ni^{2+}$ overlap.
- The choice of parameters for MSM has a strong influence on the cluster analysis results. There are several methods of choosing parameters in a systematic way. For the material studied here they give similar results. The use of a higher order decreases the possibility of detecting small clusters.
- The cluster analysis can be improved by removing volumes of low and high density.

Acknowledgments

SKC, Swedish Centre for Nuclear Technology, is acknowledged for funding this research. Vattenfall Ringhals AB kindly provided the material. VTT is acknowledged for cutting the material.

References

Cerezo, A. & Davin, L. (2007). Aspects of the observation of clusters in the 3-dimensional atom probe. *Surf Interface Anal* **39**(2–3), 184–188.

Chen, Y., Chou, P.H. & Marquis, E.A. (2014). Quantitative atom probe tomography characterization of microstructures in a proton irradiated 304 stainless steel. *J Nucl Mater* **451**(1–3), 130–136.

Efsing, P., Jansson, C., Mager, T. & Embring, G. (2007). Analysis of the ductile-to-brittle transition temperature shift in a commercial power plant with high nickel containing weld material. *J ASTM Int* **4**(7), 44–55.

Efsing, P., Roudén, J. & Nilsson, P. (2014). Flux effects on radiation induced aging behaviour of low alloy steel weld material with high nickel and manganese content. *Effect Radiat Nucl Mater* **26**, 119–134.

Gault, B., Moody, M.P., Cairney, J.M. & Ringer, S.P. (2012). *Atom Probe Microscopy*. New York: Springer.

Gault, B., Müller, M., La Fontaine, A., Moody, M.P., Shariq, A., Cerezo, A., Ringer, S.P. & Smith, G.D.W. (2010). Influence of surface migration on the spatial resolution of pulsed laser atom probe tomography. *J Appl Phys* **108**(4), 044904.

Heinrich, A., Al-Kassab, T.a. & Kirchheim, R. (2003). Investigation of the early stages of decomposition of Cu–0.7at.% Fe with the tomographic atom probe. *Mater Sci Eng A* **353**(1–2), 92–98.

Hyde, J.M., Burke, M.G., Gault, B., Saxey, D.W., Styman, P., Wilford, K.B. & Williams, T.J. (2011*a*). Atom probe tomography of reactor pressure vessel steels: an analysis of data integrity. *Ultramicroscopy* **111**(6), 676–682.

Hyde, J.M. & English, C.A. (2000). An analysis of the structure of irradiation induced Cu-enriched clusters in low and high nickel welds. *Mat Res Soc Symp Proc* **650**, R6.6.1–R.6.6.12.

Hyde, J.M., Marquis, E.A., Wilford, K.B. & Williams, T.J. (2011*b*). A sensitivity analysis of the maximum separation method for the characterisation of solute clusters. *Ultramicroscopy* **111**(6), 440–447.

Jägle, E.A., Choi, P.P. & Raabe, D. (2014). The maximum separation cluster analysis algorithm for atom-probe tomography: Parameter determination and accuracy. *Microsc Microanal* **20**(6), 1662–1671.

Kolli, R.P. & Seidman, D.N. (2007). Comparison of compositional and morphological atom-probe tomography analyses for a multicomponent Fe-Cu steel. *Microsc Microanal* **13**(4), 272–284.

Larson, D.J., Foord, D.T., Petford-Long, A.K., Liew, H., Blamire, M.G., Cerezo, A. & Smith, G.D.W. (1999). Field-ion specimen preparation using focused ion-beam milling. *Ultramicroscopy* **79**(1–4), 287–293.

Marquis, E.A. & Hyde, J.M. (2010). Applications of atom-probe tomography to the characterisation of solute behaviours. *Mater Sci Eng R* **69**(4–5), 37–62.

Meslin, E., Lambrecht, M., Hernández-Mayoral, M., Bergner, F., Malerba, L., Pareige, P., Radiguet, B., Barbu, A., Gómez-Briceño, D., Ulbricht, A. & Almazouzi, A. (2010*a*). Characterization of neutron-irradiated ferritic model alloys and a RPV steel from combined APT, SANS, TEM and PAS analyses. *J Nucl Mater* **406**(1), 73–83.

Meslin, E., Radiguet, B., Pareige, P. & Barbu, A. (2010*b*). Kinetic of solute clustering in neutron irradiated ferritic model alloys and a French pressure vessel steel investigated by atom probe tomography. *J Nucl Mater* **399**(2–3), 137–145.

Miller, M.K., Chernobaeva, A.A., Shtrombakh, Y.I., Russell, K.F., Nanstad, R.K., Erak, D.Y. & Zabusov, O.O. (2009). Evolution of the nanostructure of VVER-1000 RPV materials under neutron irradiation and post irradiation annealing. *J Nucl Mater* **385**(3), 615–622.

Miller, M.K., Powers, K.A., Nanstad, R.K. & Efsing, P. (2013). Atom probe tomography characterizations of high nickel, low copper surveillance RPV welds irradiated to high fluences. *J Nucl Mater* **437**(1–3), 107–115.

Odette, G.R. & Lucas, G.E. (1998). Recent progress in understanding reactor pressure vessel steel embrittlement. *Radiat Effect Defect Solids* **144**(1–4), 189–231.

Stephenson, L.T., Moody, M.P., Liddicoat, P.V. & Ringer, S.P. (2007). New techniques for the analysis of fine-scaled clustering phenomena within atom probe tomography (APT) data. *Microsc Microanal* **13**(6), 448–463.

Styman, P.D., Hyde, J.M., Wilford, K. & Smith, G.D. (2013). Quantitative methods for the APT analysis of thermally aged RPV steels. *Ultramicroscopy* **132**, 258–264.

Vaumousse, D., Cerezo, A. & Warren, P.J. (2003). A procedure for quantification of precipitate microstructures from three-dimensional atom probe data. *Ultramicroscopy* **95**, 215–221.

Williams, C.A., Haley, D., Marquis, E.A., Smith, G.D. & Moody, M.P. (2013). Defining clusters in APT reconstructions of ODS steels. *Ultramicroscopy* **132**, 271–278.

Paper II

Evolution of precipitation in reactor pressure vessel steel welds under neutron irradiation

K. Lindgren, M. Boåsen, K. Stiller, P. Efsing, and M. Thuvander

Journal of Nuclear Materials 488, 222-230 (2017)

Journal of Nuclear Materials 488 (2017) 222–230

Contents lists available at ScienceDirect

Journal of Nuclear Materials

journal homepage: www.elsevier.com/locate/jnucmat

Evolution of precipitation in reactor pressure vessel steel welds under neutron irradiation

Kristina Lindgren [a, *], Magnus Boåsen [b], Krystyna Stiller [a], Pål Efsing [b, c], Mattias Thuvander [a]

[a] Department of Physics, Chalmers University of Technology, SE-412 96 Göteborg, Sweden
[b] Department of Solid Mechanics, Royal Institute of Technology (KTH), SE-100 44 Stockholm, Sweden
[c] Vattenfall Ringhals AB, SE-430 22 Väröbacka, Sweden

HIGHLIGHTS

- Clustering in a low Cu, high Ni reactor pressure vessel steel weld is studied.
- The clusters nucleate and grow during irradiation, and consist of Ni, Mn, Si, and Cu.
- High flux neutron irradiated material is compared to surveillance material.
- High flux was found to result in smaller clusters with a larger number density.
- Hardness follows the same dependence on fluence, independent of flux.

ARTICLE INFO

Article history:
Received 21 December 2016
Received in revised form
14 February 2017
Accepted 12 March 2017
Available online 14 March 2017

ABSTRACT

Reactor pressure vessel steel welds are affected by irradiation during operation. The irradiation results in nanometre cluster formation, which in turn affects the mechanical properties of the material, e.g. the ductile-to-brittle transition temperature is shifted to higher levels. In this study, cluster formation is characterised in high Ni (1.58%) low Cu (0.04%) steel welds identical to Ringhals R4 welds, using atom probe tomography in both surveillance material and in material irradiated at accelerated dose rates. Clusters containing mainly Ni and Mn, but also some Si and Cu were observed in all of the irradiated materials. Their evolution did not change drastically during irradiation; the clusters grew and new clusters were nucleated. Hence, both the cluster number density and the average size increased with irradiation time. Some flux effects were observed when comparing the high flux material and the surveillance material. The surveillance material has a lower cluster number density, but larger clusters. The resulting impact on the mechanical properties of these two effects cancel out, resulting in a measured hardness that seems to be on the same trend as the high flux material. The dispersed barrier hardening model with an obstacle strength factor of 0.15 was found to reproduce the increase in hardness. In the investigated high flux materials, the clusters' Cu content was higher.

1. Introduction

The reactor pressure vessel (RPV) is potentially a life-limiting component of nuclear power plants, due to the complexity of a replacement. During operation, the RPV is subjected to both heat (around 290 °C in pressurized water reactors (PWRs)) and radiation. During operation, neutron radiation in combination with thermal processes changes the mechanical properties of the RPV steel, e.g. the ductile-to-brittle transition temperature (DBTT) increases [1]. Ageing of RPV steels has received substantial attention in terms of microstructural characterisation (in particular using small angle neutron scattering, positron annihilations spectroscopy, transmission electron microscopy (TEM) and atom probe tomography (APT)), modelling and structural integrity investigations [2]. The embrittlement is due to changes in the microstructure of the material, which occur in various ways. Firstly, direct matrix damage, vacancies and interstitials, increases the hardness, as well as the diffusion in the matrix. Another irradiation-induced

* Corresponding author.
E-mail address: kristina.lindgren@chalmers.se (K. Lindgren).

http://dx.doi.org/10.1016/j.jnucmat.2017.03.019
0022-3115/

phenomenon is the segregation of mainly P to grain boundaries. This paper concerns a third type of radiation damage, namely nanometre size clusters, that are formed during long term irradiation and are of large importance for the mechanical properties [3,4]. The clusters can be subdivided into two categories, Cu-rich clusters and NiMnSi-rich clusters [1,5]. The type of cluster formed depends on the chemical composition of the steel and the irradiation conditions [6–8].

Odette and Lucas have proposed an accelerating NiMnSi-rich cluster formation and growth in low-Cu, high-Ni steels at high fluences, and called the precipitates late blooming phases [2]. Furthermore, they suggest that these clusters affect the DBTT, and the result is sudden deterioration of the mechanical properties. Hence, it is vital to understand how clusters nucleate and grow, as well as the connection between nanometre features and mechanical properties. Models based on characteristics such as cluster size and number density contribute to predictions of mechanical properties, thus reducing the need for numerous expensive irradiation experiments.

In this type of evaluation, all surveillance materials are irradiated at higher flux than the actual RPV, due to their positioning in the reactor. Therefore, it is important to understand flux effects on the evolution of the microstructure and the coupling to changes in mechanical properties when interpreting surveillance material results in order to make conservative estimates of the embrittlement of the RPV.

The welds in the RPV of Ringhals R4 have an unusually high Ni and Mn content (1.58 at% and 1.37 at%, respectively), and a comparatively low Cu content (0.04 at%). The high Ni and Mn content is believed to be the reason for the DBTT shift of Ringhals R4 material being as high as 162 °C for surveillance material irradiated to 6.0×10^{23} n/m^2 [9]. Surveillance material from Ringhals R3 and R4 have been studied earlier by Miller et al. and Styman et al. [9,10], but no microstructural studies have been done on high flux material. In this paper, welds identical to Ringhals R4 welds have been investigated using APT in order to further understand cluster formation. The material has been irradiated at high flux to two different fluences, the highest 6.4×10^{23} n/m^2. The material is compared to a surveillance material irradiated at lower flux in R4 in order to confirm the validity of high flux experiments for prediction of the evolution of the mechanical properties.

2. Materials and methods

The materials studied have the same composition and fabrication process as the weld material in Ringhals R4 RPV. The welds were produced using submerged arc welding, and the composition can be seen in Table 1. Four different conditions were studied, see Table 2. One unirradiated specimen was studied as well as one irradiated to 2.0 and one to 6.4×10^{23} n/m^2 (E > 1.0 MeV) in the OECD Halden materials test reactor (Norway). The irradiation temperature was 290–295 °C, and the neutron energy spectrum of the Halden reactor is similar to that of a PWR [11]. These materials were compared to one lower flux surveillance specimen irradiated to 4.6×10^{23} n/m^2 in Ringhals R4 at a temperature of 284 °C. Note that the neutron flux for the surveillance specimen is around four times higher than for the actual RPV and that the flux in Halden was about 20 times higher than for the surveillance material.

Table 1
Chemical composition of the RPV weld in atomic % [42].

Cu	Ni	Mn	Mo	Si	C	P	S	Cr	Al	Co	Fe
0.04	1.58	1.37	0.29	0.28	0.31	0.027	0.007	0.04	0.05	0.01	bal.

Table 2
Fluence and flux for the studied materials. For the fluence and flux neutrons with higher energies than 1 MeV are considered. In the names "H" refers to Halden and "S" to surveillance.

Name	Fluence (10^{23} n/m^2)	Flux (10^{16} n/(m^{2}s))
Reference	0	–
H2.0	2.0	2.3
H6.4	6.4	3.8
S4.6	4.6	0.15

Mechanical testing was performed utilizing Vickers hardness testing, with a Struers Duramin-A300 hardness tester at room temperature. The testing was conducted on specimens with a thickness of 2.0 mm with an indentation load of 5.00 kg, based on availability and experience. The indentation centre-centre placement was increased to 5–6 times the indentation diagonal as a conservative safety of indent to indent influence, rather than the 2.5 times the indentation diagonal as specified in the ASTM E384-11 [12], which otherwise was followed during the hardness testing. Results from the hardness measurements, as a function of fluence, can be seen in Fig. 1 [13]. The initial increase is large, but for higher fluence the slope of the trend is lower than the initial change in hardness. The surveillance material seems to follow the same hardness trend as the material irradiated in Halden.

As the material is slightly active it was chosen to prepare APT specimens using focused ion beam/scanning electron microscopy (FIB/SEM) instead of electropolishing. A standard lift-out technique finished with annular milling was used [14,15] in an FEI Versa 3D FIB/SEM instrument. The unirradiated reference material was prepared using a two-step electropolishing process [16]. Remaining surface oxides were removed by millisecond voltage pulsing in electrolyte (2% perchloric acid in butoxyethanol).

APT analysis was performed in a 3000X HR LEAP from Imago Scientific Instruments equipped with an energy compensating reflectron. Laser pulsed analyses were used as a complement to voltage pulsed analyses in order to obtain larger analysed volumes. However, surface diffusion results in an incorrect Si distribution when using laser pulsing [17]. Thus, voltage pulsed analysis was used for obtaining cluster compositions, whereas both voltage and laser pulsed analysis were used for cluster number density and size measurements. Voltage pulsed APT was performed at 50 K with a

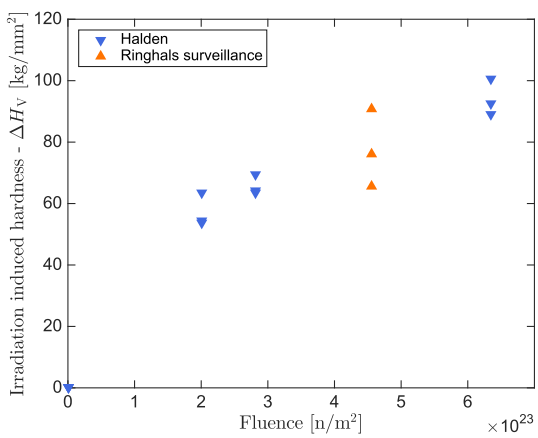

Fig. 1. Hardness as a function of fluence for the Halden irradiated and surveillance material [13].

pulse fraction of 20%, whereas laser pulsing was performed at 30 K with a laser pulse energy of 0.30 nJ [17]. The pulse frequency was 200 kHz for all analyses.

The IVAS™ 3.6.10 software was used for the reconstruction of the atom probe data. The reconstruction parameters were chosen so that the plane distances found at low index poles in the reconstruction correspond to the known distance (α-Fe has a lattice parameter of 0.28 nm). This made most of the clusters appear spherical. For laser pulsed analyses the reconstruction evaporation field was set to 23 V/nm with a k-factor of 4.0. Most voltage pulsed runs were reconstructed with an evaporation field set to 33 V/nm and a k-factor of 5.3. The image compression factor was 1.65 for all reconstructions.

Clusters were identified using the maximum separation method (MSM) with erosion [18–20], and Ni and Mn were used for identification of the clusters. However, the peak at mass-to-charge ratio of 29 Da was not used for cluster identification due to the $^{58}Fe^{2+}/^{58}Ni^{2+}$ peak overlap (however, for determination of cluster composition this peak was decomposed for each layer of the clusters, as the layers close to the centre contain more Ni and less Fe than layers close to the surface, and hence affect the peak decomposition). The MSM parameters were chosen in order to avoid random matrix fluctuations being identified as clusters but to still identify small clusters. The d_{max} was set to 0.50 nm, N_{min} to 18, and L and e both to 0.50 nm. This gave a cluster Fe content of around 50%, with decreasing gradients towards the centre of the clusters. As the clusters have an unphysically high density in the analysed data, Fe was not considered to be part of the clusters but being present there mostly due to trajectory aberrations occurring due to the clusters in the material having lower evaporation fields than the matrix. This would result in matrix Fe ions being focused into the clusters [4].

Dislocation lines and grain boundaries were removed before cluster analysis was performed since clusters on dislocations might have other nucleation processes, and hence other compositions, number densities and size distributions than clusters in the matrix, that are of interest here. The parts of the analysis containing dislocation lines and boundaries were removed by cutting the volumes and hence also removing some of the adjacent volume. These were not included in the total volumes used for calculating the cluster number density.

The cluster diameters were calculated assuming matrix coherent spherical clusters, containing no Fe, and a 37% detection efficiency of the LEAP. There is a cut-off at about 1.0 nm diameter due to the N_{min} value of 18 clustering atoms (Mn and Ni, without $^{58}Ni^{2+}$).

3. Results

No clusters enriched in Ni, Mn, Si and Cu were found in the unirradiated reference material. A few dislocation lines enriched in Mn and Mo were present in the analyses, as well as a few small clusters enriched in V (presumably VN). In one analysis, a few nanometre-scale MnS precipitates were found. The observed deviations from a random distribution are believed to have insignificant influence on the mechanical properties of the as-welded material.

Table 3 gives the composition of the voltage pulsed and laser pulsed analyses. As the materials are weldments, there are some variations in the composition between the analyses. Laser and voltage pulsed analysis gave similar compositions, and there was no significant difference in composition between the material conditions. A high Ni content is accompanied by a high Mn content in most cases, and the Si content is close to the expected one. Some of the C is forming carbides that are not included in these analyses, explaining the low C content (compared to the nominal composition of 0.31 at%).

Fig. 2 shows an APT reconstruction of the high flux, high fluence material H6.4. The clusters are visualized using isoconcentration surfaces. In some cases, the Cu atoms are mainly located in one part of the clusters, as shown in the lower inset in Fig. 2. In the figure, a dislocation line is marked. Clusters were found on the dislocation lines, in addition to enrichment of phosphorous. Clusters on dislocations, such as these, were not further analysed and do not

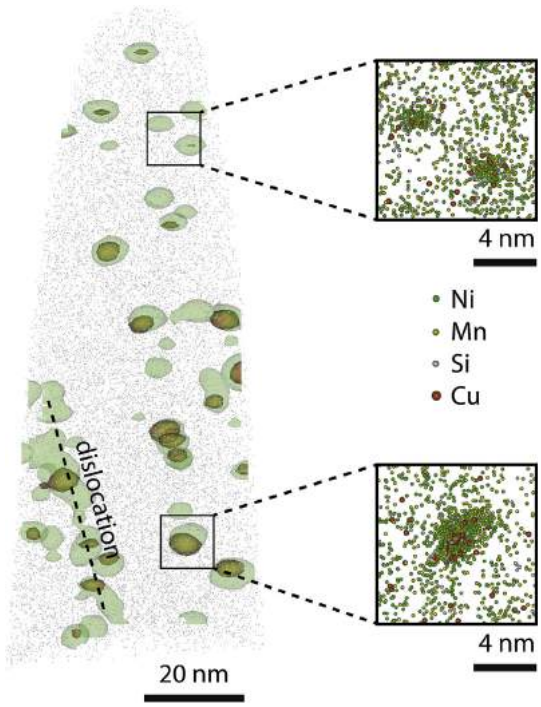

Fig. 2. Reconstruction of volumes in irradiated material, the H6.4 voltage run. A dislocation line is marked. The small boxes are 10 × 10 × 10 nm. The green isoconcentration surfaces correspond to 5% Ni + Mn + Si, orange surfaces to 1.2% Cu. Grey shows the extent of the analysis to the left and correspond to 1% of the Fe ions detected (i e around 0.37% of the total Fe atoms). (For interpretation of the references to colour in this figure legend, the reader is referred to the web version of this article.)

Table 3
Chemical composition of the RPV welds from the APT analysis, for both voltage pulsed and laser pulsed analysis, in atomic %. The uncertainty is the standard deviation between the different analyses (at least one for each materials condition and pulsing mode).

	Cu	Ni	Mn	Mo	Si	C	P	Cr	Co	Fe
voltage	0.05 ± 0.02	1.49 ± 0.21	1.10 ± 0.13	0.23 ± 0.05	0.28 ± 0.03	0.02 ± 0.01	0.02 ± 0.01	0.15 ± 0.03	0.01 ± 0.01	bal.
laser	0.06 ± 0.02	1.46 ± 0.20	1.18 ± 0.17	0.19 ± 0.05	0.26 ± 0.06	0.01 ± 0.01	0.01 ± 0.01	0.06 ± 0.02	0.02 ± 0.01	bal.

contribute to the cluster statistics that follow. Clusters that are not associated with dislocation lines are in general not enriched in phosphorous.

In Fig. 3, a comparison of 10 nm thick cross sections of the volumes can be seen for the three irradiated materials. The Cu content is much lower than the Ni, Mn and Si contents. The

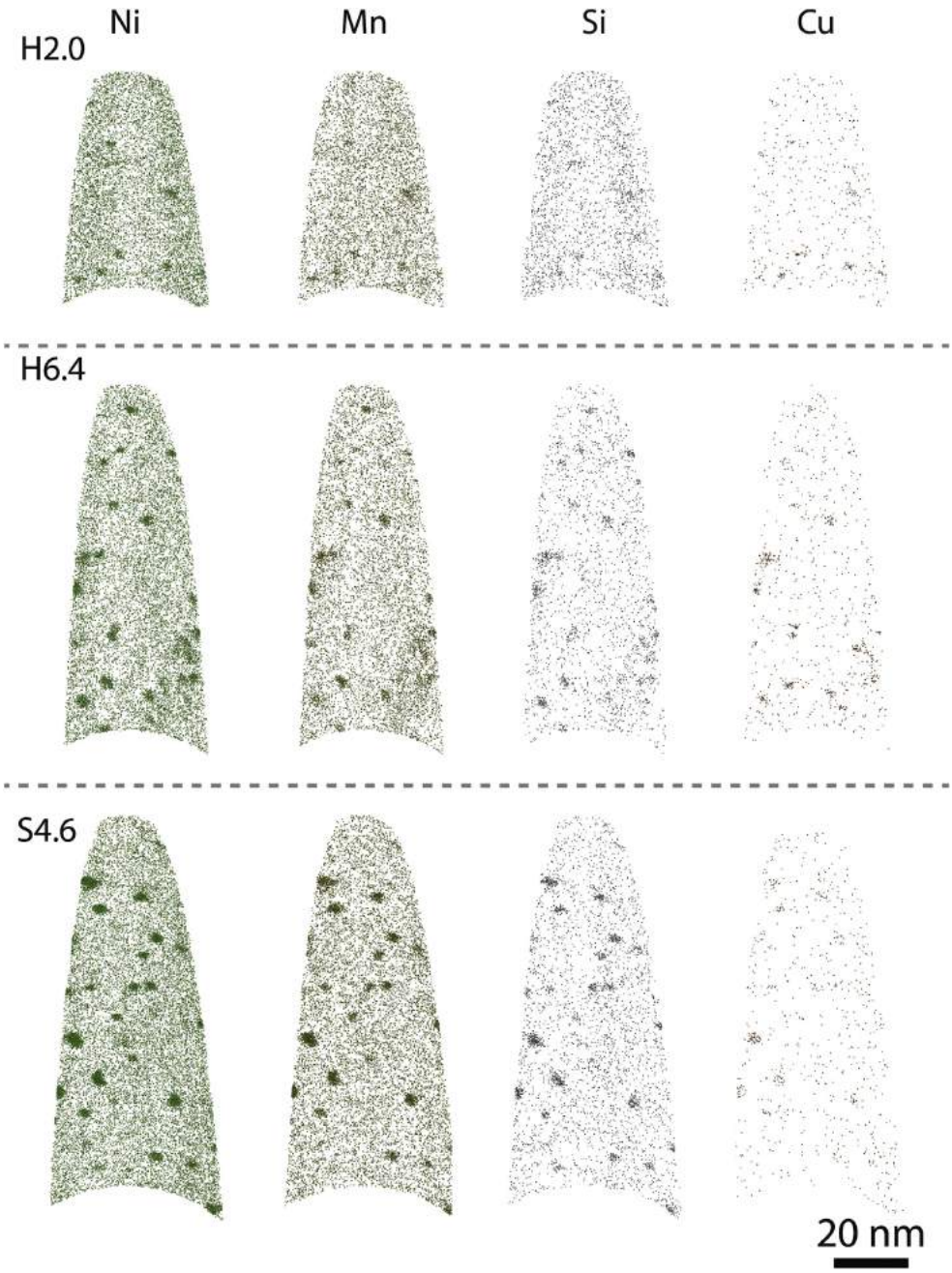

Fig. 3. Reconstructions of irradiated materials showing Ni, Mn, Si and Cu distributions. The slices are 10 nm thick.

corresponding atom maps for the unirradiated reference are not included, since the elemental distributions of the relevant species are random before irradiation.

The cluster number density as a function of fluence is presented in Fig. 4. For each fluence all individual measurements are plotted. There is a spread in the results, due to the small volumes analysed in APT and the non-homogeneous microstructure of the welds. The high flux specimens irradiated in Halden show an increased cluster number density for high fluences. The surveillance material cluster number density is lower than what would have been expected from the fluence of 4.6×10^{23} n/m^2 if the flux had been the same as for the Halden samples.

In Fig. 5, the cluster size distributions for the three irradiated materials can be seen. In material H2.0, irradiated to 2.0×10^{23} n/m^2, there are many small clusters and a decreasing number of larger clusters up to diameters of 3.0 nm. In material H6.4, there are clusters up to diameters of 3.5 nm. The distribution has an elongated shape, with many clusters around 2.5 nm in diameter. The surveillance material S4.6 contains larger clusters than the high flux (Halden) materials, with cluster diameters up to 5.0 nm. The number of clusters at the cut-off size of 1.0 nm is relatively low and comparatively many of the clusters have diameters between 2.0 and 4.0 nm.

In Fig. 6, the cluster compositions are given in terms of cluster concentration profiles in order not to bias the composition for the solute elements (Ni and Mn) used in the MSM algorithm for defining the clusters. Unity at the normalised distance given at the x-axis corresponds to the border of the cluster. Zero corresponds to the cluster centre. The parts of the clusters that are not Ni, Mn, Si and Cu consist mainly of Fe. However, as mentioned above, the Fe content is overestimated due to the trajectory effects. Consequently, smaller clusters appear to contain a larger fraction of Fe, even though this may not be the case in reality. Hence, the composition inside the clusters can be further analysed by normalising the content with respect to the clustering elements Ni, Mn, Si, and Cu, see Fig. 7. In a) the cluster compositions are shown with respect to neutron fluence. In b) the same data is shown with respect to mean cluster size, that is dependent on both fluence and flux (Fig. 5). Si is found to increase with fluence, whereas the Ni content is found to increase, and Mn and Cu decrease, with mean cluster size. The clusters in the surveillance material are found to be more enriched in Ni than in Mn relative to the matrix composition, whereas the Halden irradiated materials have similar enrichment factors of Ni and Mn.

Fig. 8 reveals that the relative distribution of Cu atoms per cluster is similar for the different fluxes, although there is a trend of less clusters without Cu atoms when the clusters are larger. The data suggest the presence of clusters without Cu atoms, but it should be noted that the detection efficiency is only 37%, and so only 1/3 of the Cu atoms are detected. The larger size (more Ni, Mn and Si atoms) of the clusters in the surveillance material gives the lower Cu percentage.

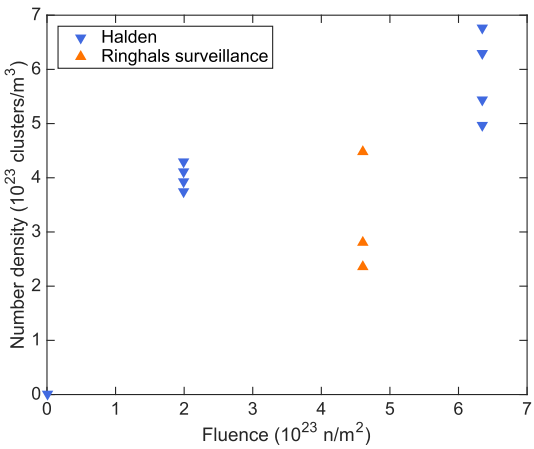

Fig. 4. Number densities of clusters in the different materials for each analysis.

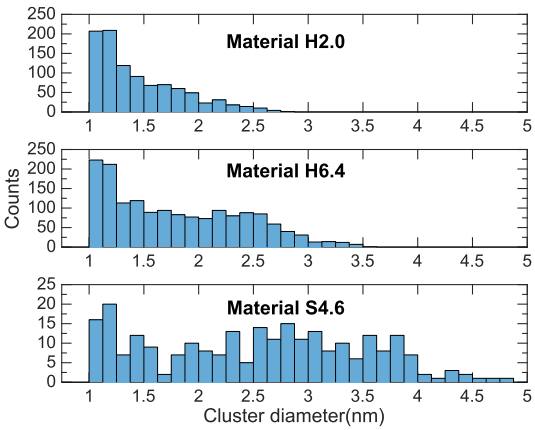

Fig. 5. Size distributions for laser runs APT analysis. Fe atoms inside clusters are not considered to contribute to the total size.

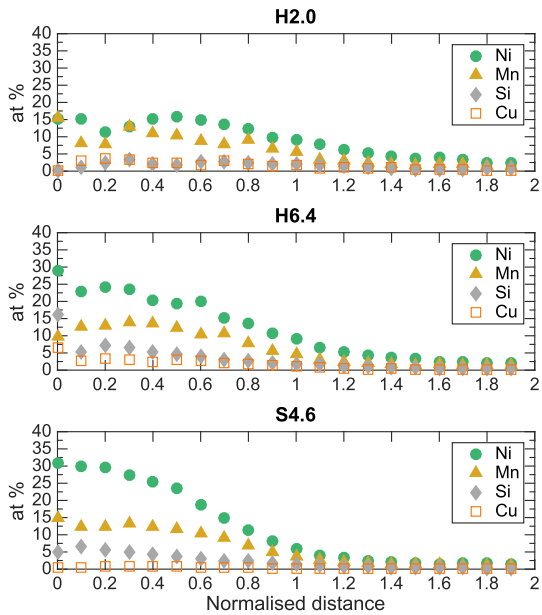

Fig. 6. Cluster concentration profiles. The normalised distance: 1 is the border of the precipitate, 0 corresponds to the centre, according to the cluster definition by MSM.

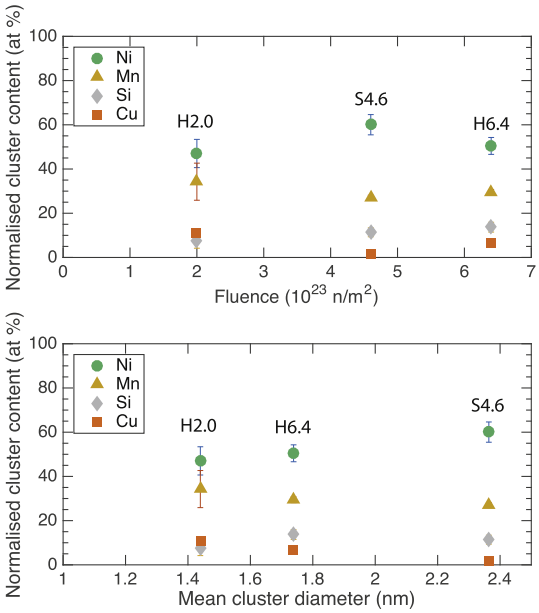

Fig. 7. The mean cluster composition as function of fluence and size. Fe is omitted, the content is normalised with respect to Ni, Mn, Si and Cu.

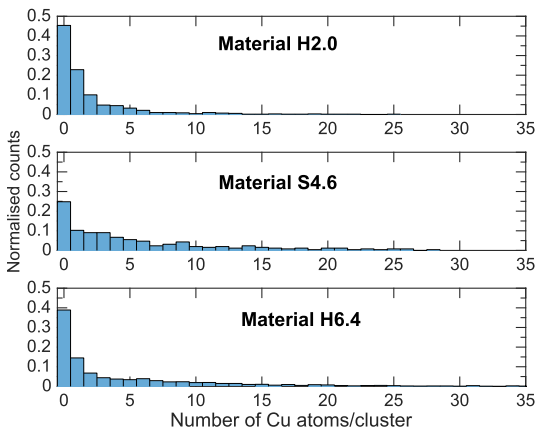

Fig. 8. The number of Cu atoms per cluster in the irradiated materials.

The depletion of Cu from the matrix to the clusters was found to be dependent on the fluence, see Fig. 9 where the difference between total Cu content and matrix Cu content is shown. The amount of Cu in the clusters is gradually increasing. The rate of transport seems to be constant with respect to fluence; there is no sign of a decrease in the supply of Cu to the clusters due to depletion.

4. Discussion

In this study, the clusters formed during accelerated irradiation

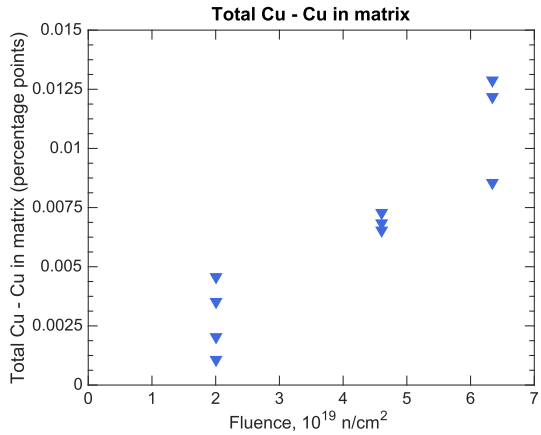

Fig. 9. The total Cu percentage minus the Cu percentage in the matrix (corresponding to the Cu transport to clusters).

of RPV steel welds were characterised using APT. Material irradiated at high flux in the Halden reactor was compared to surveillance material. The surveillance weld results are in good agreement with earlier studies on the same material, for instance Miller et al. and Styman et al. found cluster number densities of around 4×10^{23}/m^3 for surveillance material for Ringhals R3 and R4 irradiated to 3.3–6.8 $\times$ 10^{23} n/m^2 [9,10]. However, the composition of the clusters is more similar to the Ringhals R3 surveillance cluster compositions presented by Styman et al. than any of the surveillance cluster compositions presented by Miller et al. who reported that the clusters contain more Mn than Ni. The clusters formed in the high flux materials were found to be smaller, have a higher number density, in agreement with other studies [21–24]. The clusters in high flux materials do also have a higher concentration of Cu compared to the surveillance material clusters.

4.1. Cluster Cu content/nucleation

NiMnSi-rich cluster nucleation is known to be accelerated by Cu; appendices of Ni, Mn and Si are formed on the Cu nuclei [9,25,26]. This can also be observed in the results presented in this paper, the main Cu contents of the clusters are located in one part of the cluster, i.e. the Cu is not completely mixed with the Ni, Mn and Si; see Fig. 2. The driving force for Cu-precipitation is the low Cu solubility in α-Fe, 30–42 appm at PWR relevant temperatures [2,7]. The Cu matrix levels after irradiation are well above this (in fact, the matrix Cu level is still higher than 75% of the initial total level in the H6.4 material). In this study, the depletion of Cu from the matrix seems to follow a close-to-linear behaviour with fluence, if it is assumed to be independent of flux (Fig. 9); there is no sign of a decreased depletion rate. The number of Cu atoms per cluster is increasing (Fig. 8) even though the Cu concentration of the clusters is decreasing, due to Ni, Mn and Si segregating at a higher rate. There seem to be clusters nucleating without Cu (although it should be noted that the detection efficiency is only 37%), in accordance with results from other studies using APT [27] and Monte Carlo simulations [28,29].

A flux effect is clearly manifested in the size of the clusters (Fig. 5). The increased size is mainly coming from a higher number of Ni, Mn and Si atoms in the cluster (but also the number of Cu atoms per cluster has slightly increased).

4.2. Cluster composition and structure

The cluster size distribution in Fig. 5 for material H6.4 is stretched towards larger clusters, it might even have a small, second peak around 2.5 nm. The distribution of the surveillance material does also have many larger clusters (>2 nm in diameter) and a bimodal tendency. One possible explanation for the different shapes of the size distributions is that it might be energetically favourable to have a phase transformation from matrix coherent clusters to another crystal structure at a critical cluster size. After transformation, the cluster growth speed might be higher and hence the cluster size distribution would be bimodal. There are suggestions based on thermodynamical calculations [25,30] and diffraction results [31] of G-phase ($Ni_{16}Mn_6Si_7$) or Γ_2-phase (Ni_3Mn_2Si) clusters forming in RPV steels. Matsukawa et al. [32] discuss the formation of G-phase in ferrite in a thermally aged duplex stainless steel, finding a critical diameter of 2.6 nm for transformation from matrix coherent clusters to an intermediate precursor phase similar to G-phase (larger clusters on dislocations were found to be normal G-phase) using APT and TEM. In their study, the cluster size distribution was found to be bimodal after the phase transformation.

The cluster compositions of the irradiated materials studied in this paper can be compared to Γ_2-phase and G-phase compositions. The cluster Mn content in relation to the Ni content is decreasing with cluster size and time (Fig. 7). In the surveillance material Ni is more enriched in the clusters than Mn. The Mn-to-Ni ratio decreases from 0.72 to 0.77 in the entire analyses (somewhat lower than the expected 0.87 due to the lower than expected Mn content), to 0.72 in the clusters in material H2.0, 0.58 in material H6.4 clusters and finally down to 0.45 in the clusters of surveillance material S4.6, see Table 4. Corresponding ratios in the Γ_2-phase and G-phase are 0.67 and 0.38, respectively. Correlating this to the size distributions (Fig. 5) might suggest that the larger clusters in the surveillance material, where many clusters should be above a critical size of phase transformation, are closer to the G-phase relation of Mn/Ni. However, the Si content of the clusters is also crucial for any possible phase transformation, and possibly even more so since Ni and Mn positions in a crystal might be interchanged or replaced by Fe, whereas Si positions are less likely to, due to the different nature of the element. The total Si-to-Ni ratios for the materials are 0.17–0.23 (Table 4). In the analysed materials, the cluster Si-to-Ni ratios were found to be 0.17, 0.27 and 0.19 for material H2.0, H6.4 and S4.6, respectively. The values can be compared to 0.33 for Γ_2-phase and 0.44 for G-phase. The Si-to-Ni ratio is increasing with a dependence on fluence rather than on mean cluster size, and thus the change in Si concentration is not consistent with a phase transformation at a critical size, as the Mn/Ni ratios might be.

A limiting factor of the atom probe is the resolution (especially for the directions perpendicular to the analysis direction), which is not good enough to give crystallographic structures, even though planes can be observed in some regions. Hence, no certain conclusions can be made on the crystal structure of the clusters for the materials analysed here. The small size of the clusters makes crystallographic information hard to obtain also using other experimental techniques such as TEM. At the end of the day, the possibility of a phase transformation can be considered as one possible explanation for the shape of the size distributions. However, the compositional information on the Si content is not pointing towards a phase transformation, that would require a critical amount of Si.

4.3. Late blooming precipitates

The existence of late blooming precipitates can be debated. They are described by Odette and Lucas as accelerating the embrittlement [1]. In the results presented in this paper, the effect is not visible in the hardness data, nor in the cluster number density or size. The irradiation has a large impact on the mechanical properties, and on cluster number density and size in the beginning of life, to level out at higher fluences. The clusters are rich in Ni, Mn and Si. One unconfirmed possibility is phase transformation at a critical cluster size. However, the clusters are not forming late during irradiation, they evolve continuously. The characterisation of the precipitates in the Ringhals R4 material does not show any accelerating tendencies, not in the composition and growth, nor in the mechanical properties – pointing toward *non-existing* late blooming phases within the studied material and fluences.

4.4. Flux effects and hardness

The flux affects the material in terms of recombination. At high flux, there is less time for vacancies and interstitials to recombine and hence the diffusion is faster [33,34], but the time for diffusion is shorter. The matrix defects might be affected, i.e. there might form a larger number of unstable matrix defects at high flux. However, Boåsen et al. [13] studied material specimens from the same weldments as the samples used in this study, this in order to identify any presence of unstable matrix defects. The experimental method in Ref. [13] is based on the hardness recovery that would occur due to the annihilation of unstable matrix defects, which according to Odette et al. [1,35] would act as dislocation obstacles, and annihilate at reactor operation temperatures (~270–330 °C) i.e. rendering their presence detectable by hardness or tensile testing combined with heat treatments as utilised in Refs. [34,35]. From this, the study by Boåsen et al. was conducted with Vickers hardness testing and post-irradiation annealing at 330, 360 and 390 °C. The study in Ref. [13] did not find any evidence for unstable matrix defects in the Halden or Ringhals-irradiated material studied in this paper, and will therefore not be considered as a potential flux effect in this study. Furthermore, studies on similar materials found no evidence of unstable matrix defects [36,37].

The ΔH_v is seemingly unaffected by flux (Fig. 1), while both cluster size distribution (Fig. 5) and cluster number density (Fig. 4) are clearly affected. Thus, the effect of these contributions to the hardness might end up compensating each other. One commonly used model to describe irradiation hardening is by the dispersed-barrier hardening model (DBH). The shift in yield strength due to the introduction of evenly dispersed dislocation obstacles into the material matrix is expressed as

Table 4
Mn-to-Ni, and Si-to-Ni ratios in both clusters (Fig. 7) and the entire analysis (Table 3). Only analyses used for cluster composition determination.

	Nominal composition	Reference	H2.0	H6.4	S4.6
Mn/Ni clusters	–	–	0.72	0.58	0.45
Si/Ni clusters	–	–	0.17	0.27	0.19
Mn/Ni clusters + matrix	0.87	0.72	0.77	0.72	0.73
Si/Ni clusters + matrix	0.18	0.15	0.23	0.17	0.17

$$\Delta\sigma = \alpha MGb\sqrt{Nd}$$

where M is the Taylor factor for polycrystalline metals (3.06 in an iron BCC-lattice [38]), G is the shear modulus, b is the Burgers vector, N is the cluster number density, d is the mean cluster diameter, and α is the obstacle strength factor, describing the pinning strength of the clusters [1,23,39]. The shift in hardness due to a shift in the yield strength can be estimated by making use of the work on hardness by Tabor [40], where the hardness is related to the flow stress at eight percent plastic strain. This is done by the relation $H_{V_p} = 2.8\sigma_f(\varepsilon_p = 8\%)$ where H_{Vp} is the Vickers hardness expressed by the projected indentation area and in MPa. This relation can be rewritten to the shift in Vickers hardness (indent surface area and kg/mm^2) as a function of shift in yield strength as $\Delta H_V = 2.6\Delta\sigma/g$, where g is the gravitational acceleration, which can be used to rewrite the DBH model to the form

$$\Delta H_V = 0.265\alpha MGb\sqrt{Nd}$$

The comparison of the measured hardness and the hardness predicted using the DBH model is shown in Fig. 10. The predicted hardness of the surveillance material falls on the same curve as the high flux Halden irradiated welds. In this case the obstacle strength factor α was fitted to 0.15, in good agreement with other studies and of Cu-rich solute clusters [23,41], and the effect of size and number density compensate each other mutually.

The DBH model is dependent on mean cluster diameter, in fact it is modelled on the idea of clusters of only one size in the material. This is not accurate in the case treated here since the size distributions are wide, slightly bimodal and have a cut-off for small clusters due to the diffuse clusters and the cluster identification method MSM. For the low fluence material the number of small clusters is large at the cut-off; there might be smaller clusters that are not possible to identify but still might affect the hardness. The cluster diameter and number density are both parameters that come from the atom probe cluster analysis. Hence, the cluster identification is crucial, since if the cluster characteristics are different, the MSM might give slightly different results, stressing the importance of parameter choice for MSM. With this said, it is satisfactory to see that the DBH model manages to reproduce the measured hardness values from the APT data analysis and take the flux effects into account.

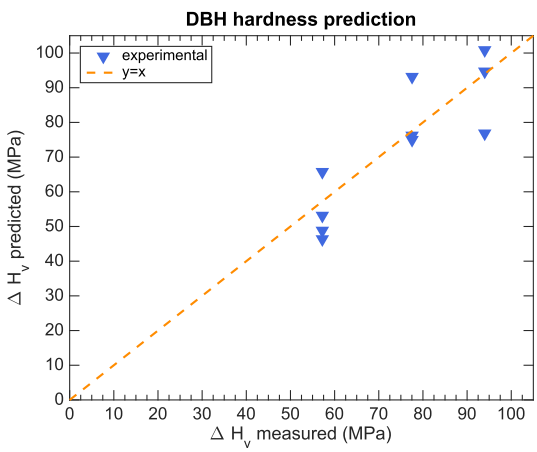

Fig. 10. The predicted hardness using the dispersed hardness (DBH) model with α fitted to 0.15 in comparison to the measured hardness.

For the RPV in operation, the flux is up to approximately four times lower than for the surveillance material. The materials irradiated in Halden are in turn exposed to a flux that is 15–25 times higher than the surveillance material. Thus, the difference between the clusters in the surveillance material and the actual RPV is probably smaller than the difference between the materials studied here. It thus is reasonable to assume the clusters being slightly larger and of lower number density than in the surveillance material, assuming there is no significant difference in terms of processes involved in the evolution of the precipitates for this specific flux difference. There are some flux effects that need to be taken into account when using accelerated tests, but the clusters are probably of the same type and order of magnitude in terms of sizes and number densities within the flux ranges studied in this paper.

What can be seen in the results from this study is a tendency that high flux irradiation promotes the formation of smaller clusters at a higher number density than that of a lower flux irradiation, which produces larger clusters at a lower number density. The effect of this on the mechanical properties seems to cancel out, as discussed above and as seen in Fig. 1. In a study by Dohi et al. hardness measurements were combined with APT-studies on material irradiated at fluxes of 0.1 and 50×10^{16} n/m^{2}s in a commercial LWR and the Halden reactor, respectively [21]. The results from their study suggest that high flux irradiation produces smaller clusters at higher number density than that of the lower flux irradiations and that the changes in hardness is non-significant with respect to flux, similarly to what is found in this study. Moreover, in a study by Soneda et al. low and high flux irradiations (0.11 and 7×10^{16} n/m^{2}s) of A508 forging and A533 plate material have been characterised by Charpy impact testing and APT [22]. The study concludes that the high flux irradiation forms smaller solute clusters at a larger number density than that of the lower flux irradiation. This is connected with the shift in T_{41J}; the low Cu-material of their study showed an increase in DBTT with fluence regardless of flux, in line with what was observed for the hardness increase in the current study.

5. Conclusions

The microstructural study of the irradiated materials of the Ringhals R4 material with different fluence and flux resulted in several conclusions:

- During the irradiation, clusters rich in Ni, Mn, Si and Cu are formed. These clusters grow during irradiation while new clusters nucleate.
- There are neutron flux effects on the microstructure of RPV materials. The clusters formed from high flux irradiation are smaller than the ones in the low flux specimen and have a higher number density but are of the same type, with an exception for the Cu content that is lower in the surveillance material.
- For the materials in this study, the flux effects compensate and the resulting hardness is not affected by flux. The irradiation-induced hardening can be described as dispersed barrier hardening with a fitted obstacle strength factor α of 0.15.
- The cluster size distributions seem to be slightly bimodal. This could be caused by a phase transformation. However, the cluster compositions (i. e. the Si content) do not suggest any probable phase such as G- or Γ_2-phase.
- The evolution of the clusters does not show any accelerating tendency, as has been suggested (i.e. there is no evidence from this data for the existence of late blooming phases).

- From the flux effects observed in this study, it can be predicted that RPVs in normal operation contain fewer but larger clusters than these observed in surveillance material.

Acknowledgements

This study was funded by the Swedish Centre of Nuclear Technology (SKC). Vattenfall Ringhals AB is acknowledged for providing the irradiated material. VTT is acknowledged for cutting the specimens in their hotlab facility.

References

[1] G.R. Odette, G.E. Lucas, Recent progress in understanding reactor pressure vessel steel embrittlement, Radiat. Eff. Defects Solids 144 (1–4) (1998) 189–231.
[2] IAEA, Integrity of Reactor Pressure Vessels in Nuclear Power Plants: Assessment of Irradiation Embrittlement Effects in Reactor Pressure Vessel Steels, International Atomic Energy Agency, Vienna, 2009.
[3] M.K. Miller, K.F. Russell, Embrittlement of RPV steels: an atom probe tomography perspective, J. Nucl. Mater. 371 (1–3) (2007) 145–160.
[4] E.A. Marquis, J.M. Hyde, Applications of atom-probe tomography to the characterisation of solute behaviours, Mater. Sci. Eng. R Rep. 69 (4–5) (2010) 37–62.
[5] G.R. Odette, B.D. Wirth, A computational microscopy study of nanostructural evolution in irradiated pressure vessel steels, J. Nucl. Mater. 251 (1997) 157–171.
[6] P. Pareige, J.C. Van Duysen, P. Auger, An APFIM study of the microstructure of a ferrite alloy after high fluence neutron irradiation, Appl. Surf. Sci. 67 (67) (1993) 342–347.
[7] E. Meslin, B. Radiguet, P. Pareige, A. Barbu, Kinetic of solute clustering in neutron irradiated ferritic model alloys and a French pressure vessel steel investigated by atom probe tomography, J. Nucl. Mater. 399 (2–3) (2010) 137–145.
[8] T. Takeuchi, A. Kuramoto, J. Kameda, T. Toyama, Y. Nagai, M. Hasegawa, T. Ohkubo, T. Yoshiie, Y. Nishiyama, K. Onizawa, Effects of chemical composition and dose on microstructure evolution and hardening of neutron-irradiated reactor pressure vessel steels, J. Nucl. Mater. 402 (2–3) (2010) 93–101.
[9] M.K. Miller, K.A. Powers, R.K. Nanstad, P. Efsing, Atom probe tomography characterizations of high nickel, low copper surveillance RPV welds irradiated to high fluences, J. Nucl. Mater. 437 (1–3) (2013) 107–115.
[10] P.D. Styman, J.M. Hyde, D. Parfitt, K. Wilford, M.G. Burke, C.A. English, P. Efsing, Post-irradiation annealing of Ni–Mn–Si-enriched clusters in a neutron-irradiated RPV steel weld using atom probe tomography, J. Nucl. Mater. 459 (2015) 127–134.
[11] P. Efsing, J. Roudén, P. Nilsson, Flux effects on radiation induced aging behaviour of low alloy steel weld material with high nickel and manganese content, Eff. Radiat. Nucl. Mater. 26 (2014) 119–134.
[12] ASTM (American Society of Testing and Materials) E384-11 Standard Test Method for Knoop and Vickers Hardness of materials, ASTM, West Conshohocken, 2011.
[13] M. Boåsen, P. Efsing, U. Ehrnstén, On flux effects in a low alloy steel from a Swedish reactor pressure vessel, J. Nucl. Mater. 484 (2017) 110–119.
[14] D.J. Larson, D.T. Foord, A.K. Petford-Long, H. Liew, M.G. Blamire, A. Cerezo, G.D.W. Smith, Field-ion specimen preparation using focused ion-beam milling, Ultramicroscopy 79 (1–4) (1999) 287–293.
[15] K. Thompson, D. Lawrence, D.J. Larson, J.D. Olson, T.F. Kelly, B. Gorman, In situ site-specific specimen preparation for atom probe tomography, Ultramicroscopy 107 (2–3) (2007) 131–139.
[16] M.K. Miller, Atom Probe Tomography: Analysis at the Atomic Level, Kluwer Academic/Plenum Publishers, New York, 2000.
[17] J.M. Hyde, M.G. Burke, B. Gault, D.W. Saxey, P. Styman, K.B. Wilford, T.J. Williams, Atom probe tomography of reactor pressure vessel steels: an analysis of data integrity, Ultramicroscopy 111 (6) (2011) 676–682.
[18] J.M. Hyde, C.A. English, in: An Analysis of the Structure of Irradiation Induced Cu-enriched Clusters in Low and High Nickel Welds, Materials Research Society Symposium, 2000, pp. R6.6.1–R6.6.12. Boston.
[19] A. Heinrich, T.a. Al-Kassab, R. Kirchheim, Investigation of the early stages of decomposition of Cu–0.7at.% Fe with the tomographic atom probe, Mater. Sci. Eng. A 353 (1–2) (2003) 92–98.
[20] D. Vaumousse, A. Cerezo, P.J. Warren, A procedure for quantification of precipitate microstructures from three-dimensional atom probe data, Ultramicroscopy 95 (2003) 215–221.
[21] K. Dohi, K. Nishida, A. Nomoto, N. Soneda, H. Matsuzawa, M. Tomimatsu, in: Effect of Neutron Flux at High Fluence on Microstructural and Hardness Changes of RPV Steels, ASME 2010 Pressure Vessels & Piping Division/K-PVP Conference, 2010. Bellevue, Washington, USA.
[22] N. Soneda, K. Nishida, A. Nomoto, K. Dohi, in: Flux Effect on Embrittlement of Reactor Pressure Vessel Steels Irradiated to High Fluences, Fontevraud 8: Conference on Contribution of Materials Investigations and Operating Experience to LWRs' Safetyy, Performance and Reliability, 2014. Avignon, France.
[23] A. Wagner, F. Bergner, R. Chaouadi, H. Hein, M. Hernández-Mayoral, M. Serrano, A. Ulbricht, E. Altstadt, Effect of neutron flux on the characteristics of irradiation-induced nanofeatures and hardening in pressure vessel steels, Acta Mater. 104 (2016) 131–142.
[24] F. Bergner, A. Ulbricht, H. Hein, M. Kammel, Flux dependence of cluster formation in neutron-irradiated weld material, J. Phys. Condens. Matter 20 (10) (2008) 104262.
[25] P.B. Wells, T. Yamamoto, B. Miller, T. Milot, J. Cole, Y. Wu, G.R. Odette, Evolution of manganese–nickel–silicon-dominated phases in highly irradiated reactor pressure vessel steels, Acta Mater. 80 (2014) 205–219.
[26] IAEA, Effects of Nickel on Irradiation Embrittlement of Light Water Reactor Pressure Vessel Steels, International Atomic Energy Agency, Vienna, 2005.
[27] M.K. Miller, A.A. Chernobaeva, Y.I. Shtrombakh, K.F. Russell, R.K. Nanstad, D.Y. Erak, O.O. Zabusov, Evolution of the nanostructure of VVER-1000 RPV materials under neutron irradiation and post irradiation annealing, J. Nucl. Mater. 385 (3) (2009) 615–622.
[28] L. Messina, M. Chiapetto, P. Olsson, C.S. Becquart, L. Malerba, An object kinetic Monte Carlo model for the microstructure evolution of neutron-irradiated reactor pressure vessel steels, physica status solidi (a) (2016).
[29] R. Ngayam-Happy, C.S. Becquart, C. Domain, L. Malerba, Formation and evolution of MnNi clusters in neutron irradiated dilute Fe alloys modelled by a first principle-based AKMC method, J. Nucl. Mater. 426 (1–3) (2012) 198–207.
[30] W. Xiong, H. Ke, R. Krishnamurthy, P. Wells, L. Barnard, G.R. Odette, D. Morgan, Thermodynamic models of low-temperature Mn–Ni–Si precipitation in reactor pressure vessel steels, MRS Commun. (2014) 1–5.
[31] D.J. Sprouster, J. Sinsheimer, E. Dooryhee, S.K. Ghose, P. Wells, T. Stan, N. Almirall, G.R. Odette, L.E. Ecker, Structural characterization of nanoscale intermetallic precipitates in highly neutron irradiated reactor pressure vessel steels, Scr. Mater. 113 (2016) 18–22.
[32] Y. Matsukawa, T. Takeuchi, Y. Kakubo, T. Suzudo, H. Watanabe, H. Abe, T. Toyama, Y. Nagai, The two-step nucleation of G-phase in ferrite, Acta Mater. 116 (2016) 104–113.
[33] G.R. Odette, T. Yamamoto, D. Klingensmith, On the effect of dose rate on irradiation hardening of RPV steels, Philos. Mag. 85 (4–7) (2005) 779–797.
[34] G.R. Odette, R.K. Nanstad, Predictive reactor pressure vessel steel irradiation embrittlement models: issues and opportunities, JOM 61 (7) (2009) 17–23.
[35] G.R. Odette, E.V. Mader, G.E. Lueas, W.J. Phythian, C.A. English, in: The Effect of Flux on the Irradiation Hardening of Pressure Vessel Steels, Effects of Radiation on Materials: 16th International Symposium, 1993. ASTM STP 1175, Philadelphia.
[36] R. Chaouadi, R. Gérard, Confirmatory investigations on the flux effect and associated unstable matrix damage in RPV materials exposed to high neutron fluence, J. Nucl. Mater. 437 (1–3) (2013) 267–274.
[37] R. Chaouadi, R. Gérard, Neutron flux and annealing effects on irradiation hardening of RPV materials, J. Nucl. Mater. 418 (1–3) (2011) 137–142.
[38] R.E. Stoller, S.J. Zinkle, On the relationship between uniaxial yield strength and resolved shear stress in polycrystalline materials, J. Nucl. Mater. 283–287 (2000) 349–352.
[39] G.S. Was, Fundamentals of Radiation Materials Science, Springer, Berlin, 2007.
[40] D. Tabor, The Hardness of Metals, Oxford University Press, 2000.
[41] F. Bergner, F. Gillemot, M. Hernández-Mayoral, M. Serrano, G. Török, A. Ulbricht, E. Altstadt, Contributions of Cu-rich clusters, dislocation loops and nanovoids to the irradiation-induced hardening of Cu-bearing low-Ni reactor pressure vessel steels, J. Nucl. Mater. 461 (2015) 37–44.
[42] P. Efsing, C. Jansson, T. Mager, G. Embring, Analysis of the ductile-to-brittle transition temperature shift in a commercial power plant with high nickel containing weld material, J. ASTM Int. 4 (7) (2007).

Paper III

Cluster formation in in-service thermally aged pressurizer welds

K. Lindgren, M. Boåsen, K. Stiller, P. Efsing, and M. Thuvander

Journal of Nuclear Materials 504, 23-28 (2018)

Journal of Nuclear Materials 504 (2018) 23–28

Contents lists available at ScienceDirect

Journal of Nuclear Materials

journal homepage: www.elsevier.com/locate/jnucmat

Cluster formation in in-service thermally aged pressurizer welds

Kristina Lindgren [a, *], Magnus Boåsen [b], Krystyna Stiller [a], Pål Efsing [b, c], Mattias Thuvander [a]

[a] Department of Physics, Chalmers University of Technology, SE-412 96 Göteborg, Sweden
[b] Department of Solid Mechanics, Royal Institute of Technology (KTH), SE-100 44 Stockholm, Sweden
[c] Ringhals AB, SE-430 22 Väröbacka, Sweden

HIGHLIGHTS

- Clustering during in-service thermal aging of a pressurizer weld is studied.
- Atom probe tomography reveals Cu-rich clusters on dislocations and boundaries.
- The clusters contribute to the hardness increase of the material.

GRAPHICAL ABSTRACT

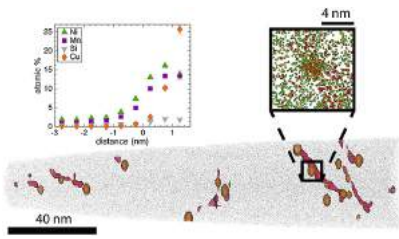

ARTICLE INFO

Article history:
Received 11 December 2017
Received in revised form
10 March 2018
Accepted 11 March 2018
Available online 12 March 2018

Keywords:
RPV steel
Atom probe tomography
Thermal aging
Precipitation

ABSTRACT

Thermal aging of reactor pressure vessel steel welds at elevated temperatures may affect the ductile-to-brittle transition temperature. In this study, unique weld material from a pressurizer, with a composition similar to that of the reactor pressure vessel, that has been in operation for 28 years at 345 °C is examined. Despite the relatively low temperature, the weld becomes hardened during operation. This is attributed to nanometre sized Cu-rich clusters, mainly located at Mo- and C-enriched dislocation lines and on boundaries. The welds have been characterized using atom probe tomography, and the characteristics of the precipitates/clusters is related to the hardness increase, giving the best agreement for the Russell-Brown model.

1. Introduction

The pressurizer is a component of the primary coolant circuit in a pressurized water reactor (PWR) with the purpose of regulating the pressure and temperature within the primary circuit (which includes the reactor pressure vessel, RPV). Hence, the structural integrity of the pressurizer is of great importance. The vessel of the pressurizer is generally made from low alloy ferritic/bainitic type steels, i.e. identical to that of a RPV. Studies of irradiated (for instance [1–6]) and thermally aged [7,8] RPV steels report finding nanometre-sized Cu-rich clusters within the microstructure, containing various amounts of Ni, Mn, and Si. The clusters are known to affect the mechanical properties by increasing the yield strength and the ductile-to-brittle transition temperature, i.e. having an embrittling effect.

The Swedish nuclear reactors Ringhals R3 and R4 are known to have RPVs containing low Cu (0.04–0.08 at.%) and high Ni

* Corresponding author.
E-mail address: kristina.lindgren@chalmers.se (K. Lindgren).

https://doi.org/10.1016/j.jnucmat.2018.03.017
0022-3115/

(1.50–1.58 at.%) and Mn (1.37–1.48 at.%) [9]. This in turn affects the radiation induced clusters, forming with low Cu content [10–12]. Still, pure thermal aging of the same material has not been much studied. Also, most studies on thermal aging of RPV materials have been performed using elevated temperatures and short aging times in order to simulate the same diffusion distances of the elements. This type of accelerated testing might, however, have limited validity, as solubilities and phase equilibria are different at lower temperatures. In this paper, the material studied has been thermally aged at 345 °C for 28 years (215,000 h) of operation as an actual pressurizer. The pressurizer was exchanged in conjunction with a major upgrade of the R4 reactor, including the replacement of steam generator tubes of Alloy 600 to Alloy 690. Atom probe tomography (APT) is used together with hardness measurements in order to characterise the effect of the thermal aging.

2. Materials and methods

The studied weld is a vertical submerged arc weld of the former R4 pressurizer, and it is compared with an archive reference material from the Forsmark nuclear power plant, manufactured using the exact same weld wire heat and according to the same specifications as the pressurizer welds.

For the APT analysis, a LEAP 3000X HR, with an energy compensating reflectron, from Imago Scientific Instruments was utilized. Both voltage and laser pulsing modes were used, in order to obtain the more accurate Si and P distribution (and more well defined clusters [13]) of voltage pulsing and to analyse large volumes using laser pulse mode. For voltage pulse mode, the specimen temperature was 50 K, and the pulse fraction 20%. For laser pulse mode, the temperature was 30 K and the laser pulse energy 0.3 nJ. In both cases the pulse frequency was 200 kHz and the target evaporation rate 0.2–0.5% (detected ions per pulse). The specimens were prepared using a two-step electropolishing method [14] with final millisecond pulsing in order to get rid of any surface oxides.

The APT data reconstruction was performed in IVAS™ 3.6 (Cameca). The reconstruction parameters were chosen in order that the plane distance of (002) or (011) planes should be equal to tabulated values (for the analyses when this was possible). For voltage pulsed runs the reconstruction parameters used were a *k*-factor of 5.3 and an evaporation field of 33 V/nm. For laser pulsed runs the corresponding values were 4.0 and 23 V/nm. The image compression factor was set to 1.65 for all reconstructions. The Cu cluster sizes were estimated based on the number of clustered atoms, and utilising the maximum separation method [1,15] with parameters $d_{max} = 0.40$ nm, $N_{min} = 20$ and order 1, and solute elements Cu, Ni and Mn. The peak overlap of $^{58}Ni^{++}$ and $^{58}Fe^{++}$ at m/n = 29 Da was ranged as Ni as the effect of increased cluster to matrix contrast by excluding the 29-peak was estimated to be insignificant for the relatively Cu-rich clusters. The use of Cu atoms only would give more well-defined clusters due to the low matrix Cu level, but would underestimate the size of the clusters due to their core-shell structure.

Table 1
Hardness measurements for the materials, including the standard deviations within the measurements.

Material	H_V10 [kg/mm^2]
Reference	203 ± 2
Pressurizer	235 ± 7

3. Results

The measured hardness of the pressurizer weld and the reference material are presented in Table 1. There is a clear increase in hardness due to the in-service aging of the pressurizer. The larger standard deviation in the measured hardness of the pressurizer than the reference material origins in the measurement; the hardness indents were made on a 10 cm line throughout the weld, whereas the indents in the reference material were made on a Charpy-specimen.

As the analysed materials are welds, some differences in the composition between analyses are expected when using APT, due to the inhomogeneity of the welds and the relatively small volume of an APT analysis. In Table 2, the measured average compositions of the reference material and the pressurizer weld are given. The composition is expected to be similar to that of the RPV of Ringhals R3 and R4, with high Ni and Mn contents and low Cu content [9]. Carbides are excluded from the analysis volumes when determining the composition, and hence the C content reported in Table 2 is lower than the nominal value.

In the thermally aged pressurizer material, Mo-enriched dislocation lines were found, decorated with Cu-rich clusters, see Figs. 1–3. The average distance between clusters along dislocation lines was 15 nm, with a distribution ranging from 7 to 35 nm. Larger distances might obviously be missed due to the limited extent of the APT analysis volumes. The clusters on the dislocation lines vary between 1 and 4 nm in diameter, with an average of 1.9 ± 0.3 nm. Hereby it was assumed that the clusters do not contain any Fe. In the analysis data, slightly less than 50% of the cluster content was Fe, with a decreasing concentration towards the centre of the clusters. It is therefore assumed that the measured Fe is mainly due to local magnification effects [16,17]. As seen in the proxigram of the clusters in Fig. 2, the Cu-rich core is surrounded by a shell of Ni, Mn and Si. The total number density of Cu-clusters in the pressurizer was found to be $0.16 \pm 0.05 \cdot 10^{23}$ m^{-3}. In the reference material, no Cu-rich clusters were observed.

The Mo-enriched dislocation lines are unevenly distributed within the volumes, see Fig. 1, where there are no dislocation lines in the first 300 nm of the reconstruction. In the same figure, the dislocations are located on a plane (arrowed). The average density of Mo-enriched dislocations is estimated to be $2.3 \pm 1.0 \cdot 10^{14}$ m^{-2}. The number of excess Mo atoms per dislocation length was found to vary from 5 to 30 atoms per nm (taking the detection efficiency of 37% into account), the number of C atoms also located on the dislocation lines varies within the same range; with no obvious correlation. In the voltage pulsed pressurizer analyses, P can also be distinguished on the dislocation lines (0.4–1.4 P atoms per nm). Dislocations are also found in the reference material, see Fig. 4 a.

Table 2
Compositions from APT analyses. Averages and the standard deviations between the analyses are given in at.%. In total four analyses are used for the reference composition and seven analyses for the pressurizer.

	Reference (at. %)	Pressurizer (at. %)
C	0.04 ± 0.01	0.04 ± 0.03
Mo	0.19 ± 0.02	0.19 ± 0.05
Si	0.31 ± 0.07	0.30 ± 0.02
P	0.01 ± 0.01	0.01 ± 0.01
V	0.0030 ± 0.0026	0.0012 ± 0.0007
Mn	1.35 ± 0.05	1.24 ± 0.12
Cr	0.03 ± 0.01	0.06 ± 0.01
Co	0.02 ± 0.01	0.02 ± 0.01
Cu	0.07 ± 0.02	0.10 ± 0.02
Ni	1.77 ± 0.33	1.68 ± 0.28
Fe	bal.	bal.

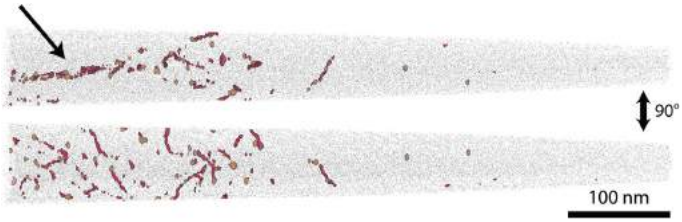

Fig. 1. APT reconstruction (laser pulsing) of the pressurizer, showing 1.1 at.% Cu isoconcentration surfaces (orange) and 2.0 at.% Mo isoconcentration surfaces (red). Grey shows the extent of the analysis. The lower image shows the reconstruction rotated 90°. The arrow marks a plane with dislocations and Cu-rich clusters. (For interpretation of the references to colour in this figure legend, the reader is referred to the Web version of this article.)

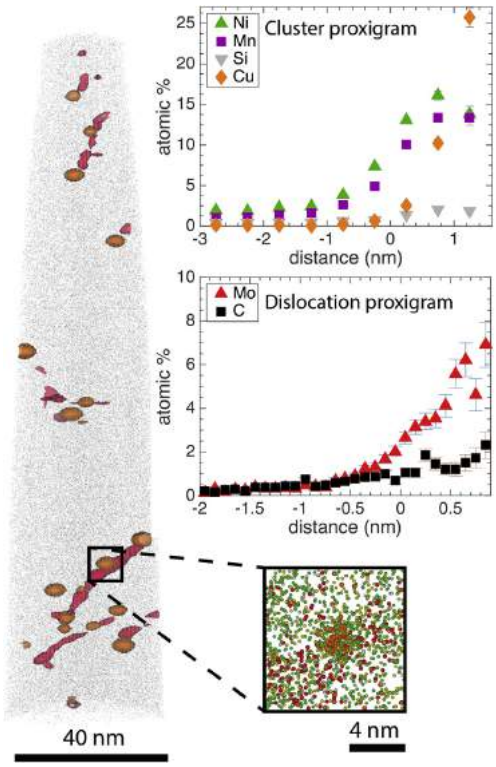

Fig. 2. APT reconstruction of a voltage pulsed analysis of the pressurizer, showing Mo (1.6 at.%) in red and Cu (1.1 at.%) in orange. The extent of the enlarged box is $10 \times 10 \times 10$ nm^3 where all Ni (green), Mn (yellow), Si (grey), Cu (orange) and Mo (red) atoms are shown within and around a cluster. The proxigrams of the Cu surfaces (clusters) and Mo surfaces (dislocations) are included. (For interpretation of the references to colour in this figure legend, the reader is referred to the Web version of this article.)

The excess of Mo and C is similar to that of the thermally aged material, hence, these elements were not noticeably affected by the thermal aging. Therefore, the segregation of Mo and C presumably occurred already in the welding process (including the stress relief annealing).

A layer, presumably a subgrain boundary, was found in one analysis of the pressurizer material, see Fig. 3. The boundary is enriched in Mn, Mo, Ni, C, Si, Cr, and P. At this boundary, a Mo-rich carbide (with a surface enriched in P and Si), together with Cu-rich clusters were present. The carbide is most likely of M_2C-type, with a measured C content of 31.1% and 58.6% Mo, 4.7% Mn, 3.7% Fe, and 1.8% Cr (all in at.%). As the atoms from carbides tend to evaporate in bursts, with several atoms evaporating by the same pulse (so-called multiple events), detector pile-up often results in some errors in the measured composition [18]. For most carbides, except for cementite, the measured C content becomes too low, so the value of 31 at.% is typical for M_2C. The clusters on this boundary were found to contain more Mn than the clusters on the dislocations. The Mn content of the clusters might be correlated with the high Mn content of the boundary layer.

In the pressurizer material, most of the Cu-rich clusters were found either on dislocation lines or on boundaries. A few Cu-rich clusters seem to be homogeneously nucleated in the matrix. However, dislocation lines might cut the analysis or not being detected if not enriched in Mo, making it impossible to state whether they are actually on a dislocation or not using APT, as dislocations are only visible if there is segregation.

In both the reference weld and the pressurizer weld, a few V-rich clusters were observed, also enriched in N, Cr and C, see Fig. 4 b. These might act as nucleation points for Cu-rich clusters. V-rich clusters are believed to be present from the manufacturing of the weld, and not to be affected by the thermal aging. V-rich clusters have previously been found in a similar RPV material [12]. In one analysis of the reference material, two clusters containing Mn and S were observed, likely traces of MnS precipitates.

4. Discussion

The thermal aging results in cluster formation, resembling the clustering induced by neutron irradiation of similar materials [10–12,19]. The increase in hardness is smaller for the material studied in this paper, 28 years at 345 °C ($\Delta H_V10 = 32$ kg/mm^2), than for similar RPV material irradiated the corresponding time ($\Delta H_V5 = 60$ kg/mm^2 [19]). In many cases, the P segregation to grain boundaries has been found to contribute to the deterioration of toughness during thermal aging [20–22]. However, this is not expected to affect the hardness of the material [20–22].

In comparison to the irradiated material, the cluster number density is lower by a factor of around 25. The observation of a core-shell structure of the clusters has been previously reported for thermally aged high Cu-materials, as has the higher cluster Cu content in comparison to irradiated material [7]. Styman et al. [8] found clusters on grain boundaries in thermally aged high Cu RPV welds. However, there is, to our knowledge, no report where the majority of the clusters are located on dislocations decorated with Mo and C.

The regions with dislocations enriched in Mo and C have a lower

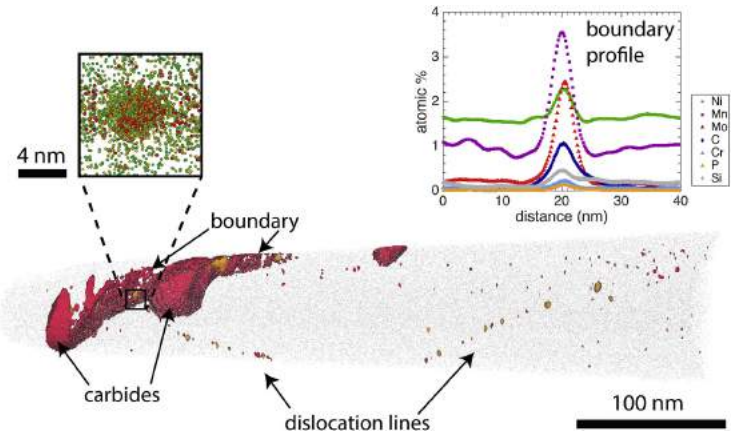

Fig. 3. Laser pulsed APT analysis of the pressurizer. Mo (1.6 at.%) is shown in red and Cu (1.1 at.%) in orange. Several Mo-rich carbides are located on a boundary. One of the Cu-clusters on the boundary is enlarged in a $10 \times 10 \times 10\ nm^3$ box where all Ni (green), Mn (yellow), Cu (orange), and Mo (red) atoms are shown. A concentration profile through the boundary in a position without Cu-clusters is shown. (For interpretation of the references to colour in this figure legend, the reader is referred to the Web version of this article.)

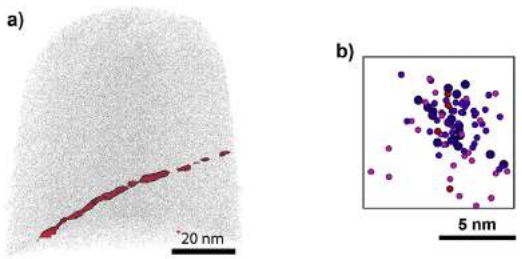

Fig. 4. a) A dislocation line enriched in Mo (red 1.6 at.% Mo isoconcentration surface) in the reference material. Grey shows the extent of the analysis. b) A V-rich cluster in the reference material, in a $10 \times 10 \times 10\ nm^3$ box where all V (purple), VN (blue), Cr (pink), and C (red) atoms are shown. (For interpretation of the references to colour in this figure legend, the reader is referred to the Web version of this article.)

total atomic density in some of the APT reconstructions. This could be an indication of a carbide phase rather than just segregation to the dislocation. However, assuming a density of around 80 atoms per nm^3 [23] for M_2C carbides (as the large Mo-rich carbide in Fig. 3), the diameter of a cylinder containing 30 Mo atoms and 15 C atoms per nm length is around 0.8 nm, that is small for being anything else than coherent with the α-Fe matrix.

4.1. Hardening models

As has been observed in this paper, the material consists of an inhomogeneous microstructure with groups of dislocations decorated with Cu-clusters, existing alongside regions with few dislocations and thus also fewer clusters. The clusters themselves are believed to give rise to a hardening of the material as they would act as obstacles to dislocation glide, preventing plastic deformation. As the dislocations observed using APT are decorated with the Cu-rich clusters, and enriched with both Mo and C it is believed that these dislocations are unable to move. Therefore, plastic deformation would accumulate from freshly formed dislocations which will interact with the already present clusters and possibly also the already present, pinned, dislocations. The hardening due to the aging will thus be a function of both the aging induced clusters and the immobilised dislocations, interacting with newly nucleated dislocations during plastic deformation.

The irradiated material studied in Refs. [12,19] has a similar chemical composition as the material in this study. A dispersed-barrier hardening (DBH) model [24] was used for estimating the cluster contribution to the hardness, to which a strength parameter $\alpha = 0.15$ was fitted (in good agreement with other studies, see for instance [25,26]). However, assuming a DBH model, see Table 3, and using the assumptions in Ref. [12], the cluster contribution to the hardness of the pressurizer weld would be only $\Delta H_V = 14\ kg/mm^2$. This is much lower than the measured value ($\Delta H_V = 32\ kg/mm^2$). In order to obtain the measured value of the hardness, α has to be 0.34, that is much higher than the 0.15 fitted for the irradiated material and seems unrealistic.

Another model that is commonly used to predict the hardness increase from the cluster characteristics is the Russell-Brown (RB) model [4,26,27]. For the thermally aged pressurizer weld, the RB model gives a hardness increase prediction of $33\ kg/mm^2$, in good agreement with the measured value, although the pinned dislocations are neglected. Assuming the RB model is describing the system implies the assumption of the interaction of new dislocations with clusters being more important than the interaction with decorated dislocations. It is interesting to note that the RB model did not describe well the hardening in the irradiated materials with similar composition in Ref. [12], where the DBH model gave a good fit. This raises the question whether this is due to the different characteristics of the clusters. The clusters in the irradiated material might contain more vacancies and/or interstitials from the cascades, that would affect the strengthening when dislocations cut through them. In the thermally aged pressurizer, the clusters do not contain such irradiation induced defects. However, other studies have found the RB model to describe the hardening of irradiated RPV steels [4,5]. One other aspect is the different composition of the clusters. The RB model in Table 3 assumes Cu-rich clusters, that is true for the thermally aged pressurizer, but not for the irradiated material where the Cu cluster content is much lower and the clusters contain mainly Ni, Mn and Si [12].

Something that both the RB model and the DBH model assumes is evenly distributed clusters, whereas in the pressurizer material,

Table 3
Hardness increase predictions from the different hardening models. α is the strength factor, M = 3.06 is the Taylor factor, G = 80 GPa is the shear modulus of the matrix, b is Burgers vector, N is the cluster number density, d is the cluster diameter, L is the spacing between clusters in the slip plane, f_v is the cluster volume fraction, and ρ_0 is the dislocation density. R = 2500b is the outer cut-off radius of the dislocation, $r_0 = 2.5b$ is the inner cut-off, and $\frac{E_1^w}{E_2^w} = 0.6$ is the ratio of the energies per unit length of a dislocation in infinite media for Fe-Cu [27]. The factor 0.265 in the equations comes from the conversion between flow stress and hardness.

Model	Equation	Hardness increase prediction [kg/mm^2]
DBH	$\Delta H_V^{DBH} = 0.265\alpha MGb\sqrt{Nd}$	14 ± 3
Russell-Brown	$\Delta H_V^{RB} = 0.265\frac{MGb}{L}\left(1-\frac{E_1^2}{E_2^2}\right)^{3/4}$	33 ± 6
	with $L = \frac{\sqrt{\pi}d}{2\sqrt{f_v}}$ and $\frac{E_1^2}{E_2^2} = \frac{E_1^w \log\left(\frac{d}{r_0}\right)}{E_2^w \log\left(\frac{R}{r_0}\right)} + \frac{\log\left(\frac{2R}{d}\right)}{\log\left(\frac{R}{r_0}\right)}$	
Taylor-like	$\Delta H_V^T = 0.265\alpha MGb\sqrt{\rho_0}$	34 ± 8

the majority of the clusters were found to be located on dislocations. Due to this, a Taylor-like model is included in Table 3.

In the proposed Taylor-like [28–30] expression, it is assumed that the clusters form on the Mo-enriched dislocations, resulting in a hardness increment due to the interaction between new dislocations nucleated during plastic deformation and the already present dislocations (with density $\rho_0 = 2.3 \cdot 10^{14}$ m^{-2}, assumed to be independent of the aging mechanism) and the clusters formed by aging. This idea is based on that the cluster strength α in the pressurizer material is similar to that found in Ref. [12], where the two materials in a reference state are similar in both chemical composition and mechanical properties. However, this assumption is somewhat arbitrary as the α factor in this case should describe the dislocations and not the clusters. In Table 3, it can be seen that the hardening from the Taylor-like model gives a prediction that is in agreement with the measured hardness, although the model is not complete as it is not taking the cluster size or distance into account.

In order to fully understand which model best describes the hardening of the material from the clustering; more data and possibly simulations are needed. However, what is clear is that there is a hardening contribution to the embrittlement of the pressurizer.

4.2. Cluster formation mechanisms

A few considerations can be made on the nucleation and growth of the Cu-rich clusters in order to better understand why clusters seem to appear on dislocations but not in the matrix. The presence of clusters mainly on dislocations must be due to either easier nucleation (i.e. inhomogeneous nucleation) or faster growth governed by enhanced diffusion along the dislocations. Dechamps et al. studied Cu-precipitation in Fe-0.8 wt% Cu at 500 °C, and found that the nucleation is promoted by the presence of dislocations [31]. Their 10% pre-strained material had clusters nucleating on the dislocations, due to the release of coherency strains.

However, the growth could also be considered, first in the case of diffusion controlled growth without dislocations. The radius of the clusters should then be $r = \sqrt{2\Omega Dt}$ [32], D being the diffusion coefficient and t the time from nucleation. $\Omega = (C_0 - C_\alpha)/(C_\beta - C_\alpha)$, where C_0 is the overall Cu concentration (0.10 at.%), C_α is the solubility of Cu in Fe (here assumed to be zero), and C_β is the amount of Cu in the clusters (assumed to be 100%). A value of D (2.9 10^{-26} m^2/s) at 345 °C is extrapolated from tabulated values of the pre-factor (0.030 m^2/s) and the activation energy (284 kJ/mol) for Cu diffusion in ferrite at higher temperatures [33]. The maximum radius that could be reached without dislocations during operation for 28 years then becomes 0.23 nm. Assuming matrix coherent clusters with a density of 85 atoms/nm^3, this would correspond to only 4 atoms. In other words, the growth is suggested to be too slow for formation of clusters of significant size in the matrix during the aging period by this model. The characteristic diffusion distance is 5 nm using the same diffusion coefficient D, but the low Cu concentration limits the growth. Of course, this treatment depends critically on the value of D, which is uncertain for low temperatures. Extrapolation to 345 °C from the values for Cu in pure Fe experimentally found by Toyama et al. [34] gives $D = 3.8\ 10^{-27}$ m^2/s, using the values found for a Japanese RPV material by Shimodaira et al. [35] gives $D = 6.0\ 10^{-28}$ m^2/s, both significantly lower than the value above. Messina et al. [36] used modelling on Cu in pure Fe and extrapolating their results gives $D = 4.9\ 10^{-26}$ m^2/s, that is close the above value. The measured average radius of the clusters (on dislocations) is 0.95 nm, and assuming that the growth is controlled by bulk diffusion, a D of 5.1 10^{-25} m^2/s would be needed. This is one to three orders of magnitude higher than the extrapolated values of D, suggesting that the growth is not controlled by bulk diffusion solely.

On the dislocations and boundaries, the Cu diffusion is much faster and Cu atoms can be provided from a larger volume close to the dislocation or boundary, and thus more Cu is provided for nucleation and growth of the clusters. The Ni, Mn and Si are assumed to segregate to the cluster surface during the growth, thus making the interfacial energy smaller, as for clusters in irradiated RPV welds [5]. This matches well with the core/shell structure of the Cu-rich clusters seen in Fig. 2.

5. Conclusions

In summary, we have investigated the detailed microstructure of a thermally aged low Cu pressurizer weld that has been in operation in a commercial nuclear power plant. The APT analysis shows an inhomogeneous structure; the long-term aging (28 years) resulted in clusters with a Cu-rich core and a Ni-, Mn- and Si-rich shell. The clusters are mainly located on dislocations and boundaries and are suggested to significantly contribute to the hardening of the material ($\Delta H_V = 32$ kg/mm^2). The Russell-Brown model was found to give a good estimate of the hardness increase from the cluster characteristics, albeit the clusters not being homogeneously distributed.

Acknowledgements

The Swedish Centre for Nuclear Technology (SKC) is acknowledged for financing the research, Ringhals AB and Forsmark Kraft AB are acknowledged for providing the material.

References

[1] J.M. Hyde, C.A. English, An analysis of the structure of irradiation induced Cu-enriched clusters in low and high nickel welds, in: Materials Research Society Symposium, Boston, 2000 pp. R6.6.1–R6.6.12.

[2] M.K. Miller, K.F. Russell, Embrittlement of RPV steels: an atom probe tomography perspective, J. Nucl. Mater. 371 (1–3) (2007) 145–160.
[3] B. Radiguet, P. Pareige, A. Barbu, Irradiation induced clustering in low copper or copper free ferritic model alloys, Nucl. Instrum. Methods Phys. Res. Sect. B Beam Interact. Mater. Atoms 267 (8–9) (2009) 1496–1499.
[4] C. English, J. Hyde, Radiation damage of reactor pressure vessel steels, in: R. Konings (Ed.), Comprehensive Nuclear Materials, Elsevier2012, pp. 151–180.
[5] G.R. Odette, G.E. Lucas, Recent progress in understanding reactor pressure vessel steel embrittlement, Radiat. Eff. Defect Solid 144 (1–4) (1998) 189–231.
[6] E. Meslin, M. Lambrecht, M. Hernández-Mayoral, F. Bergner, L. Malerba, P. Pareige, B. Radiguet, A. Barbu, D. Gómez-Briceño, A. Ulbricht, A. Almazouzi, Characterization of neutron-irradiated ferritic model alloys and a RPV steel from combined APT, SANS, TEM and PAS analyses, J. Nucl. Mater. 406 (1) (2010) 73–83.
[7] J.M. Hyde, G. Sha, E.A. Marquis, A. Morley, K.B. Wilford, T.J. Williams, A comparison of the structure of solute clusters formed during thermal ageing and irradiation, Ultramicroscopy 111 (6) (2011) 664–671.
[8] P.D. Styman, J.M. Hyde, K. Wilford, A. Morley, G.D.W. Smith, Precipitation in long term thermally aged high copper, high nickel model RPV steel welds, Prog. Nucl. Energy 57 (2012) 86–92.
[9] P. Efsing, C. Jansson, T. Mager, G. Embring, Analysis of the ductile-to-brittle transition temperature shift in a commercial power plant with high nickel containing weld material, J. ASTM Int. (JAI) 4 (7) (2007).
[10] M.K. Miller, K.A. Powers, R.K. Nanstad, P. Efsing, Atom probe tomography characterizations of high nickel, low copper surveillance RPV welds irradiated to high fluences, J. Nucl. Mater. 437 (1–3) (2013) 107–115.
[11] P.D. Styman, J.M. Hyde, D. Parfitt, K. Wilford, M.G. Burke, C.A. English, P. Efsing, Post-irradiation annealing of Ni–Mn–Si-enriched clusters in a neutron-irradiated RPV steel weld using Atom Probe Tomography, J. Nucl. Mater. 459 (2015) 127–134.
[12] K. Lindgren, M. Boåsen, K. Stiller, P. Efsing, M. Thuvander, Evolution of precipitation in reactor pressure vessel steel welds under neutron irradiation, J. Nucl. Mater. 488 (2017) 222–230.
[13] K. Lindgren, K. Stiller, P. Efsing, M. Thuvander, On the analysis of clustering in an irradiated low alloy reactor pressure vessel steel weld, Microsc. Microanal. 23 (2) (2017) 376–384.
[14] M.K. Miller, R.G. Forbes, Atom-probe Tomography: the Local Electrode Atom Probe, Springer, New York, 2014.
[15] D. Vaumousse, A. Cerezo, P.J. Warren, A procedure for quantification of precipitate microstructures from three-dimensional atom probe data, Ultramicroscopy 95 (2003) 215–221.
[16] E.A. Marquis, J.M. Hyde, Applications of atom-probe tomography to the characterisation of solute behaviours, Mater. Sci. Eng. R Rep. 69 (4–5) (2010) 37–62.
[17] A. Morley, G. Sha, S. Hirosawa, A. Cerezo, G.D. Smith, Determining the composition of small features in atom probe: bcc Cu-rich precipitates in an Fe-rich matrix, Ultramicroscopy 109 (5) (2009) 535–540.
[18] M. Thuvander, J. Weidow, J. Angseryd, L.K. Falk, F. Liu, M. Sonestedt, K. Stiller, H.O. Andren, Quantitative atom probe analysis of carbides, Ultramicroscopy 111 (6) (2011) 604–608.
[19] M. Boåsen, P. Efsing, U. Ehrnstén, On flux effects in a low alloy steel from a Swedish reactor pressure vessel, J. Nucl. Mater. 484 (2017) 110–119.
[20] H. Nakata, K. Fujii, K. Fukuya, R. Kasada, A. Kimura, Grain boundary phosphorus segregation in thermally aged low alloy steels, J. Nucl. Sci. Technol. 43 (7) (2006) 785–793.
[21] Y.I. Shtrombakh, B.A. Gurovich, E.A. Kuleshova, D.A. Maltsev, S.V. Fedotova, A.A. Chernobaeva, Thermal ageing mechanisms of VVER-1000 reactor pressure vessel steels, J. Nucl. Mater. 452 (1–3) (2014) 348–358.
[22] B.A. Gurovich, A.A. Chernobaeva, D.Y. Erak, E.A. Kuleshova, D.A. Zhurko, V.B. Papina, M.A. Skundin, D.A. Maltsev, Chemical composition effect on VVER-1000 RPV weld metal thermal aging, J. Nucl. Mater. 465 (2015) 540–549.
[23] B. Lönnberg, Thermal expansion studies on the subcarbides of group V and VI transition metals, J. Less Common Met. 120 (1986) 135–146.
[24] G.S. Was, Fundamentals of Radiation Materials Science, Springer, Berlin, 2007.
[25] F. Bergner, F. Gillemot, M. Hernández-Mayoral, M. Serrano, G. Török, A. Ulbricht, E. Altstadt, Contributions of Cu-rich clusters, dislocation loops and nanovoids to the irradiation-induced hardening of Cu-bearing low-Ni reactor pressure vessel steels, J. Nucl. Mater. 461 (2015) 37–44.
[26] A. Wagner, F. Bergner, R. Chaouadi, H. Hein, M. Hernández-Mayoral, M. Serrano, A. Ulbricht, E. Altstadt, Effect of neutron flux on the characteristics of irradiation-induced nanofeatures and hardening in pressure vessel steels, Acta Mater. 104 (2016) 131–142.
[27] K.C. Russell, L.M. Brown, A dispersion strenghtening model based on differing elastic moduli applied to the iron-copper system, Acta Mater. 20 (1972) 969–974.
[28] F.F. Lavrentev, The type of dislocation interaction as the factor determining work hardening, Mater. Sci. Eng. 46 (1980) 191–208.
[29] G.I. Taylor, The mechanism of plastic deformation of crystals part I - Theoretical, Proc. R. Soc. London, Ser. A 145 (855) (1934) 362–387.
[30] G.I. Taylor, The mechanism of plastic deformation of crystals part II - comparison with observations, Proc. R. Soc. London, Ser. A 145 (855) (1934) 388–404.
[31] A. Deschamps, M. Militzer, J. Poole, Precipitation kinetics and strengthening of a Fe–0.8wt%Cu alloy, ISIJ Int. 41 (2) (2001) 196–205.
[32] R.D. Doherty, Diffusive phase transformation in the solid state, in: R.W. Cahn, P. Haasen (Eds.), Physical Metallurgy, North-Holland, 1996.
[33] Smithells Metals Reference Book, 8 ed., Elsevier, 2004.
[34] T. Toyama, F. Takahama, A. Kuramoto, H. Takamizawa, Y. Nozawa, N. Ebisawa, M. Shimodaira, Y. Shimizu, K. Inoue, Y. Nagai, The diffusivity and solubility of copper in ferromagnetic iron at lower temperatures studied by atom probe tomography, Scripta Mater. 83 (2014) 5–8.
[35] M. Shimodaira, T. Toyama, F. Takahama, N. Ebisawa, Y. Nozawa, Y. Shimizu, K. Inoue, Y. Nagai, Diffusivity and solubility of Cu in a reactor pressure vessel steel studied by atom probe tomography, Mater. Trans. 56 (9) (2015) 1513–1516.
[36] L. Messina, M. Nastar, N. Sandberg, P. Olsson, Systematic electronic-structure investigation of substitutional impurity diffusion and flux coupling in bcc iron, Phys. Rev. B 93 (18) (2016) 184302.

Paper IV

Thermal ageing of low alloy steel weldments from a Swedish nuclear power plant - the evolution of the microstructure

K. Lindgren, M. Boåsen, K. Stiller, P. Efsing, and M. Thuvander

Proceedings Fontevraud 9: Contribution of Materials Investigations and Operating Experience to Light Water NPPs Safety, Performance and Reliability (2018)

Thermal ageing of low alloy steel weldments from a Swedish nuclear power plant – the evolution of the microstructure

Kristina Lindgren[1*], Magnus Boåsen[2], Krystyna Stiller[1], Pål Efsing[2,3], Mattias Thuvander[1]

[1] Department of Physics, Chalmers University of Technology, SE-412 96 Göteborg, Sweden
[2] Department of Solid Mechanics, Royal Institute of Technology (KTH), SE-100 44 Stockholm, Sweden
[3] Ringhals AB, SE-430 22 Väröbacka, Sweden

[*] Main Author, E-mail: kristina.lindgren@chalmers.se

Keywords: thermal ageing, clustering, atom probe tomography, pressurizer

Introduction

Cu-clusters formed during irradiation of reactor pressure vessels (RPVs) are known to affect the mechanical properties, by increasing the ductile-to-brittle transition temperature, making it embritteled [1-5]. It is also well known that clusters form during thermal ageing in the same type of materials, but at higher temperatures than common operation temperatures of pressurized water reactors (PWRs) [6-9]. In most cases, the welds of the pressurizer of a PWR are very similar to the welds of RPVs; in the case of Ringhals R4 the welding parameters, as well as the welding wires and powders used in the submerged arc welding process, are in essence identical. However, the pressurizer is not subjected to irradiation but only to heat, the highest temperature of the primary circuit, 345°C.

The nature of these clusters is slightly different from the ones in the irradiated material, partly due to the fact that they are formed by different atomic scale processes. Neutrons bombarding the materials during irradiation will create cascades of atoms being knocked out from their positions, creating vacancies and interstitials that might either recombine or contribute to changes in the microstructure, and the cluster formation. Solute atoms are dragged by the vacancies formed, and some of them (Mn and P) are also dragged by the interstitials [10, 11]. In thermally aged materials, Cu-clusters are formed due to the low Cu solubility in α-Fe, and the formation is controlled by diffusion. In this paper, the term cluster is used, and no distinction is made between clusters and precipitates, as their crystallographic nature is unknown.

The paper with the title *Thermal ageing of low alloy steel weldments from a Swedish nuclear power plant – a study of mechanical properties* in the same proceedings by Boåsen et al. [12] discusses the mechanical properties of a similar, thermally aged, weld from the same pressurizer. However, in this paper, the clusters formed in the pressurizer weld and in irradiated surveillance material found by atom probe tomography (APT) is shown, side by side, to clearly show the differences and similarities emerging from the difference in the mechanisms of formation.

Materials and Methods

The pressurizer, from which the analysed weld comes from, was in operation for around 28 years at 345°C in Ringhals R4 [6], whereas the surveillance material weld was exposed to 4.6 10^{23} n/m^2 (E > 1.0 MeV) with a flux of 0.15 10^{16} n/(m^{2}s) at a temperature of 289°C in Ringhals R4 [1, 13-16]. This flux corresponds to a lead factor of approximately three. The aged welds are compared to a reference archive material from a unit at Forsmark power plant, manufactured according to the same specifications. All welds were subjected to a standard post weld heat treatment at 620°C. The composition, as measured by APT, can be seen in Table 1 (partly from [6]). The uncertainty given in the table is the standard deviation between the different analyses of the materials (at least four), as the local compositions are different due to the normal inhomogeneity of welds. It can be seen that the surveillance material has a lower alloying content in general, but it is still high (for a RPV steel) in both Ni and Mn. The Cu contents ranges from low, 0.03% for the surveillance material, to medium, 0.10% for the pressurizer.

	Reference (at. %)	Pressurizer (at. %)	Surveillance (at. %)
C	0.04 ± 0.01	0.04 ± 0.03	0.02 ± 0.01
Mo	0.19 ± 0.02	0.19 ± 0.05	0.19 ± 0.06
Si	0.31 ± 0.07	0.30 ± 0.02	0.24 ± 0.04
P	0.01 ± 0.01	0.01 ± 0.01	0.02 ± 0.01
V	0.0030 ± 0.0026	0.0012 ± 0.0007	0.0023 ± 0.0031
Mn	1.35 ± 0.05	1.24 ± 0.12	1.19 ± 0.07
Cr	0.03 ± 0.01	0.06 ± 0.01	0.17 ± 0.04
Co	0.02 ± 0.01	0.02 ± 0.01	0.01 ± 0.01
Cu	0.07 ± 0.02	0.10 ± 0.02	0.03 ± 0.01
Ni	1.77 ± 0.33	1.68 ± 0.28	1.47 ± 0.23
Fe	bal.	bal.	bal.

Table 1: **Composition from APT analyses, including the error that is the standard deviations between the multiple analyses for each material.**

The pressurizer and the reference material specimens were prepared using a two-step electropolishing technique [17] with final millisecond pulsing to get rid of surface oxides. The surveillance material, as it was active, was prepared using a standard focused ion beam scanning electron microscope (FIB/SEM) lift out technique, finished with annular milling [18, 19] in a FEI Versa 3D instrument.

The material was analysed using a LEAP 3000X HR (Imago Scientific Instruments), equipped with a reflectron. The detection efficiency of the instrument is 37%. Both voltage and laser modes were used in order to get both high spatial resolution of Si (and other elements [20]) and long runs without premature fracturing. In voltage pulsing mode, the temperature was 60-70 K and the pulse fraction 20%. In laser pulsing mode, the temperature was 30 K and the laser energy 0.30 nJ. In both cases, the pulse frequency was 200 kHz.

The IVAS^{TM} 3.6 software was used for reconstructing the atom probe data. Reconstruction parameters were chosen so that features did not have an artificial elongation in any direction. The clusters were identified using the maximum separation method [21, 22] with Cu, Ni (excluding the peak at mass to charge state ratio 29 Da due to the $^{58}Ni^{2+}/^{58}Fe^{2+}$ overlap) and Mn atoms, a d_{max}=L=e of 0.5 nm and N_{min} 18 atoms. For cluster compositions, the 29-peak was decomposed according to the natural isotopic abundance. For cluster sizes, the Fe ions were excluded and the size of the clusters calculated from the number of Ni, Mn, Si and Cu atoms, as most of the Fe is expected to come from local magnification effects due to the different evaporation fields of the clusters and the matrix [23, 24]. The different evaporation fields of the clusters and the matrix result in a higher atomic density inside the clusters, observed in the analyses.

Results and discussion

Using APT, Cu-rich clusters were found in the thermally aged pressurizer material, mainly in connection with dislocation lines, see Figure 1. The number density was found to be 0.16±0.05 10^{23} clusters/m^3 [6]. In APT data, dislocation lines can only be observed if there is a presence of segregation of solute elements, in this case mostly Mo and C (or if there are closely spaced clusters delineating the dislocation). As the clusters are mainly found on dislocations, their distribution is obviously inhomogeneous. A cluster that was cut out from this analysis is shown in Figure 2, clearly showing how the cluster sits on the dislocation. It appears as if the cluster is rather sitting next to the dislocation than being located at the dislocation core, although this observation is not certain, as there could be effects making the Mo atoms artificially displaced from the dislocation core.

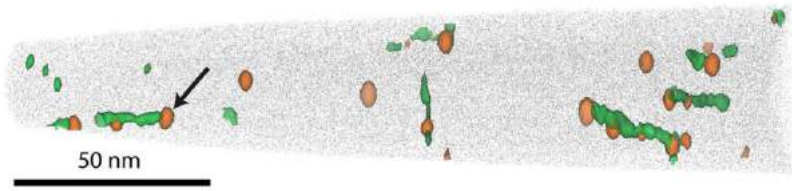

Figure 1: **Clusters on Mo-enriched dislocations in the thermally aged material. Orange correspond to Cu (1.0 at.%) isoconcentration surfaces and green to Mo (1.4 at.%). Grey shows the extent of the analysis and the arrow indicates the cluster shown in Figures 2, 5 and 6.**

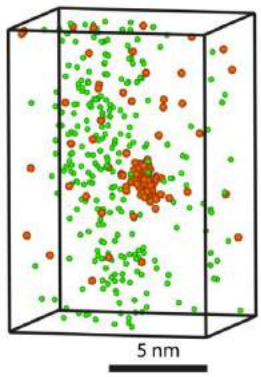

Figure 2: **A single Cu-rich cluster (orange) sitting on a Mo-enriched dislocation (green). Other clustering elements are left out for clarity. The box is 10x10x20 nm^3.**

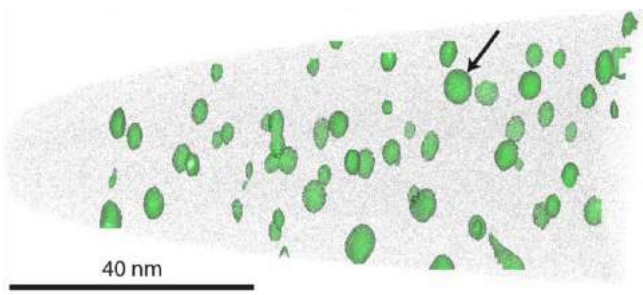

Figure 3: **Clusters in the irradiated surveillance material weld. Green corresponds to Ni 7.7 at.% isoconcentration surfaces. Grey shows the extent of the analysis and the arrow indicates the cluster shown in Figures 5 and 6.**

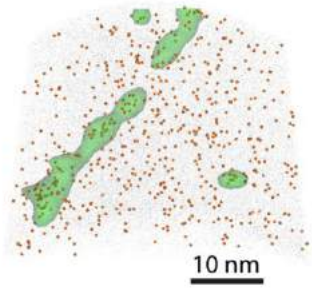

Figure 4: **Dislocation decorated with clusters in the irradiated surveillance weld. Green corresponds to Ni 7.7 at.% isoconcentration surfaces and orange to individual Cu atoms. Grey shows the extent of the analysis.**

In Figure 3, a reconstruction of the irradiated material can be seen. A high number density of clusters ($3.1\pm0.9\ 10^{23}$ clusters/m^3 [1]) containing Ni, Mn, Si and Cu is found in the matrix, in this figure shown as Ni isoconcentration surfaces. In some cases, dislocation lines with clusters on them are found as well, see Figure 4. In this case, the clusters are growing into each other on the dislocation, unlike the case of the pressurizer where the clusters are clearly separated. In the reference material, no clusters were found in the matrix or on dislocations. Thus, the cluster formation is driven by the temperature of the pressurizer and the irradiation (and to a less extent of temperature) of the surveillance material.

In Figures 1 and 3, two clusters are marked with arrows. These clusters are further shown in Figures 5 and 6, including all Ni, Mn, Si and Cu atoms detected. There is plenty of Ni, Mn, and Si left in the matrix in both cases. In Figures 5 a) and c), the full clusters are shown. In Figures 5 b) and d), the clusters are cut in half (approximately). This exposes the Cu-rich core of the clusters formed in the thermally aged weld. In the irradiated material, the few Cu atoms are distributed evenly within the cluster.

In Figure 6, the same cluster can be seen, with one element showed at the time. Again, it is possible to see the Cu-rich core of the thermally aged pressurizer. Furthermore, we can see that the amount of Si in the irradiated material cluster is higher than in the thermally aged material.

Compositional profiles are shown in Figure 7. The Cu-rich core with a Ni and Mn shell can be seen for the pressurizer clusters. For this profile, Ni and Mn are chosen as clustering elements together with Cu. It is also possible to use only Cu as a clustering element, resulting in even more clear core-shell structures, as the Cu atoms would then always be defined as the central part of the clusters. There is a small increase in the Si content inside the clusters compared to the matrix. The amount of Ni and Mn in this shell appears to be similar. In the surveillance material, the amount of Ni is larger than the amount of Mn. The cluster Cu content is very low in comparison to the thermally aged material.

The cluster Ni, Mn, Si and Cu content is also shown cluster by cluster in Figure 8. Most clusters of each material have similar composition. There are small clusters in the surveillance material that do not contain any Cu atoms at all. Clusters on dislocations in the surveillance material (such as those in Figure 4) were checked separately and were found to have the same composition as the clusters in the bulk, with the exception of small levels of segregation of other elements to the dislocation such as P and Mo. As the segregation of elements to the dislocations in the pressurizer was found to vary in terms of Mo (5 to 30 excess atoms per nm), C (5 to 30 atoms per nm), and P (0.4 to 1.4 atom per nm) [6], the low number of dislocations makes it impossible to tell the exact difference between the dislocations for the thermally aged and irradiated material. However, in the examples of dislocations in the surveillance material, more P was found (around 18 atoms per nm in the dislocation seen in Figure 4). Segregation of P to clusters was investigated, and it was found that the clusters sitting on dislocations in the surveillance material were clearly containing more P than the matrix clusters in the surveillance material. In the pressurizer, the P enrichment was less, only occasional P atoms were found in the clusters.

In the surveillance material, there seems to be a trend for larger clusters to contain more Ni. Trends such as these found in atom probe data need to be carefully treated, as cluster analysis of nanometre

sized clusters or precipitates is very dependent on clustering parameters. However, it is less likely to be an artefact as Ni is included as a clustering element in the maximum separation cluster analysis.

In Figure 9, the cluster size distributions are given. The clusters are in the same size range for both materials, from the cut-off due to the definition of clusters at 1 nm to the largest clusters with a diameter of 5 nm. The lower number of clusters in the pressurizer gives poorer statistics for this material, and hence no conclusions can be made on the shape of the distribution.

The low Cu cluster content of the surveillance material could partly be due to the lower amount of Cu in the material (see Table 1). However, the difference is significant, and other studies also found thermally aged clusters containing more Cu than those formed in irradiated materials [4, 8]. In high flux irradiated material of similar composition, the Cu content of the clusters was higher, and Cu-rich cores or parts of some of the clusters were observed [1]. Thus, the core-shell structure might appear after irradiation as well as after thermal ageing.

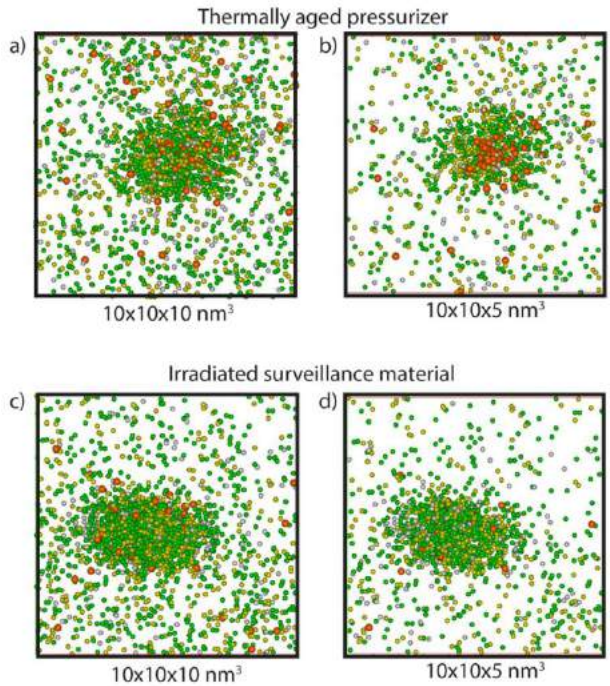

Figure 5: **a) a thermally aged cluster. b) the same cluster, cut in half to expose the Cu-rich core. c) a cluster of similar size from the surveillance material. d) the surveillance cluster cut in half. Ni atoms are green, Mn atoms yellow, Si atoms grey, and Cu atoms are orange.**

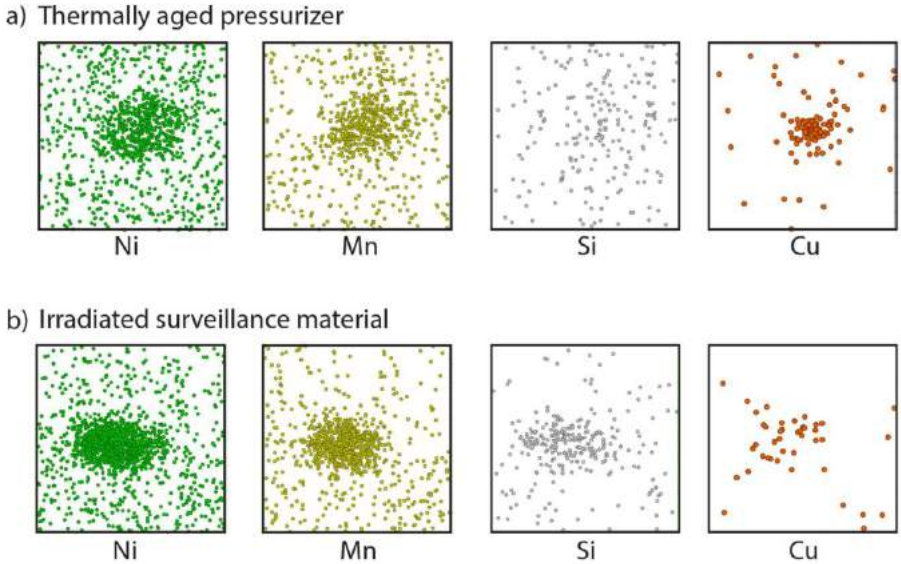

Figure 6: **The same clusters as in Figure 5, shown separately for the clustering elements. The side of the box is 10 nm.**

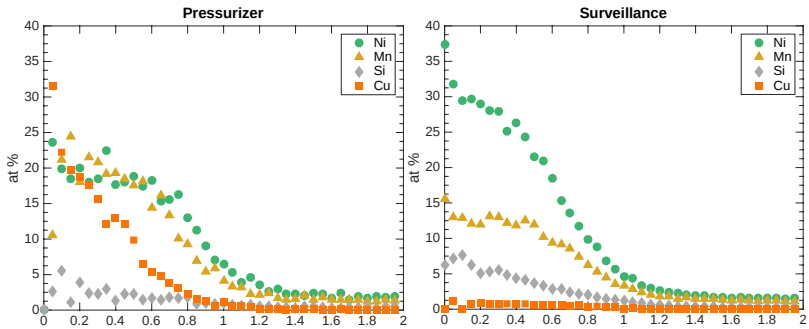

Figure 7: **Cu-rich cluster radial composition profile. The cluster profiles are normalised, 1 corresponds to the surface of the clusters, and 0 to the cluster centre.**

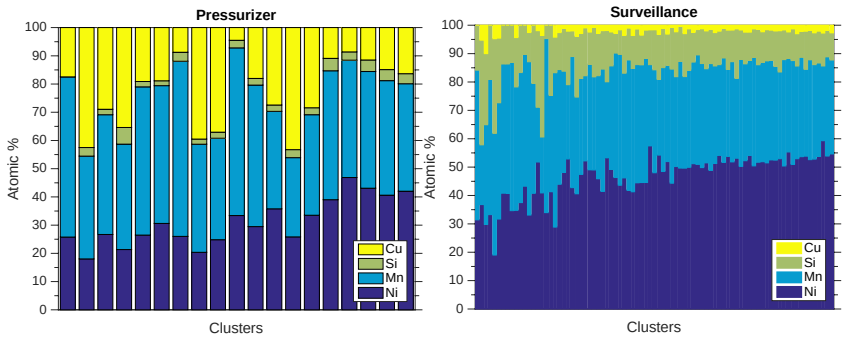

Figure 8: **A number of cluster compositions, Fe omitted, for the pressurizer and the surveillance material. Sorted from small clusters (left in figures) to large clusters (right).**

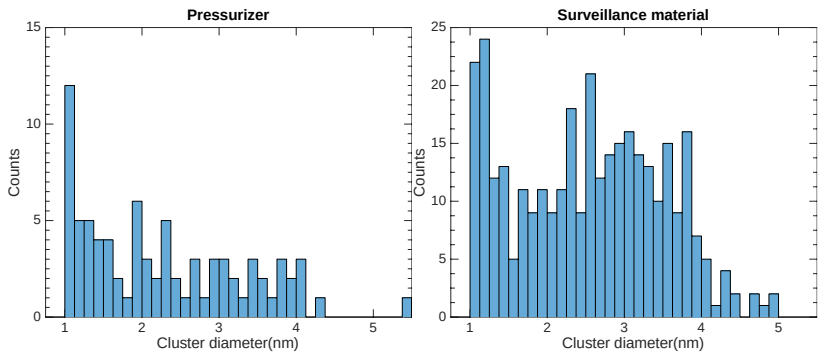

Figure 9: **The cluster size distribution of the pressurizer and the surveillance material clusters, when Fe is not considered part of clusters.**

Occasional larger carbides were also found, as well as V-rich nanometre sized precipitates, containing N, C and sometimes Cr were found in all materials [1, 6]. As they were found in both aged and reference materials, they are believed to not be affected by the thermal ageing or irradiation, and thus not contribute to any change in mechanical properties. However, they might act as points of nucleation for clusters containing Ni, Mn, Si, and Cu, as they were in some cases found in connection with the clusters.

The hardness (HV10) was measured for all three materials, and was found to be 203±2 for the reference material, 235±7 for the pressurizer, and 292±14 for the irradiated surveillance material [1, 6, 16]. The reasons of the difference between the hardness values reported here and in [12] are unknown, but different reference materials were used. The hardness of the reference reported here is close to other, very similar reference materials [16]. Thus, as opposed to some other results [25], the thermal ageing gives an increased hardness that cannot be due to phosphorous segregation to grain boundaries that gives a non-hardening contribution to the embrittlement.

Conclusion

APT was used in order to characterise Cu-rich clusters in a thermally aged pressurizer and an irradiated surveillance material. As expected, the cluster characteristics were slightly different. It was found that:

- During both thermal ageing at 345°C and irradiation clusters containing Ni, Mn, Si and Cu formed.

- The thermally aged clusters were mainly sitting on dislocation, whereas the irradiated clusters were found also in the matrix. The sizes of the clusters are similar, although the clusters on dislocations in the irradiated material tend to grow into each other whereas the thermally aged material has well separated clusters. The number density of clusters in the irradiated material is one order of magnitude larger than for the thermally aged pressurizer.

- The thermally aged clusters contain more Cu. The clusters contain a Cu-rich core surrounded by Ni and Mn, and a little bit of Si. The clusters of the irradiated material contain less Cu and Si. The clusters in the irradiated material do not seem to have a clear core-shell structure. However, this might be due to local variations and the Cu levels being very low in the surveillance material.

- The clusters do contribute to an increased hardness in both the thermally aged and irradiated materials.

Acknowledgment

Ringhals and Forsmark are acknowledged for providing material, and SKC (the Swedish Centre for Nuclear Technology) for funding this research. Furthermore, Chalmers Forskningsstiftelse is acknowledged for funding the conference attendance of the first author.

References

[1] K. Lindgren, M. Boåsen, K. Stiller, P. Efsing, M. Thuvander, Evolution of precipitation in reactor pressure vessel steel welds under neutron irradiation, Journal of Nuclear Materials 488 (2017) 222-230.
[2] G.R. Odette, G.E. Lucas, Recent progress in understanding reactor pressure vessel steel embrittlement, Radiation Effects and Defects in Solids 144(1-4) (1998) 189-231.
[3] P. Pareige, B. Radiguet, A. Suvorov, M. Kozodaev, E. Krasikov, O. Zabusov, J.P. Massoud, Three-dimensional atom probe study of irradiated, annealed and re-irradiated VVER 440 weld metals, Surface and Interface Analysis 36(56) (2004) 581-584.
[4] M.K. Miller, K.F. Russell, Embrittlement of RPV steels: An atom probe tomography perspective, Journal of Nuclear Materials 371(1-3) (2007) 145-160.
[5] E. Meslin, M. Lambrecht, M. Hernández-Mayoral, F. Bergner, L. Malerba, P. Pareige, B. Radiguet, A. Barbu, D. Gómez-Briceño, A. Ulbricht, A. Almazouzi, Characterization of neutron-irradiated ferritic model alloys and a RPV steel from combined APT, SANS, TEM and PAS analyses, Journal of Nuclear Materials 406(1) (2010) 73-83.
[6] K. Lindgren, M. Boåsen, K. Stiller, P. Efsing, M. Thuvander, Cluster formation in in-service thermally aged pressurizer welds, Journal of Nuclear Materials 504 (2018) 23-28.
[7] P.D. Styman, J.M. Hyde, K. Wilford, A. Morley, G.D.W. Smith, Precipitation in long term thermally aged high copper, high nickel model RPV steel welds, Progress in Nuclear Energy 57 (2012) 86-92.
[8] J.M. Hyde, G. Sha, E.A. Marquis, A. Morley, K.B. Wilford, T.J. Williams, A comparison of the structure of solute clusters formed during thermal ageing and irradiation, Ultramicroscopy 111(6) (2011) 664-71.
[9] M. Kolluri, A. Kryukov, A.J. Magielsen, P. Hähner, V. Petrosyan, G. Sevikyan, Z. Szaraz, Mechanical properties and microstructure of long term thermal aged WWER 440 RPV steel, Journal of Nuclear Materials 486 (2017) 138-147.
[10] L. Messina, M. Nastar, T. Garnier, C. Domain, P. Olsson, Exact ab initio transport coefficients in bcc Fe–X(X=Cr,Cu,Mn,Ni,P,Si) dilute alloys, Physical Review B 90(10) (2014).
[11] L. Messina, Multiscale modeling of atomic transport phenomena in ferritic steels, Reaktorfysik, Royal Institute of Technology (KTH), Stockholm, 2015.
[12] M. Boåsen, K. Lindgren, J. Roudén, M. Öberg, J. Faleskog, M. Thuvander, P. Efsing, Thermal ageing of low alloy steel weldments from a Swedish nuclear power plant – a study of mechanical properties, Fontevraud, Avignon, 2018.
[13] P.D. Styman, J.M. Hyde, D. Parfitt, K. Wilford, M.G. Burke, C.A. English, P. Efsing, Post-irradiation annealing of Ni–Mn–Si-enriched clusters in a neutron-irradiated RPV steel weld using Atom Probe Tomography, Journal of Nuclear Materials 459 (2015) 127-134.
[14] M.K. Miller, K.A. Powers, R.K. Nanstad, P. Efsing, Atom probe tomography characterizations of high nickel,

low copper surveillance RPV welds irradiated to high fluences, Journal of Nuclear Materials 437(1-3) (2013) 107-115.
[15] P. Efsing, C. Jansson, T. Mager, G. Embring, Analysis of the Ductile-to-Brittle Transition Temperature Shift in a Commercial Power Plant With High Nickel Containing Weld Material, Journal of ASTM International 4(7) (2007).
[16] M. Boåsen, P. Efsing, U. Ehrnstén, On flux effects in a low alloy steel from a Swedish reactor pressure vessel, Journal of Nuclear Materials 484 (2017) 110-119.
[17] B. Gault, M.P. Moody, J.M. Cairney, S.P. Ringer, Atom Probe Microscopy, Springer, New York, 2012.
[18] D.J. Larson, D.T. Foord, A.K. Petford-Long, H. Liew, M.G. Blamire, A. Cerezo, G.D.W. Smith, Field-ion specimen preparation using focused ion-beam milling, Ultramicroscopy 79(1-4) (1999) 287-293.
[19] K. Thompson, D. Lawrence, D.J. Larson, J.D. Olson, T.F. Kelly, B. Gorman, In situ site-specific specimen preparation for atom probe tomography, Ultramicroscopy 107(2-3) (2007) 131-9.
[20] K. Lindgren, K. Stiller, P. Efsing, M. Thuvander, On the Analysis of Clustering in an Irradiated Low Alloy Reactor Pressure Vessel Steel Weld, Microsc Microanal 23(2) (2017) 376-384.
[21] J.M. Hyde, C.A. English, An Analysis of the Structure of Irradiation induced Cu-enriched Clusters in Low and High Nickel Welds, Materials Research Society Symposium, Boston, 2000, pp. R6.6.1-R6.6.12.
[22] D. Vaumousse, A. Cerezo, P.J. Warren, A procedure for quantification of precipitate microstructures from three-dimensional atom probe data, Ultramicroscopy 95 (2003) 215-221.
[23] P.D. Edmondson, C.M. Parish, R.K. Nanstad, Using complimentary microscopy methods to examine Ni-Mn-Si-precipitates in highly-irradiated reactor pressure vessel steels, Acta Materialia 134 (2017) 31-39.
[24] E.A. Marquis, J.M. Hyde, Applications of atom-probe tomography to the characterisation of solute behaviours, Materials Science and Engineering: R: Reports 69(4-5) (2010) 37-62.
[25] H. Nakata, K. Fujii, K. Fukuya, R. Kasada, A. Kimura, Grain Boundary Phosphorus Segregation in Thermally Aged Low Alloy Steels, Journal of Nuclear Science and Technology 43(7) (2006) 785-793.

Paper V

Post irradiation annealing of high flux irradiated reactor pressure vessel weld

K. Lindgren, M. Boåsen, P. Efsing, K. Stiller, and M. Thuvander

In manuscript

Post-Irradiation Annealing of High Flux Irradiated Reactor Pressure Vessel Welds

Kristina Lindgren*, Magnus Boåsen**, Ulla Ehrnstén***, Krystyna Stiller*, Pål Efsing**,****, Mattias Thuvander*

Corresponding author: kristina.lindgren@chalmers.se, phone: +46 31 772 3337

* Department of Physics, Chalmers University of Technology, SE-412 96 Göteborg, Sweden
** Department of Solid Mechanics, Royal Institute of Technology (KTH), SE-100 44 Stockholm, Sweden
*** VTT Technical Research Centre of Finland Ltd, FI-02044 Espoo, Finland
**** Vattenfall Ringhals AB, SE-430 22 Väröbacka, Sweden

Abstract

In this study, high flux irradiated high Ni and Mn and low Cu welds identical to those in the belt-line region of Ringhals R4 were subjected to annealing at 390, 405, 420 and 450°C for 24-30 h, in order to study the characteristics of the clusters and possibly matrix defect dissolution using hardness testing and atom probe tomography. It was found that the cluster characteristics did not change during annealing at 390°C. Thus, the change in hardness during annealing is believed to be due to dissolution of matrix defects that are stable at the operating temperature (325°C). Cluster dissolution was observed at temperatures from 405°C, leaving around 10% of the original clusters, containing more Cu and less Ni and Mn than before annealing. Dissolution of the clusters follows a trend where the volume fraction decreases at annealing from 405°C to 450°C, where only a couple of clusters were observed.

Keywords: atom probe tomography, high flux, irradiation hardening, embrittlement, post irradiation annealing, clusters, matrix defects

1. Introduction

During operation of a nuclear power plant, the reactor pressure vessel (RPV) is embrittled due to microstructural changes that are driven by neutron irradiation. The neutrons interact with the atom nuclei of the material, creating vacancies and interstitials. Most of them recombine quickly, but some remain and subsequently cause the formation of nanometre sized clusters containing Cu, Ni, Mn, and Si [1], which can be characterised using atom probe tomography (APT) [2-7]. These clusters hinder dislocation movement, causing a hardening, and thereby contribute to the embrittlement of the material. The welds of the belt line region get the highest exposure to neutron irradiation and are hence most prone to cluster formation. As the RPV is considered to be a non-replaceable component, and thus possibly a life limiting

component of a nuclear reactor, it is vital to understand the long-term effects of operation on the RPV. It is also the most important component for the safety of a nuclear power plant.

Usually, a number of capsules containing surveillance material, manufactured to the same specifications as the RPV itself, is put inside the RPV. This enables the removal of a capsule after some time to investigate any changes in the surveillance material, which has then been exposed to higher fluence than the RPV itself due to a shorter distance to the reactor core. Thus, it gives a prediction of what will happen in the future to the RPV, assuming a low dependency of neutron flux on the microstructure development and the mechanical properties. The lead factor of surveillance materials is usually around 2-5, i. e. the same fluence is achieved 2-5 times faster than in the RPV. Another way to simulate the degradation of the RPV is to use a materials test reactor (MTR). In these cases, a significantly higher flux is usually used to reach the same dose level, as this decreases the time needed for exposure to something that is practically achievable and gives the opportunity to start new ageing experiments long after the commissioning of the reactor. In these cases, of course, the lead factors are much higher. The need for justifying that these high fluxes affect the materials in the same way is crucial if the data are to be used for safety assessments. High flux irradiation to a similar fluence is known to give smaller clusters with a higher number density than surveillance material, although in many cases resulting in a similar degree of embrittlement after the same fluence [2, 4, 8, 9].

In addition to clustering of Ni, Mn, Si and Cu, matrix defects are known to form during irradiation of RPV welds and contribute to the hardening [10, 11]. Matrix defects are divided into stable matrix defects and unstable matrix defects, depending on their stability at reactor relevant temperatures. Unstable matrix defects are believed to both form and disappear at reactor relevant temperatures, and thus their contribution to the hardening is expected to be larger at high flux neutron irradiation. Matrix defects consists of vacancies, small clusters of vacancies, interstitials, combinations thereof, and possibly carbo-nitrides and phosphides [11]. Due to their small size, direct measurement of these features is difficult, and in many cases modelling or indirect measurements are used for their characterisation. Combining hardness measurements with post-irradiation annealing (PIA) is one way to approach this issue, and to simultaneously use characterisation techniques such as APT and small angle neutron scattering (SANS) to track changes in the clusters containing Ni, Mn, Si and Cu, also affecting the mechanical properties. PIA is also used to study the stability and dissolution of clusters, in order to further understand the cluster properties, and in some cases to regain mechanical properties by eliminating the clusters [12-14].

Ringhals R4 RPV weld metal has been exposed to high flux irradiation, and subsequently been subjected to hardness and impact toughness testing as well as APT analysis [2, 15]. The results of the mechanical testing of the high flux and the surveillance irradiated welds indicate that the hardening develops similarly in both cases, i. e. along a similar trend line with respect to irradiation dose.

The APT results revealed that the higher flux results in a higher number density of smaller clusters containing Ni, Mn, Si and Cu, contributing to the same increase in hardness as the lower flux (surveillance) irradiation. Furthermore, the same high flux

irradiated welds and surveillance irradiated welds were annealed at 330, 360 and 390°C, and hardness was measured with intervals of one hour, in order to study the presence of unstable matrix defects by Boåsen et al. [16]. Annealing at 330°C and 360°C did not affect the hardness of any of the materials. In the high flux material and after annealing at 390°C, a decrease in hardness was found that was not observed in the surveillance material. The different behaviours of the materials were speculatively attributed to the different cluster characteristics, assuming the dissolution of small clusters in the high flux material.

In this paper, the high flux irradiated Ringhals weld metal annealed at 390°C is analysed using APT to study the cluster characteristics. Furthermore, the annealing study of the high flux Ringhals R4 weld is continued at higher temperatures (405°C, 420°C and 450°C), and the cluster dissolution is studied.

2. Methods and materials

The weld metals studied were irradiated in high flux ($3.8\ 10^{16}$ n/(m^{2}s), corresponding to a lead factor of around 40) to a fluence of $6.4\ 10^{23}$ n/m^2 in Halden OECD MTR (Norway) [2, 15, 16]. The nominal composition, as well as the composition from APT, is given in Table 1. The contents of the alloying elements were found to vary between the APT analyses, as expected for welds, which often show inhomogeneity. Ni was found to vary significantly, the Cu content was found to be higher than the nominal composition, while the content of Mn was measured to be lower. Most of the other elements match the nominal composition well. No significant difference was found between laser and voltage pulsed analyses, more than that the Cr content was slightly lower in all laser pulsed analyses. The C content of the material is expected to be lower in the APT analyses as the nominal content also includes occasional sparsely distributed large carbides that are not analysed in this paper. The quantification of the small expected Al content is not included, since there is only one naturally occurring Al isotope, ^{27}Al, that overlaps with both $^{54}Fe^{2+}$ and $^{54}Cr^{2+}$. Sulphur is overlapping with oxygen and is not considered in the overall composition either.

Table 1. Chemical composition of the RPV weld in atomic%, nominal [17] and experimentally found by APT, including standard deviations of the different analyses.

at.%	Cu	Ni	Mn	Mo	Si	C	P	S	Cr	Al	Co	V
Nom.	0.04	1.58	1.37	0.29	0.28	0.31	0.027	0.007	0.04	0.05	0.01	-
APT	0.08 ± 0.01	1.50 ± 0.19	1.12 ± 0.09	0.18 ± 0.09	0.24 ± 0.06	0.07 ± 0.06	0.01 ± 0.01	-	0.14 ±0.08	-	0.02 ± 0.01	0.002 ± 0.001

Procedures of the annealing at 390°C are described elsewhere [16]. Annealing at 405°C, 420°C, and 450°C was performed in nitrogen atmosphere in a tube furnace. The temperature was found to vary from the desired value with about ± 5°C, that leaves the temperature of the different annealing experiments well separated. In Table 2, the specimens are listed. The annealing time of the H6.4-390 material is 30 h, whereas the other materials were annealed for 24 h.

Table 2. The specimens including annealing conditions. The designation "H6.4" refers to Halden and the fluence of 6.4 10^{23} n/m², as in previous investigations [2, 16], and the number to the annealing temperature .

Name	Annealing temperature (°C)	Annealing time (h)
H6.4	-	0
H6.4-390	390	30
H6.4-405	405	24
H6.4-420	420	24
H6.4-450	450	24

Specimen preparation for APT analysis was performed using a standard focused ion beam/scanning electron microscopy (FIB/SEM) lift-out technique, annular milling, and a final low-voltage mill to get rid of most ion damage and implantation [18, 19]. An FEI Versa 3D was used for this purpose.

An Imago LEAP 3000X HR was used for the APT analysis of the materials. The instrument has a detection efficiency of 37%. In addition to voltage pulsing (with high spatial resolution and giving good analysis of the Si and P distributions [20]), laser pulsing was used in order to obtain larger analysis volumes before specimen fracture of the specimen. The analysis parameters were 60-70 K, 20% pulse fraction and 0.2% target evaporation rate for voltage pulsed analyses. Laser pulsing was done with a pulse energy of 0.30 nJ, temperature of 30 K and a target evaporation rate of 0.5-1.0%. In both cases the pulse frequency was 200 kHz. The APT data reconstruction was done in the IVAS 3.6 software from Cameca.

Cluster analysis was performed using the maximum separation method (MSM) [21, 22], where the 29 Da peak was excluded due to the $^{58}Ni^{2+}/^{58}Fe^{2+}$ overlap in accordance with [20]. After cluster identification, the 29 Da peak was decomposed and the Ni fraction was included in the cluster content. Cluster parameters and solute elements for the MSM were chosen differently dependent on the composition of the clusters, in order to avoid random matrix features being classified as clusters. In the H6.4 and H6.4-390 materials, the clusters were defined by Ni (29 Da excluded) and Mn as solute elements, d_{max} = 0.50 nm and N_{min} = 18. In the H6.4-405, H6.4-420 and H6.4-450 materials these parameters often identified random variations in the matrix as clusters, due to the low cluster Ni and Mn content. Hence, Cu was used as solute element for cluster identification for these materials, with d_{max} = 1.0 nm and N_{min} = 8. In all cases, the MSM parameters envelope distance and erosion distance were chosen equal to d_{max}. In order to visualize clusters and dislocations, iso-concentration surfaces (isosurfaces) were used. These were constructed using a voxel size of 1.0 nm³, with delocalization of 1.5×1.5×3.0 nm³.

APT analysis of the clusters in RPV steels is known to give cluster Fe contents that are higher than expected, and higher than what has been found using complimentary techniques such as transmission electron microscopy (TEM) and SANS [23-25]. In most clusters analysed in this paper, at least 50% of all atoms are identified as Fe. When cluster sizes and compositions are given, it is here assumed that Fe appearing in the clusters originates from local magnification effects [26]. This is supported by the unphysically high atomic density within the clusters in the APT reconstructions, which is caused by the low evaporation field of the clusters. Hence, the cluster sizes were calculated from the number of Cu, Ni, Mn and Si atoms detected in the clusters, together

with the detection efficiency, and assuming matrix coherent clusters (thus, the volume per cluster atom is assumed to be equal to the volume per atom in Fe).

Cluster number densities were determined by counting the number of clusters in each analysis, whereby clusters cutting the edge of the analysis were counted as one half.

3. Results

3.1 General microstructure

A reconstruction of a laser pulsed APT analysis of material H6.4-390 can be seen in Figure 1. There is a high number density of evenly distributed Ni-Mn-Si-clusters visualised with Ni isosurfaces within the entire reconstructed volume. A Mo-enriched dislocation, visualised with a red isosurface, is marked in the figure. On the dislocation, there are clusters sitting, with the same composition as the clusters in the matrix. In addition to Mo, the dislocation is also enriched in C and P (although this is a laser pulsed analysis, and thus the P is expected to diffuse on the surface prior to evaporation, there is still a clear P segregation to the dislocation). Further down in the reconstruction, two more dislocations are cutting the edge of the analysis. The H6.4-390 material appears to be identical to the non-annealed H6.4 material, in terms of cluster characteristics.

In Figure 2, a reconstruction of similar size as the one in Figure 1 is shown, for material H6.4-405. There is an obvious difference between this material and H6.4-390. Here, the number density of clusters is considerably lower and the distribution of clusters is uneven, leaving an empty volume in the middle of the reconstruction. The clusters that are left consist mainly of Cu instead of Ni and Mn, and are therefore visualised using Cu isosurfaces. Many of the clusters are situated on dislocations, whereas some clusters appear to be in the matrix. Some of these matrix clusters are close to the edge of the analysis, while some are close to the centre. It is impossible to tell whether also these clusters are located on dislocations, as it is possible that not all dislocations contain segregants, such as Mo and C. APT does usually not give sufficient crystallographic information to identify dislocations unless they are decorated with segregating species.

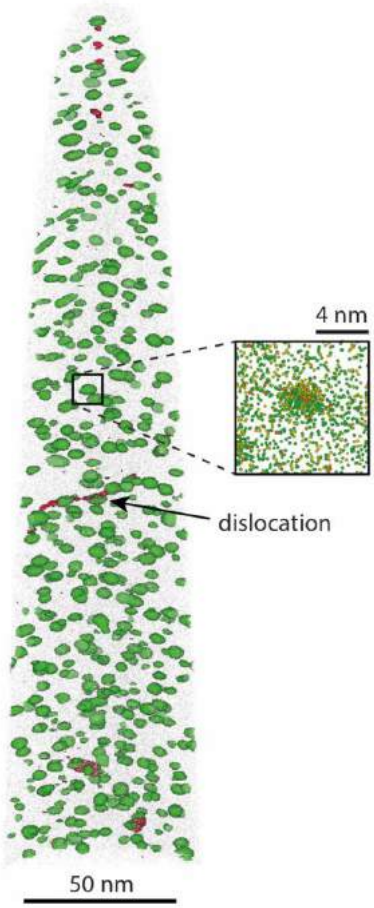

Figure 1. Material H6.4-390. Green isosurfaces correspond to 5% Ni and red isosurfaces to 1.5% Mo. Grey shows the extent of the analysis. Cluster cut out: 10×10×10 nm³ box, green dots are Ni atoms, yellow are Mn and orange are Cu.

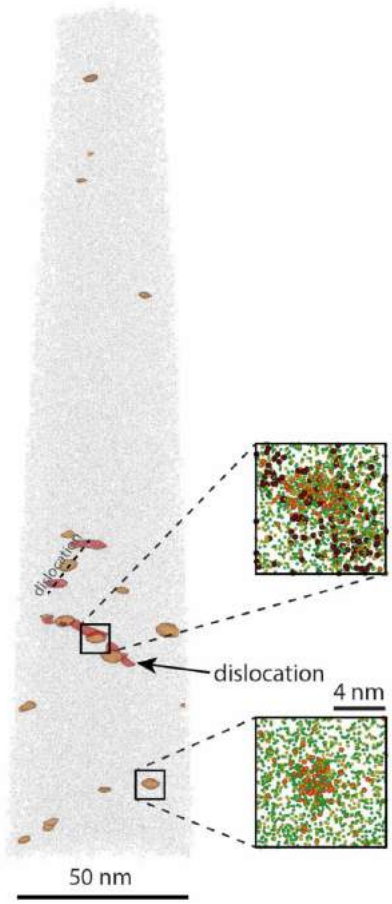

Figure 2. Material H6.4-405. Orange isosurfaces correspond to 1.3% Cu, red to 1.7% Mo. Grey shows the extent of the analysis. The boxes are 10×10×10 nm³ and Ni atoms are green, Mn yellow, Cu orange and Mo dark brown.

Material H6.4-420 was found to be qualitatively similar to H6.4-405. The clusters found are located both on dislocations enriched in Mo and C, and sometimes without any apparent dislocation in the matrix. In material H6.4-450, a total of only three clusters were found, out of which none could be identified as being located on a dislocation, but two were on the edge of the analysis, opening for the possibility that they were actually located on dislocations passing right outside the analysis volume.

In all materials, occasional clusters containing some or all of V, N, C and Cr were found. These often coincided with clusters of Ni-Mn-Si or Cu, or Mo-rich dislocations, but not always. These clusters are believed not to be affected by the irradiation as they previously also have been found in reference materials and in thermally aged materials of similar composition [2, 27].

3.2 Cluster sizes and number densities

The cluster characteristics were found to vary a lot depending on annealing temperature. In Figure 3, the cluster number densities of the different materials are shown. There is no appreciable difference between H6.4 and H6.4-390. However, annealing at a temperature above 390°C results in a significantly reduced cluster number density. In the H6.4-450 material, most clusters have dissolved during annealing and only a total number of three clusters were found.

Table 3 gives the average cluster diameters and number densities. The difference between H6.4 and H6.4-390 number densities is believed to be insignificant, an effect of the heterogeneous weld, as the individual analysis results are within the same interval. The average cluster size is decreasing with increased annealing temperature. The cluster size distributions have a cut-off for low sizes due to the $N_{\min}$ of the MSM (compare with Figure 5 in [2]), that might affect the average size slightly, but it is unavoidable when using this method. There are no bimodal tendencies in the shapes of the size distributions.

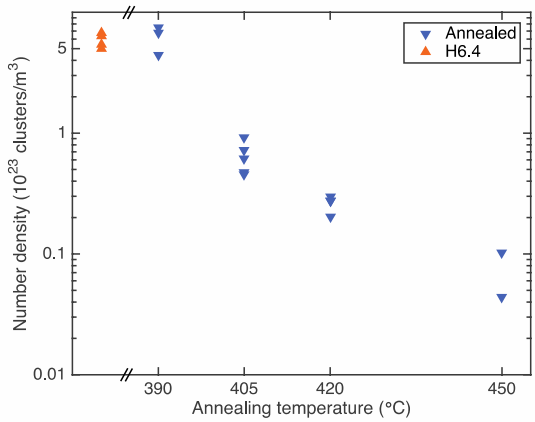

Figure 3. Cluster number density for all the analysed materials. The y-axis is logarithmic to make the large differences clear.

Table 3. Average cluster sizes (deduced from the number of Cu, Ni, Mn, and Si atoms) and number densities, with the standard deviation between analyses given as error.

Material	Average cluster diameter (nm)	Average cluster number density (10^{23}/m^3)	Cluster volume fraction (%)
H6.4	1.8±0.1	6.6±0.8	0.37
H6.4-390	1.8±0.1	7.3±1.6	0.41
H6.4-405	1.5±0.2	0.6±0.2	0.02
H6.4-420	1.4±0.2	0.2±0.04	0.007
H6.4-450	1.3±0.3	0.06±0.04	0.001

3.3 Cluster compositions

The composition of the clusters was also found to vary between the different materials. In Figure 4, it can be seen that there is no obvious difference between the composition of the clusters in H6.4 and H6.4-390. The Ni content is around 55%, Mn around 40%, and

both Cu and Si are low (<8%). For the Si content, only voltage pulsed analyses were used. The materials annealed at 405°C and higher temperatures contain much more Cu (70-80%) and less Ni and Mn (around 15% each). The cluster content of Si is 1% or less for the clusters in materials H6.4-405, H6.4-420 and H6.4-450.

In Figure 5, the total solute content is compared with the matrix solute content. This gives improved statistics on composition and distribution of solutes since the cluster volume fraction is very low (less than 1%). Still, the total content subtracted by the matrix content is found to vary between analyses of the same material, but usually the variations are smaller than one order of magnitude. From Figure 5, there is no difference between no annealing and annealing at 390°C regarding Cu, Ni, Mn and Si. However, annealing at 405°C significantly causes Ni, Mn and Si to dissolve into the matrix. Although there are large variations between analyses of the same materials condition, and the absolute difference between total and matrix content is small, the amount of Ni, Mn and Si in the clusters is decreasing from 405°C to 450°C. After annealing at 450°C, no Si atoms were observed in the few clusters found.

The amount of Cu in the clusters is unchanged up to 405°C, see Figure 5. At 420°C, the Cu is dissolving into the matrix, like Ni, Mn, and Si at 405°C. If the effect of annealing was growth and coarsening of Cu clusters for all annealing temperatures, the risk is that no Cu clusters would have been found in the specimens with higher annealing temperatures due to the low number density, and the difference between matrix and total solute concentration would also end up small. However, this is most probably not the case as there is no obvious decrease of the total Cu content. The average total Cu content is 0.08% for H6.4-450 as well as for the other materials. The same applies for the total Ni, Mn and Si contents, which are found to vary as much within one condition as between the different conditions.

Figure 6 shows the total number of detected Cu atoms per cluster. Note that the detection efficiency of 37% is not used to adjust the numbers, i. e. the actual number of atoms is larger. The graphs of H6.4-405, H6.4-420 and H6.4-450 have a lower cut-off at 8 (N_{min}) due to the cluster definition used (at least 8 Cu atoms are needed). In material H6.4 and H6.4-390 most of the clusters contain none or very few Cu atoms. None of these contain more than 50 Cu atoms (corresponding to 135 atoms when compensating for detection efficiency). In H6.4-405, the number of Cu atoms per cluster has increased significantly. In fact, the largest two clusters are outside the size range of the graph (due to space limitations and comparability of the graphs), and contain 250 and 375 Cu atoms, respectively (676 and 1014 atoms when correcting for detection efficiency). After annealing at 420°C, there are not as many clusters containing a large number of Cu atoms left. In material H6.4-450, the three clusters left contain 11, 33, and 51 detected Cu atoms (30, 89, and 138 corrected Cu atoms). Clusters on the edges are not removed from this analysis, and thus some of the clusters in the graphs might correspond to parts of clusters.

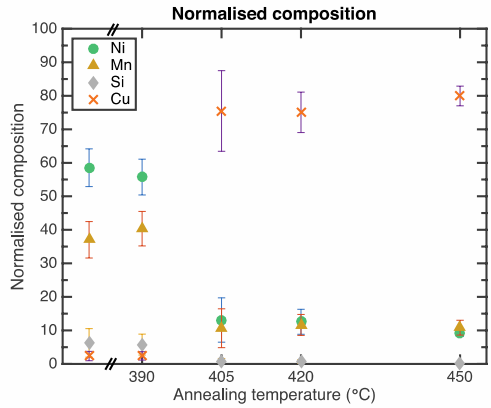

Figure 4. Normalised cluster compositions, Fe removed. Standard deviation of clusters within category are given as error bars. Note broken axis to show the H6.4 material in the same diagram.

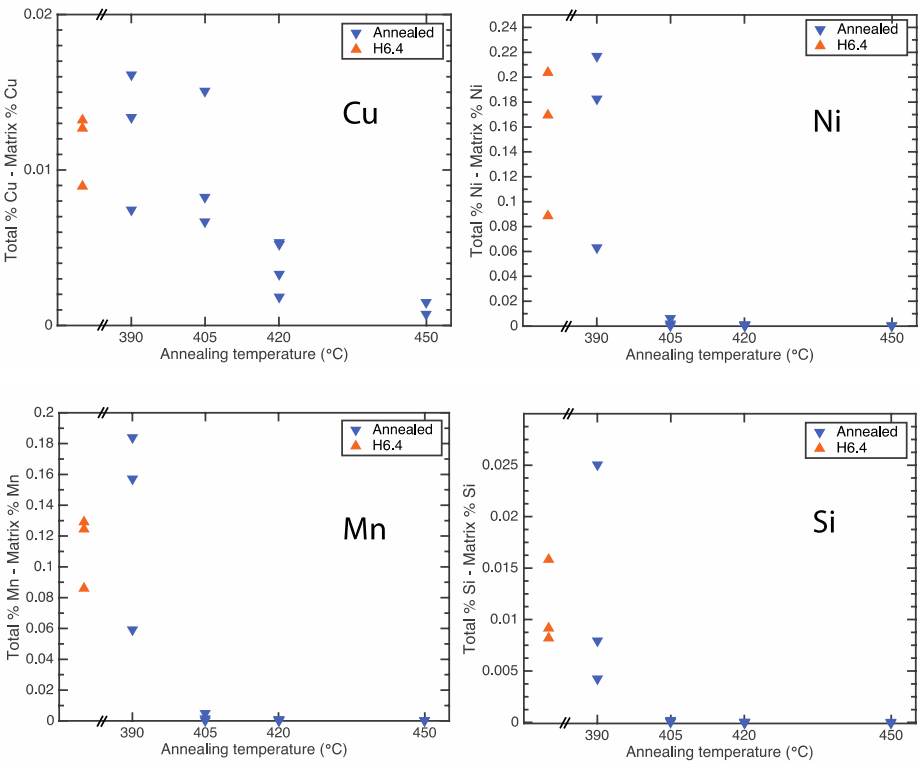

Figure 5. The total solute content minus the matrix solute content for Cu, Ni, Mn and Si for annealing at different temperatures.

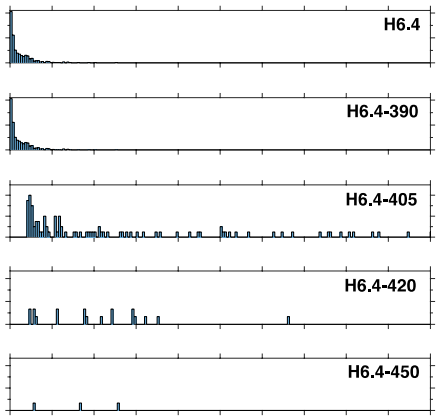

Figure 6. Number of detected Cu atoms per cluster. Note that different cluster definitions give different cut-off at low values. Two clusters in H6.4-405 contained more than 200 Cu atoms (250 and 375, respectively) and are not shown.

3.4 Matrix RDFs

In order to further investigate any difference between H6.4 and H6.4-390, the Ni-Ni radial distribution functions (RDFs) of the matrices were compared, Figure 7. This was done by first removing the clusters, defined using isosurfaces (Ni+Mn+Si equal to 9.7%, including all Ni-isotopes), from the analysed volumes. The threshold value of 9.7% was chosen so that the entire clusters and the compositional variation in direct connection to them should be removed, while avoiding creating extra clusters that were not included in the earlier cluster analysis. In theory, this should tell whether there is any difference in the matrix distribution of Ni. Both analyses show some degree of clustering at small distances. For very small distances (< 2 nm) the statistics is poor and hence the RDF values scatter. The RDFs of H6.4 and H6.4-390 are strongly overlapping.

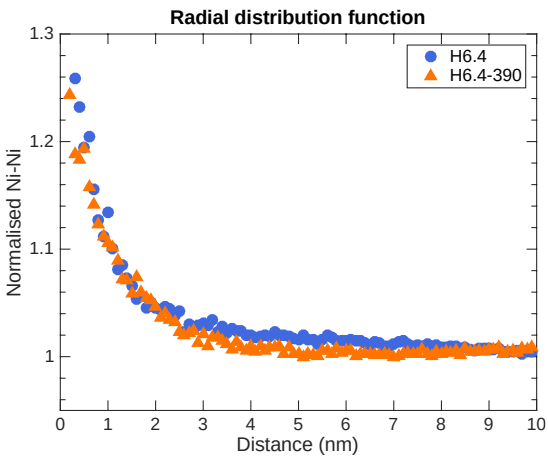

Figure 7. Ni-Ni radial distribution function of the matrix of material H6.4 and H6.4-390.

4. Discussion

4.1 PIA behaviour of clustering elements

In this study, Ringhals R4 weld metals irradiated at high neutron flux to a high fluence were annealed at four different temperatures; 390, 405, 420, and 450°C, for 24-30 h. It was found that the annealing at 390°C had no apparent effect on the cluster characteristics. When annealing at 405°C, the clusters are clearly dissolving and the number density decreases by a factor of ten. Ni, Mn and Si are dissolved into the matrix. The Cu atoms diffuse to form Cu-rich precipitates, many on dislocations, whereas some appear to be in the matrix. Probably the Cu-rich precipitates formed at the position of previous clusters, but this cannot be proven. Annealing at 420°C leads to dissolution of Cu as well into the matrix. After annealing at 450°C, occasional Cu-rich clusters can still be found, but have a very low number density, as well as a very low volume fraction. The results are in agreement with the results on model alloys by Bergner et al. [28], who did step-wise PIA of Fe-Cu, Fe-Mn-Ni and Fe-Mn-Ni-Cu at increasing temperatures. Using SANS, they found that the clusters dissolve at annealing temperatures above 400°C, and that the Ni atoms in the Cu clusters were removed at the same temperatures, in accordance with the findings of this study. The low Cu content of the irradiated materials (H6.4) is expected to make PIA resulting in cluster dissolution rather than coarsening and growth [29].

Annealing of Ringhals R3 surveillance weld metal was characterised by APT by Styman et al. [30]. The material irradiated at a low flux contains larger clusters with a lower number density than the high flux material studied here, but apart from that the materials are very similar. Annealing for 30 minutes at 450°C resulted in a changed cluster size distribution. After additional 10 min at 500°C the average size of the clusters was smaller. It was observed that Mn was leaving the clusters first. This could be compared to the cluster composition after PIA for 24h in the temperature range 405-450°C found in this paper, where the Ni and Mn contents are similar, although the Ni content before annealing was higher than the content of Mn, i.e. more Ni than Mn atoms have left the clusters during annealing. This could be an effect of time. In the thermally aged pressurizer of Ringhals R4 (28 years at 345°C) with very similar composition to the material studied here, the Ni and Mn cluster contents are equal [27].

The materials annealed at and above 405°C have some similarities with thermally aged material, like the Ringhals R4 pressurizer weld metal, where Cu-rich clusters with a Ni-Mn shell are found situated on dislocations [27, 31]. However, the higher annealing temperatures make Ni, Mn and Si dissolve to a larger extent, rather than go to the clusters as in the thermally aged pressurizer material.

There is no apparent compositional difference between the clusters in the matrix and those sitting on dislocations, neither before nor after annealing. However, number densities are affected - as can be seen in Figure 2, the clusters on dislocations are sitting closer to each other than the ones in the matrix, indicating that the matrix clusters dissolve to a larger extent than the clusters sitting on dislocations, which are more

stable. Furthermore, the clusters sitting on dislocations have access to larger volumes through pipe diffusion, to attract Cu and grow.

4.2 Annealing at 390°C - hardness and stable matrix defects

In the paper by Boåsen et al. [16], the hardness of the H6.4 material was measured during 30 h annealing at 390°C. It was found that the hardness decreased from 305 HV down to 280 HV, that is ~92% of the hardness of as-irradiated H6.4 during the first three hours. This is still well above the unirradiated hardness of 210 HV. After this, the hardness changes were negligible. In the same paper, results from annealing of Ringhals surveillance weld metal were presented, but no decrease in hardness was found. This was speculatively attributed to dissolution of small clusters in the high flux material (H6.4), as it contains a higher number density of small clusters [2]. An alternative explanation would be the dissolution of flux dependent matrix defects, which are stable at both 330°C and 360°C, but dissolve at temperatures close to 390°C. The results presented in this paper show no difference in cluster characteristics before and after annealing at 390°C (Figures 3, 4, 5 and 6), and no clear difference in the matrix Ni distribution (Figure 7). Due to the heterogeneity of the welds, the error bars of the APT measurements are, however, large, making small changes hard to quantify. But, cluster dissolution has, unlike cluster formation, no energy barrier [32], and thus, the dissolution should happen to all Ni-Mn-Si clusters, until they were completely dissolved, and not discontinue after a couple of hours at a hardness that is higher than in the unirradiated reference material. Here it is assumed that the solubility limit was not reached. Nagai et al. studied a dilute Fe-Cu model alloy using APT and positron annihilation spectroscopy, and found that nanovoids dissolved after 30 min at 400°C [33], supporting this theory.

It is possible that the materials irradiated in MTR have less stable matrix defects than the surveillance material, as proposed by Fukuya et al. [34]. Then, the matrix defects of the surveillance material would not dissolve at 390°C, but at higher temperatures, when clusters are also dissolving, hiding their contribution to the hardness.

The 6 h longer annealing time of H6.4-390 in comparison to the other annealed materials is not a problem, as there is no difference between this material and the non-annealed H6.4. In the hardness measurements by Boåsen et al. [16] the hardness decreases initially at 390°C, but the hardness after 24 h and 30 h are estimated to be practically identical. The difference in annealing times are due to practicalities.

5. Conclusions

The investigation of a high flux irradiated Ringhals R4 weld, post-irradiation annealed at 390, 405, 420 and 450°C, led to the following conclusions:
- There is a probable contribution from stable matrix defects in the material irradiated in an MTR at high flux. It is, however, small in comparison to the hardness contribution from the clusters.
- Cluster dissolution takes place for annealing at temperatures above 405°C. Ni, Mn, and Si dissolve at 405°C, leaving a small number of Cu-rich clusters, which tend to coarsen. Annealing at higher temperatures, the Cu-clusters dissolve.

The results will be complemented with hardness measurements following annealing at 405, 420, and 450°C in the future publication.

Acknowledgements

Ringhals is acknowledged for providing the materials. VTT for help with annealing, cutting and sending specimen. The Swedish Centre for Nuclear Technology (SKC) and the Swedish Radiation Safety Authority (SSM) are acknowledged for financial support, and Burcak Ebin at the Department of Chemistry and Chemical Engineering at Chalmers for assistance by annealing.

References

[1] L. Messina, M. Chiapetto, P. Olsson, C.S. Becquart, L. Malerba, An object kinetic Monte Carlo model for the microstructure evolution of neutron-irradiated reactor pressure vessel steels, Physica Status Solidi (a) (2016).
[2] K. Lindgren, M. Boåsen, K. Stiller, P. Efsing, M. Thuvander, Evolution of precipitation in reactor pressure vessel steel welds under neutron irradiation, Journal of Nuclear Materials 488 (2017) 222-230.
[3] E. Meslin, M. Lambrecht, M. Hernández-Mayoral, F. Bergner, L. Malerba, P. Pareige, B. Radiguet, A. Barbu, D. Gómez-Briceño, A. Ulbricht, A. Almazouzi, Characterization of neutron-irradiated ferritic model alloys and a RPV steel from combined APT, SANS, TEM and PAS analyses, Journal of Nuclear Materials 406(1) (2010) 73-83.
[4] N. Soneda, K. Nishida, A. Nomoto, K. Dohi, Flux effect on embrittlement of reactor pressure vessel steels irradiated to high fluences, Fontevraud 8: Conference on Contribution of Materials Investigations and Operating Experience to LWRs' Safetyy, Performance and Reliability, Avignon, France, 2014.
[5] Y.I. Shtrombakh, B.A. Gurovich, E.A. Kuleshova, A.S. Frolov, S.V. Fedotova, D.A. Zhurko, E.V. Krikun, Effect of Ni content on thermal and radiation resistance of VVER RPV steel, Journal of Nuclear Materials 461 (2015) 292-300.
[6] M.K. Miller, K.F. Russell, Embrittlement of RPV steels: An atom probe tomography perspective, Journal of Nuclear Materials 371(1-3) (2007) 145-160.
[7] M.K. Miller, K.A. Powers, R.K. Nanstad, P. Efsing, Atom probe tomography characterizations of high nickel, low copper surveillance RPV welds irradiated to high fluences, Journal of Nuclear Materials 437(1-3) (2013) 107-115.
[8] A. Wagner, F. Bergner, R. Chaouadi, H. Hein, M. Hernández-Mayoral, M. Serrano, A. Ulbricht, E. Altstadt, Effect of neutron flux on the characteristics of irradiation-induced nanofeatures and hardening in pressure vessel steels, Acta Materialia 104 (2016) 131-142.
[9] K. Dohi, K. Nishida, A. Nomoto, N. Soneda, H. Matsuzawa, M. Tomimatsu, Effect of Neutron Flux at High Fluence on Microstructural and Hardness Changes of RPV Steels, ASME 2010 Pressure Vessels & Piping Division / K-PVP Conference, Bellevue, Washington, USA, 2010.
[10] G.R. Odette, E.V. Mader, G.E. Lueas, W.J. Phythian, C.A. English, The effect of flux on the irradiation hardening of pressure vessel steels, Effects of Radiation on Materials: 16th International Symposium, ASTM STP 1175, Philadelphia, 1993.

[11] G.R. Odette, G.E. Lucas, Recent progress in understanding reactor pressure vessel steel embrittlement, Radiation Effects and Defects in Solids 144(1-4) (1998) 189-231.
[12] P. Pareige, B. Radiguet, A. Suvorov, M. Kozodaev, E. Krasikov, O. Zabusov, J.P. Massoud, Three-dimensional atom probe study of irradiated, annealed and re-irradiated VVER 440 weld metals, Surface and Interface Analysis 36(56) (2004) 581-584.
[13] M.K. Miller, K.F. Russell, Atom probe characterization of copper solubility in the Midland weld after neutron irradiation and thermal annealing, Journal of Nuclear Materials 250 (1997) 223-228.
[14] P. Auger, P. Pareige, S. Welzel, J.-C. Van Duysen, Synthesis of atom probe experiments on irradiation-induced solute segregation in French ferritic pressure vessel steels, Journal of Nuclear Materials 280(3) (2000) 331-344.
[15] P. Efsing, J. Roudén, P. Nilsson, Flux Effects on Radiation Induced Aging Behaviour of Low Alloy Steel Weld Material with High Nickel and Manganese Content, Effects of radiation on nuclear materials 26 (2014) 119-134.
[16] M. Boåsen, P. Efsing, U. Ehrnstén, On flux effects in a low alloy steel from a Swedish reactor pressure vessel, Journal of Nuclear Materials 484 (2017) 110-119.
[17] P. Efsing, C. Jansson, T. Mager, G. Embring, Analysis of the Ductile-to-Brittle Transition Temperature Shift in a Commercial Power Plant With High Nickel Containing Weld Material, Journal of ASTM International 4(7) (2007).
[18] D.J. Larson, D.T. Foord, A.K. Petford-Long, H. Liew, M.G. Blamire, A. Cerezo, G.D.W. Smith, Field-ion specimen preparation using focused ion-beam milling, Ultramicroscopy 79(1-4) (1999) 287-293.
[19] K. Thompson, D. Lawrence, D.J. Larson, J.D. Olson, T.F. Kelly, B. Gorman, In situ site-specific specimen preparation for atom probe tomography, Ultramicroscopy 107(2-3) (2007) 131-9.
[20] K. Lindgren, K. Stiller, P. Efsing, M. Thuvander, On the Analysis of Clustering in an Irradiated Low Alloy Reactor Pressure Vessel Steel Weld, Microsc Microanal 23(2) (2017) 376-384.
[21] D. Vaumousse, A. Cerezo, P.J. Warren, A procedure for quantification of precipitate microstructures from three-dimensional atom probe data, Ultramicroscopy 95 (2003) 215-221.
[22] J.M. Hyde, C.A. English, An Analysis of the Structure of Irradiation induced Cu-enriched Clusters in Low and High Nickel Welds, Materials Research Society Symposium, Boston, 2000, pp. R6.6.1-R6.6.12.
[23] A. Morley, G. Sha, S. Hirosawa, A. Cerezo, G.D. Smith, Determining the composition of small features in atom probe: bcc Cu-rich precipitates in an Fe-rich matrix, Ultramicroscopy 109(5) (2009) 535-40.
[24] S. Shu, B.D. Wirth, P.B. Wells, D.D. Morgan, G.R. Odette, Multi-technique characterization of the precipitates in thermally aged and neutron irradiated Fe-Cu and Fe-Cu-Mn model alloys: Atom probe tomography reconstruction implications, Acta Materialia 146 (2018) 237-252.
[25] P.D. Edmondson, C.M. Parish, R.K. Nanstad, Using complimentary microscopy methods to examine Ni-Mn-Si-precipitates in highly-irradiated reactor pressure vessel steels, Acta Materialia 134 (2017) 31-39.
[26] E.A. Marquis, J.M. Hyde, Applications of atom-probe tomography to the characterisation of solute behaviours, Materials Science and Engineering: R: Reports 69(4-5) (2010) 37-62.

[27] K. Lindgren, M. Boåsen, K. Stiller, P. Efsing, M. Thuvander, Cluster formation in in-service thermally aged pressurizer welds, Journal of Nuclear Materials 504 (2018) 23-28.
[28] F. Bergner, A. Ulbricht, P. Lindner, U. Keiderling, L. Malerba, Post-irradiation annealing behavior of neutron-irradiated FeCu, FeMnNi and FeMnNiCu model alloys investigated by means of small-angle neutron scattering, Journal of Nuclear Materials 454(1-3) (2014) 22-27.
[29] A. Ulbricht, F. Bergner, C.D. Dewhurst, A. Heinemann, Small-angle neutron scattering study of post-irradiation annealed neutron irradiated pressure vessel steels, Journal of Nuclear Materials 353(1-2) (2006) 27-34.
[30] P.D. Styman, J.M. Hyde, D. Parfitt, K. Wilford, M.G. Burke, C.A. English, P. Efsing, Post-irradiation annealing of Ni–Mn–Si-enriched clusters in a neutron-irradiated RPV steel weld using Atom Probe Tomography, Journal of Nuclear Materials 459 (2015) 127-134.
[31] K. Lindgren, M. Boåsen, K. Stiller, P. Efsing, M. Thuvander, Thermal ageing of low alloy steel weldments from a Swedish nuclear power plant – the evolution of the microstructure, Proceedings - Fontevraud 9: Contribution of Materials Investigations and Operating Experience to Light Water NPPs' Safety, Performance and Reliability (2018).
[32] R.W. Cahn, P. Haasen, Physical Metallurgy, 4 ed., North-Holland, Amsterdam, 1996.
[33] Y. Nagai, Z. Tang, M. Hassegawa, T. Kanai, M. Saneyasu, Irradiation-induced Cu aggregations in Fe: An origin of embrittlement of reactor pressure vessel steels, Physical Review B 63(13) (2001).
[34] K. Fukuya, K. Ohno, H. Nakata, S. Dumbill, J.M. Hyde, Microstructural evolution in medium copper low alloy steels irradiated in a pressurized water reactor and a material test reactor, Journal of Nuclear Materials 312(2-3) (2003) 163-173.

Paper VI

Integrated effect of thermal ageing and low flux irradiation on microstructural evolution of welded stainless steels

K. Lindgren, M. Bjurman, P. Ekström, P. Efsing, and M. Thuvander

In manuscript

Integrated Effect of Thermal Ageing and Low Flux Irradiation on Microstructural Evolution of Welded Stainless Steels

K. Lindgren[1], M. Bjurman[2,3], P. Ekström[4], P. Efsing[2,5] and M. Thuvander[1]

[1] Chalmers University of Technology, Göteborg, Sweden
[2] Royal Institute of Technology (KTH), Stockholm, Sweden
[3] Studsvik Nuclear AB, Nyköping, Sweden
[4] Swedish Radiation Safety authority (SSM), Solna, Sweden
[5] Ringhals AB, Väröbacka, Sweden

Abstract

The microstructure of aged 308-type austenitic welds with a ferrite content of 5-7% has been analysed using atom probe tomography (APT). The weld metal of the core barrel of a decommissioned reactor, neutron irradiated to 0.15 dpa, 1 dpa and 2 dpa at 280-285°C (231,000 h) are compared to two thermally aged welds (70,000 h at 291°C and 325°C, respectively, and then 22,000 h more at temperatures around 20°C lower for both welds). In the ferrite of the irradiated welds, there is spinodal decomposition into Cr-rich α' and Fe-rich α, with a similar degree of decomposition for all investigated doses. The ferrite of the thermally aged material was decomposed when aged at 325°C, but not when aged at 291°C. There is G-phase precipitation in the ferrite of all the weld metals except the one that was thermally aged at the lowest temperature. There is no apparent difference in the G-phase formation after 1 and 2 dpa. Furthermore, segregation to the ferrite/austenite phase boundaries were observed, mainly of Ni and Si. The austenite of the thermally aged weld metals was found to be unaffected by the ageing, whereas Ni-Si precipitates were found after irradiation. It is concluded that the neutron irradiation has a major effect on the degradation of the weld metals.

Keywords: spinodal decomposition, G-phase, atom probe tomography, neutron irradiation, austenitic welds

1. Introduction

Austenitic stainless steels are used in internals of nuclear power plants due to their good weldability and corrosion properties. During operation, they are affected by the temperature (around 290-320°C in a typical pressurized water reactor) and neutron irradiation inside the reactor, and their properties degrade, making the material embrittled. Austenitic welds and castings contain some 5-30% of ferrite, to avoid solidification cracking.

The changes occurring in the material leading to degradation take place on the nanometre scale. In ferrite, spinodal decomposition into a Cr-poor α and a Cr-rich α'

phase and G-phase formation on the interfaces of these structures take place in reactor relevant environments. G-phase has a nominal composition of $Ni_{16}Si_7Ti_6$ [1]. However, other metallic elements (such as Cr, Fe, Mn, Mo) can substitute Ni and Ti [2, 3]. In the case of the austentic alloys as in this paper, the Ti is generally exchanged for Mn, resulting in $Ni_{16}Si_7Mn_6$.

The austenite also undergoes changes during neutron irradiation, forming precipitates containing Ni and Si (γ' - Ni_3Si and its precursors), and dislocation loops are formed [4-7]. In addition to this, the chemistry at grain boundaries are changed due to irradiation induced segregation (decreased Cr and increased Ni and Si), increasing the risk of grain boundary failure.

The effect of thermal ageing on spinodal decomposition has been studied in both model alloys and in commercial steels [2, 8-13]. Irradiated materials have also been studied [14, 15]. It is common to accelerate the ageing by having higher temperatures or higher neutron flux, or to use ion irradiation to simulate neutron irradiation. The validity of the results then has to be transferred to the actual conditions of the components. In this study, material retrieved from actual power plants, which have been in operation, have been analysed.

In this paper austenitic weld metals from the main recirculating loops of Ringhals R2 pipes that are thermally aged for 70,000 h are compared with weld metals that have been exposed to neutron irradiation in the core barrel of the Spanish José Cabrera (Zorita) nuclear power plant are analysed using atom probe tomography (APT). The effects of ageing on both the ferrite and the austenite are discussed, with main focus on the ferrite.

2. Materials and Methods

The ageing conditions of the investigated samples can be seen in Table 1. The irradiated materials originate from welds of the decommissioned José Cabrera core barrel, welded with type 308 consumables [16, 17]. The ferrite content of the this material was found to be 5-7%, measured by ferritescope [16]. The composition of the irradiated material can be seen in Table 2. The thermally aged material is a weld from the cast material that was investigated by Bjurman et al. [18], from the reactor coolant pump elbows of Ringhals R2, and contain slightly more ferrite, 10±0.5% [17].

Table 1. Investigated materials. CB stands for core barrel, CL for cross-ocer leg and HL for hot leg.

Name	Dose (dpa)	Temperature (°C)	Time (h)
CB-0.15	0.15	280-285	231,000
CB-1	1	280-285	231,000
CB-2	2	280-285	231,000
CL	0	291 (274)	70,000 (22,000)
HL	0	325 (303)	70,000 (22,000)

Table 2. The composition of the José Cabrera core barrel welds, given in wt% [19].

	C	Mn	S	Cr	Fe	Ni	Mo	Ti	Al	Cu	Co	V
Analysis	0.06	1.47	0.017	21.5	70.5	9.9	0.04	0.024	0.010	0.13	0.11	0.063
Uncertainty	0.004	0.07	0.003	1.0	3.0	0.4	0.004	0.001	0.003	0.01	0.01	0.001

The samples CB-0.15 and CB-1 come from the same weld, whereas CB-2 comes from a different weld of the same component. The CL (cross-over leg) weld metal is thermally aged at a relevant temperature, 291°C, that is close to the operating temperature of the irradiated materials. The HL (hot leg) weld metal is aged at a considerably higher temperature, 325°C, resulting in an equivalent ageing of more than 10 times the CL material [17]. Both the CL and HL welds are aged 22,000 h at lower temperatures (274 and 303°C, respectively) after the initial 70,000 h.

The APT analysis was performed in a LEAP 3000X HR equipped with a reflectron. The analysis was done in voltage pulsed mode with a frequency of 200 kHz. The specimen temperature was 70 K, the pulse fraction was 20% and the target evaporation rate was 0.2%.

Specimen preparation for APT was carried out using a standard lift-out technique ending with annular milling [20, 21] in a FEI Versa 3D focused ion beam/scanning electron microscope. A final polishing at 5 kV was done in order to minimize Ga implantation and to remove any amorphous layer.

The reconstruction was made in IVAS 3.6. The image compression factor was kept constant at 1.65 and the field was set to 33 V/nm. The reconstruction parameter k (field factor) was adjusted individually for each analysis containing decomposed ferrite, assuming that the extent of spinodal decomposition is isotropic, i.e. equal in z and, x and y directions. This was done by comparing the normalised radial distribution functions (RDFs) of some different k-value reconstructions, see the example in Figure 1. A well-defined RDF displaying a deep minimum and a first maximum with a decreasing value for longer distances is desirable, as this should correspond to equal typical distances between the Cr-rich and Cr-poor volumes in x- y-, and z-directions. With this criterion, the k-factor was found to vary significantly between the different reconstructions, from 4.3 to 5.9. The results were found to correspond well to what was found using manual inspection of the reconstructions.

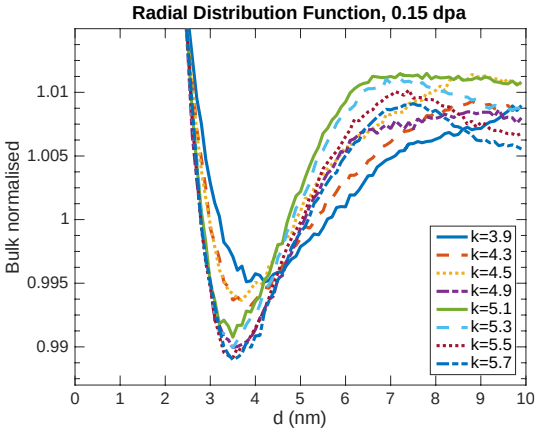

Figure 1. Cr-Cr radial distribution function of one of the analyses, showing the values for different k.

The amplitude A of the spinodal decomposition was evaluated using the Cr-Cr RDF based method by Zhou et al. [22]. The extrapolated value of the normalised Cr-Cr RDF at zero distance ($RDF(0)$) is used: $A = C_{Cr}\sqrt{RDF(0) - 1}$, where C_{Cr} is the Cr concentration in the analysis. This method is user independent and easy to use. The use of this method is assuming sinusoidal concentration variations, which is a good approximation for small amplitudes in the beginning of the phase decomposition, but a less good approximation at later stages. Independent of method, the wavelength of spinodal decomposition is dependent on the reconstruction. Here, the wavelength is determined as the first local maximum of the Cr-Cr RDF. For instance, in Figure 1, the wavelength varies between 6.8 nm and 8.9 nm dependent on the k-value used. In some of the larger APT analyses (containing ferrite extending at least 150 nm), it was found that the wavelength of the spinodal decomposition could vary from the top part to the end of the reconstruction in a systematic way. When reconstructed separately, it was found that the optimum k-value varied within the analysis, and with adjusted k-value dependent on position, the difference in wavelength within the same analysis became smaller. There was, however, some remaining differences in the appearance of the RDF. These might be due to the need of an adjusted image compression factor as well as k, that is also known to differ during analysis, and neither of their variations are accounted for by the reconstruction algorithms used [23, 24]. The impact of these effects is estimated to be small, since the k value is optimised for the average of the ferrite in each analysis. Furthermore, the ferrite is in most cases not present in that large parts of the reconstruction, and thus the optimised k and wavelength should be accurate.

The G-phase was analysed using both isoconcentration surfaces and proximity histograms (proxigrams) [25] and the maximum separation method (MSM) [26, 27]. The MSM parameters were chosen with solute atoms Ni, Mn and Si, and a d_{max} = 0.45 nm and N_{min} = 25, that were found to be reasonable parameters for these materials considering the reasoning in [28]. In HL and CB-0.15, the clusters were diffuse and the separation of small clusters and random fluctuations was a trade-off. For the number density, the clusters on the edges were counted as one-half. Using isoconcentration surfaces, the cluster number density was found to vary with the total Ni content of the analysis. Furthermore, many clusters were found to intersect each other when using isoconcentration surfaces. The MSM was found to separate closely located clusters

better. The G-phase sizes were calculated using MSM, assuming only Ni, Mn and Si being part of the precipitate, and that the atomic density is close to that of the surrounding ferrite. The normalised radial concentration profiles were used to obtain the precipitate compositions, at distances where the profile is reasonably flat (0.2 to 0.5 where 1 is normalised as the cluster surface) in order to get the cluster centre composition. The enrichment of solutes in clusters is given by the cluster content divided by the average content of the analysis. Ferrite/austenite, ferrite/carbide and austenite/carbide interfaces were studied using proxigrams [25].

3. Results

An overview of a typical part of a CB weld can be seen in Figure 2. The ferritic volumes are seen with a dark contrast and are surrounded by austenite. The shape of the ferrite is thin layers, with widths as small as a few hundred nanometres. These welds have been cooled fast and thus the ferrite structures are relatively thin. The angle of the ferrite into the material is varying, some of the ferrite volumes go straight down into the material whereas others are close to parallel to the specimen surface, making the specimen preparation for APT a little more challenging. The dark spherical particles in Figure 2 are presumably oxide inclusions that are present in the weld metal from the manufacturing.

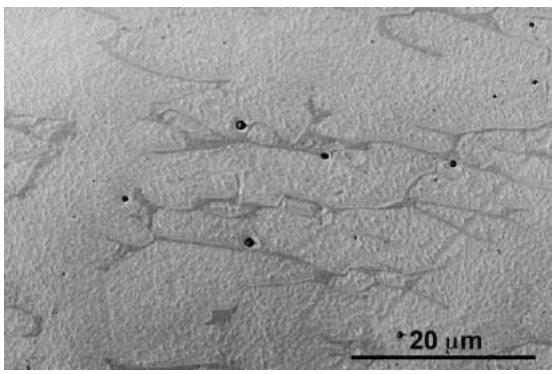

Figure 2. Scanning electron micrograph of the CB-2 specimen. The ferrite is seen as dark contrast.

3.1. Ferrite

The overall compositions of ferrite as measured by APT is given in Table 3. From the standard deviations given, it is seen that the composition varies significantly between the analyses. First of all, the Cr content is different in the different analyses; for instance in the CB-2 material the Cr content varies between 25.3 and 27.3 at.%. There is also a significant spread among the analyses of irradiated material, but also between the irradiated materials and the thermally aged materials in terms of the Ni content. Furthermore, the Si content of material CB-1 is considerably lower (0.9-1.2%) than in the other materials (1.9-2.5%). The differences between thermally aged and irradiated material might be partly due to differences during manufacturing, for instance in the cooling rate, that will influence the kinetics and thus the partitioning of elements between the ferrite and the austenite. There could also be overall differences in the

compositions between the welds. On top of that, there seems to be local differences within the composition that are caught due to the local analysis using APT, probably due to the complex structure. The ferrite composition might vary between different grains. Within the same APT reconstruction, the ferrite composition was found to be fairly constant, also in the vicinity of ferrite/austenite boundaries.

Table 3. The composition of the analysed ferrite in the APT analyses. The standard deviations between analyses are given.

at. %	0.15 dpa	1 dpa	2 dpa	CL	HL
C	0.03±0.04	0.07±0.03	0.06±0.05	0.05±0.01	0.02±0.01
N	0.06±0.08	0.06±0.05	0.04±0.03	0.05±0.01	0.03±0.01
Mo	0.10±0.01	0.08±0.01	0.10±0.01	0.28±0.01	0.38±0.03
Si	2.50±0.04	1.08±0.14	2.46±0.08	1.94±0.03	2.30±0.11
W	0.01±0.01	0.01±0.01	0.01±0.01	0.02±0.03	0.02±0.01
P	0.07±0.01	0.10±0.05	0.11±0.04	0.07±0.04	0.14±0.01
V	0.09±0.01	0.11±0.01	0.09±0.01	0.09±0.01	0.08±0.01
Mn	0.87±0.03	0.90±0.02	0.74±0.06	0.99±0.01	0.91±0.12
Cr	25.57±0.96	24.81±0.59	26.51±1.04	27.81±0.21	26.04±0.51
Co	0.06±0.01	0.05±0.01	0.05±0.01	0.13±0.08	0.12±0.01
Fe	68.22±0.89	70.87±0.96	67.32±1.37	64.25±0.14	65.83±0.33
Cu	0.04±0.01	0.03±0.01	0.03±0.01	0.08±0.01	0.08±0.01
Ni	2.33±0.07	1.77±0.29	2.42±0.22	3.39±0.04	4.01±0.20

Thin slices of the ferrite of all five materials studied can be seen in Figure 3, where volumes of 20×20×4 nm^3 are presented. The spinodal decomposition of the materials is visualized by only displaying the distribution of Cr atoms. In CL, no spinodal decomposition is seen. In HL, there are some small Cr density variations within the ferrite. In all irradiated materials, on the other hand, the phase separation is clear and the difference between CB-0.15, CB-1 and CB-2 is small. The difference between CB-1 and CB-2 is as small as the variation within the same ageing condition.

Also in Figure 3, the distribution of Ni, Mn and Si is seen for the same volumes. Again, the distribution appears to be random in CL. In HL and CB-0.15, clusters have started to form. In CB-1 and CB-2, the G-phase precipitates are well developed and can be clearly separated from the matrix. In this study, we have no crystallographic information on the clusters, but the word precipitate is still used.

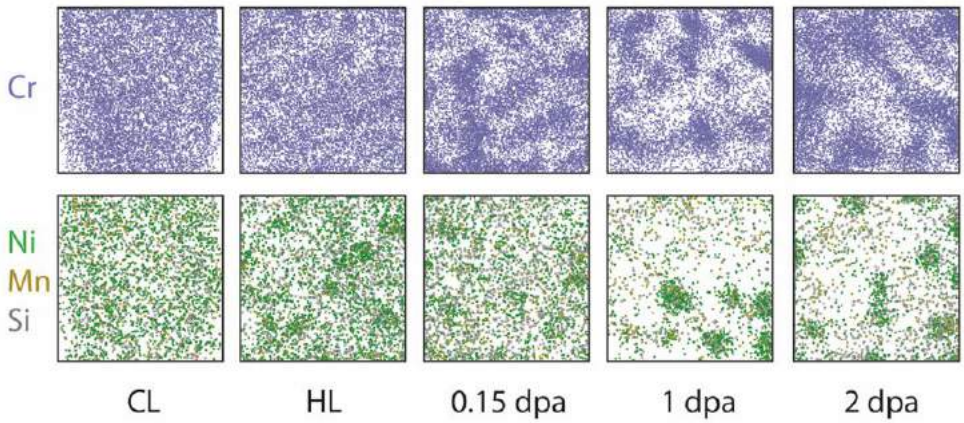

Figure 3. Thin slices (thickness 4 nm) of APT analyses showing the distribution of Cr and Ni, Mn and Si in the ferrite for all different conditions. The side of the boxes are 20 nm. The decreased Cr content in the bottom corners of the CL image is due to the ferrite volume being too small to fill the 20×20×4 nm³ box, leaving the corners outside the reconstruction.

3.1.1 Spinodal decomposition

The spinodal decomposition of all analyses was studied in terms of wavelength and amplitude. The dose-wavelength dependence of all materials except CL, which showed no clear spinodal decomposition and therefore is left out, can be seen in Figure 4. As seen in the figure, there is no clear dependency on dose in the analyses of the irradiated materials. The material irradiated to 1 dpa even has a shorter average wavelength than the material irradiated to 0.15 dpa. The spread within each condition is large in comparison to the difference between the different conditions. The measurement error is estimated to be smaller (±1 nm based on the reasoning in the methods section) than the variation between the analyses of the same materials.

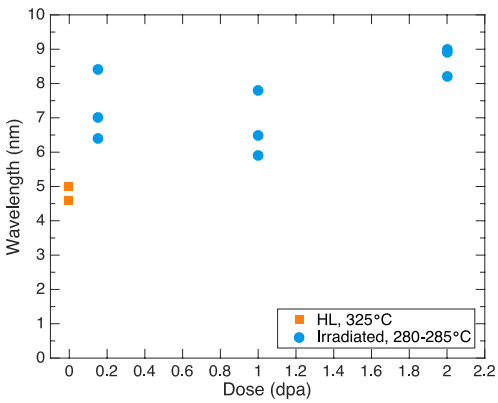

Figure 4. Wavelength of the spinodal decomposition as a function of dose. The thermally aged material included, the HL weld, is aged at a higher temperature (325°C), than the irradiated materials (280-285°C).

When instead comparing the wavelength with the measured Cr concentration of each analysis, there is a trend for a longer wavelength with higher Cr for the irradiated materials, see Figure 5, and possibly the same trend is valid also for unirradiated material, but at shorter wavelengths.

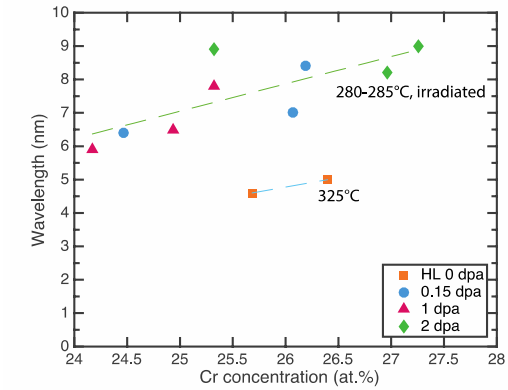

Figure 5. Wavelength vs Cr concentration of the materials except CL. The thermally aged material included, the HL weld, is aged at a higher temperature (325°C), than the irradiated materials (280-285°C).

The amplitude of the spinodal decomposition shows a small increase from CB-0.15 to CB-1, see Figure 6. Materials CB-1 and CB-2 appear to have similar amplitudes of around 25 at.%. Material HL has lower amplitude, 14 at.%, and CL is not included in the figure as there is no clear spinodal decomposition. A full comparison of amplitude and wavelength can be seen in Figure 7. The spinodal decomposition in the irradiated materials is much more developed than in the thermally aged HL, although the temperature during irradiation was lower. It appears to be only small differences between CB-1 and CB-2 that might be due to the composition of the ferrite. Already after irradiation to 0.15 dpa the spinodal decomposition is well developed and close to saturated as the amplitude is close to the Cr content, around 25 at.% (Table 3).

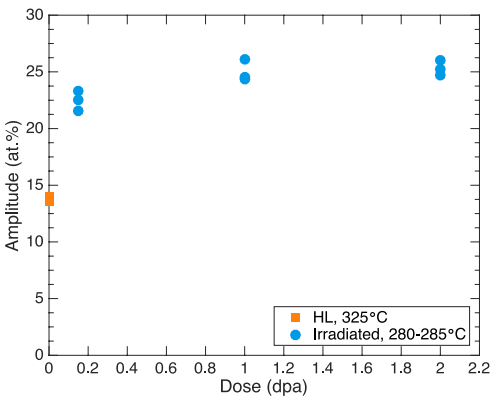

Figure 6. Amplitude of the spinodal decomposition as a function of dose. The thermally aged material included, the HL weld, is aged at a higher temperature (325°C), than the irradiated materials (280-285°C).

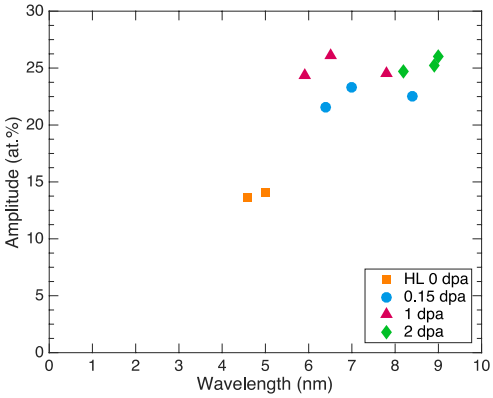

Figure 7. A summary of the amplitude and wavelength for the spinodally decomposed ferrite. The thermally aged material included, the HL weld, is aged at a higher temperature (325°C), than the irradiated materials (280-285°C).

3.1.2 G-phase formation

The absolute Ni-Ni RDFs of all materials are shown in Figure 8. In all materials except CL, Ni is found to cluster (Mn and Si also cluster with Ni, but this is not shown in the figure), indicating formation of G-phase. The absolute RDFs are shown rather than the normalised RDFs, so that the effect of Ni content can also be seen. The difference in Ni content does not seem to significantly affect the cluster composition, and thus the values at small distances end up closer to each other when not normalised to the bulk content. From Figure 8 it can be seen that the RDFs of Ni in CB-1 and CB-2 are considerably higher than for CB-0.15, and they are overlapping, indicating a saturation with respect to dose in the Ni content. The HL and CL materials have higher ferrite Ni content (as also shown in Table 3). In the CL material, no apparent clustering is indicated by the RDF.

The composition of the G-phase precipitates found in all materials except CL was analysed and the results are presented in Figure 9, where both the absolute content and a normalised composition (only Ni, Mn, and Si) for comparison to the stochiometric $Ni_{16}Si_7Mn_6$ G-phase composition are shown. The Mn content is in general a bit lower than expected from the stoichiometry, whereas the Si content is higher. The Mn and Ni might be replaced by Fe or Cr in the G-phase, which were removed from the precipitate content in the normalisation. There is no obvious difference between the materials. Worth noting is that using only APT, no conclusions can be made on the crystal structure, and thus whether the clusters or precipitates are really a different phase. Regardless of this, the term G-phase is used in this paper.

The enrichment of Ni, Mn, Si, P and Cu in the clusters is shown in Figure 10. Most of the irradiated materials show similar enrichment factors of the solutes. The analysis of CB-1 that has high enrichments has similar cluster contents, but low total contents and thus low matrix contents, giving the high enrichment. HL has similar or slightly lower enrichments of all solutes except P, which clearly becomes less enriched after thermal ageing than after irradiation.

The average G-phase size (radius or diameter?) for the CB-1 and CB-2 materials was found to be around 2 nm, with distributions ranging from 1 to 3 nm. Hereby any Fe and

Cr atoms inside clusters were removed (assuming they were detected inside clusters due to local magnification effects), thus possibly underestimating the size. In the HL and CB-0.15 material, the clusters are more diffuse and thus harder to define. In general, applying MSM results in a smaller number of atoms in the clusters in these materials, but the results are very much dependent on the MSM parameter choice and a very sharp cut-off in the size distribution occurs due to the N_{min} parameter, indicating that the MSM is not a suitable technique to quantify these diffuse features.

The G-phase number densities were found to be high, between 15-45 $10^{23}/m^3$. For HL the average was 36 $10^{23}/m^3$, for CB-0.15 25 $10^{23}/m^3$, for CB-1 25 $10^{23}/m^3$, and for CB-2 43 $10^{23}/m^3$, thus with a weak increasing trend with dose, but below that trend for CB-1 that also contains less Ni.

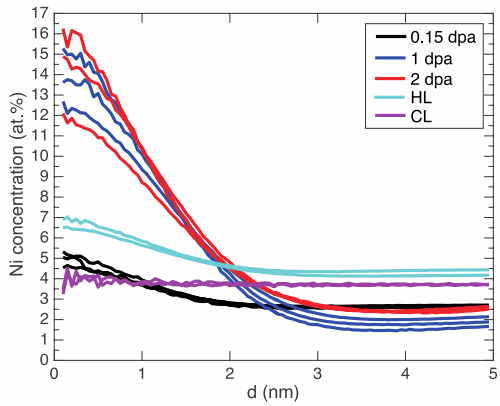

Figure 8. The absolute Ni-Ni RDFs for the ferrite of all materials, with two or three analyses per material.

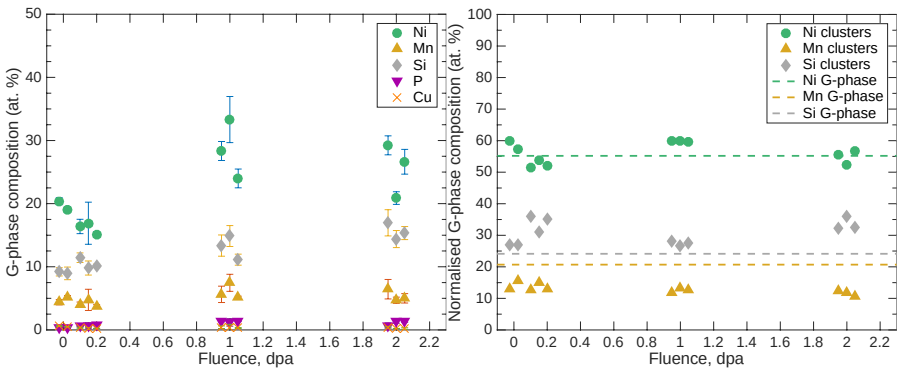

Figure 9. G-phase composition for materials HL, CB-0.15, CB-1 and CB-2. Also, the normalised contents are shown and compared to stoichiometric G-phase composition. The thermally aged material included, the HL weld, is aged at a higher temperature (325°C), than the irradiated materials (280-285°C).

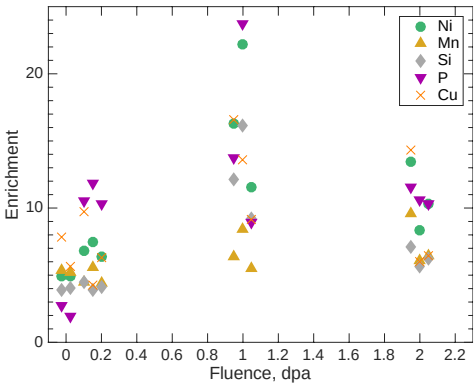

Figure 10. Enrichment (relative to the matrix) of Ni, Mn, Si, P, and Cu in the G-phase, for material HL, CB-0.15, CB-1 and CB-2. The thermally aged material included, the HL weld, is aged at a higher temperature (325°C), than the irradiated materials (280-285°C).

3.2 Austenite

The distribution of elements was found to be random in the austenite of HL and CL materials that are not exposed to irradiation. After irradiation to 0.15 dpa, P clusters appear in some, but not all, analyses, see example in Figure 11. They typically contain less than 110 P detected atoms. Analysing the normalised P RDFs of these analyses, a small tendency of Ni and Si (extrapolation to RDF(0)=1.05-1.10 for P-Ni and 1.10-1.15 for P-Si) to cluster together with P was observed, whereas the Cr, Mn, Cu and Fe atoms were randomly distributed with respect to P.

A small number of Ni-Si particles were found in the CB-0.15 material, with a Ni/Si ratio of 1.4, and a slight enrichment of P. After irradiation to 1 dpa, clear examples of Ni-Si enriched particles are found. Their Ni/Si ratios vary between 1.9 and 2.5, also within the same analysis and they are depleted in Fe, Cr and Mn. Furthermore, there are Cu clusters in connection to the Ni-Si particles, see Figure 12. The number densities and sizes vary significantly between analyses as seen in the figure. There are also P segregating to what appears to be dislocations. Occasional loops are found, decorated with Ni and Si, and in the case shown in the figure, a Cu cluster. The Ni/Si ratios of the segregation to loops are found to be the same as to the Ni-Si particles. Close to ferrite-austenite phase boundaries, there is a volume without Ni-Si particles, a precipitate free zone of about 40 nm. After irradiation to 2 dpa, the austenite looks similar, with an even larger Ni/Si ratio variation between particles analysed; 1.6 to 2.7.

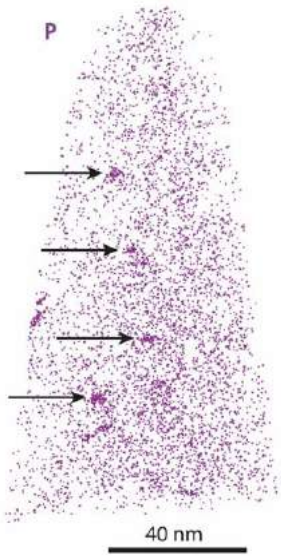

Figure 11. APT reconstruction of austenite irradiated to 0.15 dpa. Only P atoms are shown. The arrows indicate round P clusters.

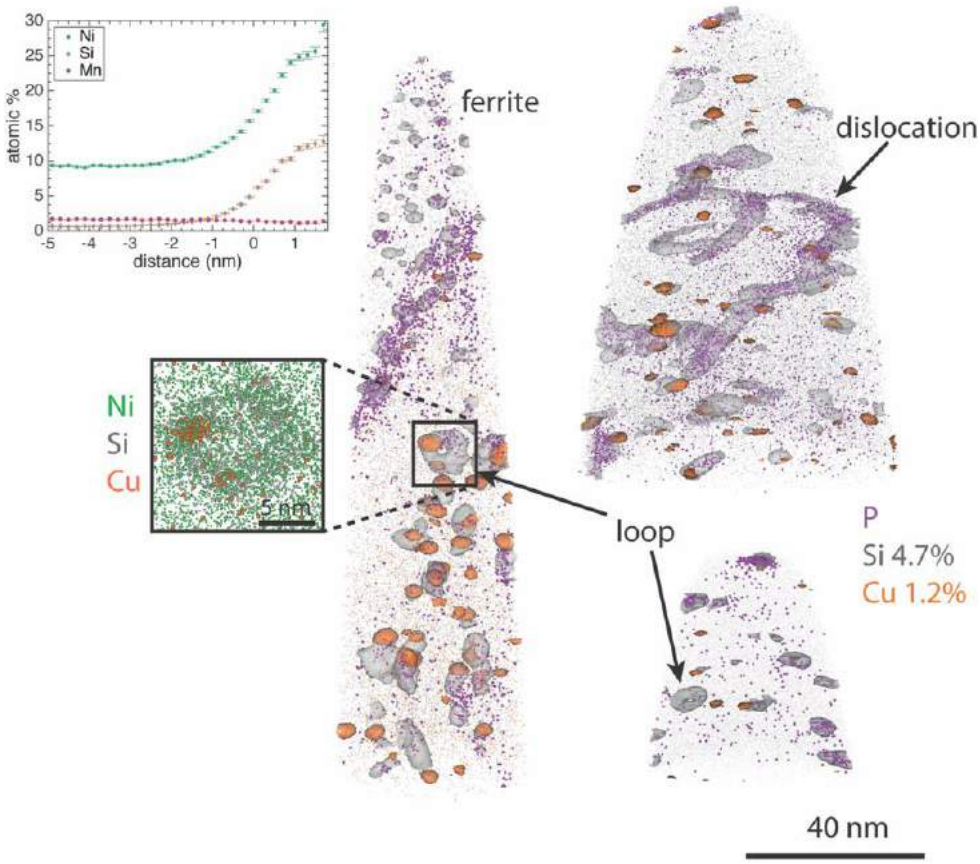

Figure 12. APT reconstructions of austenite irradiated to 1 dpa. The box contains a loop decorated with Ni atoms (green dots) and Si (grey dots). A Cu-cluster (orange dots) sits on the loop. The histogram corresponds to the Si 4.7% isoconcentration surfaces shown.

3.3 Phase boundaries

3.3.1 Ferrite-austenite

In Figure 13, examples of the ferrite-austenite interfaces are shown for material CL, CB-0.15, CB-1 and CB-2. In CL and CB-0.15, the solutes are evenly distributed on the interfaces. In CB-1 and CB-2, the solutes (foremost Ni and Si) are concentrated to lines, marked in the figure with dotted lines. The interfaces are mostly enriched in Ni and Si, but also in Mn, Mo, P, and in the CL case C. The Ni enrichment appears to increase from CL and CB-0.15 to CB-1 and CB-2. In CB-2, there are features (Ni-Si particles) closer to, or going out from, the phase boundary than in the other analyses, thus the varying Ni content in the austenite. The CB-0.15 material shows a larger extent of P segregation to the boundary than the other materials. In the irradiated materials, there is in general a depleted zone in the ferrite (around 10 nm thick) close to the boundary where no G-phase precipitates are found, as the boundary itself is attracting Ni and Si and thus

depleting the volume. In CB-1 and CB-2, there is also a depleted zone where no Ni-Si particles appear in the austenite close to the boundary (seen for instance in the left reconstruction of Figure 12).

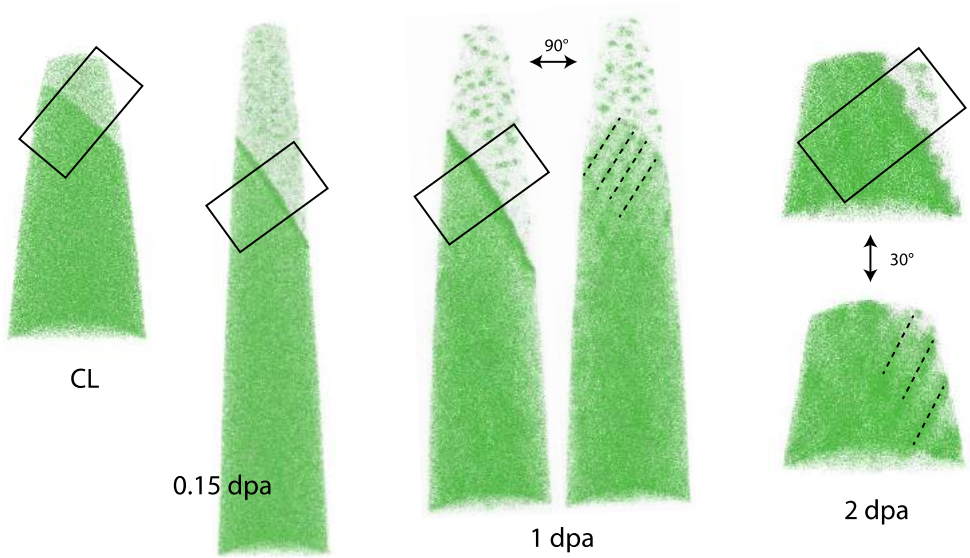

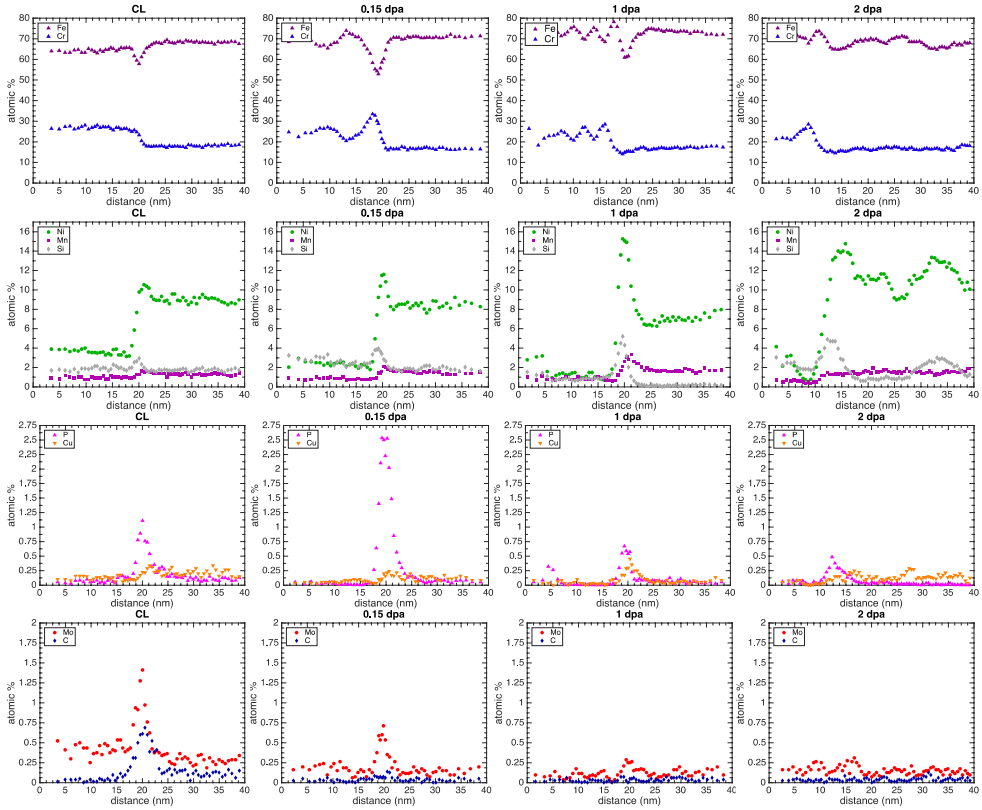

Figure 13. The austenite/ferrite boundaries. Ni atoms are shown as green and Si atoms as grey. CB-1 and CB-2 are rotated to show the lines of solutes in the interfaces. The boxes (20×20×40 nm³) show the volumes used for the concentration profiles (ferrite to the left and austenite to the right) displayed beneath the reconstructions.

3.3.2 Carbides

Cr-rich carbides, also enriched in Mo and V, were found at the phase boundaries in the irradiated materials. An example of this is shown in Figure 14, where the carbide sits in a ferrite/austenite boundary of the CB-2 material. The carbide appears to be facetted towards the ferrite in the top part of the figure. There is clear P segregation to the carbide boundaries towards both ferrite and austenite. In addition to this, the carbide contain an internal interface, with a layer of P and Si going through (marked with iii) in the figure). The carbide composition appears to be similar close to the ferrite and to the austenite interfaces. One other instance of a carbide-austenite boundary was found in the CB-2 material, with surface proxigrams almost identical to the ones in Figure 14. This carbide also showed internal boundaries enriched in P and Si.

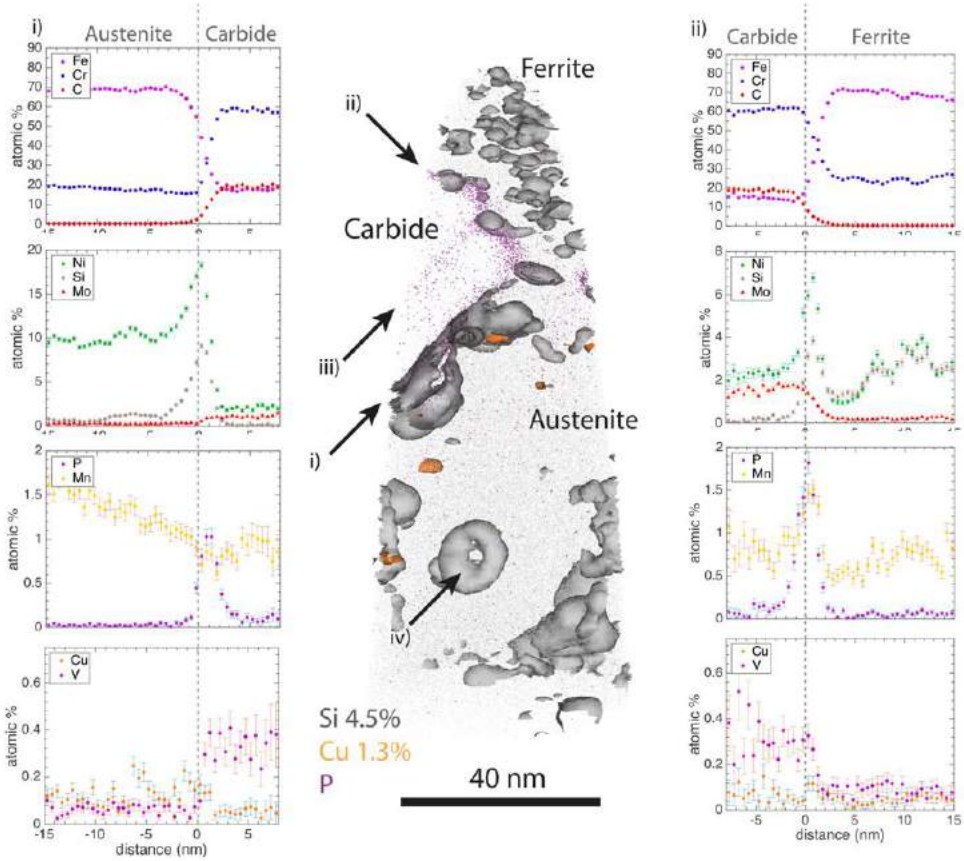

Figure 14. Material irradiated to 2 dpa. Ferrite, austenite and a carbide in the boundary. i) Austenite/carbide interface including proxigrams of Fe, Cr, C, Ni, Si, Mo, P, Mn, Cu, and V. ii) Carbide/ferrite interface including proxigrams of the same elements. iii) a boundary in the carbide enriched in P and Si. iv) a loop enriched in Ni and Si.

Figure 14 contains the only analysis where the carbide/ferrite interface was captured using APT. A difference between the carbide/ferrite and the carbide/austenite interface is that Mn was segregated to the former. Austenite/carbide boundaries were also observed in CB-0.15, shown in Figure 15. The proxigrams of Fe, Cr, and C are similar to the material irradiated to higher dose. The amount of Ni and Si segregating to the austenite/carbide boundary is significantly lower than in CB-2. Unlike at the ferrite/austenite interfaces, the P segregation is similar in CB-0.15 and CB-2. In this carbide, a layer of P and Si is found as well (marked ii) in the figure).

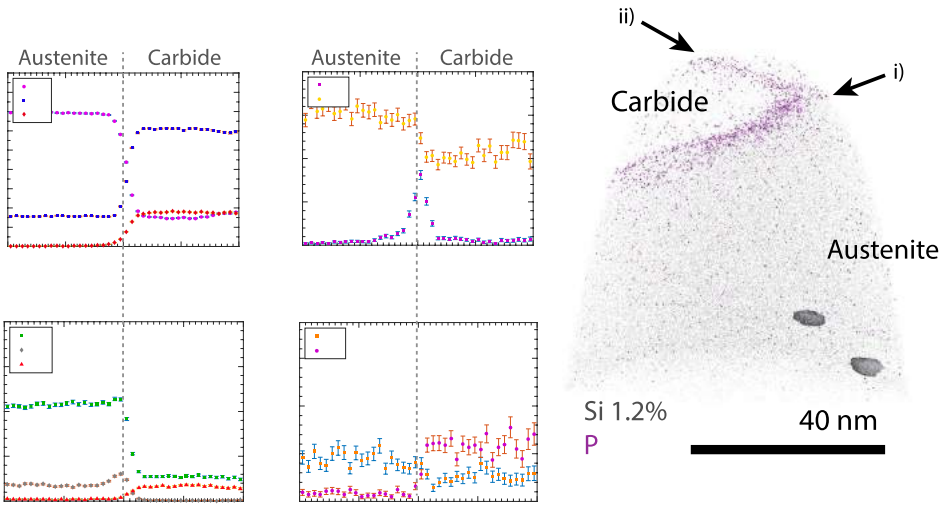

Figure 15. Material irradiated to 0.15 dpa. i) an austenite/carbide interface decorated with P. The corresponding proxigrams are shown to the left in the figure. ii) a layer in the carbide. Two Ni-Si precipitates are present in the bottom right corner of the analysis.

4. Discussion

In this study we have found significant microstructural changes that are attributed to the neutron irradiation and thermal ageing of the material, in both the ferrite, in the austenite and at the boundary between the two phases.

4.1 Ferrite

In the CL material, no apparent spinodal decomposition was found to take place after thermal ageing for 70,000 h. CL is a relevant comparison and reference to the irradiated materials, as the ageing temperature of 291°C is only slightly higher than the 280-285°C that is the temperature experienced by the irradiated materials. The equivalent ageing can, assuming 281°C for the irradiated core barrel welds, and using the Arrhenius equation with activation energy of 243kJ/mole, be calculated for CL and HL to 188,000 h and 3,590,000 h, respectively [29]. Comparing the results of the CL weld and the irradiated materials, it is obvious that the neutron irradiation is central in the degradation of the materials, as CL shows no degradation in terms of spinodal decomposition and G-phase formation. The degree of spinodal decomposition, in terms of both wavelength and amplitude, seems to be almost independent of dose (at least in the range of 0.15-2 dpa), but there is an effect of the local Cr concentration. The observation that a higher Cr content speeds up the decomposition is expected [22].

The G-phase was found to be more well-developed in CB-1 and CB-2 than in CB-0.15 and HL. Thus, the G-phase is the largest difference between CB-0.15 and the materials irradiated to higher doses, as the spinodal decomposition appears to be close to saturation already in the CB-0.15 material. In CL, no G-phase precipitation was

observed. The G-phase number density being lower after irradiation to 1 dpa than 2 dpa is probably at least partly due to the considerably lower Ni content in the CB-1 material analysed.

4.2 Austenite

In the austenite, Ni-Si precipitates were found in the irradiated materials, in accordance with what is expected from other studies of neutron irradiated austenite [7, 31]. The Ni/Si ratio was lower than 3, that is expected for γ'-Ni_3Si precipitates. Furthermore, a few dislocation loops were found in the APT reconstructions, due to the Ni and Si segregation (Figures 12 and 14). Loops cannot be seen using APT as long as they are not decorated with any solute atoms. Thus, transmission electron microscopy (TEM) is needed to quantify the loops, also because larger volumes can be studied. A question is if some, or all, of the Ni-Si particles might be nucleated on loops, but grown into a different shape after the initial nucleation step, as the amount of Ni and Si attracted increased. Chen et al. found a difference in number density of particles and loops with more than a factor of ten in proton irradiated 304 steel, with more Ni-Si precipitates than loops [32]. The same difference in number density was found for 24 dpa neutron irradiated 304 steel by Toyama et al. [31], indicating that the Ni-Si precipitates can nucleate without the presence of loops observable by TEM, so it is realistic to believe that not all observed Ni-Si precipitates are related to loops and that all loops are enriched in Ni and Si.

4.3 Ferrite/austenite boundaries

When considering the boundaries between ferrite and austenite (Figure 13), many of the solutes appear to be affected by the ageing, as their segregation differs from that in the CL material. The degree of ageing of CL itself cannot be stated in this study due to the absence of unaged reference materials. The level of Ni and Si segregated to the phase boundaries is clearly affected, with more segregation in CB-0.15 than in CL, and even more in CB-1 and CB-2 than in CB-0.15.

When irradiated to 1 and 2 dpa, elongated Ni-Si particles are formed on the interface with periodical distances. Their presence in only these materials might be due to the higher Ni- and Si-segregation to the phase boundaries. They have an appearance similar to segregations at low angle grain boundaries, and it is thus probable that their spacing is related to the relative crystallographic directions of the ferrite and the austenite grains. In duplex steels ferrite and austenite often have orientation relationships of either Kurdjumov-Sachs or Nishyiama–Wassermann [33], although it was not investigated here.

The Mn trend is hard to distinguish from the profiles, as there is no apparent enrichment in the CB-2 material. Also the P enrichment trend is unclear, with much more in the CB-0.15 phase boundary (up to 2.5 at.%) than in the other materials (0.5-0.75 at.%). There might be a dependence on the level of segregation and the crystallography of the phase boundaries, but, in this study we have no information on the angles and types of boundaries. However, it is also possible that a low level of irradiation (0.15 dpa) promotes P segregation (radiation induced segregation [34]), but that with higher dose,

P is rather enriched at Ni-Si precipitates in the austenite and in the G-phase precipitates in the ferrite, thus leaving the boundary.

A significant difference between CL and the irradiated materials is the level of Mo and C at the phase boundaries, that is much higher in the thermally aged material. For Mo, there might be a decreasing enrichment with dose. The higher C and Mo at CL phase boundaries might partly be explained by that the C content is higher in CL (<0.02 wt%) than in the irradiated material (0.06 wt%) [17, 19]. On the other hand, it seems likely that the increase in segregation of Ni, Si, etc. will make C and Mo leave the boundary. Furthermore, C and Mo could have a driving force for entering the Cr-carbides already existing at the phase boundary.

4.4 Carbides

Cr-carbides were observed at the ferrite/austenite boundaries in CB-0.15 and CB-2, but not in any of the thermally aged materials. This might be a coincidence due to the small volumes analysed when using APT. There could also be differences in the carbide presence in thermally aged and irradiated material, either from fabrication or due to the neutron irradiation. The higher nominal C content of the irradiated materials most probably results in a higher carbide content from fabrication. From the measured C concentration (about 20 at.%) and the metallic content, it is assumed that the carbides are of the $M_{23}C_6$ type. These carbides are commonly seen in similar welds in the ferrite/austenite boundary [35]. There are also indications of the carbides precipitating during ageing, at higher temperatures (for instance at 475°C [36], or 400°C [9]).

4.5 Influence of microstructure on mechanical properties

The question of the impact of the microstructure on the mechanical properties is complex, due to the many different degradation modes in the material. Spinodal decomposition is known to affect the mechanical properties of duplex steels. The influence of G-phase formation is debated, with some results suggesting that it does affect the properties marginally and some that it does significantly impact the mechanical properties [2]. There is also a possibility of an indirect dependence due to the changed composition of the surrounding G-phase, that in turn affects the spinodal decomposition [2, 9].

In addition to the contribution to mechanical properties from the ferrite, the ferrite/austenite interface needs to be considered. The Ni and Si forming a layer (CL and CB-0.15) or particles (CB-1 and CB-2) at the phase boundary might increase the tendency of intergranular fracture. The segregation of for instance P could lead to embrittlement [37]. Carbides also affect the mechanical properties [38]. As carbides are very hard and brittle, they are common starting points for cracks. Thus, the question if they are there from the manufacturing of the welds and if they grow during ageing is important to consider when considering the change in mechanical properties. The adhesion between the carbides and the ferrite and austenite might also affect the brittleness of the material. Figure 14 and 15 show P around the carbide. Further work needs to be done to characterize the amount of carbides in the phase boundaries,

presumably using electron microscopy, to get a larger field of view and obtain better statistics on their presence and the amount of ferrite/austenite interface they are covering.

In the irradiated materials, the ferrite constitutes only 6% of the total volume, and thus changes in the austenite are inevitably important for the mechanical properties. In the austenite of the irradiated materials, Ni-Si precipitates were found to varying extent. These surely make the material harder and might also make the material embritteled [7]. In addition to the precipitates, a few loops decorated with Ni and Si were found, which might also affect the mechanical properties [5].

It is known that the irradiated José Cabrera materials show significant irradiation hardening [19]. In a future publication (or a future version of this publication), the effects of the different degradation mechanisms on mechanical properties will be further discussed.

5. Conclusions

Both welds irradiated up to 2 dpa during 231,000 h and thermally aged welds (70,000 h at 291 and 325°C) have been studied. In general, the difference between irradiation to 1 and 2 dpa was small. It was found that:

- The spinodal decomposition of the ferrite was almost saturated after neutron irradiation to 0.15 dpa. There were no significant differences between CB-1 and CB-2 in the decomposition. The wavelengths were 6-9 nm irrespective of dose. The Cr amplitudes were found to be 21-24 at.%, 24-26 at. % and 24-26 at.% for CB-0.15, CB-1 and CB-2, respectively.
- The spinodal decomposition was more developed in grains with higher Cr content, with a linear relasionship between wavelength and Cr concentration.
- Thermal ageing at 291°C (the CL material) was not enough to obtain spinodal decomposition. However, thermal ageing at 325°C for the same time (the HL material) significantly changed the Cr and Fe distributions in the ferrite, giving spinodal decomposition with a wavelength of 5 nm and Cr amplitude of 13-14 at.%.
- G-phase was found in the HL, CB-0.15, CB-1 and CB-2 materials. There is a significant difference between CB-0.15, and CB-1 and CB-2, with larger (2 nm in diameter) and more well defined G-phase precipitates after higher dose. The composition of the G-phase is close to the nominal $Ni_{16}Si_7Mn_6$.
- The Ni and Si enrichment of the ferrite/austenite boundaries increased from CB-0.15 to CB-1 and CB-2, where precipitates were formed in the boundary.
- Ni-Si precipitates with Ni/Si ratios between 1.6 and 2.7 were found in the austenite of the irradiated materials. Also Cu-rich clusters and loops decorated with Ni and Si were found in the CB-1 and CB-2 materials. In the thermally aged materials, the distribution of solute elements of the austenite was found to be random.
- P cluster were observed in the austenite irradiated to 0.15 dpa.
- Cr-rich carbides, presumably in the ferrite/austenite boundary, were found. It is unclear if they were formed during fabrication or during irradiation.

At this stage, it is unclear which of all of these types of degradation that is contributing most to the degradation of the properties of the material. In order to say anything on this, further studies are needed.

Acknowledgements

EPRI is thanked for funding and contributing with the irradiated materials. Furthermore, the Swedish Radiation Safety Authority (SSM) is acknowledged for funding, and Ringhals for providing the thermally aged weld metals.

References

[1] K.H. Lo, C.H. Shek, J.K.L. Lai, Recent developments in stainless steels, Materials Science and Engineering: R: Reports 65(4-6) (2009) 39-104.
[2] F. Danoix, P. Auger, Atom Probe Studies of the Fe–Cr System and Stainless Steels Aged at Intermediate Temperature: A Review, Materials Characterization 44(1-2) (2000) 177-201.
[3] M.K. Miller, J. Bentley, APFIM and AEM investigation of CF8 and CF8M primary coolant pipe steels, Materials Science and Technology 6(3) (1990) 285-292.
[4] A. Etienne, B. Radiguet, P. Pareige, J.P. Massoud, C. Pokor, Tomographic atom probe characterization of the microstructure of a cold worked 316 austenitic stainless steel after neutron irradiation, Journal of Nuclear Materials 382(1) (2008) 64-69.
[5] C. Pokor, Y. Brechet, P. Dubuisson, J.P. Massoud, X. Averty, Irradiation damage in 304 and 316 stainless steels: experimental investigation and modeling. Part II: Irradiation induced hardening, Journal of Nuclear Materials 326(1) (2004) 30-37.
[6] Z. Jiao, G.S. Was, Novel features of radiation-induced segregation and radiation-induced precipitation in austenitic stainless steels, Acta Materialia 59(3) (2011) 1220-1238.
[7] E.A. Kenik, J.T. Busby, Radiation-induced degradation of stainless steel light water reactor internals, Materials Science and Engineering: R: Reports 73(7-8) (2012) 67-83.
[8] C. Pareige, S. Novy, S. Saillet, P. Pareige, Study of phase transformation and mechanical properties evolution of duplex stainless steels after long term thermal ageing (>20years), Journal of Nuclear Materials 411(1-3) (2011) 90-96.
[9] H.M. Chung, T.R. Leax, Embrittlement of laboratory and reactor aged CF3,CF8, and CF8M duplex stainless steels, Materials Science and Technology 6(3) (1990) 249-262.
[10] W. Guo, D.A. Garfinkel, J.D. Tucker, D. Haley, G.A. Young, J.D. Poplawsky, An atom probe perspective on phase separation and precipitation in duplex stainless steels, Nanotechnology 27(25) (2016) 254004.
[11] T. Hamaoka, A. Nomoto, K. Nishida, K. Dohi, N. Soneda, Accurate determination of the number density of G-phase precipitates in thermally aged duplex stainless steel, Philosophical Magazine 92(22) (2012) 2716-2732.
[12] T.G. Lach, A. Devaraj, K.J. Leonard, T.S. Byun, Co-dependent microstructural evolution pathways in metastable δ-ferrite in cast austenitic stainless steels during thermal aging, Journal of Nuclear Materials 510 (2018) 382-395.

[13] P. Hedström, F. Huyan, J. Zhou, S. Wessman, M. Thuvander, J. Odqvist, The 475°C embrittlement in Fe–20Cr and Fe–20Cr–X (X=Ni, Cu, Mn) alloys studied by mechanical testing and atom probe tomography, Materials Science and Engineering: A 574 (2013) 123-129.
[14] K. Fujii, K. Fukuya, Effects of radiation on spinodal decomposition of ferrite in duplex stainless steel, Journal of Nuclear Materials 440(1-3) (2013) 612-616.
[15] O.A. Korchuganova, M. Thuvander, A.A. Aleev, S.V. Rogozhkin, T. Boll, T.V. Kulevoy, Microstructural evolution of Fe22%Cr model alloy under thermal ageing and ion irradiation conditions studied by atom probe tomography, Journal of Nuclear Materials 477 (2016) 172-177.
[16] M. Bjurman, K. Lindgren, M. Thuvander, P. Ekström, P. Efsing, Microstructural Evolution of Welded Stainless Steels on Integrated Effect of Thermal Aging and Low Flux Irradiation, in: J.H. Jackson, D. Paraventi, M. Wright (Eds.) the 18th International Conferece on Environmental Degradation of Materials in Nucler Power Systems - Water Reactors, Springer, 2018, pp. 703-710.
[17] M. Bjurman, M. Thuvander, K. Lindgren, P. Efsing, Thermal aging and irradiation of cast and welded stainless steels and the influence on LTO, Fontevraud 9, Avignon, 2018.
[18] M. Bjurman, M. Thuvander, F. Liu, P. Efsing, Phase Separation Study of In-service Thermally Aged Cast Stainless Steel – Atom Probe Tomography, 17th International Conference on Environmental Degradation of Materials in Nuclear Power Systems – Water Reactors, Ottawa, 2015.
[19] A. Jenssen, J. Stjärnsäter, K. Kese, R. Carter, J. Smith, A. Demma, M. Hiser, Fracture toughness testing of an irradiated PWR core barrel weld, Fontevraud 9, Avignon, 2018.
[20] D.J. Larson, D.T. Foord, A.K. Petford-Long, H. Liew, M.G. Blamire, A. Cerezo, G.D.W. Smith, Field-ion specimen preparation using focused ion-beam milling, Ultramicroscopy 79(1-4) (1999) 287-293.
[21] K. Thompson, D. Lawrence, D.J. Larson, J.D. Olson, T.F. Kelly, B. Gorman, In situ site-specific specimen preparation for atom probe tomography, Ultramicroscopy 107(2-3) (2007) 131-9.
[22] J. Zhou, J. Odqvist, M. Thuvander, P. Hedstrom, Quantitative evaluation of spinodal decomposition in Fe-Cr by atom probe tomography and radial distribution function analysis, Microsc Microanal 19(3) (2013) 665-75.
[23] F. Vurpillot, B. Gault, B.P. Geiser, D.J. Larson, Reconstructing atom probe data: a review, Ultramicroscopy 132 (2013) 19-30.
[24] B. Gault, S.T. Loi, V.J. Araullo-Peters, L.T. Stephenson, M.P. Moody, S.L. Shrestha, R.K. Marceau, L. Yao, J.M. Cairney, S.P. Ringer, Dynamic reconstruction for atom probe tomography, Ultramicroscopy 111(11) (2011) 1619-24.
[25] O.C. Hellman, J.A. Vandenbroucke, J. Rüsing, D. Isheim, D.N. Seidman, Analysis of Three-dimensional Atom-probe Data by the Proximity Histogram, Microscopy and Microanalysis 6(5) (2000) 437-444.
[26] J.M. Hyde, C.A. English, An Analysis of the Structure of Irradiation induced Cu-enriched Clusters in Low and High Nickel Welds, Materials Research Society Symposium, Boston, 2000, pp. R6.6.1-R6.6.12.
[27] D. Vaumousse, A. Cerezo, P.J. Warren, A procedure for quantification of precipitate microstructures from three-dimensional atom probe data, Ultramicroscopy 95 (2003) 215-221.
[28] K. Lindgren, K. Stiller, P. Efsing, M. Thuvander, On the Analysis of Clustering in an Irradiated Low Alloy Reactor Pressure Vessel Steel Weld, Microsc Microanal 23(2) (2017) 376-384.

[29] M. Bjurman, B. Forssgren, P. Efsing, Fracture Mechanical Testing of In-Service Thermally Aged Cast Stainless Steel, in: Z. Wei, P.C. McKeighan, D.G. Harlow (Eds.), Fatigue and Fracture Test Planning, Test Data Acquisitions and Analysis, ASTM STP1598, ASTM international, West Conshohocken, PA, 2017, pp. 58-80.
[30] P. Auger, F. Danoix, A. Menand, S. Bonnet, J. Bourgoin, M. Guttmann, Atom probe and transmission electron microscopy study of aging of cast duplex stainless steels, Materials Science and Technology 6(3) (1990) 301-313.
[31] T. Toyama, Y. Nozawa, W. Van Renterghem, Y. Matsukawa, M. Hatakeyama, Y. Nagai, A. Al Mazouzi, S. Van Dyck, Irradiation-induced precipitates in a neutron irradiated 304 stainless steel studied by three-dimensional atom probe, Journal of Nuclear Materials 418(1-3) (2011) 62-68.
[32] Y. Chen, P.H. Chou, E.A. Marquis, Quantitative atom probe tomography characterization of microstructures in a proton irradiated 304 stainless steel, Journal of Nuclear Materials 451(1-3) (2014) 130-136.
[33] E.F. Monlevade, I.G.S. Falleiros, Orientation Relationships Associated with Austenite Formation from Ferrite in a Coarse-Grained Duplex Stainless Steel, Metallurgical and Materials Transactions A 37(3) (2006) 939-949.
[34] G.S. Was, Fundamentals of Radiation Materials Science, Springer, Berlin, 2007.
[35] R.W.K. Honeycombe, Transformation from Austenite in Alloy Steels, Metallurgical Transactions A 7A (1976) 915-936.
[36] J.M. Vitek, S.A. David, D.J. Alexander, J.R. Keiser, R.K. Nanstad, Low Temperature Aging Behaviour of Type 308 Stainless Steel Weld Metal, Acta Metallurgica et Materialia 39(4) (1991) 503-516.
[37] C.L. Briant, P.L. Andresen, Grain Boundary Segregation in Austenitic Stainless Steels and Its Effect on Intergranular Corrosion and Stress Corrosion Cracking, Metallurgical Transactions A 19A (1988) 495-504.
[38] S. Mburu, R.P. Kolli, D.E. Perea, S.C. Schwarm, A. Eaton, J. Liu, S. Patel, J. Bartrand, S. Ankem, Effect of aging temperature on phase decomposition and mechanical properties in cast duplex stainless steels, Materials Science and Engineering: A 690 (2017) 365-377.